Scuola Internazionale Superiore di Studi Avanzati - Trieste

Doctoral Thesis

Gamma-ray burst prompt emission: new insights into spectral characterization

Author:
Gor Oganesyan

Supervisors:
Prof. Annalisa Celotti
Dr. Lara Nava
Dr. Giancarlo Ghirlanda

A thesis submitted in fulfillment of the requirements for the degree of Doctor of Philosophy

in

Astrophysics

October 2018

SISSA - Via Bonomea 265 - 34136 TRIESTE - ITALY

Abstract

The origin of gamma-ray burst (GRB) prompt emission is a debated issue, strictly connected to fundamental open problems such as jet composition, energy dissipation and radiation mechanisms. The radiative processes responsible for the prompt radiation are remaining uncertain. The typical observed prompt emission spectrum in the νF_ν representation consists of two power-laws smoothly connected at a peak energy. Its non-thermal spectral shape calls for synchrotron or inverse Compton radiation, but the hardness characterizing the low-energy part of the spectra is inconsistent with these processes. The unestablished nature of the prompt radiation has strong repercussions on our understanding of the GRB phenomenon, preventing us from constraining macro- and micro-physical properties of the source. While the prompt emission is usually observed only between 10 and 10^3 keV, in this thesis I extend the energy range for prompt studies down to soft X-rays for those cases where Swift/XRT (0.3-10 keV) started observations during the prompt phase (34 GRBs). My analysis revealed for the first time that prompt spectra often ($\sim 65\%$) display spectral break at a few keV. Below the break, the spectrum is well described by a power-law with hard photon index (-2/3). The overall shape is consistent with synchrotron radiation, where the break energy corresponds to the cooling break. I added, when available, simultaneous optical observations, providing an additional and independent test on the presence of the low-energy break. In the synchrotron scenario, the small ratio between peak energy and cooling energy points toward a moderately-fast cooling regime. In a simple scenario where electrons are accelerated only once, this regime implies weak magnetic fields ($<$ 10-100 G in the fluid comoving frame). In alternative scenarios, these strong constraints on the magnetic field can be relaxed by invoking almost balanced electron cooling and heating rates and/or multiple acceleration in magnetic reconnection islands.

Thesis overview

The physics of the GRB prompt emission is under debate. We still do not fully understand the mechanisms of relativistic jet formation and its constituents. The dissipation of the jet energy causes the observed prompt emission. However, the dominant radiative processes responsible for the observed spectra of the prompt emission are not identified yet.

The proposed synchrotron radiation scenario in fast-cooling regime (Rees and Meszaros, 1994a; Katz, 1994; Tavani, 1996; Sari, Narayan, and Piran, 1996; Sari, Piran, and Narayan, 1998) fails to describe the shapes of the observed prompt emission spectra. The typical photon index below the peak energy seen in the prompt emission spectra $< \alpha >\sim -1$ is much harder than predicted $\alpha = -1.5$ (Preece et al., 1998; Frontera et al., 2000; Ghirlanda, Celotti, and Ghisellini, 2002a; Kaneko et al., 2006a; Sakamoto et al., 2011b; Nava et al., 2011a; Goldstein et al., 2012; Gruber et al., 2014; Lien et al., 2016).

The inability of interpreting the observed spectra of the prompt emission in terms of known non-thermal radiative processes prevents us to further constrain the physical properties of the emitting region. Therefore, the identification of the dominant radiative mechanism responsible for the prompt emission is one of the most crucial tasks we face.

This thesis attempts to widen our knowledge on the nature of the prompt emission. I focus on the observational properties of prompt emission spectra. The most explored energy window of prompt emission is 10 keV - 10 MeV. The systematic study of prompt emission spectra in this energy did not lead to a clear idea about its origin. The shape of the spectra below the peak contradicts the basic radiative processes proposed in the literature. I extend the spectral characterization of the prompt emission down to soft X-rays and optical range through a systematic spectral analysis.

In Chapter 1 I give a general introduction to the gamma-ray burst (GRB) phenomenon. A detailed introduction on the prompt emission spectral observables and the basic theoretical ingredients of the radiative processes are discussed in Chapter 2. The instruments providing the spectral data that were analyzed in this thesis are also described in Chapter 2.

Chapter 3 is devoted to the joint X- and γ-ray time-resolved analysis of prompt emission spectra. To better characterize the spectral shape at low energy, I analyzed 14 GRBs for which the Swift X-ray Telescope started observations ($0.5 - 10\,\mathrm{keV}$) during the prompt. When available, Fermi-GBM spectra ($8\,\mathrm{keV} - 40\,\mathrm{MeV}$) have been included in the analysis. For 67% of the spectra, models that usually give

a satisfactory description of the prompt (e.g., the cutoff power-law model) fail to reproduce the 0.5-1000 keV spectra: low-energy data outline the presence of a spectral break around a few keV. I introduce an empirical fitting function that includes a low-energy power law α_1, a break energy E_{break}, a second power law α_2, and a peak energy E_{peak}. I find $< \alpha_1 >$ =-0.66 ($\sigma = 0.35$), $< \log(E_{break}/keV) >= 0.63$ ($\sigma = 0.20$), $< \alpha_2 >= -1.46(\sigma = 0.31)$, and $< \log(E_{peak}/keV) >= 2.1(\sigma = 0.56)$. The values $< \alpha_1 >$ and $< \alpha_2 >$ are very close to expectations from synchrotron radiation. In this context, E_{break} corresponds to the cooling break frequency. The relatively small ratio $E_{peak}/E_{break} \sim 30$ suggests a regime of moderately fast cooling, which might solve the long-lasting problem of the apparent inconsistency between measured and predicted low-energy spectral index.

In Chapter 4, I test with an enlarged sample of joint X- and γ-ray prompt emission spectra for presence of low-energy breaks. The study of 34 GRBs confirms previous results with break energy varying between 3 keV and 30 keV. As a test, if I exclude XRT data from the fits I find typical results: the spectrum below the peak energy is described by a power law with $< \alpha >= -1.15$.

In Chapter 5, I discuss the results on the spectral modeling of bright GRB 160625B prompt emission performed in Ravasio et al. (2018). The spectral breaks at $100 - 300$ keV were found in the time-resolved spectra of the prompt emission. The photon indices below and above the break energy are close to synchrotron values.

In Chapter 6, I show the direct test of the synchrotron model on joint X- and γ-ray prompt emission spectra. I also compare the prediction of the synchrotron model in optical range with the data available for 21 GRBs.

In Chapter 7, I discuss the future observational prospects on the prompt emission. I briefly summarize the capabilities of upcoming space missions that have a potential to shed light on our understanding of the origin of prompt emission. More particularly, I make an example of how future wide field X-ray missions can help us to distinguish prompt emission models in its unexplored low-energy extension. I discuss the advantages of THESEUS mission presented in Nava et al. (2018).

I conclude with a brief summary about the results of the thesis in Chapter 8.

Declaration of Authorship

This thesis is a summary of the research projects performed during my Ph.D. Most of the work is based on the following papers/proceedings:

Chapter 3: G. Oganesyan, L. Nava, G. Ghirlanda, A. Celotti, *Detection of Low-energy Breaks in Gamma-Ray Burst Prompt Emission Spectra*, 2017, ApJ, 846, 137

Chapter 4: G. Oganesyan, L. Nava, G. Ghirlanda, A. Celotti, *Characterization of Gamma-Ray Burst prompt emission spectra down to soft X-rays*, 2018, A&A, 616, A138

Chapter 5: M. E. Ravasio, G. Oganesyan, G. Ghirlanda, L. Nava, G. Ghisellini, A. Pescalli, A. Celotti, *Consistency with synchrotron emission in the bright GRB 160625B observed by Fermi*, 2018, A&A, 613, A16, 11

Chapter 6: G. Oganesyan, L. Nava, A. Melandri, G. Ghirlanda, A. Celotti, *Prompt optical emission as signature of synchrotron radiation in Gamma-Ray Bursts*, in preparation

Chapter 7: L. Nava, G. Oganesyan, M. E. Ravasio, L. Amati, G. Ghirlanda, P. O'Brien, J. P. Osborne, R. Willingale, *THESEUS and Gamma-Ray Bursts: a valuable contribution to the understanding of prompt emission*, the Proceedings of the THESEUS Workshop 2017

Acknowledgements

This thesis is not only my performance but it is a work done under active supervision of my advisors Annalisa, Lara and Giancarlo. For my PhD, I was exceptionally lucky since I was learning how to do a research in a free, healthy and friendly environment. My experience at SISSA was little short of amazing. It started when I met Annalisa who spent tons of patience to help me building my first steps towards research. She organized my chaotic sentences into simple and clear research goals and plans. I met Lara and Giancarlo who were supervising me throughout these years by kindly sharing their experience with me. This thesis is a result of infinite loops of interactions with my advisors; my failures and mistakes and some successful moments. However, this thesis is also a result of different experiences I was having from many people at SISSA and outside whom I also want to thank.

I am infinitely thankful to Lara, who spent a huge amount of energy and time teaching me the principal components of a scientific performance. In each step of my research trials she oriented me for developing critical thinking, clearness of scientific purposes and methods. She has played a key role in establishing the results I have obtained during my PhD. The lessons she taught me have influenced a lot my research strategies.

I am infinitely thankful to Giancarlo. He was guiding my research projects all these years with a lot of enthusiasm and encouragement. He was continuously sharing with me his knowledge on experimental astrophysics, highly motivating to search for the results. His huge emotional and scientific energy has resulted in a very entertaining research process.

I am infinitely thankful to Annalisa. She provided me a necessary amount of freedom and challenged me to develop my own views and ideas. She was always open to share her knowledge and experience with me. Her support in each step of my work was crucial for me to not lose the path I was taking.

During my PhD I had a chance to visit the Astronomical Observatory of Brera several times. It was always a fantastic experience to interact with the GRB group. There I met Gabriele Ghisellini whom I want to thank for very useful discussions and conversations. I would like to thank Sergio Campana and Francesco Nappo for the very important instrumental help. I am particularly happy that I met Om, Alessio and Mery there. Working with them is always enjoying and fun!

In the very same building where I was working for my PhD, I found Elly, Franca, Andrej, Riki, Lorry, Hrach and Pacilio. I want to thank them for the amazing time we spent together! I am happy I met Elly whose philosophical perspectives often oppose

to mine, letting my views evolve. These years would be much darker without Franca, who was always ready to support any of our crazy ideas. I am proud to know Andrej who is always standing for high moral positions that became an example for me. Riki has opened to me a completely new way of perceiving the life. He also introduced me to the endless island of Sardinia where I met Mariangela, Anto, Laura Pillosu, Rita, Zambelli and many others whose support and love was very important these years.

I have special thanks to the dozen of individuals from my pre-SISSA life. They were constantly supporting me during the period I was far from them. Time-independent Lena and Vadi are always near, sharing their love and making things more interesting and adventurous. I am so happy to know Makarova and Igor with their particularities. They always allow me to feel free and out of standards. I was constantly happy and was keeping to move forward with a human exception named Alika. I could not reach any point without my closest friend Danil who passed away recently.

I would not reach the point of starting PhD without my incredible scientific advisor Gregory Beskin. He has introduced me to high-energy astrophysics years before coming to SISSA. Gregory was always believing in me even in the moments when I didn't have any trust in myself. His unique scientific culture has become a lesson for me I follow till now.

I finish my acknowledgments with the source of my life energy. It is about my family. They have a never-finishing budget of love. Ruzanna and Alik have sacrificed a lot for me from the war years till now. Anything I can give them is incomparable to what they have done for me. My little brother Hajk is challenging me to re-consider my views. My crazy "qujriks" Sona and Nelly are always near to support and share their love. My lovely Violetta is transmitting the wisdom of generations, not allowing anyone to give up. I could not be anything of who I am without Emma who based the spectrum of colors I know. I dedicate this thesis to her memory.

Contents

Chapter 1

Introduction

In this Chapter I give a general introduction to the gamma-ray burst (GRB) phenomenon. I first present a short history of the GRB discovery and observational/theoretical progresses. Then I describe briefly the observational properties of GRB prompt and afterglow radiation and I present the basic theoretical scenario widely used to interpret the observations. I conclude the Chapter with a discussion of the current understanding of GRB progenitors and the central engine.

1.1 A historical overview

In 1967 the military *Vela* satellites discovered a new class of astrophysical sources (Klebesadel, Strong, and Olson, 1973), characterized by non-repeating variable emission of sub-MeV radiation lasting for tens of seconds with total fluence of $10^{-5}\,\mathrm{erg\,cm^{-2}}$. This emission is now called *prompt emission*. An example of time profile of a GRB discovered by *the Vela* satellites is shown in Fig. 1.1: The GRB light curve is composed by random pulses with a total duration of ~ 10 seconds.

The distance of GRBs and the possible existence of a counterpart at different frequencies were initially unknown since the gamma-ray detectors could not localize GRBs precisely enough. As a consequence, the proposed astrophysical origin of these events could either be Galactic or extragalactic and the total energy released in a typical GRB was the unknown.

Relevant progresses in the understanding of GRBs were made more than twenty years later, thanks to the Burst and Transient Source Experiment (*BATSE*) on board the Compton Gamma-Ray Observatory (*CGRO*) that started operations in 1991. *BATSE* detected about 3000 GRBs in the energy range $20\,\mathrm{keV} - 30\,\mathrm{MeV}$. *BATSE* showed that their angular distribution in the sky is isotropic (Meegan et al., 1992) thus providing the first hint for their extragalactic origin. The distribution of prompt emission duration T_{90}, was found to be bimodal (Kouveliotou et al., 1993) suggesting the existence of two classes with a rough separation around 2 s: short (T_{90}<2 s) and long (T_{90}>2 s) GRBs.

The *BeppoSAX* satellite, launched five years later, had an improved positioning accuracy (~ 4 arcmin) thanks to its X-ray detectors (the Wide Field Cameras, *WFC*). Before the launch of *BeppoSAX* only the prompt emission of GRBs was known and

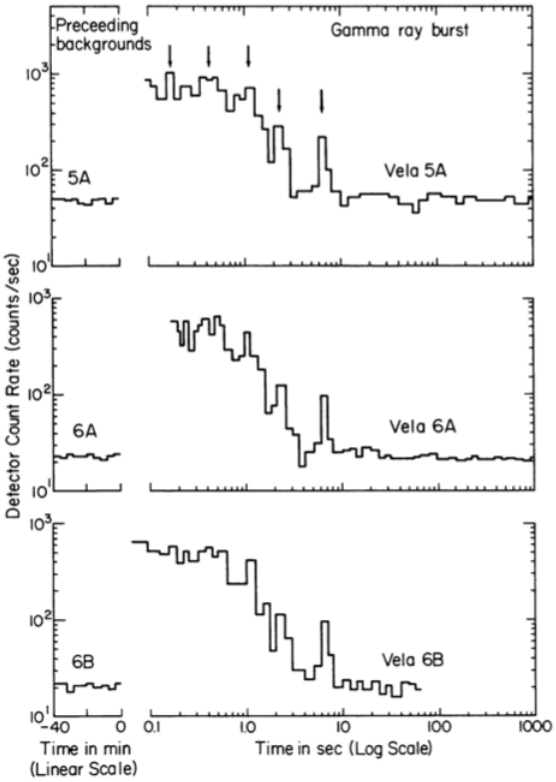

FIGURE 1.1: Light curve of a GRB detected by the Vela satellite in 1970. The emission corresponds to photons' energies in the range 0.2-1 MeV (Vela 5) and 0.3-1.5 MeV (Vela 6). Credit: Klebesadel, Strong, and Olson, 1973

no counterparts at any other wavelength could be associated with these short elusive events. BeppoSAX had the merit to discover the long-lived, monotonically fading with time, counterpart, known as *the afterglow*. The X-ray afterglow of GRB 970228 (Fig.1.2) was detected after almost 8 hours by *the WFC* (Costa et al., 1997). The improved localization of the GRB source by *the WFC* allowed the detection of the first optical afterglow less than 21 hours after GRB 970228 detection (van Paradijs et al., 1997). This discovery led to the localization of the faint host galaxy and to the measurement of its redshift directly proving the extragalactic origin of GRBs.

Today we know that GRBs are cosmological sources detected up to redshift z ∼9.4 with the observed redshift distribution which peaks around a typical $z \sim 2$. The cosmological distances of GRBs require an extreme luminosity $\sim 10^{52}\,\mathrm{erg\,s^{-1}}$.

The widely accepted hypothesis on the nature of the GRB progenitor was the birth of a compact object. The merging of compact objects (Eichler et al., 1989) and the core-collapse of Wolf-Rayet stars (Woosley, 1993) end up with the birth of stellar mass black hole and mass ejection, leading to the production of a GRB. Compact objects merging was expected to explain the origin of short GRBs and the death of a massive star (over $10M_{\odot}$) of long GRBs. The first evidence of a supernova associated with GRB was discovered in 1998 (Galama et al., 1998). Further discovered supernovae associated with long GRBs supported the idea of them to originate from

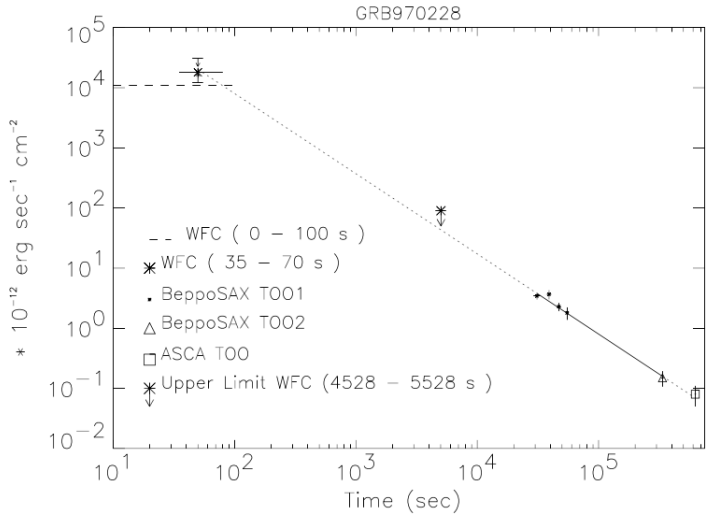

FIGURE 1.2: The first X-ray counterpart detected by *BeppoSAX* after almost 8 hours from the detection time of the prompt emission. Credit: Costa et al., 1997

the core-collapse of massive stars. The confirmation of the merging hypothesis for the short GRBs was found only recently thanks to the detection of the gravitational wave event GW170817 in association to the short GRB 170817A (Abbott et al., 2017). The gravitational wave signal of GW170817 corresponds to the merging of two neutron stars.

The interest in GRB physics had generally grown from the time they were discovered, motivating the launch of several X-ray and $\gamma-$ray instruments, such as KONUS on board of the WIND spacecraft in 1994 (*KONUS/WIND*), the High Energy Transient Explorer (*HETE-2*) in 2000, the INTErnational Gamma-Ray Astrophysics Laboratory (*INTEGRAL*) in 2002, the Neil Gehrels Swift Observatory (*Swift*) in 2004, the Astro-Rivelatore Gamma a Immagini Leggero (*AGILE*) in 2007, and the Fermi Gamma-ray Space Telescope (*Fermi*) in 2008. Moreover, the active follow-up of GRB counterparts is performed by ground based optical and radio telescopes. Recently, GRBs became subject of study of the multi-messenger astronomy which involves the search of gravitational wave signals and neutrinos.

The high rate of GRB detections (a few per week) with the following observations on their counterparts at X-ray, optical and radio bands allow us not only to study the physics of GRBs and their progenitors but also to explore the early Universe e.g. using GRBs as cosmological probes (Ghirlanda et al., 2004; Amati et al., 2008).

1.2 The general concept

The basic model of the GRB phenomenon hitherto established is summarized here. The death of a massive star (over $10M_{\odot}$) or the merging of compact objects (neutron stars or a system of a neutron star and a black hole) gives the birth of a black hole. Accretion into the newly formed black hole launches a relativistic jet. The internal

dissipation of the jets energy through shocks at $R_\gamma \sim 10^{12}\,\mathrm{cm} - 10^{16}\,\mathrm{cm}$ produces the observed short-duration ($10^{-3} - 10^{3}\,\mathrm{s}$) prompt emission seen in the keV-MeV energy range. The deceleration of the jet in the surrounding medium gives rise to the long-lived afterglow observed in the X-ray, optical and radio bands. The characteristic physical size of the afterglow emitting region is $R_{\mathrm{aft}} \sim 10^{16} - 10^{17}\,\mathrm{cm}$. The sketch of the basic model of the GRB phenomenon is shown in Fig. 1.3.

In the following Sections I describe the observations of the prompt/afterglow emission and I also present the theoretical models circumstantially.

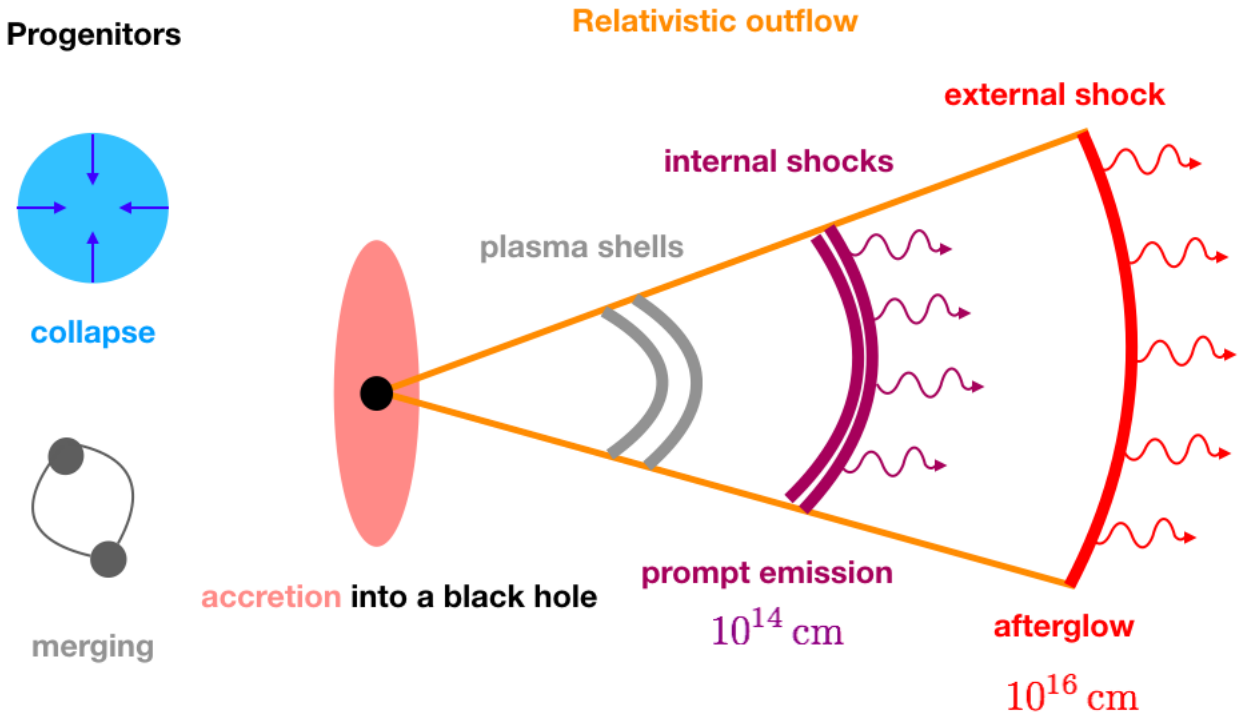

FIGURE 1.3: The sketch of the basic model of the GRB: The core-collapse of a massive star or the coalescence of binary neutron stars ends with a formation of a black hole. The accretion into the black hole launches an ultra-relativistic outflow in a form of a jet. Internal dissipation of the jet's energy through shocks produces the short-duration prompt emission in the keV-MeV range. The interaction of the jet with circumburst medium forms the long-lived afterglow radiation observed in the X-ray, optical and radio bands.

1.3 Prompt emission

1.3.1 Observations

The prompt radiation is the first emission phase of a GRB and the brightest and shortest in duration. The prompt emission is typically observed in the 10 keV - 1 MeV range. Its duration is estimated as a time during which a specific GRB detector

accumulates 90% of the photons (T_{90}). The GRB duration distribution extends over several orders of magnitude ($\sim 10^{-3} - 10^{3}$ s).

Examples of *Fermi* GRB light curves at 8 keV - 1MeV are shown in Fig. 1.4. The prompt emission light curves are irregular and different from burst to burst. A fraction ($\sim 10\%$) of long GRBs shows the presence of precursors, which are emission episodes preceding (tens to hundreds of seconds) the main GRB event. The prompt emission pulses are sometimes separated by quiescent periods of time.

Individual pulses of the prompt phase, if resolved, show a "fast rise - exponential decay" shape. Prompt emission pulses appear narrower in higher energy bands (Norris et al., 2005). Additionally, non-zero spectral lags are often observed in long GRBs typically with positive sign (pulses peak at earlier times in higher energy bands).

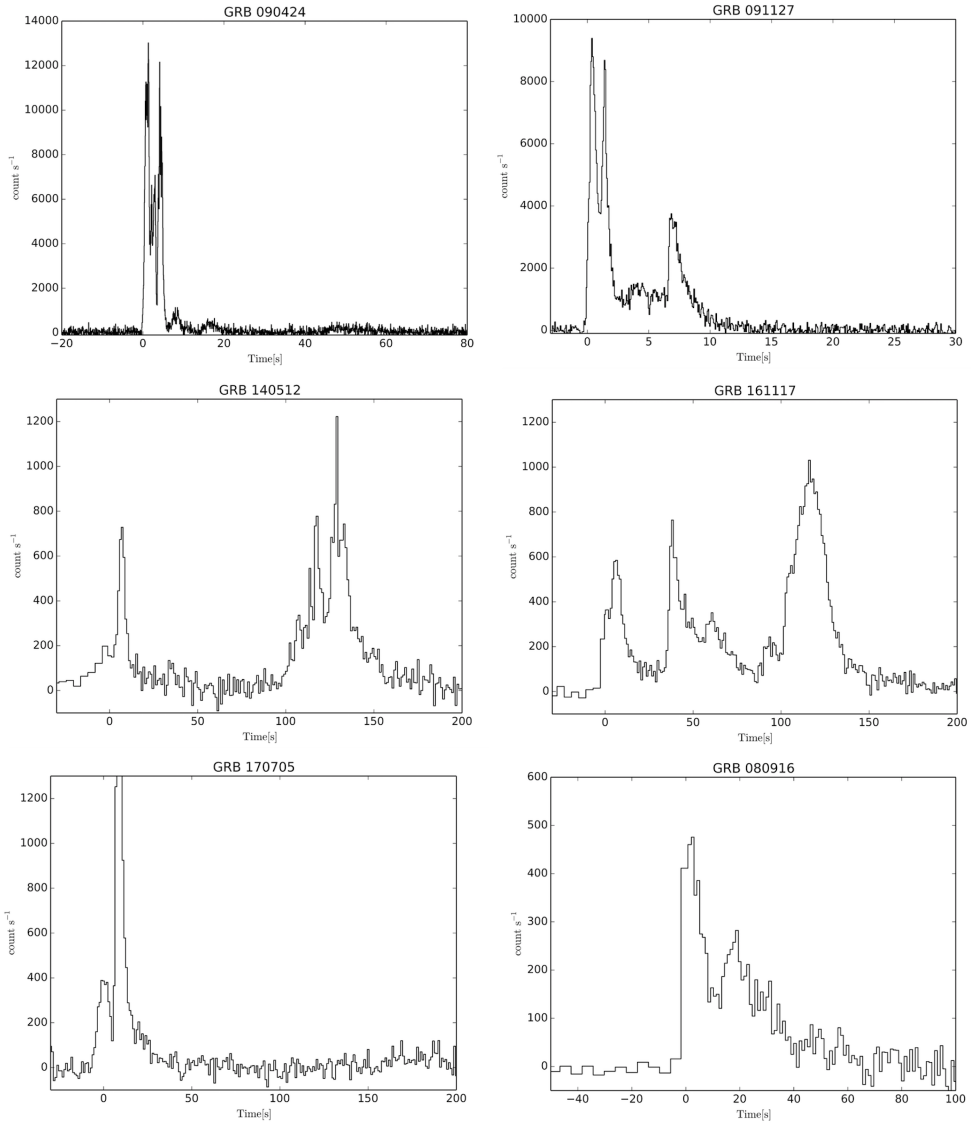

FIGURE 1.4: Examples of prompt emission light curves (background-subtracted) observed by the Fermi/GBM instrument in the range 8 keV - 1 MeV.

The typical photon counts spectrum (N_ν) of the prompt emission is modeled by

two power-law functions smoothly connected at a break energy. The spectrum N_ν is a decaying function of the energy. The function is steeper above the break energy. The power-law slopes below and above the break energy are characterized by the low- and high-energy photon indices α and β, respectively. The typical values are $\alpha \sim -1$ and $\beta \sim -2.3$ (e.g. Band et al., 1993, Ghirlanda, Celotti, and Ghisellini, 2002b, Kaneko et al., 2006b Nava et al., 2011b). The power-law shape at high energy favors a non-thermal nature.

The energy power spectrum (νF_ν) is defined as $\nu^2 N_\nu$. The typical prompt emission spectrum in the νF_ν representation is a peaked function. The characteristic peak energies of the prompt emission spectra are few hundreds of keV. The average flux of a prompt emission spectrum in the range $8\,\mathrm{keV} - 40\,\mathrm{MeV}$ (accumulated over the time interval of the prompt emission) is $\sim 3 \times 10^{-7} \mathrm{erg\,cm^{-2}\,s^{-1}}$ (e.g. Goldstein et al., 2012). The average flux ranges roughly between $10^{-7} \mathrm{erg\,cm^{-2}\,s^{-1}}$ and $10^{-5} \mathrm{erg\,cm^{-2}\,s^{-1}}$. The typical energy fluence in the range $8 - 1000\,\mathrm{keV}$ is $10^{-6} \mathrm{erg\,cm^{-2}}$ and its distribution extends over three orders of magnitude ($10^{-7} - 10^{-4} \mathrm{erg\,cm^{-2}}$).

1.3.2 The theoretical model

It was established that GRBs are extragalactic sources with typical redshift $z \sim 2$. A source at $z \sim 2$ with an observed fluence $\sim 10^{-6} \mathrm{erg\,cm^{-2}}$ corresponds to the isotropic energy release of $\sim 10^{52}\,\mathrm{erg}$. The typical variability-time scale of $10^{-2}\,\mathrm{s}$ defines the causally connected region to have a size of $\sim 3 \times 10^8\,\mathrm{cm}$. Such huge radiation energy packed in the small region would prevent high energy photons to leave the system. The optical depth to photon-photon annihilation (e.g. Piran and Shemi, 1993) exceeds 10^{10} for these observed parameters. The high energy power-law tail of the observed prompt emission spectra extends into the MeV range. The physical system should be accelerated to high bulk Lorentz factors ($\Gamma \sim 100$) in order to lower the optical depth to photon-photon annihilation of the high energy photons that we observe (e.g. Fenimore, Epstein, and Ho, 1993).

The astrophysical source with the above-mentioned parameters has a temperature of $\sim 10^{10}\,\mathrm{K}$ suggesting a co-existence of electron-positron pairs with photons in the thermal equilibrium. Paczynski (1986) and Goodman (1986) proposed the hot fireball model. A hot fireball made by an opaque photon-lepton reservoir is a consequence of a sudden release of high energy photons in a compact physical region. The fireball expands and its temperature decreases allowing photons to escape. A pure radiation fireball produces a thermal spectrum that is inconsistent with observed non-thermal prompt emission spectra.

If the fireball contains some amount of baryons, then the energy of the fireball will be transfered to the kinetic energy of baryons (Shemi and Piran, 1990). To provide an ultra-relativistic motion of the fireball ($\Gamma \sim 100$), the baryon load should be small. The kinetic energy of baryons can be transfered back to electrons through dissipation processes. Accelerated electrons produce non-thermal spectra through synchrotron and inverse Compton radiative processes.

The duration of pulses of the prompt emission do not change with time (Ramirez-Ruiz and Fenimore, 2000). This suggests a static emission region where prompt high energy photons are released. The distance of the emission region from the GRB central engine $R_\gamma \sim 10^{12} - 10^{16}$ cm can be estimated from the variability time-scale and the fact that the fireball should be optically thin.

Prompt emission is originated by internal dissipation of the relativistic outflow's energy. Two competing dissipation mechanisms are proposed. If most of the energy of the outflow is in the form of kinetic energy of baryons (protons), then internal shocks (Rees and Meszaros, 1994b) are the preferred dissipation mechanism. In this model the central engine of a GRB produces plasma shells (fireballs made of electron-positron pairs, photons and protons) with velocity contrast. As a faster shell catches a slower one, shocks propagate in both shells accelerating electrons which radiate prompt emission. The internal shock model easily accounts for the high temporal variability ($10^{-3} - 10^{-2}$ s) of the prompt emission and its non-thermal spectrum. Alternatively, if the outflow is dominated by magnetic energy, then magnetic reconnection is the dominant process for the dissipation. In both cases, the internal energy of the outflow is given to accelerate electrons which emit through synchrotron and/or inverse-Compton.

The accurate link of the prompt emission spectral properties to the radiative processes is one of the key points to understand the nature of the outflow composition and dissipation processes. The characterization of the prompt emission spectral features in a broad-band energy range is the main objective of this thesis. More detailed discussion of prompt emission spectral properties and the general theoretical implications on the physics of GRBs are presented in Chapter 2.

1.4 The Afterglow

1.4.1 Observations

The afterglow is observed as long-lived multi-wavelength emission in the X-ray, optical and radio bands. The observations of the afterglow emission were made mainly in optical range before the launch of *Swift*. Therefore, the basic afterglow theory was first tested on optical observations. The typical temporal behavior of the afterglow emission is a decaying power-law. Some optical afterglow light curves are shown in Fig. 1.5.

1.4.2 The theoretical model

The afterglow photons are assumed to arise from the external dissipation of the outflow energy. The supersonic flow of plasma interacts with the circumburst medium developing shocks. There are two main processes happening in such shocks: local magnetic field amplification and particle acceleration. The pre-existing magnetic field is amplified locally, most likely by Weibel instability (Weibel, 1959). The Fermi

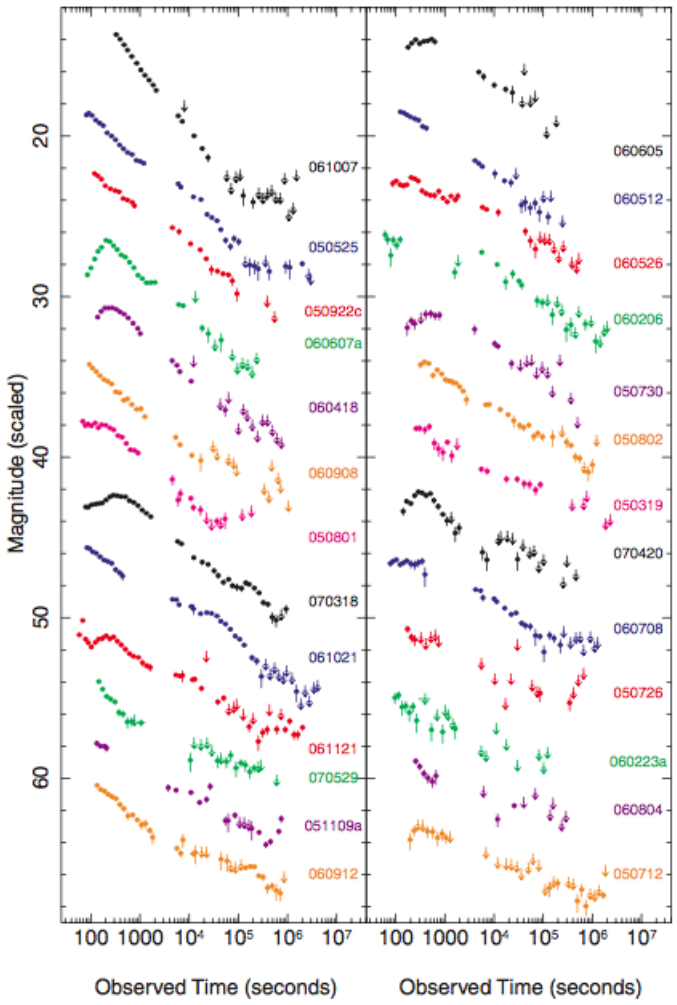

FIGURE 1.5: Light curves of a sample of optical afterglows. Credit: Oates et al., 2009

acceleration mechanism (Fermi, 1949) is widely accepted to be responsible for the formation of the non-thermal population of accelerated charged particles $N_\gamma \propto \gamma^{-p}$. In such process, charged particles repeatedly cross the shock front gaining an energy proportional to the velocity of the shock front. The shocks are propagating in two directions (Mészáros and Rees, 1997; Sari, Piran, and Narayan, 1998): into the external medium (forward shock or a blast wave) and into the outflow itself (reverse shock).

The forward shock (FS) sweeps up and accelerates the surrounding material. It is responsible for the production of the afterglow emission which is observed up to days/months after the prompt emission. If one considers a single spherical shell being released by the central machine of a GRB during a timescale t_0 with and energy E_0 and a mass M, then the deceleration radius of the forward shock can be roughly estimated as the radius r_{dec} at which the initial Lorentz factor of the shell $\Gamma_0 = E_0/Mc^2$ decreases by a factor of two ($\Gamma_{dec} = \Gamma_0/2$). Considering a homogeneous medium with hydrogen particles number density n one gets

$$E_0 = \frac{4\pi}{3} r_{dec}^3 n m_p c^2 \Gamma_{dec}^2 \tag{1.1}$$

Assuming an isotropic energy $E_0 \sim 10^{53}$ erg, $n \sim 1\,\mathrm{cm}^{-3}$, $\Gamma_0 \sim 500$ the typical radius is $r_{dec} \sim 6 \times 10^{16}$ cm. The corresponding timescale for the deceleration of the forward shock is then $t_{dec} \sim r_{dec}/2c\Gamma_{dec}^2$ and for the above mentioned parameters it is $t_{dec} \sim 10$ s. The dynamics of the decelerating blast wave (at times $t > t_{dec}$) can be described by self-similar spherical relativistic expansion given by Blandford and McKee (1976). The radiative mechanism responsible for the afterglow emission is assumed to be the synchrotron emission.

The reverse shock (RS) propagating into the ejecta differs by its physical conditions. The number density of particles is larger in the outflow and it is smaller the energy gained by a single particle when crossing a shock. The intrinsic magnetic field in the ejecta is much stronger than in the circumburst medium and the intensity of the synchrotron emission should be higher than one expected from FS. The duration of the emission is limited by the size of the shell. Qualitatively, one expects to have short-lived optical flashes arising from RS. The importance of RS comes from the fact that one can infer the magnetization of the GRB outflow.

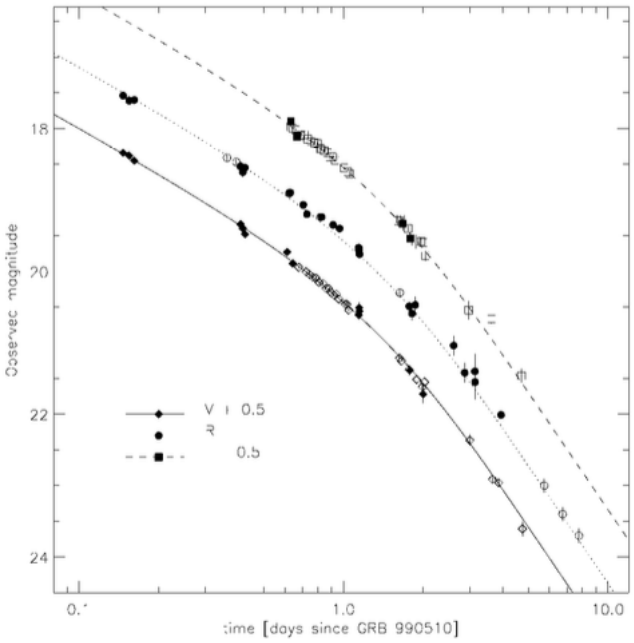

FIGURE 1.6: Light curve of GRB 990510 afterglow in V,R and I filters. The achromatic steepening gives an estimate of the jet angle $\theta \sim 5^o$ Credit: Harrison et al., 1999

Late-time afterglow observations can provide information on the geometry of the outflow. One can consider an emission region to be a narrow cone (jet) rather isotropic flow. Initially the jet has a high Lorentz factor and an observer gets the collimated radiation if aligned with the jet opening angle θ. At times when the Lorentz factor of the jet Γ drops, the observed flux gets fainter. The steepening of the light curve is

predicted to happen approximately when $\Gamma \sim 1/\theta$ (Rhoads, 1999). The measure of the jet break time (as an achromatic steepening of the afterglow light curve) allows us to estimate θ. This feature was observed in some optical afterglows (e.g. Harrison et al., 1999) and it implies $\theta \sim 2 - 10^{o}$. An example of jet-break in the optical afterglow light curve of GRB 990510 is shown in Fig. 1.6.

The measure of jet opening angles is fundamental for an accurate estimate of the GRB energy budget. If the source is assumed to emit isotropically, the total energy of the prompt emission can reach the extreme value of 10^{54} erg. GRB energies, corrected for the jet collimation angles, are reduced to $\sim 10^{51} - 10^{52}$ erg.

1.5 X-ray Afterglow

Before the launch of *the Swift* satellite the observations of GRB afterglows were mainly performed in the optical band at relatively late times. The observed light curves were consistent with a basic afterglow theory which suggests a deceleration of the blast wave in the external medium and predicts a flux decaying with time. However, the X-Ray Telescope (XRT) on board of *the Swift* shed new light onto the afterglow physics. The newly found X-ray counterparts at 0.3-10 keV have complex light curves which deviate from the simple blast wave deceleration profile. The newly discovered features in several X-ray light curves are summarized in the "canonical" form which is sketched in Fig. 1.7.

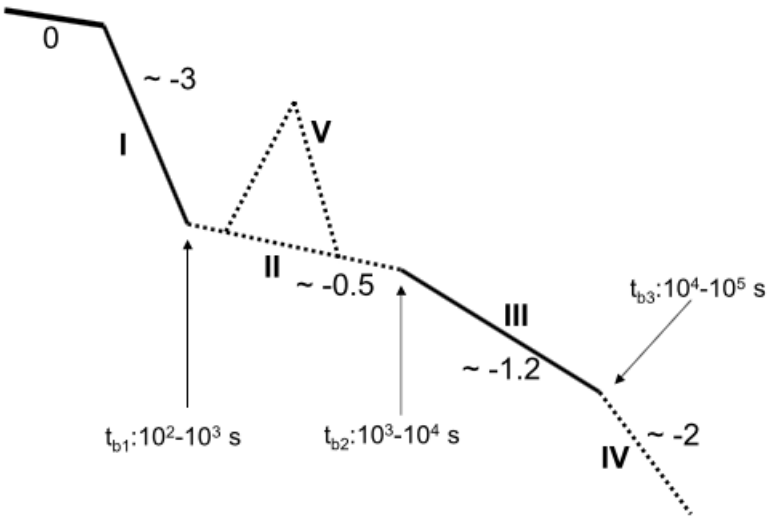

FIGURE 1.7: The canonical X-ray light curve is made of (I) fast decay phase, (II) plateau phase, (III) afterglow emission, (IV) late-time fading, (V) X-ray flares. Credit: Zhang et al., 2006

The earliest phase of the GRB X-ray emission, as observed by XRT, shows a steep decay. The temporal index α ($F \propto t^{-\alpha}$) is much larger than 2 and contradicts the classic afterglow predictions. Such an early X-ray steep decay is often interpreted as the tail of the prompt emission. If the emission region is curved, an observer receives

the radiation from higher latitudes after the prompt emission source is switched off (Kumar and Panaitescu, 2000).

Several X-ray afterglows show a plateau phase characterized by a shallow ($\alpha \sim 0.5$) temporal decay inconsistent with a simple afterglow scenario. The interpretation of an X-ray plateau is debated and can require the injection of additional energy into the forward shock.

X-ray flares are often found in XRT light curves sometimes occurring at late time ($> 10^3$ s). Their temporal behavior is similar to the prompt emission pulses. If produced by internal energy dissipation, late-time X-ray flares require a re-activation of the GRB central machine.

The usual segments of X-ray afterglows are also found by XRT: decay phases with $\alpha \sim -1$ (consistent with standard afterglow theory) and late time fading with $\alpha \sim -2$ suggesting that a jet break occurred.

1.6 Progenitors and the central engine

The identification of GRB progenitors is a hard task since we observe the consequence of a destroyed progenitor. The first hypothesis about the progenitor nature comes from the duration distribution of the GRB prompt emission. The existence of two populations of GRBs is suggested by the bimodal distribution of their duration T_{90}: short GRBs with $T_{90} < 2$ s and long GRBs with $T_{90} > 2$ s (Kouveliotou et al., 1993). The duration distribution of BATSE GRBs is shown in Fig. 1.8.

The energy release of 10^{52}erg on a time-scale of tens of seconds is pointing towards a catastrophic process. Supposing that accretion into a new-born compact object is the mechanism responsible for the jet energy injection, one can speculate that the progenitors of short GRBs have smaller masses.

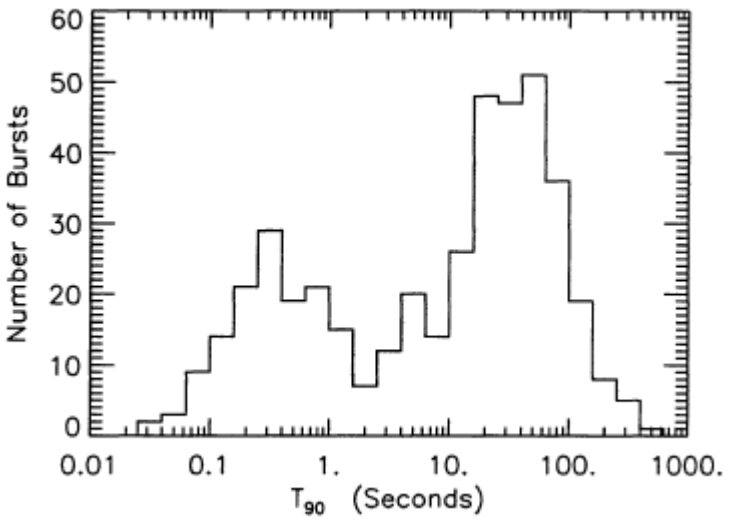

FIGURE 1.8: Duration distribution of 427 BATSE GRBs. Credit: Meegan et al., 1996

1.6.1 Progenitors of long GRBs

Hints on the nature of GRB progenitors are coming from the studies of their host galaxies and the afterglow features. A fraction of long optical GRB afterglows show late-time (in few weeks) bumps linked to supernovae Ib/c type by their spectra. In some cases, signs of radioactive decay from ^{56}Ni are found. This connection associates empirically the sources of long GRBs with the death of massive stars (masses $M > 20M_{\odot}$) (Filippenko, 1997). Supernovae Ib/c are believed to be produced by core-collapse of Wolf-Rayet stars which lose their hydrogen and helium envelopes prior to the explosion (Woosley and Heger, 2006). Resolved host galaxies of long GRBs are typically irregular and star forming galaxies (Fruchter et al., 2006). Moreover, long GRBs are preferentially located in the brightest spots of their host galaxies, i.e. highly star forming regions where the massive stars are born. Both the signature of supernovae and the preferential location of long GRBs in actively star forming regions, give a strong support to the hypothesis that the progenitors of long GRBs are massive stars. An example of a supernova emission dominating the optical GRB afterglow at its late-time both in the light curve and spectra is shown in Fig.1.9.

1.6.2 Progenitors of short GRBs

Most of the host galaxies of short GRBs have relatively low star formation rate (typical of elliptical and early type) (Fong, Berger, and Fox, 2010). In the cases when short GRBs are in star-forming galaxies, they appear to be located at edges of the hosts, again suggesting low star formation rate. The hypothesis for short GRB progenitors is that they originate from the merger of compact objects. Compact binaries, such as neutron star binaries (NS-NS) or system composed of a neutron star and a black hole (NS-BH), end up merging due to the loss of their orbital rotational energy. The catastrophic process of compact objects merging is considered as a source of jet launch and production of a short GRB (Eichler et al., 1989). The proof of this hypothesis can be found by the observation of gravitational waves (GW) detected during the final stages of compact objects evolution. The revolutionizing detection of GW170817 associated with the short GRB 170817A finally confirmed this hypothesis (Abbott et al., 2017). It was found that GW170817 is produced by the merger of two NS with a total mass of the system of $2.74^{+0.04}_{-0.01}M_{\odot}$. The time-frequency map of GW170817 and the GRB170817A light curve are shown in Fig.1.10.

1.6.3 The GRB central engine

One of the unresolved fundamental question in GRB physics lies on the identification of the central machine powering the relativistic jet. The proposed candidates for the central engine of GRBs should satisfy some of the minimum physical requirements. The basic requirement is that the central engine should be able to form an extreme jet with the Super-Eddington luminosity. To have an efficient launch of a relativistic outflow (bulk Lorentz factor $\Gamma \geq 100$), the formed jet should contain a small amount

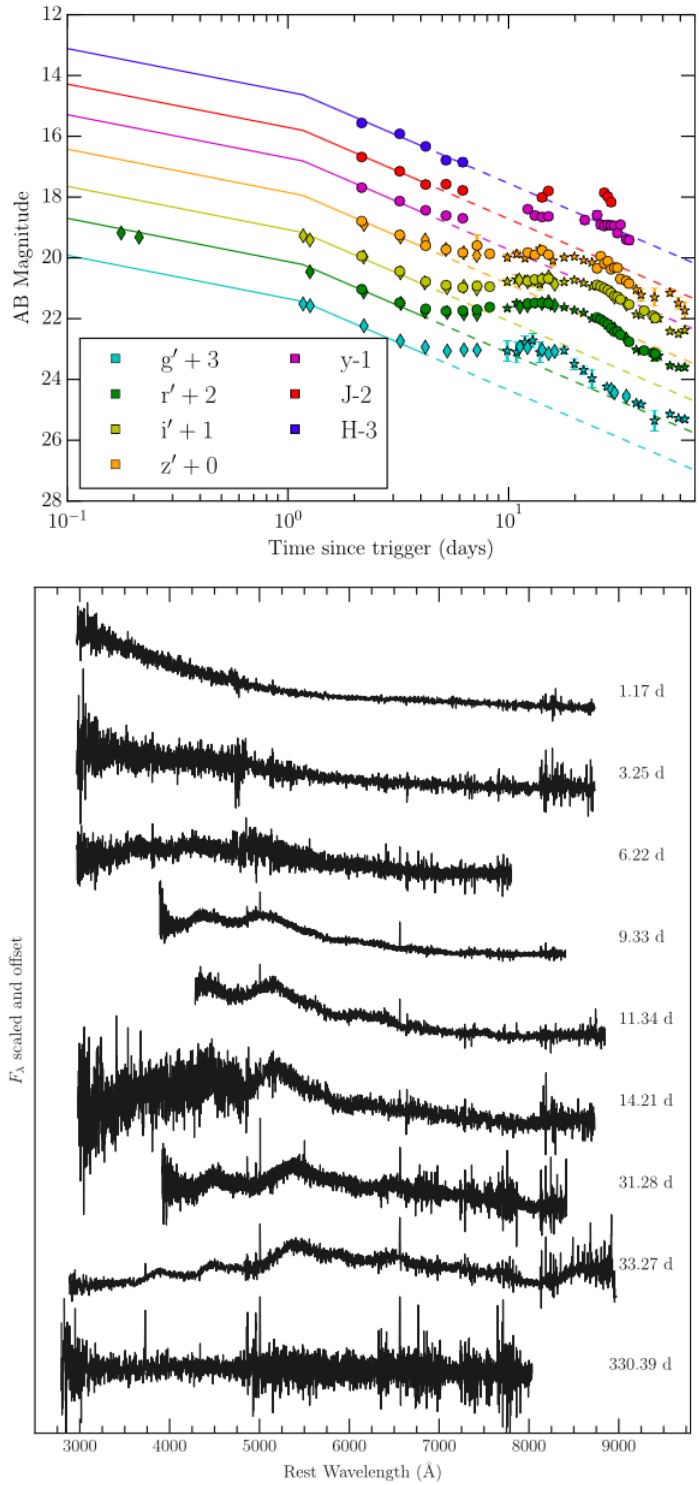

FIGURE 1.9: An example of supernova (SN 2013dx) associated with GRB (130702A). Top panel: Optical and NIR light curves of GRB 130702A. After about 10 days from the GRB trigger there is a re-brightening. Bottom panel: Uncorrected optical spectra of GRB 130702A. At early times we see only the afterglow spectrum which becomes dominated by the supernova features after about a week. Credit: Toy et al., 2016

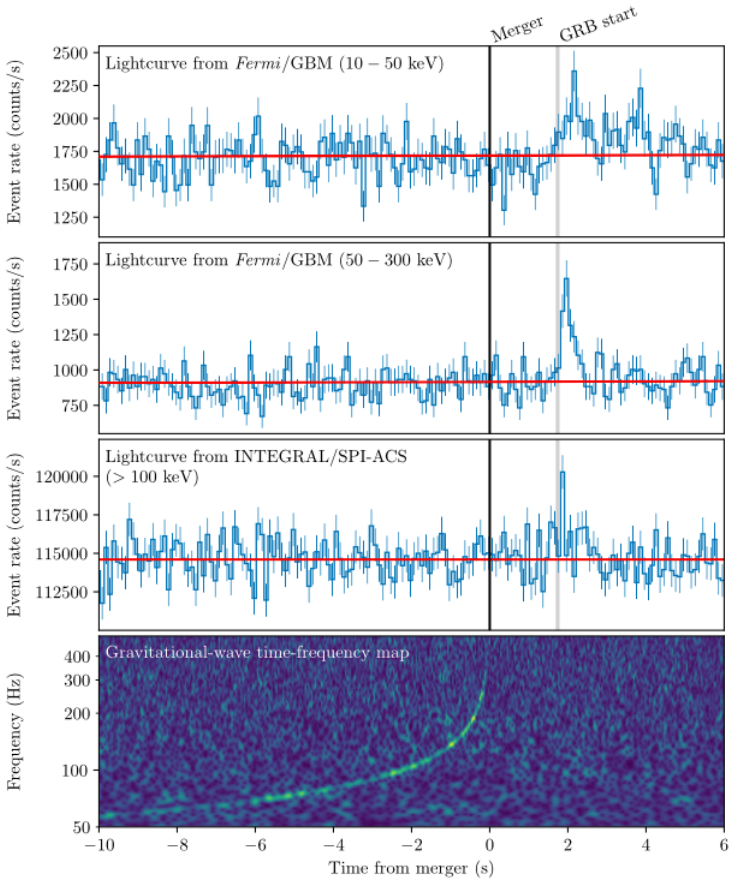

FIGURE 1.10: Detection of GW170817 and GRB 170817A. Top 3 panels: the light curve of GRB. Bottom: The time-frequency map of GW170817. Credit: Abbott et al., 2017

of baryons otherwise the spread of energy in protons would prevent the fast motion. Moreover, highly variable light curves of the prompt emission suggest a discontinuous release of the energy. The main candidate that satisfies the above mentioned requirements is the hyper-accretion of a stellar mass black hole (Woosley, 1993). Alternatively, a magnetar with extreme rotation (periods of milliseconds) can power the relativistic jet by its spin-down energy (Usov, 1992). The duration of prompt emission is another constrain on the nature of the central engine. While the prompt emission lasts for tens of seconds we can observe late-time X-ray flares (at $10^3 - 10^4$ s). If we interpret them as a continuation of the prompt emission, then we would require the central engine to be reactivated at such late times.

Accretion at Super-Eddington luminosities with an accretion rate $\dot{M}$ has a power of $\dot{M}c^2$. An extreme case with $\dot{M} \sim 1 M_\odot\, s^{-1}$ gives the total power $P \sim 2 \times 10^{55}$ erg/s. A fraction of that power $\eta \sim 10^{-3} - 10^{-2}$ is enough to explain observed prompt emission luminosities. The accreted energy can be transfered to the jet by different mechanisms. The most discussed are the neutrino-cooling process (Goodman, Dar, and Nussinov, 1987) and the Blandford-Znajek mechanism (Blandford and Znajek, 1977).

In the hottest inner part of the accretion disk the neutrino cooling becomes efficient for some period of time. An expanding fireball (electron-positron plasma mixed with photons) can be created in that case. An estimate of an expected luminosity of the jet in this scenario comes from the power of neutrino-anti-neutrino annihilation and it is $\sim 10^{52}$ erg/s for a three solar masses black hole with an accretion rate $\dot{M} \sim 1 M_{\odot} s^{-1}$ (Zalamea and Beloborodov, 2011).

Another way to extract the energy from accretion is from the rotational energy of a Kerr black hole (Blandford-Znajek mechanism). A rotating black hole is threaded by the magnetic field lines coming from the accretion disk. It induces a charge separation between the poles and the equator near the event horizon. As a result, an electric field is produced and it accelerates charged particles provided by the flow. These particles are placed in a magnetosphere and therefore, emit $\gamma-$ray photons. The $\gamma-$ray photons create a cascade of electron-positron pairs production and the lepton plasma is established. The black hole looses its angular momentum giving it to the outgoing Poynting flux with lepton plasma in the form of a jet. The power of Poynting flux in Blandford-Znajek mechanism is 10^{50} erg/s if extreme parameters are assumed: solar mass black hole, spin of $a = 1$, magnetic field of 10^{15} G (Popham, Woosley, and Fryer, 1999).

Rapidly (periods of milliseconds) rotating neutron star (magnetar) with an extreme magnetic field ($\sim 10^{15}$ G) is an alternative to the black hole as a machine for a relativistic jet production. The rotation of a magnetized neutron star produces strong electric fields and therefore, a plasma with an electron-positron content. The typical loss rate of the rotational energy of the magnetar is $\sim 2 \times 10^{52}$ erg/s if we assume a neutron star (the Chandrasekhar limit gives a mass of $1.4 M_{\odot}$) with a size 10^6 cm and a period of a rotation 10^{-3} s. This value of power is an upper limit for the luminosity of the GRB. Therefore, any GRB that exceeds this value is going to contradict the hypothesis of a magnetar as a powering source. However, a mixed situation can happen. An accretion can go to the neutron star (instead of a black hole) powering the prompt emission and if the neutron star survives it can power the X-ray afterglow by its spin-down energy (Bernardini et al., 2013). In that case, the rotational energy of the magnetar is not the luminosity limit anymore.

Chapter 2

Prompt emission

In this Chapter I provide a more detailed description of the prompt emission physics. I first discuss the observational properties of the prompt emission emphasizing its spectral modeling. I also present the theoretical models proposed to explain the dissipation processes happening within the jet and the radiation mechanisms responsible for the prompt emission. I discuss the open issues on the physics of prompt emission and I give the motivations of the research project of this thesis. A brief description of the instruments providing the data analyzed throughout the thesis is given in the end of this Chapter.

2.1 Observational properties

The prompt emission of GRBs has been studied mostly in the 10 keV - 1 Mev range. The time-resolved and time-averaged spectra of GRB prompt emission have been extensively analyzed. The *BATSE* and the *Fermi* catalogs provide spectra of thousands of GRBs. The vast majority of the spectra are non-thermal and they are often fitted by the empirical model introduced by Band (Band et al., 1993). This model consists of two power-law functions smoothly connected by an exponential shape.

The Band function used to fit the photon spectrum is defined as

$$N(E) = \begin{cases} CE^{\alpha} exp(-E/E_0) & \text{for } E < (\alpha-\beta)E_0 \\ C[(\alpha-\beta)E_0]^{\alpha-\beta} exp(\beta-\alpha)E^{\beta} & \text{for } E \geq (\alpha-\beta)E_0 \end{cases} \tag{2.1}$$

where α and β are the photon indices below and above the break energy. If the νF_ν spectrum is peaked ($\beta < -2$) then the peak energy can be find as $E_{peak} = (2+\alpha)E_0$. When the high-energy photon index (β) cannot be determined, a cutoff power-law function $CE^{\alpha}exp(-E/E_0)$ is a good description. In the case of an unconstrained peak energy, a simple power-law function is sometimes used. The observed peak energies are widely distributed from around 20-30 keV up to few MeV, with a typical value of $\sim$ 200 keV. The spectral indices are also highly dispersed with typical values $\alpha \sim -1$ and $\beta \sim -2.3$ (e.g. Band et al., 1993, Ghirlanda, Celotti, and Ghisellini, 2002b, Kaneko et al., 2006b, Nava et al., 2011b). An example of GRB spectrum fitted by the Band function is shown in Fig. 2.1.

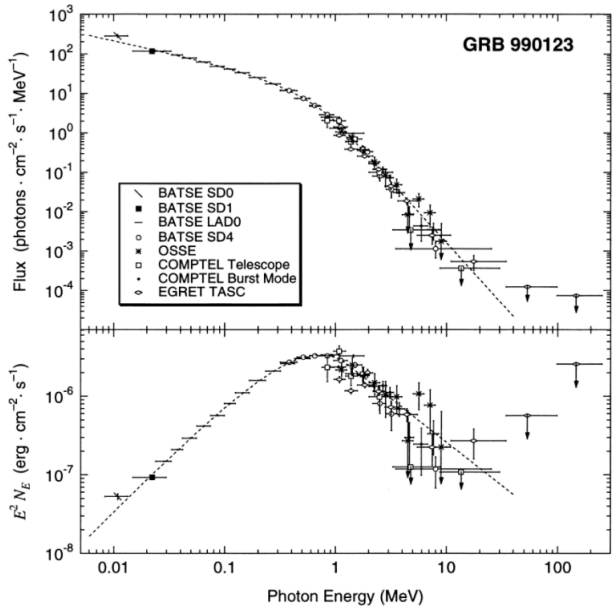

FIGURE 2.1: An example of prompt emission spectrum fitted by Band function. The photon spectrum (top panel) of GRB 990123 and its νF_ν representation (bottom panel) are shown. Credit: Briggs et al., 1999

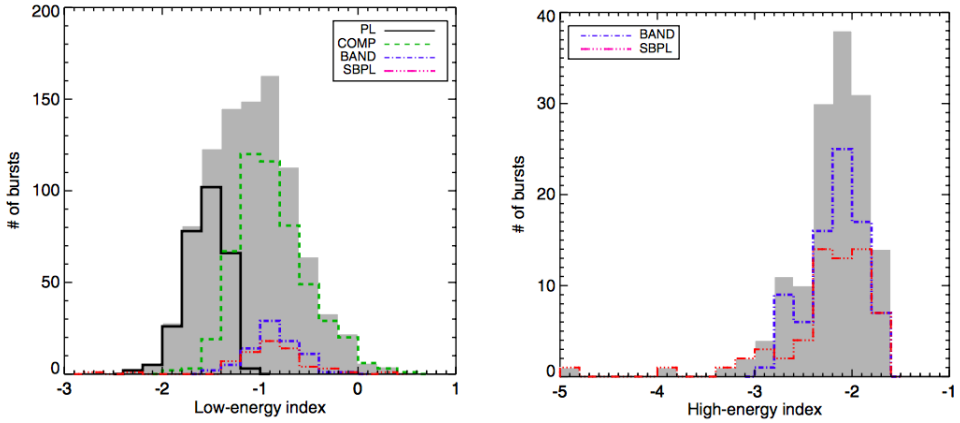

FIGURE 2.2: Distributions of low-energy (left panel) and high-energy photon indices (right panel). The overall distributions are shown by the gray shaded histogram. The contributions by different models to the overall distribution are shown by colored lines. Credit: Gruber et al., 2014

The standard set of prompt emission spectral models, adopted to fit GRB spectra, include the Band function (BAND), the smoothly broken power-law function (SBPL), the cutoff power-law function (COMP) and a simple power-law function (PL). The most complex models in this set are BAND and SBPL. They are used to account for two power-law segments below and above the peak energy. The actual difference between BAND and SBPL is the smoothness around the peak energy: while in BAND it is fixed to an exponential shape, in SBPL the smoothness is a free parameter. The best fit model is chosen by the statistical comparison and depending on the possibility to constrain the parameters of BAND or SBPL (the peak energy and/or the high

energy photon index).

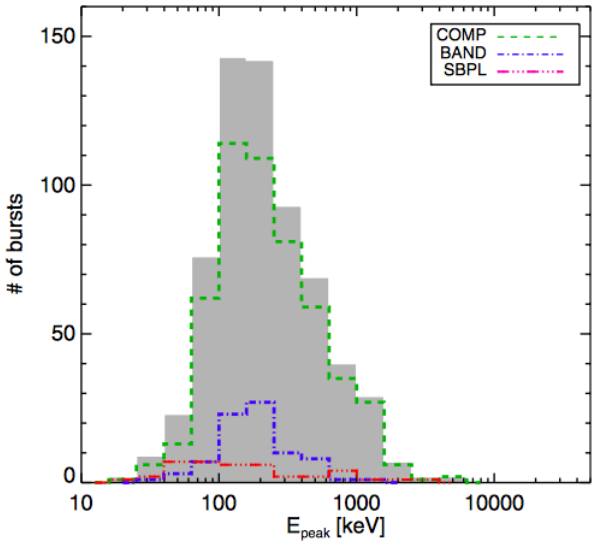

FIGURE 2.3: The distribution of the observed peak energy of the νF_ν spectra. The overall distribution is shown by gray shaded region. The contributions by different fitted models to the overall distribution are shown by colored lines. Credit: Gruber et al., 2014

The findings of the analysis of the first four years of *Fermi* observation for time-integrated GRB spectra (Gruber et al., 2014) are shown in Fig. 2.2 - 2.4. This catalog contains 943 GRBs. The spectra are modeled in the range of $8\,\mathrm{keV} - 40\,\mathrm{MeV}$. The averaged values of photon indices and its 1σ scatter are $\alpha = -1.08^{+0.43}_{-0.44}$ and $\beta = -2.14^{+0.27}_{-0.37}$ (Fig. 2.2).

The mean peak energy in the observer frame is $E_{peak} = 196^{+336}_{-100}\,\mathrm{keV}$ (Fig. 2.3). The observed flux in the $10\,\mathrm{keV} - 1\,\mathrm{MeV}$ range is $3.03^{+7.41}_{-1.40}\,10^{-7}\,\mathrm{erg\,cm^{-2}\,s^{-1}}$ (2.4). For

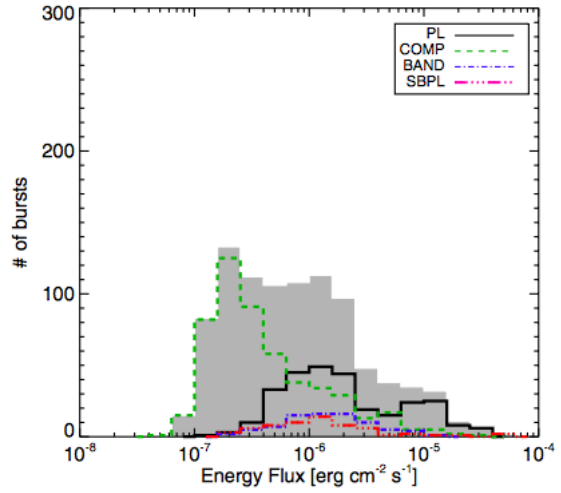

FIGURE 2.4: The distribution of the observed fluxes in in the $10\,\mathrm{keV} - 1\,\mathrm{MeV}$ range. The overall distribution is shown by gray shaded region. The contributions by different fitted models to the overall distribution are shown by colored lines. Credit: Gruber et al., 2014

the subsample of GRBs with known redshift, the isotropic energy E_{iso} and isotropic luminosity L_{iso} of the prompt emission are computed in the 1 keV − 10 MeV range in the rest frame (Fig. 2.5). The typical isotropic energy is $E_{iso} \sim 10^{53}$ erg and spans over more than three orders of magnitude. The averaged isotropic luminosity is $\sim 10^{52}$ erg/s and it extends over three orders.

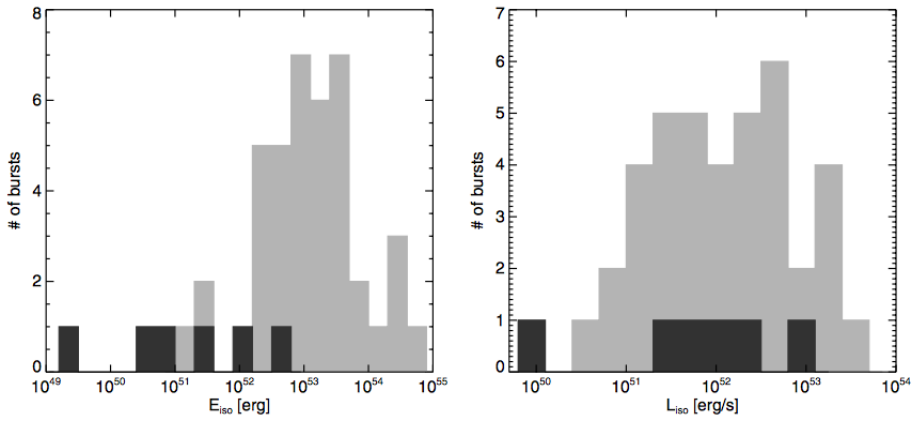

FIGURE 2.5: The distribution of the isotropic energy E_{iso} and isotropic luminosity L_{iso} of prompt emission in the 1 keV − 10 MeV range in the rest frame. The histograms in light gray are for long GRBs, dark gray for short GRBs. Credit: Gruber et al., 2014

Modeling GRB spectra is more complicated once the high energy data is included (>100 MeV with *Fermi/LAT*). Widely applied Band function fits the dominant (in νF_ν) component in the 10 keV - 1 MeV range (observed by Fermi/GBM), while the high energy data sometimes require for an additional non-thermal component fitted by a single power-law function.

The spectral shapes and the peak energies are varying in time within a GRB. However, the spectral evolution is not chaotic. Two trends are observed: (1) peak energy decreases from the beginning (Norris et al., 1986) and (2) peak energy tracks the flux (Golenetskii et al., 1983).

2.2 Theoretical model

2.2.1 Dissipation processes

The observed prompt emission is originated by the dissipation of the jet's energy. The variability of prompt emission light curves suggests internal origin of the dissipation because the external shocks have a variability time-scale $\delta t \sim t$.

The most explored scenario is the hot fireball model (Paczynski, 1986; Goodman, 1986). If we use the typical observed prompt emission luminosity $L \sim 10^{52}$ erg/s and the variability time-scale of 10^{-2} s, we can estimate the initial temperature of the ejecta as $T \sim \left(L/4\pi(c\delta t)^2\sigma_B\right)^{1/4} \sim 2 \times 10^{10} K$. At this high temperature photons are coupled with leptons and baryons in the jet. Jets with small amount of baryons will undergo an adiabatic expansion while photons cool. Therefore, the initial energy

of photons, electrons and positrons is transfered to protons. The acceleration of the jet continues until photons de-couple from baryons. The photosphere can be defined as a surface at which the optical depth to the Thomson scattering (τ) is equal to 1. The optical depth is $\tau \sim n_p \sigma_T R/2\Gamma$, where R is the radius of the ejecta and n_p is the proton density in the outflow. The comoving proton density estimate comes by the proton flux in the jet $\dot{M}$ as $n'_p = \dot{M}/(4\pi R m_p c \Gamma)$. Defining the ratio between the radiation luminosity L and the baryonic load $\dot{M}$ as $\eta = L/\dot{M}c^2$ we can get the photosphere radius $R_{ph} = R(\tau = 1)$ as $R = L\sigma_T/8\pi m_p c^3 \eta \Gamma^2$. Its typical value is $R_{ph} \sim 6 \times 10^{12}$ cm (if we use $L \sim 10^{52}$ erg/s, $\eta \sim 100$ and $\Gamma \sim 100$). The parameter η is the test parameter for identification of the jet composition. If thermal emission from the fireball is observed in the prompt emission spectra, its temperature constrains η and we have knowledge of the initial form of the jet's energy. Unfortunately, we do not have significant observational claims on the thermal components in GRBs spectra to answer to this question.

The internal shocks model is widely used as a dissipation mechanism in baryon dominated jets (Rees and Meszaros, 1994b). In that model the central engine produces outflows with random Lorentz factors. The faster part of the outflow catches the slower one. The shocks propagate in both shells converting the kinetic energy into internal particle energy and local magnetic field amplification. Relativistic electrons in magnetic field are expected to radiate their energy through synchrotron and inverse Compton processes.

The main advantage of the internal shocks model is the possibility to have short variability time-scale. For simplicity, let's consider that the central engine produces two shells (with bulk Lorentz factors Γ_1 and Γ_2) with time difference δT. If the first shell is slower $\Gamma_1 < \Gamma_2$ then they collide at time t_{coll} defined by $v_1 t_{coll} = v_2(t_{coll} - \delta T)$ (where v_1 and v_2 are shells' velocities). The radius at which shells collide is $R_{coll} = t_{coll} v_1 \sim 2c\Gamma_1 \delta T \kappa$ where $\kappa = \Gamma_2/\Gamma_1$. The observed variability tracks then the intrinsic central engine variability. However, the efficiency of internal shocks dissipation is very low (about 20% or lower) (Kobayashi, Piran, and Sari, 1997) and it represents one of the main issues of this model.

Another possibility is that the dominant fraction of energy in the jet is carried by the Poynting flux. The basic dissipation mechanism in this case is magnetic reconnection. Basically, the highly magnetized plasma in ideal magnetohydrodynamics (MHD) has large magnetic Reynolds number ($R_B >> 1$) and the magnetic field is frozen into the plasma. However, if oppositely oriented magnetic lines are pushed by the plasma flow and get closer, magnetic gradient increases. In the thin region with large magnetic gradient R_B decreases violating the ideal MHD condition. Magnetic field lines slip through the plasma and reconnect changing their topology. The dissipated magnetic field energy goes into electric field and kinetic energy of the particles. The particles are accelerated both by the strong electric field in the reconnection zone and also by usual Fermi mechanism by crossing of magnetic islands produced in reconnection events. The first phenomenological model of magnetic reconnection

was proposed by Peter Sweet in 1956 and later described in Parker (1957). However, the theory of relativistic magnetic reconnection is under intense development.

2.2.2 Radiative processes

The typical observed spectrum of GRB prompt emission is much wider than the thermal Planck spectrum and has a power-law behavior above the peak. This empirical information by itself would give a preference for non-thermal radiative processes responsible for the prompt emission. Both in the fireball or magnetic jet models we expect non-thermal energetic particles and a strong magnetic field. The radiation of relativistic charged particles in a magnetic field (synchrotron radiation) is proposed to be the main radiative mechanism responsible for GRB prompt emission. In this section, I will briefly summarize the basics of synchrotron radiation and also I will refer to the inverse Compton radiation as the component in the configuration with photons and hot electrons. The detailed analysis of these radiative processes can be found in Rybicki and Lightman (1986).

Synchrotron radiation

A charged particle in a magnetic field gets accelerated in the direction perpendicular to its velocity by the Lorentz force. Emission produced by the relativistic particles in a magnetic field is called a synchrotron radiation. We will consider an ultra-relativistic electron placed in a constant in time magnetic field. The latter is homogeneous on the typical volume of space corresponding to the electron's dynamics.

The total power emitted by a single electron is

$$P_{syn} = \frac{4}{3} U_B \sigma_T c \gamma^2 \beta^2 \tag{2.2}$$

where $U_B = B^2/8\pi$ is the magnetic field energy density, σ_T is the Thomson cross section and $\beta = v/c$. The distribution of the angle between the velocity of the electron with respect to the vector of magnetic field (pitch angle) is assumed to be isotropic.

The cooling time of an electron can be roughly estimated as

$$t_c \sim \frac{\gamma m c^2}{P_{syn}} \propto 1/B^2\gamma \tag{2.3}$$

The typical synchrotron frequency is

$$\nu_s = \gamma^2 \frac{eB}{2\pi mc} \tag{2.4}$$

To find the exact form of the observed synchrotron spectrum of a single electron one needs to perform Fourier transform of the electric field function $E(t)$. Here I just mention the results of Fourier transform and I give a qualitative estimate of the result.

The spectrum of a single electron (i.e. the power per specific frequency, so called F_ν spectrum) is a function which peaks at a specific frequency $\nu \sim 0.29\nu_c$. The spectrum much below the characteristic frequency $\nu \ll \nu_c$ is a power-law function $F_\nu \propto \nu^{1/3}$. Above the peak $\nu \gg \nu_c$ it is a power-law with an exponential cutoff $F_\nu \propto \nu^{1/3} e^{-\nu/\nu_c}$.

Since the synchrotron spectrum of a single electron is known, we can extend the discussion of the spectrum by a population of electrons. The distribution of shock-accelerated electrons is a power-law function $dN/d\gamma \propto \gamma^{-p}$ (N is the number of electrons) for $\gamma > \gamma_m$ where γ_m is the minimum Lorentz factor of electrons accelerated. The observed spectrum made by this population of electrons is discussed further. Two regimes of radiation exist. Slow-cooling regime is relevant when the cooling time of electrons is much larger than the dynamical time of the system. In the opposite situation, fast-cooling regime takes a place.

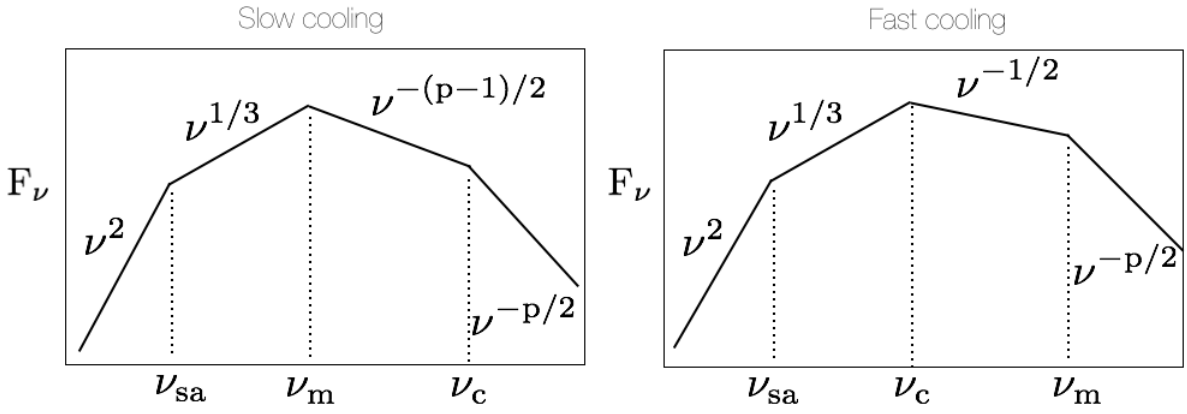

FIGURE 2.6: Synchrotron spectrum (in F_ν) in the slow and fast cooling mode.

In the slow-cooling regime one can ignore the fact that some amount of electrons loose their energy and the resulting spectrum in F_ν is characterized by three power-law segments: below and above the frequency that corresponds to the frequency ν_m. Most of the electrons have γ_m and therefore the synchrotron spectrum is peaked at ν_m. The spectrum at $\nu \ll \nu_m$ is that of the single electron spectrum $F_\nu \propto \nu^{1/3}$. If one uses the relation 2.4 $\gamma \propto \nu^{1/2}$ the spectrum at $\nu \gg \nu_m$ can be easily found as

$$F_\nu = \int_{\nu_m}^{\infty} d\gamma \frac{dN}{d\gamma} P_\nu(\nu) \propto \nu^{-(p-1)/2} \tag{2.5}$$

where we used the power per unit frequency $P_\nu(\nu) = P/\nu_s$.

To describe the spectrum in the fast-cooling regime one needs first to estimate the cooling frequency as the frequency above which electrons effectively cool. Combining the cooling time-scale 2.3 with the synchrotron frequency 2.4 one gets the

characteristic cooling frequency as

$$\nu_c \sim \frac{36\pi emc}{\sigma_T^2 B^3 t_c^2}. \tag{2.6}$$

Note that β is set to 1.

Now, if one thinks about the spectrum in fast cooling regime the difference with respect to slow-cooling regime spectrum appears at frequencies $\nu > \nu_c$ and therefore the spectrum below ν_c is still $F_\nu \propto \nu^{1/3}$. The cooling of electrons is important above ν_c. One can think about a typical Lorentz factor of electrons γ_c (from 2.3). Electrons with $\gamma > \gamma_c$ cool rapidly to γ_c on time-scale t_c and the frequency varies as $\nu \propto \gamma^2$ (2.4). The energy of an electron $\gamma m_e c^2 \propto \gamma$ is lost and the spectrum is then $F_\nu \propto \nu^{-1/2}$. Electrons with the highest energies ($\gamma > \gamma_m$ in fast cooling regime and $\gamma > \gamma_c$ in slow cooling regime) loose almost all their energy forming the uppermost part of the synchrotron spectrum. The shape of the spectrum ($\nu > \nu_m$ in fast cooling regime and $\nu > \nu_c$ in slow cooling regime) can be estimated as the radiation of the total energy of electrons $\propto \gamma \int \gamma^{-p} d\gamma$ at frequency range $\nu \propto \gamma^2$ (2.4) and it is $F_\nu \propto \nu^{-p/2}$.

At the lowest frequencies $\nu < \nu_{sa}$ the photons are absorbed by the inverse-synchrotron process. The shape of the spectrum depends on the electrons distribution and it scales as $F_\nu \propto \nu^2$ or $F_\nu \propto \nu^{5/2}$. For a typical parameters the self-absorption frequency $\nu < \nu_{sa}$ lies in the radio band. The sketch of the synchrotron spectrum in F_ν in slow and fast cooling regimes is shown in Fig. 2.6.

Inverse Compton radiation

A low energy photon ($h\nu$) gains energy when it is scattered by a hot electron with an energy $\gamma_e m_e c^2$. The scattering is elastic (with no electron recoil) when $h\nu\gamma_e << m_e c^2$ (in the electron rest frame the incoming photon is blue-shifted). The scattered energy of a photon is $\nu_{IC} \sim h\nu\gamma_e^2$ on average. The power of Inverse Compton (IC) radiation from an electron in a photon field with u_{ph} (radial energy density) is $P_{IC} \sim \sigma_T u_{ph} \gamma_e^2 c$. The functional form of the IC power is similar to the synchrotron one.

There is a particular interest in the case when the seed photons for IC radiation are those of synchrotron radiation (Synchrotron Self Compton, SSC). A system of hot electrons in magnetic field necessarily have synchrotron and SSC radiation components. However, it is interesting to know the relative importance of these components. In the SSC case, the radiation field has u_{ph} coming from the synchrotron emission $u_{ph} = \Delta R \sigma_T n_e B^2 \bar{\gamma}^2 / 6\pi$ where ΔR is the size of the emitting region and $\bar{\gamma}$ is the averaged Lorentz factor of electrons. The relative importance of the IC process can be expressed through the Compton Y parameter which is $Y = P_{IC}/P_{syn} \sim \sigma_T \Delta R n_e \bar{\gamma}^2 \sim \tau_e \bar{\gamma}^2$ where τ_e is the optical depth of Thomson scattering.

The situation is different when $h\nu\gamma_e$ gets closer to $m_e c^2$ (the Klein-Nishina regime). The scattering is not elastic anymore and the cross section is smaller than σ_T. It depends on the frequency of a photon as ν^{-1} and the gain of energy by photons is

limited to half of the electron's energy. Since the cross section depends on the seed photons' frequency, the seed photons spectrum is distorted.

2.3 Open issues and the motivation

The origin of the prompt emission is still a mystery and represents one of the most pressing questions in the GRB field. The nature of both the dissipation and radiative mechanisms has not been firmly identified yet. This lack of knowledge on what is powering and shaping the prompt radiation is strictly related to a series of open questions about fundamental properties of GRBs, such as the jet composition, the location of the dissipation region, the efficiency and nature of the acceleration mechanism, and the strength and properties of the magnetic field in the emission region. Even though the most natural radiative process expected to dominate the emission is synchrotron radiation (Katz, 1994; Rees and Meszaros, 1994a; Sari, Narayan, and Piran, 1996; Sari, Piran, and Narayan, 1998; Tavani, 1996), the inconsistency between the observed spectral shape at low energies and predictions from the synchrotron theory represents a serious challenge for this interpretation. As inferred from the spectral analysis, the photon index α describing the data at low energy (i.e. below the νF_ν peak energy) is distributed around a typical value $\alpha \sim -1$, harder than the value expected in the case of fast-cooling synchrotron radiation (Cohen et al., 1997; Crider et al., 1997; Preece et al., 1998). This result is independent of the spectral function adopted to fit the spectra (e.g., cutoff power law, smoothly broken power law, Band function), and it has been found to be similar from the analysis of the spectral data collected by different instruments (Preece et al., 1998; Frontera et al., 2000; Ghirlanda, Celotti, and Ghisellini, 2002b; Kaneko et al., 2006b; Nava et al., 2011b; Sakamoto et al., 2011b; Goldstein et al., 2012; Gruber et al., 2014; Lien et al., 2016; Yu et al., 2016). The so called synchrotron "line of death" problem (see Fig.2.7) created a noticeable platform for debates in the literature.

The problem has been widely discussed in the literature. The proposed solutions can be classified into two types: models that invoke emission mechanisms different than synchrotron radiation, and models that propose modifications to the basic synchrotron scenario. Among the first class of models, I recall scenarios invoking Comptonization and/or thermal components (Liang et al., 1997; Blinnikov, Kozyreva, and Panchenko, 1999; Ghisellini and Celotti, 1999; Lazzati et al., 2000; Mészáros and Rees, 2000; Stern and Poutanen, 2004; Rees and Mészáros, 2005; Ryde and Pe'er, 2009; Guiriec et al., 2011; Guiriec et al., 2015b; Guiriec et al., 2015a; Guiriec et al., 2016b; Guiriec et al., 2016a; Ghirlanda, Pescalli, and Ghisellini, 2013; Burgess et al., 2014).

For the second class of models (studies that consider synchrotron radiation) effects producing a hardening of the low-energy spectral index have been invoked:

- One possibility is to have the cooling frequency close to the characteristic synchrotron frequency (marginally fast cooling synchrotron emission) (e.g. Daigne,

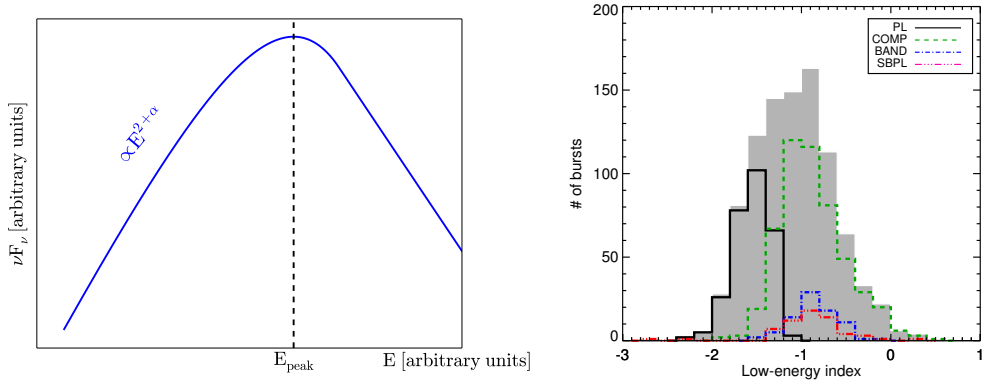

FIGURE 2.7: The synchrotron "line of death" problem. **Left panel:** the typical prompt emission spectrum in the νF_ν (α is the photon index below the peak energy). **Right panel:** the distribution of α (Gruber et al., 2014) (gray filled histogram). Most of the spectra have $\alpha > -1.5$ which is inconsistent with the predictions of the fast-cooling synchrotron scenario.

Bošnjak, and Dubus 2011): this regime would harden the observed spectra up to $\alpha \sim -2/3$.

- Another possibility is to have inverse Compton radiation in Klein-Nishina regime (e.g. Nakar, Ando, and Sari 2009): if the synchrotron radiation is in fast cooling regime and the electron's cooling via inverse Compton is in Klein-Nishina regime, the resulting spectrum below the peak energy becomes harder (with photon index up to $\alpha \sim -1$ Daigne, Bošnjak, and Dubus, 2011).

- If the magnetic field is assumed to decay with the emitting region radius, the harder spectra can be obtained in classic fast cooling synchrotron scenario (e.g. Uhm and Zhang 2014).

- Another solution includes the anisotropic distribution of electrons' pitch angles (Lloyd and Petrosian, 2000; Medvedev, 2000).

All these proposals suggest specific configuration of the physical environments in which the observed emission is produced. In spite of all theoretical efforts, there is still no consensus on the origin of the prompt emission. Theoretical studies would benefit from a better characterization of prompt spectra, especially in the low-energy part, where observations are in contradiction with the synchrotron theory.

2.4 Instruments in use

2.4.1 The Neil Gehrels Swift Observatory

The Neil Gehrels Swift Observatory (hereafter *Swift*) is a multi-wavelength satellite launched in November 20, 2004 to detect GRBs and accurately localize them (Gehrels et al., 2004). GRBs are primarily detected by the Burst Alert telescope (BAT) which operates in the 15-350 keV range. Once a GRB is triggered, the co-aligned to BAT

X-ray Telescope (XRT) and UV/Optical Telescope (UVOT) search for low energy counterparts allowing for further shrink of the GRB localization error region. The robust detection technique of BAT and the precise localization by the XRT and UVOT instruments allow ground-based telescopes to identify GRB counterparts more efficiently and earlier than in the pre-*Swift* era.

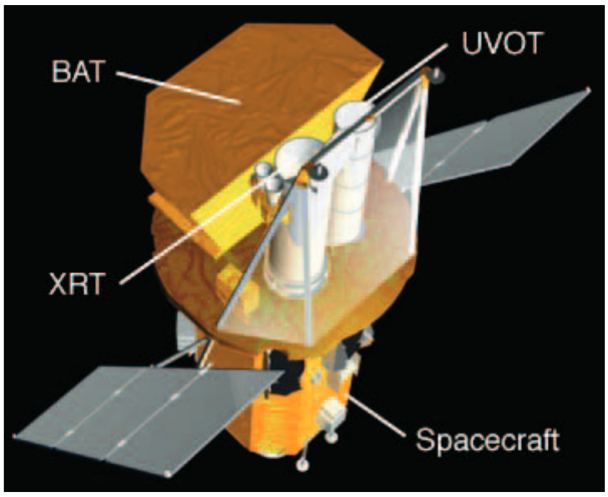

FIGURE 2.8: Swift satellite Credit: Gehrels et al., 2004

The Burst Alert telescope

The BAT instrument was designed by the NASA Goddard Space Flight center. It is a large field of view (FOV) instrument (FOV of 1.4 sr) detecting about 100 GRBs per year. The sensitivity of BAT is very high ($\sim 10^{-8}$erg cm^{-2} s^{-1}) and therefore, it is able to detect much fainter GRBs than *BATSE*. Another advantage of BAT is its on-board GRB localization. The estimate of the GRB position is made withing 10 seconds from the trigger time. On this short times the BAT algorithm is able to estimate the need of the spacecraft slew.

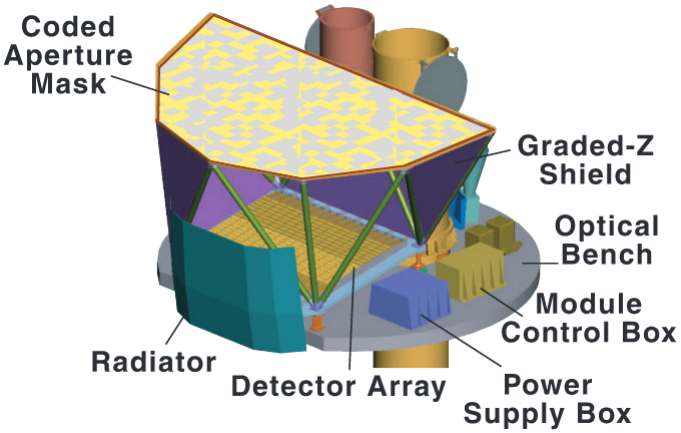

FIGURE 2.9: The BAT instrument. Credit: Gehrels et al., 2004

The BAT detector (an area of 5240 cm^2) is an array made of CdZnTe (CZT) elements. The detection of a signal is based on the photoelectric and Compton effects in CZT elements. The incident photons of 15-350 keV energy create electron and hole clouds moving to anode and cathode, respectively. The circuits detect the electric current and the photon is counted. The localization of a GRB is performed due to the coded aperture mask which is positioned one meter above the detector. It is made of randomly distributed lead tiles which cover half of the surface. When the GRB source illuminates the coded aperture mask, it produces a shadow pattern on the detector. This shadow is used to localize the GRB source and it reaches an accuracy of 1-4 arcmin. To protect the detector from a radiation outside of the aperture, BAT is covered by the radiation shield.

TABLE 2.1: BAT characteristics

Parameter	Value
Energy range	15-150 keV
Energy resolution	$\sim$ 7 keV
Aperture	Coded mask
Detection area	5240 cm^2
Detection material	CdZnTe
Detection operation	Photon counting
FOV	1.4 sr (half-coded)
Detector elements	256 modules of 128 elements module
Detector element size	$4 \times 4 \times 2$ mm^2
Coded mask cell size	$5 \times 5 \times 1$ mm^2
Source position	1-4 arcmin
Sensitivity (exposure time t)	$\sim 2 \times 10^{-10}\,erg\,cm^{-2}\,(t/20\,ks)^{-0.5}$
Rate of GRB detection	$\sim$ 100 per year

I extensively include BAT data for the spectral analysis performed in the thesis. I extract BAT data in the following way. I download the *BAT* event files from the *Swift* data archive[1]. I extract the *Swift*-BAT spectra and light curves using the latest version of the HEASOFT package (v6.17). The background-subtracted mask-weighted BAT light curves are extracted in the energy range 15-150 keV using the *batmaskwtevt* and *batbinevt* tasks in FTOOLS. BAT spectral files are produced using the *batbinevt* task and are corrected through the *batupdatephakw* and *batphasyserr* tasks to include systematic errors. The final BAT spectral data are mask-weighted and background subtracted. The data has normal distribution and requires to use gaussian likelihood for the fitting procedure. Using *batdrmgen*, I generate different response matrices for intervals before, during, and after the satellite slew. The latest calibration files (CALDB release 2015 November 13) are adopted.

[1] http://heasarc.gsfc.nasa.gov/cgi-bin/W3Browse/swift.pl

The X-ray Telescope

The XRT instrument was partially designed by the University of Leicester and its major components are made of the left-over bits of the earlier X-ray experiments. The X-ray CCD is a duplicate of an XMM EPIC MOS CCD and X-ray mirror (Wolter I) from the previous Italian Jet-X experiment. The Wolter I mirror focuses X-rays into a CCD detector with dimensions of 600×600 pixels.

XRT operates in 0.3-10 keV energy range with the narrow FOV (23.6 arcmin square). Typically it takes at most 90 seconds (slewing time of the spacecraft) to localize the GRB source caught by BAT. The accurate measure of the GRB position ($\sim$ 3 arcsec versus $\sim$ 3 arcmin of BAT) is used to localize the GRB counterparts in the optical range and search for the host galaxy. The XRT operates in 3 readout modes

TABLE 2.2: XRT characteristics

Parameter	Value
Telescope	Jet-X Wolter I
Energy range	0.3-10 keV
Energy resolution	$\sim$ 260 eV (at 5.895 keV)
Effective area	110 cm^2(at1.5keV)
Detector	EEV CCD-22,600×600 pixels
Detection operation	Imaging, Timing, Photon counting
FOV	23.6 arcmin square
Sensitivity	$\sim 10^{-13}$ erg cm^{-2} s^{-1} (10^4 s)

determined automatically by the installed software. In the Imaging mode the total energy per pixel is accumulated which determines the position of bright X-ray sources without an information on their spectra. Photon-counting (PC) mode is chosen to get spectral and spatial information but with loss on the time-resolution. PC mode is useful for faint late-time GRB counterparts. The fast read of CCD (Timing mode) allows to gain the high time-resolution of X-ray sources and spectral information without spatial information. The brightest variable X-ray sources are analyzed in Window Timing mode (WT) which is a single strip of data. The data in WT mode has the highest time-resolution (1.8 milliseconds) and full energy resolution. I use the XRT data in WT mode throughout the thesis. The XRT light curves are retrieved from the *Swift* Science Data Center, provided by the University of Leicester[2] (Evans et al., 2009). To extract the spectra, I download the XRT event files from the *Swift*-XRT archive[3]. Since for all our GRBs XRT data are heavily piled up, data from the central region[4] have been excluded (Romano et al., 2006). For each GRB, the size of the exclusion region are determined so that the maximum count rate in the time interval of interest does not exceed 150 counts s^{-1}. I extract source and background spectra in each time bin using the *xselect* tool. For each time bin, the ancillary response file are

[2] http://www.swift.ac.uk/xrt_curves/

[3] http://www.swift.ac.uk/archive/

[4] By “central region" I mean the circular region centred on the pixel with the largest number of counts detected within the time of interest (Romano et al., 2006).

generated using the task *xrtmkarf*. I exclude from the spectral analysis all channels below 0.5 keV. The XRT source and background data are Poisson distributed and, therefore require to use Cash statistics for the spectral fitting. However, if the data is re-binned on energies, the gaussian likelihood can be used. I further make notations which likelihood I use depending on the analysis.

2.4.2 The Fermi Gamma-ray Space Telescope

The Fermi Gamma-ray Space Telescope (*Fermi*) was launched at 11 June 2008. The *Fermi* mission is a product of an international collaboration including NASA and agencies in Italy, France, Germany, Japan and Sweden. *Fermi* is composed of two kinds of instruments: the Large Area Telescope (LAT) and the Gamma-Ray Burst Monitor (GBM).

LAT is the pair-conversion telescope with extremely wide FOV (> 2 sr) and large effective area (>8000 cm^2) operating from 30 MeV with an extension to > 300 GeV.

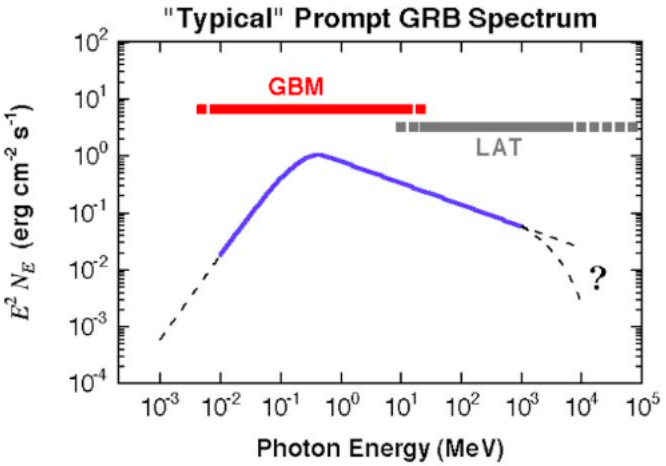

FIGURE 2.10: GRB spectral coverage of the *Fermi* GBM and the LAT instruments.

The GBM instrument operates at 8 keV - 40 MeV energy range. GBM consists 12 thallium activated sodium iodide (NaI) scintillation detectors and 2 bismuth germanate (BGO) scintillation detectors. NaI detectors are made of crystal disks attached to a photomultiplier tube (PMT). When photons interact with scintillation crystals, they are converted to lower energy photons detected by PMT. NaI detectors are distributed around the spacecraft with different orientations to fulfill FOV. The comparison of count rates from different NaI detectors provides an information to localize the GRB (~ 5 deg).

I use the GBM data throughout the thesis for the spectral analysis. I select CSPEC data, i.e. time sequences of 128 energy-channel spectra with integration time of 1024 ms each. Channels with energies in the range $8-800$ keV and 200 keV-1 MeV were selected for the NaI and BGO detectors, respectively. The extraction of spectra and light curves are performed using RMFIT (v4.3.2). I select pre- and post-burst

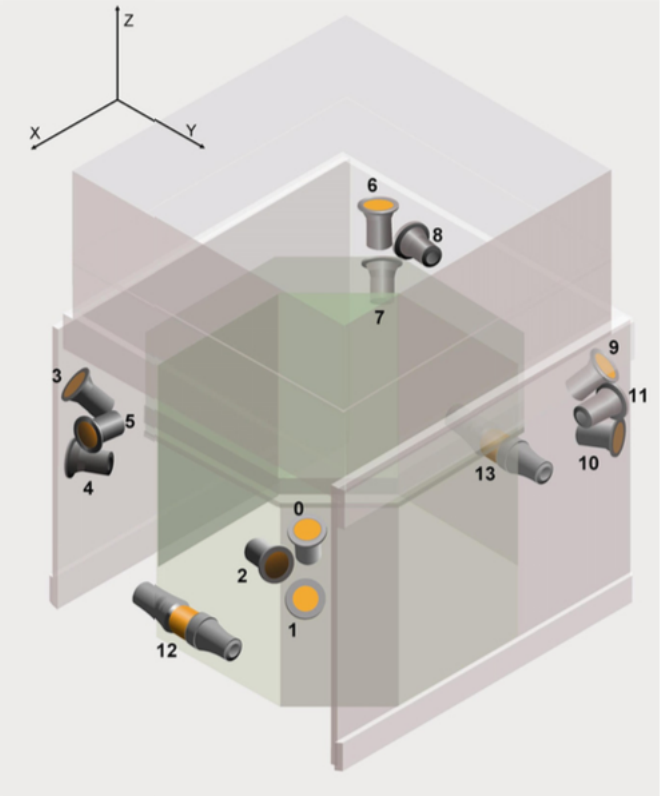

FIGURE 2.11: Distribution of NaI (0-11) and BGO detectors(12-13) on *Fermi* instrument. Credit: Meegan et al., 2009

data to model the background and fit an energy- and time-dependent polynomial. Spectra and background files are exported from RMFIT to XSPEC(v12.7.1) format in order to fit GBM spectra jointly with BAT and XRT spectra. The extraction of GBM spectra is compliant with the standard procedures adopted in the literature (e.g. Goldstein et al. 2012; Gruber et al. 2014). The extracted GBM data have Poisson distribution. Since NaI detectors are not collimated, the observed transients contain a diffuse background radiation which should be modeled and removed manually for each source. The modeling of the background assumes a Gaussian distribution on errors. Therefore, the proper likelihood for the spectral analysis with GBM data is PGSTAT (Poisson data with Gaussian background). However, for the specified cases I group energy channels using the *grppha* tool.

Chapter 3

Discovery of low energy breaks in prompt emission spectra

Radiative processes responsible for GRB prompt emission spectra are remaining unknown tens of years after their discovery. As discussed previously in Chapter 2, most of the observed prompt emission spectra are not consistent with the predicted synchrotron radiation. This inconsistency appears at energies below the spectral peak (in νF_ν): a typical low-energy photon index $\alpha \sim -1$ is in a contradiction with a predicted $\alpha_{\rm syn} = -1.5$ in a fast-cooling synchrotron scenario.

Theoretical studies would benefit from a better characterization of prompt spectra, especially in the low-energy part, where observations are inconsistent with the synchrotron theory. In this Chapter, I collect a sample of 14 GRBs for which the X-Ray Telescope (XRT, 0.3-10 keV), on board the *Swift* satellite, started observations during the prompt emission, observed in the range 15-150 keV by the Burst Alert Telescope (BAT). For these GRBs, I perform spectral analysis of the prompt emission from 0.5 keV to 150 keV, thanks to the joint analysis of XRT and BAT data, and from 0.5 keV to $\gtrsim 1$ MeV when observations from the *Fermi* Gamma-Ray Burst Monitor (GBM) are available. I find that the spectrum below ~ 10 keV does not lie on the extrapolation of the low-energy power law of the Band function (or similar functions that usually provide a satisfactory description of prompt spectra), but a spectral break around a few keV is required by the low-energy data.

3.1 Sample selection

In order to extend the characterization of prompt spectra down to the soft X-ray band, I selected a sample of GRBs for which the prompt emission (or part of it) has been observed by the XRT in the 0.3-10 keV range, in addition to the BAT in the 15-150 keV energy range. To this aim, I inspected the XRT light curves of all events detected up to 2016 January reported in the online *Swift*-XRT GRB catalog[1] (Evans et al., 2009). The online tool automatically identifies the presence of pulses (defined as statistically significant positive deviations from an underlying power-law emission)

[1] http://www.swift.ac.uk/xrt_live_cat

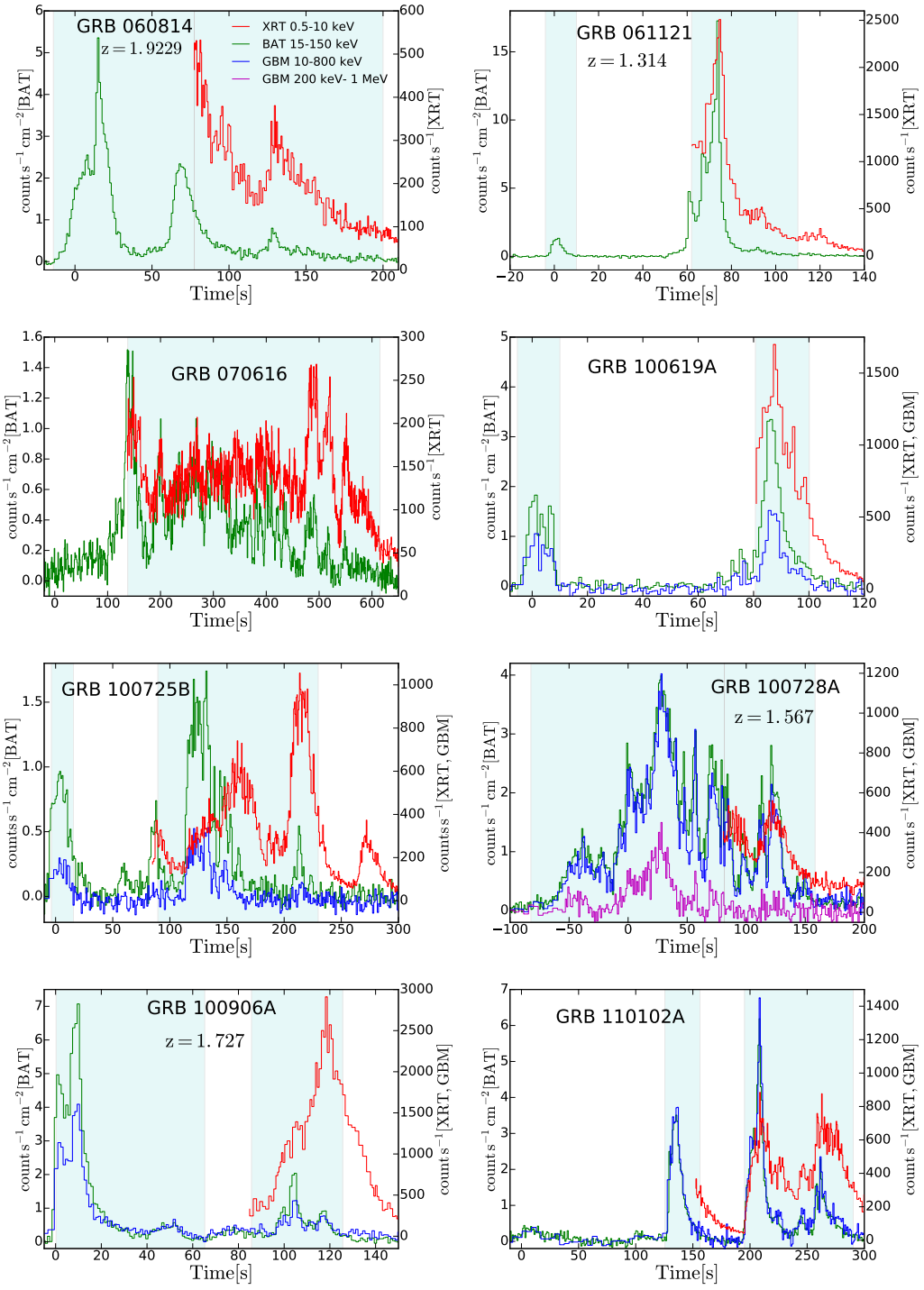

FIGURE 3.1: Examples of some background-subtracted light curves of GRBs analyzed in this Chapter. The time refers to the BAT trigger. *Swift*-XRT light curves (in the range 0.5-10 keV) are shown in red, *Swift*-BAT (15-150 keV) in green, *Fermi*-GBM (8-800 keV) in blue, and *Fermi*-GBM (200 keV-1 MeV) in purple. The time intervals where spectral analysis has been performed (light-blue shaded areas) have been determined on the basis of an S/N criterion applied to BAT data.

and returns the time intervals where the pulses are present. This selection resulted in 329 GRBs with at least one significant pulse in X-rays.

The scope of the sample selection is to find GRBs with simultaneous signal in the XRT and BAT instruments that can be combined for a joint spectral analysis. I then checked whether for these 329 GRBs the emission detected by the XRT was simultaneously observed also by the BAT. To this aim, I extracted background-subtracted count rate BAT light curves in the energy range 15-150 keV. First, using the *batgrbproduct* tool, I estimated the bust duration T_{100}, which corresponds to the duration that contains 100% of the burst emission. Then, I estimated the count rate outside the T_{100} time interval and found that its value is always smaller than ~ 0.01 counts/s/detector, which is then chosen as reference value. Adopting as initial time the starting time of XRT observations, I applied the Bayesian block algorithm (Scargle, 1998) to identify the possible presence of significant changes in the BAT signal during the XRT-detected emission, by requiring a BAT count rate higher than 0.01 counts/s/detector. This selection resulted in 77 GRBs with simultaneous signal detected by the BAT and the XRT. Since the goal of this study is to perform reliable spectral analysis combining BAT and XRT data, I further limited the sample: I required it to have at least four time bins with BAT signal-to-noise ratio (S/N) larger than 30 during the time interval where the emission is simultaneously observed by the BAT and the XRT. The choice of the threshold value ($S/N > 30$) is based on the study of Savchenko and Neronov (2009), where they show that BAT spectra with $S/N > 30$ return photon indices similar to those of the complete catalog of BATSE time-resolved spectra (Kaneko et al., 2006a). After applying all these selection criteria, I ended up with a sample of 15 GRBs. Among these, I excluded GRB 130427A because data extraction for this GRB requires a nonstandard pipeline processing (Maselli et al., 2014). The final sample includes 14 GRBs (Table 3.1). In seven cases, *Fermi*-GBM observations are also available and have been included in the spectral analysis. The light curves of some GRBs analyzed in this Chapter are shown in Figure 3.1. In each panel I show the XRT ($0.5 - 10$ keV; red curve), BAT ($15 - 150$ keV; green), and when available also the GBM ($8 - 800$ keV in blue and 200 keV-1 MeV in purple) count light curves. Note that in most cases XRT observations are available during the brightest part of the prompt emission, while in the remaining few cases they cover the less intense part of the prompt phase. The redshift (available for eight GRBs) ranges between $z = 0.725$ and $z = 2.73$ (Table 3.1).

3.2 Data extraction and spectral analysis

In this section I describe how spectral data have been extracted and prepared for the analysis. I explain in detail how the spectral analysis has been performed. I discuss the method adopted to account for absorption in the soft X-ray band. Then, I introduce the spectral models and the criteria adopted for the selection of the best-fit model.

TABLE 3.1: List of GRBs analyzed in this Chapter. The name and redshift are reported in the first and second column. The third column lists the values of the N_H, derived from spectral analysis of late time XRT observations. The late time interval (LTI, from BAT trigger time) chosen for the derivation of N_H can be found in the last column.

GRB	redshift	N_H 10^{22} cm^{-2}	LTI 10^4 s
060814	1.92	3.05	16.83 – 137.78
061121	1.314	0.72	3.46 – 9.25
070616	...	0.49	0.46 – 37.11
100619A	...	0.76	5.34 – 100.59
100725B	...	0.59	2.18 – 80.35
100728A	1.567	3.25	0.50 – 68.29
100906A	1.727	1.32	1.06 – 46.86
110102A	...	0.20	1.04 – 24.32
110205A	2.22	0.59	0.14 – 38.29
121123A	...	0.12	1.66 – 13.91
130907A	1.238	1.15	0.76 – 238.41
140108A	...	0.71	1.05 – 43.16
140206A	2.73	1.40	2.12 – 8.71
140512A	0.725	0.44	2.79 – 32.94

3.2.1 Data extraction

The extraction of *Swift* and *Fermi* data is performed following the standard procedures described previously in Section 2.4. The proper likelihoods for XRT/Swift, BAT/Swift and GBM/Fermi spectral fits are CSTAT, gaussian and PGSTAT, respectively. I adjust the spectral binning of XRT/Swift and GBM/Fermi data in order to use gaussian likelihood for joint fitting. In order to use χ^2 statistics, energy channels of XRT/Swift and GBM/Fermi spectra have been grouped together using the *grppha* tool by requiring at least 20 counts per bin.

3.2.2 Spectral analysis

The spectral analysis has been performed using XSPEC(v12.7.1). To account for intercalibration uncertainties between the different instruments, I introduced multiplicative factors in the fitting models. In particular, when GBM data are not available, I multiplied the XRT model by a factor left free to vary between 0.9 and 1.1. When GBM data are available, I froze to 1 the factor between XRT and BAT and multiplied the GBM model by a free factor. Inspecting the results inferred from the best-fit models, I found that in all cases the calibrations between the GBM and XRT/BAT agree within 15%.

The time intervals for the temporally resolved analysis have been defined so that in each bin the BAT S/N is larger than 30. Moreover, when possible, I redefined the time bins (provided that the criterion on the BAT S/N is always satisfied) in order not to mix the rising and decaying parts of a pulse, or, if a pulse is composed by the

superposition of many spikes, in order not to mix different spikes. The analysis was applied also to the initial part of the emission, before XRT observations started. The total number of time-resolved spectra analyzed is 128. For 86 of these, XRT data are available.

Absorption model

For GRBs with known redshift, I accounted for both Galactic and intrinsic metal absorption using the XSPEC models *tbabs* and *ztbabs*, respectively (Wilms, Allen, and McCray, 2000). The Galactic contribution to absorption in the direction of the burst has been estimated from Kalberla et al. (2005). The intrinsic absorption has been fixed to the value estimated from spectral analysis of late-time ($\gtrsim 10^4$ s) XRT data (Butler and Kocevski, 2007a). During XRT pulses, indeed, if the intrinsic $N_{\rm H}$ is left as a free parameter, a dramatic variation (even by a factor of 10) of its value is often observed. While an increase of $N_{\rm H}$ could be induced by photoionization effects of the circumburst medium by the prompt radiation (e.g. Perna and Lazzati 2002; Lazzati and Perna 2003; Perna, Lazzati, and Fiore 2003; Frontera et al. 2004), a fast decrease of $N_{\rm H}$ is more difficult to explain. This could hide a temporal evolution of the spectrum, e.g. the passage of any spectral break across the XRT energy band (Butler and Kocevski, 2007a). Therefore, the best estimate of $N_{\rm H}$ could be obtained when there is no strong spectral evolution and the light curve is well described by a simple power-law decay. I chose the latest-available XRT time interval (provided that no spectral evolution is apparent and the light curve is well described by a power-law decay) and modeled the extracted spectrum with an absorbed power law. When extracting the late-time spectrum, I considered an integration time large enough to constrain the intrinsic $N_{\rm H}$. This value of $N_{\rm H}$ has then been used as an input (fixed) parameter for the early-time spectral analysis.

For GRBs with unknown redshift, the late-time X-ray spectrum has been fitted by applying the *tbabs* model only. I verified that in all cases the best-fit value of $N_{\rm H}$ derived from this fit was larger than the Galactic value estimated from Kalberla et al. (2005). This value of $N_{\rm H}$ has then be used as a fixed input parameter for early-time spectral analysis, where this time only the *tbabs* model was applied.

For each GRB, the value of the intrinsic $N_{\rm H}$ inferred from late-time data and the late-time interval (LTI) chosen for the analysis are listed in Table 3.1.

Spectral models

Spectral models commonly applied to GRB prompt spectra include a single power law (PL), a power law with an exponential cutoff (CPL), and a Band function (Preece et al., 2000; Kaneko et al., 2006a; Nava et al., 2011a; Goldstein et al., 2012; Gruber et al., 2014; Narayana Bhat et al., 2016; Lien et al., 2016). These empirical models usually return a satisfactory fit to most spectra. However, as I will show in the following, all these models are in most cases inadequate when the energy range available for the

analysis is extended down to 0.5 keV by the inclusion of XRT data. Stated differently, XRT spectra do not lie on the low-energy extrapolation of the spectral shape defined by > 10 keV data. A spectral break in the soft X-ray band must be introduced in order to fit with one single spectral component the prompt spectrum from $\sim$0.5 keV to $\sim$1 MeV. I then extend the standard models (PL, CPL, and Band) to include a low-energy break. This leads us to introduce three additional models: a broken PL (BPL), a CPL with a break at low energies (BCPL), and a Band model with a break at low energies. However, the high-energy spectral index of the Band model and that of the Band model with a low-energy break are always unconstrained. This is due to the fact that for half of the sample, GBM data are not available. Moreover, even when they are available, the relatively small S/N of the time-resolved analysis makes it difficult to constrain the value of β. The value of β is constrained in a few cases where a BPL is the best-fit model. I also tried to apply a smoothly broken power-law model with a high-energy cutoff, but I did not succeed in constraining the smoothness parameter and/or the shape of the spectrum below the break energy. Summarizing, I found that all the spectra analyzed in this Chapter are well described (i.e., the best-fit model gives a reduced chi-square $\chi^2_{\rm red} < 1.15$, except for one case, where $\chi^2_{\rm red} = 1.3$) by one of the following four models: PL, CPL, BPL, or BCPL (see Figure 3.2).

I use the following conventions. A photon index is called α if its value is larger than -2 in the notation $dN(\nu)/d\nu \propto \nu^{\alpha}$, where dN represents the photon number (i.e., α identifies a part of the spectrum that is rising in the $\nu F_\nu = \nu^2 N_\nu$ representation). If there are two (consecutive) segments where the spectrum is rising (which is a common case in my analysis), I call them α_1 and α_2. The break energy that separates these two rising power-law segments is called $E_{\rm break}$. Following the traditional notation, when the spectrum has a peak in νF_ν, I refer to it as the peak energy $E_{\rm peak}$. Finally, I use the letter β when the photon index is lower than -2 (i.e., describing a part of the spectrum that is decreasing in νF_ν). I found few cases where the photon spectral index has a value around -2. In these cases, I refer to it as β if it is smaller than -2 within 1σ error.

A schematic representation of all the models, the notation, and different cases found in this analysis is shown in Figure 3.2. As can be seen in this plot, a BPL model can describe two different situations: either both indices are > -2 (α_1 and α_2, separated by a break energy $E_{\rm break}$), or the first index is > -2 and the second one is < -2 (in this case I call them α and β, and they are separated by the peak energy $E_{\rm peak}$). For PL, CPL, and BCPL models, instead, I find only cases where the photon indices are > -2.

I fitted all the time-integrated and time-resolved spectra to all the models, and for each spectrum I identified the best-fit model. In general, the $F-test$ is used to compare different models and choose the best one, but only when the models to be compared are nested (Protassov et al., 2002). Since I am testing the existence of a new feature (i.e., a spectral break), I decided to perform a conservative analysis and set at 3σ the significance level of the $F-test$ required to select a more complex

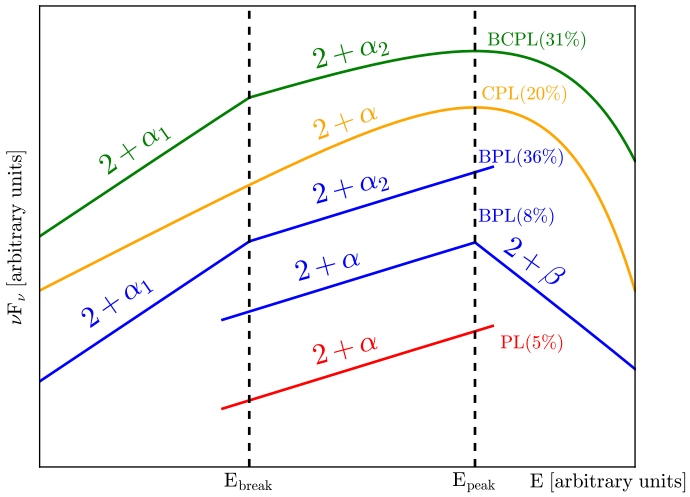

FIGURE 3.2: Summary of the four spectral models adopted in this Chapter, and definition of the adopted notation for the spectral indices and characteristic energies. Each one of the analyzed spectra is well described by one of these models. From top to bottom: a broken power law with a high-energy exponential cutoff (BCPL; green), a cutoff power law (CPL; orange), a broken power law (BPL; blue), and a single power law (PL; red). For the BPL model, I found two different cases in this analysis: both indices are larger than -2 (in this case they are called α_1 and α_2), or the first index is > -2 and the second one is < -2 (in this case they are called α and β, respectively). The percentages quoted next to each model name refer to time-resolved analysis for periods where XRT data are available.

model. In Figure 3.3 I provide a scheme of the method applied to determine the best-fit model. I start with the simplest function (PL) and consider progressively more complex functions. A single PL can be generalized in two different ways: by adding a break or by adding a high-energy exponential cutoff. In both cases the fit obtained with the resulting model (BPL and CPL, respectively) can be compared with the PL fit through an $F-test$. Depending on the result of the comparison, different cases are possible:

- Neither of the two models significantly (at more than 3σ) improves the fit. In this case the best-fit model is a PL;
- Only one of the two models improves the PL fit. I then select this model (either a CPL or BPL) and compare it to the fit performed with a BCPL, through an $F-test$. A BCPL model is chosen only if the improvement is significant at more than 3σ;
- Both models (CPL and BPL) improve the PL fit. First, I compare them one to each other. Note that they are not nested, and the $F-test$ cannot be performed. Since the number of parameters is different (3 for the CPL and 4 for the BPL), if the total χ^2 of the BPL is the largest between the two, then a CPL is preferred and is compared to the BCPL. In the opposite case ($\chi^2_{\rm CPL} > \chi^2_{\rm BPL}$), I separately compare each of them to the BCPL fit. If the BCPL significantly

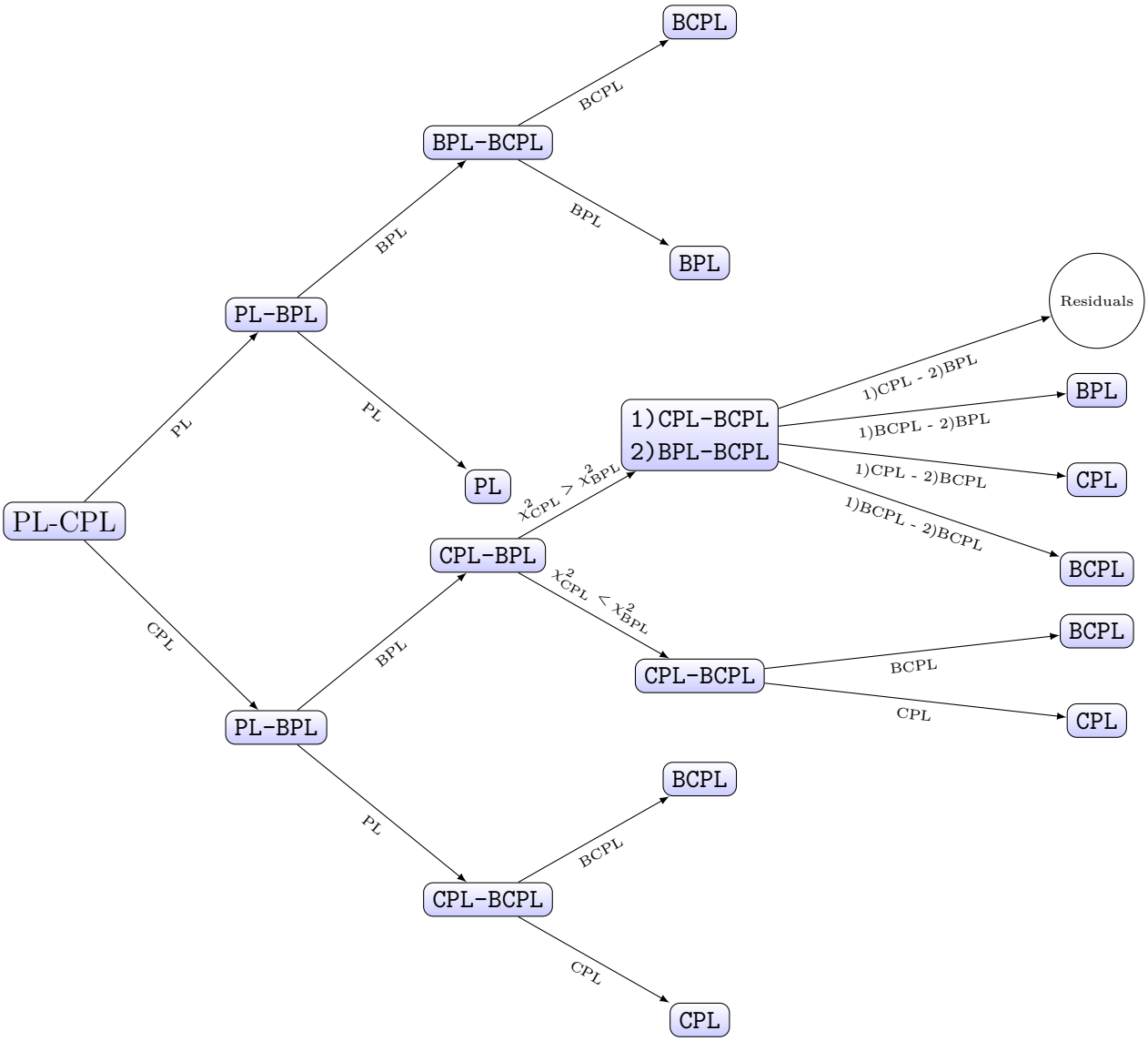

FIGURE 3.3: Flow chart summarizing the procedure adopted to select the best-fit model among four models: power law (PL), cutoff power law (CPL), broken power law (BPL), and broken power law with high-energy cutoff (BCPL). The selection proceeds from left to right. The nodes represent the models that are compared using the $F-test$ (except for the case CPL-BPL, where models are not nested and the total chi-square is compared). Next to the arrows it is reported the model chosen as a result of the comparison is reported. There is a special case in the scheme where there is no possibility to find statistical difference between CPL and BPL models and select the best-fit model on the basis of the chi-square or $F-test$. In this case (which occurred six times) visual inspection of the residuals is adopted.

improves both of them, then I choose the BCPL. If the improvement over a CPL is significant, but the improvement over a BPL is not, it means that the spectrum has a significant break, but not a significant exponential cutoff, and a BPL is then chosen. If the opposite case is verified (BCPL is better than a BPL but not better than a CPL), it means that a high-energy cutoff is clearly

present, while the low-energy break is not significant. A CPL is then chosen. The validity of this method is confirmed by the inspection, case by case, of the shape of the residuals. A peculiar situation (which is realized only in six spectra) is provided by the case when a BCPL is not improving either the CPL or the BPL fit, and one of the latter models must be chosen. In these cases, I inspect the residuals and choose the model fit for which the residuals do not show evidence of systematic trends.

I verified that for all spectra the selected best-fit model gives a reduced chi-square $\chi^2_{\rm red} < 1.15$, except for one case, where $\chi^2_{\rm red} = 1.3$.

3.3 Results

I first present and discuss in detail the results of this analysis applied to one event, GRB 140512A, as an example. In the second part of this section, I present the results obtained by applying the same analysis to all GRBs in this sample.

3.3.1 GRB 140512A

The light curve of GRB 140512A is composed of two separated emission episodes (see the top panel of Figure 3.5), which I call the first and second pulses. During the first pulse, only BAT and GBM observations are available. For the second episode (where most of the radiation is emitted) there are also XRT data. First, I discuss the time-integrated spectral analysis, which has been performed on the two pulses separately. The time intervals chosen for the analysis are shown by the cyan-shaded regions in Figure 3.5 (top panel). The time-integrated spectra of each pulse are shown in Figure 3.4. The spectrum of the first pulse (top left panel) is well fitted by a CPL model (solid line, $\chi^2 = 196.9$, for 317 degrees of freedom [dof]), which according to the $F-test$ improves the PL fit ($\chi^2 = 235.0$, for 318 dof) with a 3σ significance. Note that both the PL model and CPL model overfit the data, since they result in a $\chi^2_{\rm red} < 1$. A Band model does not improve the CPL fit (i.e., a high-energy power law is not required by the data). The best-fit parameters are $\alpha = -1.09^{+0.12}_{-0.11}$ and $E_{\rm peak} = 439^{+293}_{-134}$ keV.

In the second pulse, a CPL model (top right panel in Figure 3.4) appears adequate for the description of > 8 keV data, but cannot account for the harder spectral shape characterizing the XRT band. The CPL model returns $\chi^2 = 613.6$ (d.o.f. $= 480$) and shows a systematic trend in the residuals (defined as the difference between the data and the model, divided by the error, and shown in the bottom sections of each spectrum). I then allow for a spectral break at low energies and verify that a BCPL model (bottom right panel) gives a significantly better description of the data. For this model $\chi^2 = 442.8$ (d.o.f. $= 478$), corresponding to an improvement (with respect to the CPL one) of 8.4σ significance. The best-fit parameters are $E_{\rm break} = 7.18^{+1.12}_{-1.0}$ keV, $\alpha_1 = -0.76^{+0.05}_{-0.04}$, $\alpha_2 = -1.26 \pm 0.04$, and $E_{\rm peak} = 532^{+190}_{-123}$ keV.

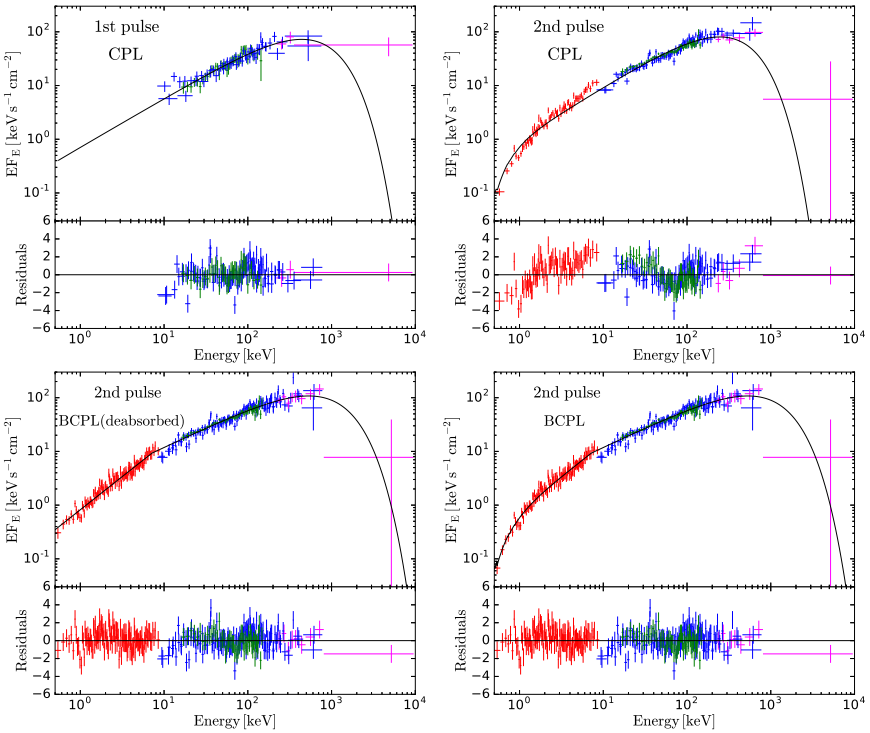

FIGURE 3.4: Time-integrated spectral analysis performed separately on the first and second pulses of GRB 140512A (see the light curve in Figure 3.5). The bottom sections of each panel show the fit residuals (see text). The joint BAT (green) and GBM (blue and purple, corresponding to the NaI and BGO detectors, respectively) spectrum of the first pulse (integrated from $t = -21.05$ s to $t = 10.70$ s since BAT trigger time) is shown in the top left panel. During this temporal window, XRT data are not available. The spectrum is well modeled by a CPL (black line). The other three panels show the spectrum integrated during the second emission episode (i.e., from $t = 102.86$ s to $t = 158.16$ s). In this time interval, XRT observations are available and are included in the analysis (red data points). The fits with a CPL (top right panel) and with a BCPL (bottom right panel) are shown. For this last fit, the de-absorbed model and data are shown in the bottom left panel.

The curvature below ~ 3 keV visible in the data and in the model is due to the absorption, which I inferred to correspond to $N_{\rm H} = 4.4 \times 10^{21}$ cm^{-2} from the spectral analysis of the data accumulated between 2.8×10^4 s and 3.3×10^5 s (see Table 3.1). For convenience, for the BCPL fit I also show (bottom left panel) the de-absorbed model and data, so that the intrinsic shape of the spectrum can be better appreciated.

The results of time-resolved spectral analysis performed on each pulse are shown in Figure 3.5 (middle and bottom panels, respectively). The first pulse is divided into two time bins. In both bins, the spectra are best fitted by a CPL. The second pulse is divided into nine time bins. In seven cases, the best-fit model is a BCPL. In the remaining two cases, a CPL model is chosen, because the addition of a low-energy break improves the fit with a 2σ significance, which, according to 3σ requirement, is not sufficient to claim the presence of a break. The spectral indices as a function of time are plotted in the middle panel of Figure 3.5. When the best-fit model is

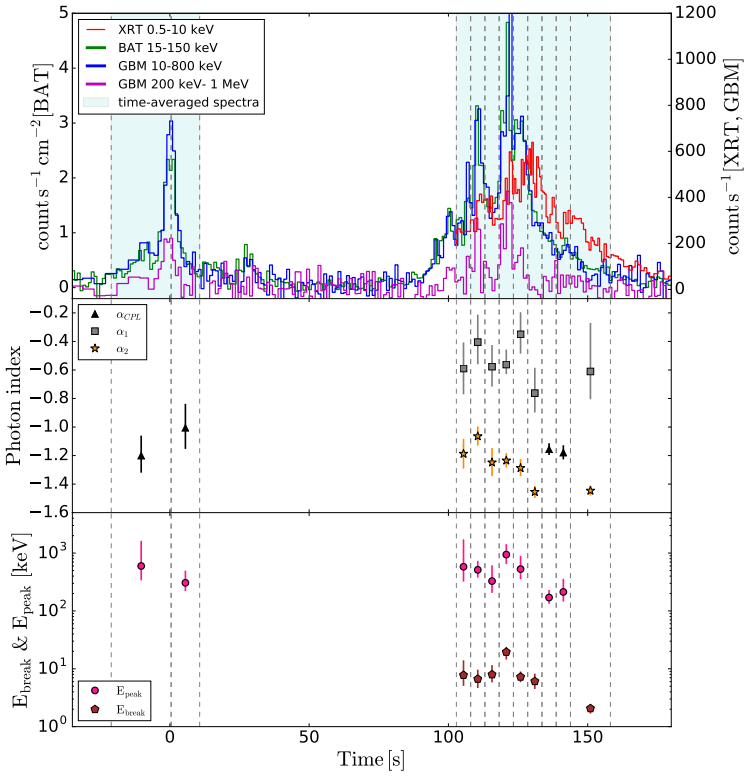

FIGURE 3.5: Results of the time-resolved spectral analysis of GRB 140512A. The top panel shows the XRT (red), BAT (green), and GBM (blue and purple) light curves. The shaded vertical stripes show the time intervals selected for the time-average spectral analysis of the first and second pulses (the corresponding spectra are shown in Fig. 3.4). The dashed vertical lines show the time bins selected for the time-resolved spectral analysis. In the first interval, XRT data are not available. The middle and bottom panels show the best-fit parameters (photon indices and break/peak energies, respectively) with 1σ level errors.

a BCPL, the spectral index α_2 (stars), representing the spectral shape just below the peak energy, is softer as compared to the standard value $\alpha \simeq -1$, i.e., I find $-1.5 < \alpha_2 < -1$. At lower energies, below the break energy, the spectral slope (squares) is higher and spans the range $-0.9 < \alpha_1 < -0.2$ (this range includes the 1σ statistical uncertainty on the smallest and largest measured values of α_1). The break energy $E_{\rm break}$ (bottom panel, pentagon symbols) assumes values between 2 and 20 keV, while for the peak energy $E_{\rm peak}$ (circles) I found standard values, between 200 keV and 1 MeV. For the first six time bins of the second pulse, the spectra and their modeling with different spectral models are shown in Figure 3.6. The six different rows refer to the six different time bins. For each time bin, the three panels show the fits and residuals obtained with a CPL (first panel), BPL (second), and BCPL (third) model. In these six time bins, the best model is always the BCPL.

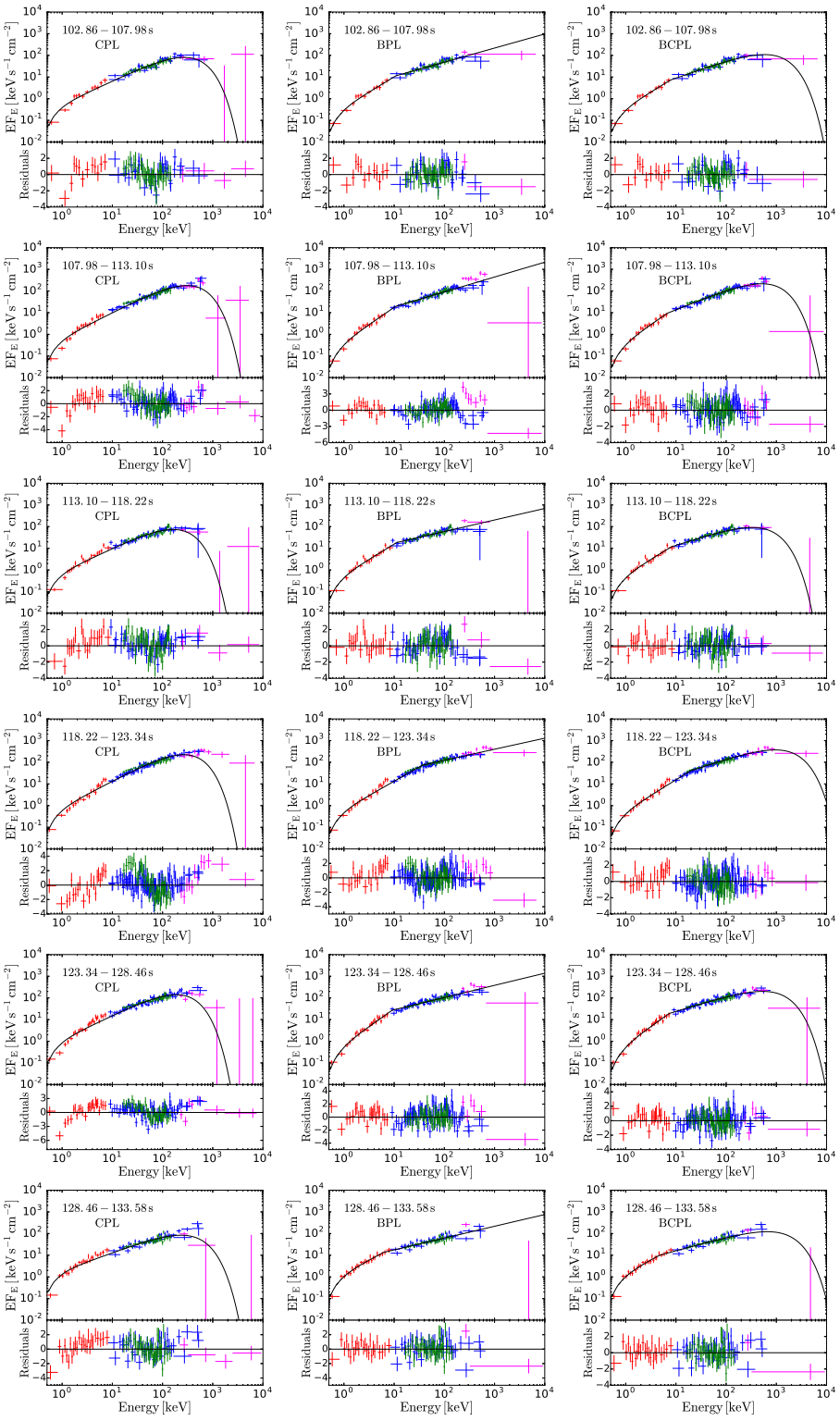

FIGURE 3.6: Time-resolved spectra of GRB 140512A for six different time bins, including XRT (red data points), BAT (green), and GBM (blue and purple) data. Each row refers to a different time bin (the time interval is reported in each panel). For each time bin, the modeling with three different models and the residuals are shown: cutoff power law (CPL; left panel), broken power law (middle panel), and broken power law with an exponential cutoff (right panel).

3.3.2 Whole sample

The results of the spectral analysis on time-integrated and time-resolved spectra for the entire sample (14 GRBs) are reported in Table 3.2. For each spectrum, I report the time interval, the name of the best-fit model, the best-fit parameters, the flux, and the instruments included in the analysis.

TABLE 3.2: Best-fit parameters for time-integrated and time-resolved spectra. The table lists the time interval (since the BAT trigger time), the best fit model (PL=power-law, CPL=cutoff power-law, BPL= broken power-law, BCPL=broken power-law with a high energy cutoff), the best fit parameters (columns 3 to 7, for a definition see Figure 3.2), the flux F (or its lower and upper limits, in square brackets), integrated in the energy range 0.5 keV - 10 MeV, the total chi-square χ^2, and the degrees of freedom (d.o.f.). The last column reports the instruments included in the spectral analysis: X=XRT, B=BAT, G=GBM. Time bins marked with a bold font identify time-integrated spectra.

Time bin s	Model	α_1	$E_{\rm break}$ keV	α/α_2	$E_{\rm peak}$ keV	β	F$_{-7}$ [erg cm^{-2}s^{-1}]	χ^2 (dof)	Instr.
				GRB 060814, z = 1.92					
[**−14.00, 77.50**]	CPL			$-1.26^{+0.13}_{-0.13}$	157^{+80}_{-32}		$2.49^{+0.33}_{-0.28}$	27.1(55)	B
[**77.50, 200.00**]	BPL	$-0.98^{+0.13}_{-0.09}$	$2.83^{+0.39}_{-0.45}$	$-1.71^{+0.04}_{-0.06}$			[0.39 − 6.42]	172.1(186)	X,B
[−14.00, 11.00]	CPL			$-0.99^{+0.21}_{-0.21}$	169^{+159}_{-44}		$2.37^{+0.56}_{-0.44}$	46.8(55)	B
[11.00, 15.00]	PL			$-1.42^{+0.06}_{-0.06}$			[2.54 − 481.03]	55.3(56)	B
[15.00, 40.00]	CPL			$-1.29^{+0.17}_{-0.16}$	160^{+162}_{-41}		$3.39^{+0.60}_{-0.49}$	34.2(55)	B
[40.00, 77.50]	CPL			$-1.42^{+0.20}_{-0.19}$	106^{+87}_{-22}		$1.58^{+0.36}_{-0.28}$	35.6(55)	B
[77.50, 97.00]	BPL	$-0.27^{+0.34}_{-0.21}$	$2.22^{+0.26}_{-0.33}$	$-1.66^{+0.06}_{-0.04}$			[0.88 − 21.35]	124.6(131)	X,B
[97.00, 120.00]	BPL	$-1.10^{+0.27}_{-0.20}$	$2.28^{+0.87}_{-0.50}$	$-1.80^{+0.08}_{-0.07}$			[0.33 − 2.83]	102.0(106)	X,B
[120.00, 130.00]	BPL	$-1.01^{+0.13}_{-0.12}$	$4.78^{+1.03}_{-1.10}$	$-1.64^{+0.07}_{-0.12}$			[0.53 − 15.73]	80.6(89)	X,B
[130.00, 200.00]	BPL	$-1.17^{+0.14}_{-0.18}$	$2.71^{+2.40}_{-0.33}$	$-1.70^{+0.04}_{-0.10}$			[0.24 − 4.37]	174.4(152)	X,B
				GRB 061121, z = 1.314					
[**−4.00, 10.00**]	PL			$-1.66^{+0.09}_{-0.10}$			[0.48 − 18.04]	58.0(56)	B
[**62.00, 110.00**]	BPL	$-0.78^{+0.10}_{-0.10}$	$4.97^{+0.96}_{-0.84}$	$-1.43^{+0.02}_{-0.03}$			[3.18 − 529.42]	137.8(150)	X,B
[−4.00, 10.00]	PL			$-1.66^{+0.09}_{-0.10}$			[0.48 − 18.04]	58.0(56)	B
[50.00, 62.00]	PL			$-1.64^{+0.10}_{-0.10}$			[0.50 − 21.60]	51.7(56)	B
[62.00, 68.00]	BPL	$-0.56^{+0.16}_{-0.15}$	$4.53^{+1.01}_{-0.64}$	$-1.47^{+0.03}_{-0.03}$			[4.73 − 574.02]	87.0(85)	X,B
[68.00, 74.00]	BPL	$-0.29^{+0.25}_{-0.21}$	$4.83^{+2.18}_{-0.91}$	$-1.46^{+0.03}_{-0.03}$			[9.98 − 1297.70]	48.8(77)	X,B
[74.00, 78.00]	BPL	$-0.29^{+0.91}_{-0.48}$	$2.52^{+1.71}_{-0.74}$	$-1.23^{+0.02}_{-0.03}$			[11.20 − 10385.00]	49.1(73)	X,B
[78.00, 90.00]	BPL	$-0.93^{+0.23}_{-0.24}$	$2.82^{+1.60}_{-0.57}$	$-1.70^{+0.06}_{-0.06}$			[1.12 − 20.48]	92.0(86)	X,B
[90.00, 110.00]	CPL			$-1.42^{+0.06}_{-0.08}$	55^{+26}_{-14}		$0.39^{+0.09}_{-0.07}$	99.4(104)	X,B
				GRB 070616					
[**138.00, 615.00**]	BCPL	$-0.84^{+0.05}_{-0.04}$	$3.22^{+0.32}_{-0.35}$	$-1.29^{+0.01}_{-0.07}$	102^{+25}_{-14}		$0.57^{+0.06}_{-0.01}$	228.7(234)	X,B
[−10.00, 95.00]	PL			$-1.66^{+0.18}_{-0.19}$			[0.11 − 3.98]	50.2(56)	B
[95.00, 138.00]	PL			$-1.38^{+0.07}_{-0.07}$			[0.43 − 135.90]	43.8(56)	B
[138.00, 175.00]	BPL	$-0.90^{+0.06}_{-0.06}$	$8.10^{+4.88}_{-0.96}$	$-1.42^{+0.05}_{-0.05}$			[0.87 − 162.03]	164.8(153)	X,B

TABLE 3.2: continued.

Time bin s	Model	α_1	$E_{\rm break}$ keV	α/α_2	$E_{\rm peak}$ keV	β	F_{-7} [erg cm^{-2}s^{-1}]	χ^2 (dof)	Instr.
$[175.00, 210.00]$	BPL	$-0.89^{+0.14}_{-0.08}$	$7.21^{+2.97}_{-0.74}$	$-1.58^{+0.09}_{-0.08}$			$[0.44 - 25.37]$	128.0(140)	X,B
$[210.00, 282.00]$	BCPL	$-0.73^{+0.11}_{-0.07}$	$4.20^{+2.90}_{-1.21}$	$-1.18^{+0.14}_{-0.06}$	122^{+38}_{-37}		$0.91^{+0.11}_{-0.16}$	188.8(186)	X,B
$[282.00, 330.00]$	BCPL	$-0.65^{+0.18}_{-0.14}$	$3.34^{+1.12}_{-0.72}$	$-1.33^{+0.13}_{-0.06}$	169^{+125}_{-69}		$1.17^{+0.11}_{-0.22}$	138.3(174)	X,B
$[330.00, 460.00]$	BCPL	$-0.75^{+0.07}_{-0.07}$	$3.32^{+0.30}_{-0.27}$	$-1.48^{+0.05}_{-0.06}$	84^{+38}_{-20}		$0.53^{+0.04}_{-0.03}$	185.4(217)	X,B
$[460.00, 500.00]$	BCPL	$-0.73^{+0.16}_{-0.13}$	$3.04^{+0.64}_{-0.43}$	$-1.45^{+0.09}_{-0.13}$	43^{+22}_{-11}		$0.37^{+0.07}_{-0.03}$	123.0(126)	X,B
$[500.00, 530.00]$	BCPL	$-0.85^{+0.21}_{-0.16}$	$2.63^{+0.48}_{-0.47}$	$-1.63^{+0.23}_{-0.19}$	18^{+30}_{-9}		$0.21^{+0.04}_{-0.02}$	128.8(112)	X,B
$[530.00, 615.00]$	CPL			$-1.33^{+0.06}_{-0.06}$	16^{+2}_{-2}		$0.13^{+0.03}_{-0.02}$	159.0(163)	X,B
				GRB 100619A					
$[\mathbf{-5.34, 10.02}]$	CPL			$-1.23^{+0.21}_{-0.19}$	110^{+46}_{-21}		$1.62^{+12.85}_{-12.34}$	184.8(204)	B,G
$[\mathbf{80.68, 100.13}]$	BPL	$-1.01^{+0.12}_{-0.12}$	$5.13^{+1.02}_{-0.60}$	$-1.93^{+0.04}_{-0.04}$			$[3.08 - 8.79]$	218.3(271)	X,B,G
$[80.68, 86.82]$	BPL	$-1.02^{+0.19}_{-0.19}$	$6.33^{+2.08}_{-1.15}$	$-1.94^{+0.06}_{-0.06}$			$[3.26 - 9.25]$	169.3(163)	X,B,G
$[86.82, 89.89]$	BCPL	$-0.79^{+0.44}_{-0.23}$	$4.75^{+1.49}_{-2.50}$	$-1.61^{+0.06}_{-0.10}$	132^{+193}_{-55}		$5.51^{+1.58}_{-1.45}$	161.1(159)	X,B,G
$[89.89, 92.97]$	BPL	$-0.90^{+0.33}_{-0.25}$	$5.41^{+1.80}_{-1.54}$	$-2.01^{+0.08}_{-0.08}$			$[2.81 - 6.58]$	123.4(130)	X,B,G
$[92.97, 100.13]$	BPL	$-1.21^{+0.33}_{-0.24}$	$3.92^{+1.46}_{-1.18}$	$-2.10^{+0.10}_{-0.09}$			$[1.35 - 2.13]$	157.5(182)	X,B,G
				GRB 100725B					
$[\mathbf{-3.70, 15.76}]$	PL			$-1.56^{+0.07}_{-0.07}$			$[2.12 - 57.27]$	152.4(144)	B,G
$[\mathbf{89.49, 229.78}]$	BPL	$-1.25^{+0.09}_{-0.06}$	$5.19^{+0.89}_{-1.23}$	$-2.06^{+0.06}_{-0.05}$			$1.47^{+0.08}_{-0.08}$	348.2(310)	X,B,G
$[109.97, 120.21]$	CPL			$-1.15^{+0.06}_{-0.05}$	94^{+33}_{-19}		$0.96^{+0.16}_{-0.14}$	255.0(226)	X,B,G
$[120.21, 129.43]$	BCPL	$-0.65^{+0.15}_{-0.11}$	$6.62^{+1.40}_{-1.88}$	$-1.46^{+0.15}_{-0.12}$	99^{+70}_{-33}		$2.07^{+0.29}_{-0.27}$	295.9(227)	X,B,G
$[129.43, 136.59]$	BCPL	$-0.73^{+0.24}_{-0.16}$	$4.51^{+2.57}_{-1.55}$	$-1.32^{+0.10}_{-0.12}$	79^{+34}_{-19}		$1.84^{+0.31}_{-0.30}$	222.0(193)	X,B,G
$[136.59, 143.76]$	BPL			$-0.84^{+0.14}_{-0.14}$	$7.47^{+1.45}_{-1.19}$	$-2.28^{+0.12}_{-0.13}$	$1.16^{+0.19}_{-0.18}$	167.8(185)	X,B,G
$[143.76, 155.03]$	BPL			$-0.76^{+0.11}_{-0.11}$	$9.29^{+0.56}_{-9.31}$	$-2.49^{+0.11}_{-0.12}$	$1.19^{+0.45}_{-0.12}$	265.6(235)	X,B,G
$[155.03, 170.39]$	BPL			$-0.98^{+0.08}_{-0.08}$	$6.63^{+0.78}_{-0.94}$	$-3.16^{+0.23}_{-0.24}$	$0.54^{+0.05}_{-0.05}$	128.7(127)	X,B,G
$[205.20, 229.78]$	BPL			$-1.07^{+0.21}_{-0.19}$	$2.86^{+0.52}_{-0.33}$	$-2.51^{+0.07}_{-0.19}$	$0.48^{+0.20}_{-0.04}$	160.0(148)	X,B,G
				GRB 100728A, z = 1.567					
$[\mathbf{-82.31, 81.53}]$	CPL			$-0.69^{+0.03}_{-0.03}$	342^{+21}_{-19}		$5.85^{+0.11}_{-0.11}$	370.1(363)	B,G
$[\mathbf{81.53, 158.33}]$	BCPL	$-0.97^{+0.19}_{-0.12}$	$2.24^{+0.54}_{-0.51}$	$-1.34^{+0.02}_{-0.02}$	186^{+33}_{-25}		$2.00^{+0.13}_{-0.14}$	360.3(350)	X,B,G
$[-82.31, -48.52]$	PL			$-1.17^{+0.07}_{-0.07}$			$[11.09 - 502.29]$	348.4(324)	B,G
$[-48.52, -13.70]$	CPL			$-0.98^{+0.07}_{-0.07}$	481^{+176}_{-107}		$4.17^{+0.20}_{-0.17}$	370.3(321)	B,G
$[-13.70, 14.97]$	CPL			$-0.74^{+0.04}_{-0.04}$	439^{+50}_{-42}		$8.84^{+0.24}_{-0.22}$	326.8(323)	B,G
$[14.97, 28.29]$	CPL			$-0.60^{+0.04}_{-0.04}$	496^{+44}_{-38}		$17.85^{+0.41}_{-0.40}$	330.1(290)	B,G
$[28.29, 52.86]$	CPL			$-0.74^{+0.04}_{-0.04}$	344^{+26}_{-23}		$10.38^{+0.25}_{-0.23}$	348.9(317)	B,G
$[52.86, 65.15]$	CPL			$-0.90^{+0.08}_{-0.08}$	269^{+56}_{-40}		$4.99^{+0.32}_{-0.27}$	284.3(270)	B,G
$[65.15, 81.53]$	CPL			$-0.76^{+0.07}_{-0.07}$	235^{+28}_{-23}		$5.55^{+0.29}_{-0.26}$	325.5(287)	B,G
$[81.53, 92.79]$	BCPL	$-0.43^{+0.69}_{-0.36}$	$2.01^{+0.63}_{-0.44}$	$-1.33^{+0.05}_{-0.05}$	188^{+94}_{-49}		$2.76^{+0.50}_{-0.53}$	167.2(166)	X,B,G
$[92.79, 106.11]$	CPL			$-1.35^{+0.04}_{-0.04}$	123^{+44}_{-26}		$1.27^{+0.14}_{-0.12}$	188.7(164)	X,B,G
$[106.11, 118.39]$	CPL			$-1.20^{+0.03}_{-0.03}$	219^{+49}_{-35}		$2.79^{+0.16}_{-0.15}$	206.5(236)	X,B,G
$[118.39, 135.80]$	CPL			$-1.19^{+0.02}_{-0.02}$	232^{+35}_{-27}		$3.62^{+0.15}_{-0.14}$	319.3(280)	X,B,G
$[135.80, 158.33]$	CPL			$-1.31^{+0.06}_{-0.07}$	43^{+11}_{-7}		$0.39^{+0.08}_{-0.07}$	114.0(106)	X,B,G

TABLE 3.2: continued.

Time bin s	Model	α_1	$E_{\rm break}$ keV	α/α_2	$E_{\rm peak}$ keV	β	F_{-7} [erg cm^{-2}s^{-1}]	χ^2 (dof)	Instr.
GRB 100906A, z = 1.727									
[**0.22, 65.24**]	CPL			$-1.42^{+0.09}_{-0.08}$	182^{+66}_{-36}		$3.23^{+0.26}_{-0.21}$	231.1(342)	B,G
[**85.72, 125.65**]	BPL			$-0.56^{+0.13}_{-0.17}$	$3.84^{+0.58}_{-0.27}$	$-2.45^{+0.04}_{-0.07}$	$1.58^{+0.16}_{-0.15}$	394.8(378)	X,B,G
[0.22, 2.77]	CPL			$-1.04^{+0.10}_{-0.09}$	289^{+98}_{-60}		$13.02^{+1.08}_{-0.89}$	159.3(171)	B,G
[2.77, 5.84]	CPL			$-1.09^{+0.11}_{-0.10}$	177^{+47}_{-30}		$9.32^{+1.06}_{-0.85}$	182.6(185)	B,G
[5.84, 10.96]	CPL			$-1.10^{+0.18}_{-0.18}$	126^{+52}_{-22}		$12.75^{+0.87}_{-0.76}$	261.8(230)	B,G
[10.96, 16.08]	CPL			$-1.27^{+0.25}_{-0.24}$	93^{+51}_{-16}		$6.33^{+0.92}_{-0.73}$	208.1(214)	B,G
[85.71, 96.98]	BPL			$-1.14^{+0.20}_{-0.16}$	$3.76^{+0.77}_{-0.82}$	$-2.14^{+0.10}_{-0.09}$	$0.69^{+0.09}_{-0.09}$	218.9(226)	X,B,G
[96.98, 105.17]	BPL			$-0.44^{+0.22}_{-0.40}$	$3.86^{+2.11}_{-0.48}$	$-2.10^{+0.05}_{-0.14}$	$3.14^{+0.51}_{-0.50}$	204.7(206)	X,B,G
[105.17, 125.65]	BPL			$-0.63^{+0.14}_{-0.15}$	$4.52^{+0.52}_{-0.40}$	$-2.65^{+0.06}_{-0.07}$	$1.85^{+0.24}_{-0.23}$	202.2(193)	X,B,G
GRB 110102A									
[**125.54, 156.26**]	CPL			$-1.39^{+0.10}_{-0.09}$	283^{+278}_{-94}		$3.55^{+0.34}_{-0.25}$	217.5(205)	B,G
[**195.17, 290.40**]	BCPL	$-0.85^{+0.06}_{-0.05}$	$4.02^{+0.56}_{-0.54}$	$-1.49^{+0.03}_{-0.03}$	686^{+731}_{-274}		$3.83^{+0.15}_{-0.15}$	352.8(315)	X,B,G
[125.54, 132.71]	CPL			$-1.24^{+0.25}_{-0.22}$	108^{+69}_{-25}		$1.63^{+0.53}_{-0.34}$	217.7(206)	B,G
[132.71, 137.83]	CPL			$-1.17^{+0.07}_{-0.06}$	344^{+111}_{-69}		$10.15^{+0.54}_{-0.47}$	225.3(205)	B,G
[137.83, 142.95]	CPL			$-1.19^{+0.14}_{-0.12}$	194^{+89}_{-45}		$4.23^{+0.56}_{-0.42}$	200.2(189)	B,G
[142.95, 156.26]	PL			$-1.75^{+0.08}_{-0.08}$			$[2.75 - 10.21]$	274.2(247)	B,G
[195.17, 200.29]	BCPL	$-0.68^{+0.27}_{-0.16}$	$4.76^{+2.48}_{-1.96}$	$-1.18^{+0.08}_{-0.07}$	679^{+840}_{-305}		$5.49^{+0.92}_{-0.94}$	165.1(205)	X,B,G
[200.29, 206.44]	BCPL	$-0.59^{+0.15}_{-0.15}$	$5.10^{+2.99}_{-1.19}$	$-1.13^{+0.05}_{-0.07}$	391^{+161}_{-88}		$9.21^{+1.38}_{-1.29}$	260.2(248)	X,B,G
[206.44, 209.51]	BCPL	$-0.37^{+0.74}_{-0.40}$	$3.17^{+4.65}_{-1.14}$	$-1.09^{+0.05}_{-0.06}$	554^{+236}_{-121}		$22.44^{+6.64}_{-6.63}$	198.3(185)	X,B,G
[209.51, 212.58]	BCPL	$-0.43^{+0.19}_{-0.19}$	$5.15^{+1.55}_{-0.85}$	$-1.24^{+0.05}_{-0.06}$	509^{+270}_{-142}		$15.99^{+3.40}_{-3.22}$	211.1(183)	X,B,G
[212.58, 218.73]	BCPL	$-0.67^{+0.18}_{-0.14}$	$4.59^{+1.52}_{-1.37}$	$-1.47^{+0.09}_{-0.10}$	220^{+285}_{-86}		$2.79^{+0.38}_{-0.37}$	228.2(224)	X,B,G
[218.73, 229.99]	BCPL	$-0.10^{+0.45}_{-0.32}$	$1.97^{+0.36}_{-0.27}$	$-1.44^{+0.08}_{-0.07}$	70^{+48}_{-23}		$0.78^{+0.10}_{-0.11}$	102.7(113)	X,B,G
[241.25, 252.52]	BPL	$-1.03^{+0.09}_{-0.09}$	$5.74^{+1.95}_{-1.11}$	$-1.85^{+0.07}_{-0.11}$			$[0.97 - 4.10]$	244.0(233)	X,B,G
[252.52, 260.71]	BPL	$-0.67^{+0.23}_{-0.22}$	$3.59^{+1.39}_{-0.73}$	$-1.70^{+0.05}_{-0.08}$			$[1.68 - 17.17]$	213.2(200)	X,B,G
[260.71, 270.95]	BPL	$-0.75^{+0.13}_{-0.11}$	$4.52^{+0.69}_{-0.69}$	$-1.74^{+0.04}_{-0.04}$			$[2.73 - 22.18]$	269.0(235)	X,B,G
[270.95, 290.40]	BPL	$-0.68^{+0.22}_{-0.19}$	$2.17^{+0.27}_{-0.20}$	$-1.91^{+0.04}_{-0.04}$			$[0.60 - 2.64]$	132.5(128)	X,B,G
GRB 110205A, z = 2.22									
[**0.00, 160.00**]	CPL			$-1.27^{+0.29}_{-0.28}$	72^{+23}_{-10}		$0.65^{+0.24}_{-0.17}$	48.5(55)	B
[**160.00, 350.00**]	BPL	$-0.88^{+0.04}_{-0.03}$	$5.79^{+0.68}_{-0.74}$	$-1.78^{+0.04}_{-0.04}$			$[0.64 - 7.11]$	272.2(281)	X,B
[0.00, 94.00]	PL			$-1.63^{+0.13}_{-0.13}$			$[0.27 - 11.72]$	52.5(56)	B
[94.00, 120.00]	PL			$-1.87^{+0.08}_{-0.09}$			$[0.51 - 5.29]$	61.8(56)	B
[120.00, 160.00]	CPL			$-1.46^{+0.24}_{-0.23}$	65^{+16}_{-8}		$1.23^{+0.35}_{-0.26}$	61.1(55)	B
[160.00, 193.00]	BPL	$-0.63^{+0.05}_{-0.05}$	$5.89^{+0.60}_{-0.46}$	$-1.85^{+0.04}_{-0.04}$			$[0.95 - 6.80]$	209.7(190)	X,B
[193.00, 210.00]	BPL	$-0.74^{+0.08}_{-0.07}$	$5.82^{+0.78}_{-0.90}$	$-1.64^{+0.05}_{-0.05}$			$[1.16 - 35.35]$	112.3(126)	X,B
[210.00, 240.00]	BCPL	$-0.57^{+0.15}_{-0.08}$	$3.85^{+0.66}_{-0.80}$	$-1.37^{+0.07}_{-0.15}$	108^{+99}_{-28}		$1.52^{+0.37}_{-0.12}$	174.3(168)	X,B
[240.00, 350.00]	BPL	$-1.15^{+0.04}_{-0.05}$	$6.19^{+1.79}_{-0.71}$	$-1.86^{+0.08}_{-0.05}$			$[0.30 - 1.91]$	235.9(225)	X,B
GRB 121123A									
[**193.15, 299.65**]	CPL			$-0.86^{+0.03}_{-0.03}$	75^{+4}_{-4}		$1.11^{+0.07}_{-0.06}$	148.1(164)	X,B
[193.15, 214.65]	CPL			$-0.73^{+0.05}_{-0.05}$	121^{+22}_{-16}		$1.33^{+0.15}_{-0.14}$	109.2(127)	X,B

TABLE 3.2: continued.

Time bin s	Model	α_1	$E_{\rm break}$ keV	α/α_2	$E_{\rm peak}$ keV	β	F_{-7} [erg cm^{-2}s^{-1}]	χ^2 (dof)	Instr.
[214.65, 231.04]	CPL			$-0.54^{+0.05}_{-0.04}$	99^{+10}_{-8}		$1.86^{+0.10}_{-0.16}$	108.7(120)	X,B
[231.04, 239.23]	CPL			$-0.84^{+0.06}_{-0.06}$	87^{+12}_{-9}		$2.02^{+0.25}_{-0.22}$	87.6(88)	X,B
[239.23, 247.42]	BCPL	$-0.19^{+0.46}_{-0.26}$	$2.63^{+1.13}_{-0.68}$	$-1.04^{+0.09}_{-0.17}$	61^{+20}_{-10}		$1.69^{+0.51}_{-0.29}$	74.4(93)	X,B
[247.42, 267.90]	BCPL	$-0.59^{+0.35}_{-0.16}$	$2.18^{+4.10}_{-0.83}$	$-0.93^{+0.07}_{-0.12}$	47^{+9}_{-6}		$0.91^{+0.17}_{-0.07}$	162.7(157)	X,B
[267.90, 299.65]	CPL			$-1.10^{+0.06}_{-0.06}$	44^{+5}_{-4}		$0.57^{+0.08}_{-0.07}$	185.4(185)	X,B
GRB 130907A, z = 1.238									
[**−80.00, 71.00**]	CPL			$-0.93^{+0.08}_{-0.08}$	284^{+91}_{-50}		$19.56^{+1.33}_{-1.24}$	22.5(55)	B
[**71.00, 550.00**]	BPL	$-1.37^{+0.10}_{-0.07}$	$2.30^{+0.62}_{-0.60}$	$-1.67^{+0.01}_{-0.01}$			[0.78 − 17.44]	307.1(281)	X,B
[−80.00, −65.00]	PL			$-1.32^{+0.32}_{-0.31}$			[0.60 − 310.90]	62.4(56)	B
[−65.00, −44.00]	PL			$-1.22^{+0.06}_{-0.06}$			[1.38 − 1550.40]	43.2(56)	B
[−44.00, −30.00]	PL			$-1.27^{+0.03}_{-0.03}$			[3.43 − 2648.80]	36.8(56)	B
[−30.00, 20.00]	CPL			$-0.95^{+0.08}_{-0.08}$	365^{+193}_{-85}		$32.84^{+2.25}_{-2.09}$	21.6(55)	B
[20.00, 40.00]	CPL			$-0.84^{+0.09}_{-0.09}$	275^{+94}_{-50}		$28.26^{+2.26}_{-2.07}$	24.4(55)	B
[40.00, 52.00]	CPL			$-1.02^{+0.11}_{-0.11}$	288^{+217}_{-76}		$18.28^{+1.90}_{-1.69}$	33.6(55)	B
[52.00, 71.00]	CPL			$-0.95^{+0.09}_{-0.09}$	249^{+86}_{-45}		$26.22^{+2.14}_{-1.96}$	25.0(55)	B
[71.00, 79.00]	BPL	$-0.58^{+0.90}_{-0.33}$	$2.75^{+2.01}_{-0.93}$	$-1.29^{+0.02}_{-0.03}$			[5.47 − 2978.90]	71.9(81)	X,B
[79.00, 87.00]	PL			$-1.12^{+0.02}_{-0.01}$			[7.28 − 18644.00]	77.1(89)	X,B
[87.00, 110.00]	BPL	$-1.03^{+0.23}_{-0.21}$	$2.58^{+0.95}_{-0.51}$	$-1.70^{+0.04}_{-0.04}$			[1.50 − 26.50]	142.6(124)	X,B
[200.00, 220.00]	PL			$-1.50^{+0.03}_{-0.07}$			[0.88 − 77.48]	68.1(79)	X,B
[220.00, 250.00]	BPL	$-1.08^{+0.25}_{-0.13}$	$4.54^{+1.61}_{-1.66}$	$-1.75^{+0.05}_{-0.05}$			[1.60 − 20.06]	120.4(133)	X,B
[250.00, 350.00]	BPL	$-1.46^{+0.11}_{-0.07}$	$4.08^{+1.03}_{-1.34}$	$-1.91^{+0.05}_{-0.04}$			[0.69 − 3.02]	215.1(232)	X,B
[350.00, 550.00]	BPL	$-1.59^{+0.03}_{-0.03}$	$5.01^{+0.69}_{-0.82}$	$-2.04^{+0.04}_{-0.03}$			[0.42 − 1.02]	341.6(297)	X,B
GRB 140108A									
[**−7.21, 16.34**]	CPL			$-1.43^{+0.14}_{-0.13}$	143^{+94}_{-36}		$2.33^{+0.37}_{-0.27}$	80.4(97)	B,G
[**76.76, 101.33**]	BCPL	$0.35^{+0.37}_{-0.55}$	$2.54^{+0.82}_{-0.22}$	$-1.33^{+0.03}_{-0.05}$	844^{+1548}_{-310}		$7.24^{+2.41}_{-1.43}$	136.1(137)	X,B,G
[−3.11, 2.01]	CPL			$-1.11^{+0.40}_{-0.32}$	105^{+89}_{-28}		$1.34^{+0.72}_{-0.37}$	104.3(135)	B,G
[2.01, 4.05]	CPL			$-1.34^{+0.23}_{-0.20}$	116^{+82}_{-30}		$3.72^{+1.05}_{-0.67}$	105.2(98)	B,G
[4.05, 7.13]	CPL			$-1.27^{+0.14}_{-0.12}$	172^{+83}_{-40}		$6.45^{+0.92}_{-0.69}$	134.7(129)	B,G
[7.13, 11.22]	PL			$-1.70^{+0.05}_{-0.05}$			[4.29 − 50.00]	96.3(99)	B,G
[76.76, 81.88]	BPL	$-0.63^{+0.40}_{-0.32}$	$7.12^{+4.75}_{-1.58}$	$-1.37^{+0.05}_{-0.05}$			[4.03 − 358.53]	134.0(165)	X,B,G
[81.88, 83.92]	BPL	$-0.61^{+0.40}_{-0.43}$	$7.54^{+14.21}_{-1.69}$	$-1.34^{+0.04}_{-0.04}$			[9.87 − 1137.50]	129.1(124)	X,B,G
[83.92, 85.97]	BPL	$-0.17^{+0.62}_{-0.48}$	$7.14^{+3.92}_{-1.55}$	$-1.37^{+0.04}_{-0.04}$			[11.18 − 1055.20]	138.2(121)	X,B,G
[85.97, 88.02]	CPL			$-1.12^{+0.06}_{-0.05}$	314^{+150}_{-81}		$10.74^{+0.89}_{-0.75}$	117.7(131)	X,B,G
[88.02, 93.14]	PL			$-1.42^{+0.03}_{-0.03}$			[4.99 − 325.48]	192.4(182)	X,B,G
[93.14, 101.33]	PL			$-1.58^{+0.05}_{-0.05}$			[1.17 − 24.19]	178.5(202)	X,B,G
GRB 140206A, z = 2.73									
[**−0.50, 11.00**]	CPL			$-0.98^{+0.19}_{-0.18}$	145^{+69}_{-28}		$4.37^{+0.88}_{-0.71}$	39.1(55)	B
[**50.25, 100.00**]	BCPL	$-0.70^{+0.11}_{-0.07}$	$5.42^{+1.96}_{-2.34}$	$-1.05^{+0.10}_{-0.08}$	102^{+18}_{-13}		$3.53^{+0.38}_{-0.26}$	78.6(99)	X,B
[−0.50, 4.30]	CPL			$-0.92^{+0.33}_{-0.31}$	98^{+53}_{-18}		$2.51^{+1.09}_{-0.72}$	48.4(55)	B

TABLE 3.2: continued.

Time bin s	Model	α_1	$E_{\rm break}$ keV	α/α_2	$E_{\rm peak}$ keV	β	F_{-7} [erg cm^{-2}s^{-1}]	χ^2 (dof)	Instr.
$[4.30, 8.60]$	PL			$-1.33^{+0.05}_{-0.05}$			$[2.95 - 1401.90]$	73.4(56)	B
$[8.60, 11.00]$	PL			$-1.30^{+0.07}_{-0.07}$			$[3.00 - 1782.70]$	58.3(56)	B
$[50.25, 55.00]$	BPL	$-0.86^{+0.10}_{-0.15}$	$8.01^{+4.11}_{-2.81}$	$-1.58^{+0.08}_{-0.09}$			$[1.87 - 90.47]$	48.9(74)	X,B
$[55.00, 58.00]$	BCPL	$0.16^{+0.16}_{-0.55}$	$2.26^{+1.64}_{-0.90}$	$-0.87^{+0.10}_{-0.12}$	128^{+39}_{-23}		$12.31^{+4.89}_{-5.75}$	52.8(67)	X,B
$[58.00, 60.00]$	BCPL	$-0.14^{+0.40}_{-0.29}$	$5.24^{+1.90}_{-1.74}$	$-0.83^{+0.10}_{-0.17}$	112^{+45}_{-18}		$15.36^{+9.88}_{-3.89}$	55.2(73)	X,B
$[60.00, 62.00]$	CPL			$-0.59^{+0.06}_{-0.08}$	95^{+5}_{-6}		$15.75^{+0.91}_{-1.07}$	88.1(78)	X,B
$[62.00, 64.00]$	BCPL	$0.39^{+1.54}_{-0.83}$	$2.14^{+2.75}_{-0.57}$	$-0.86^{+0.08}_{-0.14}$	87^{+23}_{-10}		$11.44^{+6.21}_{-4.17}$	60.1(77)	X,B
$[64.00, 70.00]$	BCPL	$-0.40^{+0.22}_{-0.17}$	$4.26^{+2.05}_{-1.09}$	$-1.36^{+0.12}_{-0.19}$	81^{+85}_{-23}		$3.44^{+0.67}_{-0.53}$	66.7(84)	X,B
$[70.00, 80.00]$	CPL			$-1.13^{+0.06}_{-0.06}$	41^{+6}_{-5}		$0.90^{+0.19}_{-0.15}$	94.1(84)	X,B
$[80.00, 100.00]$	CPL			$-1.34^{+0.07}_{-0.10}$	47^{+22}_{-13}		$0.28^{+0.09}_{-0.02}$	135.1(122)	X,B
				GRB 140512A, z = 0.725					
$[\mathbf{-21.05, 10.70}]$	CPL			$-1.09^{+0.12}_{-0.11}$	439^{+293}_{-134}		$3.32^{+1.50}_{-1.12}$	196.9(317)	B,G
$[\mathbf{102.86, 158.16}]$	BCPL	$-0.76^{+0.05}_{-0.04}$	$7.18^{+1.12}_{-1.00}$	$-1.26^{+0.04}_{-0.04}$	532^{+190}_{-123}		$5.52^{+0.27}_{-0.27}$	442.8(478)	X,B,G
$[-21.05, 0.46]$	CPL			$-1.20^{+0.14}_{-0.12}$	598^{+1030}_{-259}		$3.03^{+0.33}_{-0.27}$	223.8(299)	B,G
$[0.46, 10.70]$	CPL			$-1.01^{+0.17}_{-0.15}$	306^{+190}_{-86}		$3.28^{+0.43}_{-0.34}$	224.6(250)	B,G
$[102.86, 107.98]$	BCPL	$-0.59^{+0.18}_{-0.18}$	$7.77^{+6.25}_{-2.69}$	$-1.19^{+0.10}_{-0.10}$	580^{+1150}_{-259}		$5.26^{+1.11}_{-1.04}$	190.7(213)	X,B,G
$[107.98, 113.10]$	BCPL	$-0.40^{+0.19}_{-0.15}$	$6.67^{+2.99}_{-2.02}$	$-1.06^{+0.07}_{-0.07}$	513^{+220}_{-135}		$9.68^{+1.79}_{-1.78}$	246.3(228)	X,B,G
$[113.10, 118.22]$	BCPL	$-0.58^{+0.15}_{-0.14}$	$7.96^{+3.63}_{-2.14}$	$-1.25^{+0.10}_{-0.10}$	328^{+287}_{-123}		$4.56^{+0.76}_{-0.75}$	196.9(225)	X,B,G
$[118.22, 123.34]$	BCPL	$-0.56^{+0.10}_{-0.07}$	$19.52^{+4.40}_{-5.08}$	$-1.23^{+0.05}_{-0.05}$	942^{+484}_{-292}		$18.52^{+2.47}_{-2.49}$	239.3(246)	X,B,G
$[123.34, 128.46]$	BCPL	$-0.35^{+0.16}_{-0.14}$	$7.24^{+1.74}_{-1.38}$	$-1.29^{+0.06}_{-0.06}$	529^{+366}_{-176}		$10.40^{+1.75}_{-1.70}$	263.3(241)	X,B,G
$[128.46, 133.58]$	BPL	$-0.76^{+0.18}_{-0.14}$	$6.08^{+2.18}_{-1.60}$	$-1.45^{+0.04}_{-0.04}$			$[20.82 - 275.19]$	223.8(228)	X,B,G
$[133.58, 138.70]$	CPL			$-1.16^{+0.04}_{-0.04}$	170^{+60}_{-37}		$1.88^{+0.22}_{-0.19}$	214.5(226)	X,B,G
$[138.70, 143.82]$	CPL			$-1.18^{+0.05}_{-0.05}$	213^{+146}_{-67}		$1.63^{+0.25}_{-0.20}$	220.3(216)	X,B,G
$[143.82, 158.16]$	BPL	$-0.61^{+0.34}_{-0.19}$	$2.07^{+0.33}_{-0.38}$	$-1.45^{+0.03}_{-0.03}$			$[5.17 - 70.95]$	367.6(340)	X,B,G

I first comment on the results for time-integrated spectra. For almost all GRBs, two integration windows can be defined: a first one where XRT has not started observations yet (and only BAT and eventually GBM data are available), and a second one where also XRT observations are available and have been included in the analysis. Note that all time-integrated spectra accumulated over epochs lacking XRT observations have best-fit functions represented by one of the standard models (PL or CPL). Conversely (with only two exceptions represented by GRB 100906A and GRB 121123A), in spectra integrated over times where XRT observations are available, a break energy $E_{\rm break}$ is firmly identified (i.e., the best model is either a BCPL or a BPL with both indices > -2, and the significance of the improvement as compared to models without a break is larger than 3σ).

I also performed time-resolved analysis and found that for time bins with XRT the best-fit model is a PL in 4 cases, a CPL in 17 cases, a peaked BPL in 7 cases, a BPL (with $\alpha_1, \alpha_2 > -2$) in 31 cases, and a BCPL in the remaining 27 cases. This

means that in 67% of the time-resolved spectra that take advantage of the presence of XRT observations, a break energy $E_{\rm break}$ is found and is firmly constrained. The significance of the break is higher than 5σ in 65% of cases, while in the remaining cases it is between 3σ and 5σ. For all GRBs except one (GRB 100906A) I can constrain the break energy at least in one time-resolved spectrum. Conversely, when XRT is not available, a break energy is never found, and the best-fit model is either a PL (15 cases) or a CPL (27 cases).

For the time-resolved spectra of all GRBs included in the sample, I show in Figure 3.7 the distributions of the best-fit parameters. I fit the distributions with gaussian functions and report the mean values and 1σ widths in Table 3.3. The $E_{\rm peak}$ distribution (blue histogram in the left panel of Figure 3.7) peaks at $\sim 120\,$keV, a value larger than that found in the BAT catalog ($\sim 80\,$keV, Lien et al. 2016), reflecting the fact that for half of the GRBs included in the sample GBM data are available, allowing the determination of $E_{\rm peak}$ even when its value is above the BAT high-energy threshold. The inclusion of XRT data allowed me to find low value $E_{\rm peak} < 20\,$keV, whose measure is usually precluded by analysis of GBM, BATSE, or BAT data alone, but whose existence has been already proven by the analysis of HETE data (Sakamoto et al., 2005) and X-ray flares (Butler and Kocevski, 2007a; Margutti et al., 2010).

The pink histogram (left panel of Figure 3.7) shows the distribution of the break energy $E_{\rm break}$. I find that its logarithmic mean value corresponds to $\langle E_{\rm break}\rangle \sim 4\,$keV, and its distribution spans one order of magnitude, from 2 to 20 keV. The largest value found for $E_{\rm break}$ is then at the bottom edge of the BAT sensitivity range. This implies that BAT or GBM observations alone would not be sufficient to firmly reveal the presence of the break. The $E_{\rm break}$ distribution covers the whole XRT energy range, down to $\lesssim 2\,$keV. Values smaller than $\sim$2 keV cannot be recovered.

The right panel of Figure 3.7 shows the distribution of the spectral indices. I distinguish between $\alpha_{\rm CPL}$, $\alpha_{\rm PL}$, α_1, and α_2 (see their definition in Figure 3.2). The distribution of β (not shown) is flat and ranges from -2 to -3. Consistently with previous spectral catalogs, the mean value for $\alpha_{\rm CPL}$ is around -1, and the mean value of $\alpha_{\rm PL}$ is softer, around -1.5 (see Table 3.3). When $E_{\rm break}$ is identified in the spectrum, the slope below and above the break (α_1 and α_2, respectively) can be defined. Their mean values are $\langle\alpha_1\rangle = -0.66$ ($\sigma = 0.35$) and $\langle\alpha_2\rangle = -1.46$ ($\sigma = 0.31$). Remarkably, these mean values are very close to expectations from synchrotron emission in a regime of fast cooling: $\alpha_1^{\rm syn} = -0.67$ and $\alpha_2^{\rm syn} = -1.5$ (vertical dashed lines). This naturally leads me to identify the peak energy $E_{\rm peak}$ with the characteristic synchrotron frequency corresponding to the minimum frequency $\nu_{\rm m}$ of the nonthermal accelerated electrons, and the break energy $E_{\rm break}$ with the cooling break frequency $\nu_{\rm c}$. However, I note that the distributions are wide and there are 14 cases with $\alpha_1 > -0.67$ (at more than 1σ), which cannot be interpreted as nonthermal emission spectra.

I note that the distributions of data points in both panels of Fig. 3.8 lie far from the equality line. The gap between the points and the line could be, in principle,

filled with points, but if $E_{\rm peak}$ and $E_{\rm break}$ are very close to each other, it is hard to distinguish them and find α_1 and α_2 from spectral analysis.

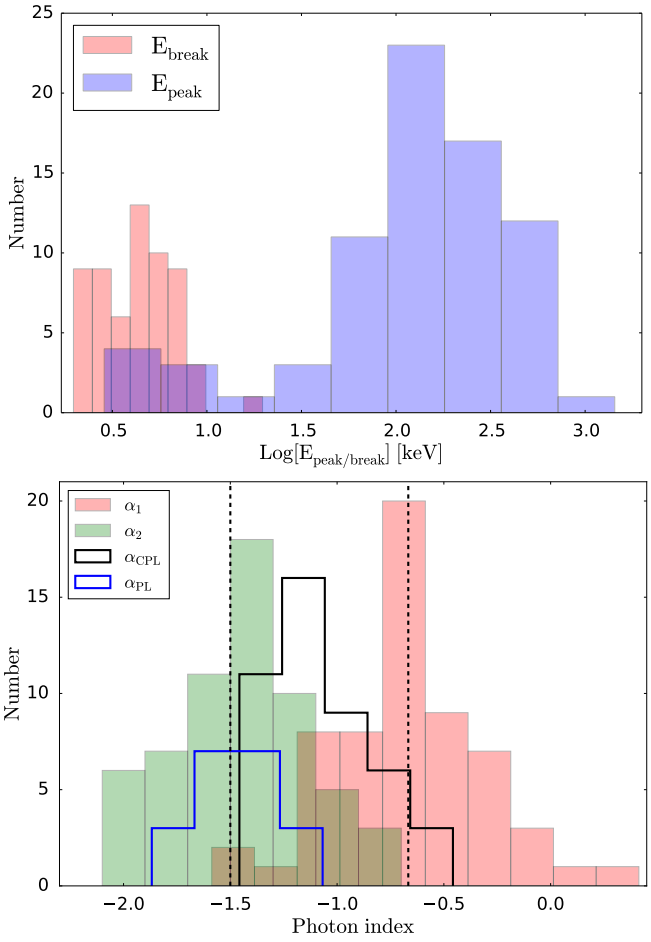

FIGURE 3.7: Distributions of the best-fit parameters for all time-resolved spectra. Left panel: the distributions of the peak and break energies are shown by the blue and red histograms, respectively. Right panel: photon index distributions. Different histograms refer to different models, according to the legend (refer to Figure 3.2 for the notation). Dashed black lines show the values of the spectral slopes theoretically expected below and above the cooling break energy in fast-cooling synchrotron emission.

Correlations among model parameters are investigated in Figure 3.8. For those spectra where both $E_{\rm break}$ and $E_{\rm peak}$ are constrained, the two quantities are plotted one versus the other in the left panel. Note that $E_{\rm peak}$ spans over two decades, while $E_{\rm break}$ is confined to a narrower range (one order of magnitude). This narrow range is clearly limited by the instrument energy threshold: values smaller than ~ 1 keV cannot be recovered. An upper bound to $E_{\rm break}$ in principle is not present. The lack of break energies in excess of 20 keV might then suggest that these values are intrinsically not present, which would also explain why these breaks have not been identified so far, with instruments sensitive at energies from 8 keV up.

In the right panel of Figure 3.8, circles show the relation between α_1 and α_2 for spectra modeled either a BCPL or a BPL with both indices larger than -2. Cases

TABLE 3.3: Summary of the mean values and 1σ width of the gaussian fits to the best-fit parameters of interest.

Parameter	Mean Value	σ
$\log E_{\rm peak}$	2.07	0.56
$\log E_{\rm break}$	0.63	0.20
α_1	-0.66	0.35
α_2	-1.46	0.31
$\alpha_{\rm PL}$	-1.47	0.20
$\alpha_{\rm CPL}$	-1.08	0.23

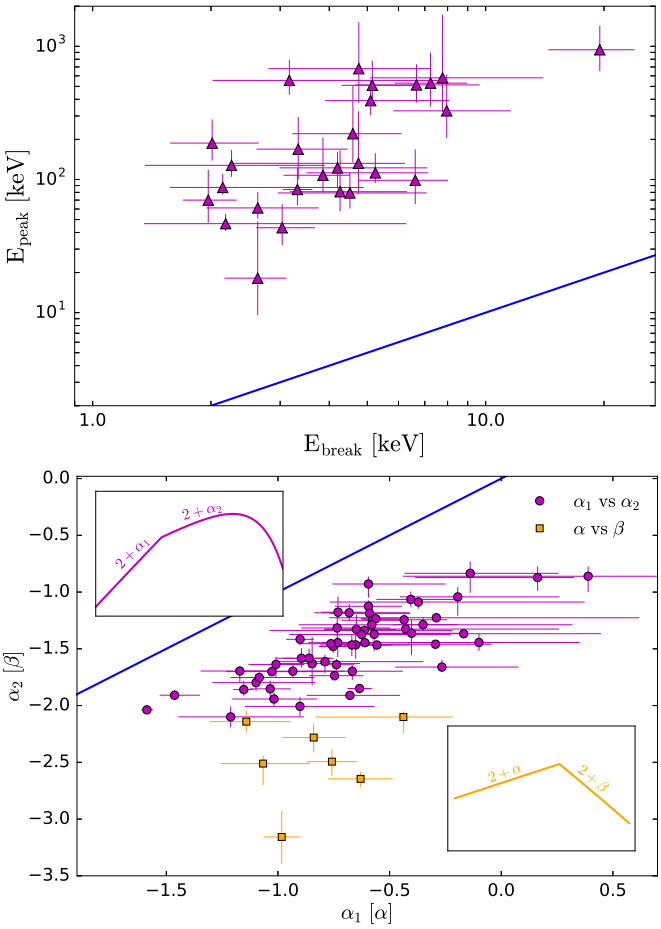

FIGURE 3.8: Correlations among best-fit parameters for time-resolved spectra. Left panel: peak energy $E_{\rm peak}$ vs. break energy $E_{\rm break}$ for spectra in which both spectral features are constrained (i.e., spectra fitted by a BCPL). Right panel: α_1 vs. α_2 (circles) for those spectra best modeled by either a BPL or a BCPL. Squares symbols show instead α vs. β for cases where the best fit is a BPL with high-energy index < -2. In both panels, the solid blue line shows the identity line.

where the best-fit model is a BPL with a high-energy index smaller than -2 are shown with squares, and refer to α versus β.

For each time-resolved spectrum, I also estimate the unabsorbed flux, in the energy range 0.5 keV - 10 MeV. When the GBM data and/or XRT data are not available, this requires an extrapolation of the best-fit model up to 10 MeV and/or down to 0.5 keV.

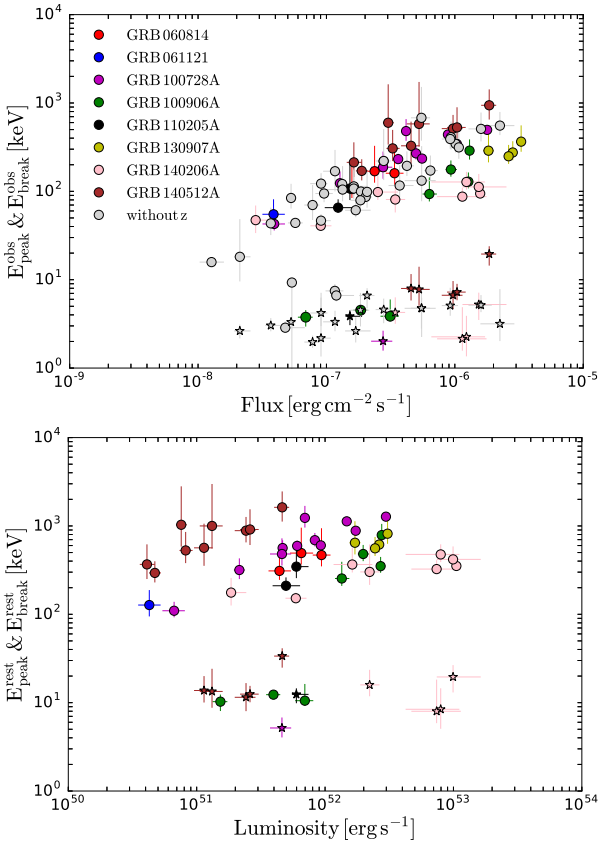

FIGURE 3.9: Left panel: time-resolved peak (circles) and break (stars) energies are plotted as a function of the flux (estimated in the energy range 0.5 keV-10 MeV). Right panel: for those GRBs with measured redshift, the rest-frame peak and break energies are plotted as a function of the luminosity. In both panels, different colours are used for different GRBs.

If the best-fit model is a peaked (in νF_ν) function, I perform the extrapolation. The value obtained (and its error) is reported in Table 3.2. When the peak energy is not constrained, I estimate a lower limit and an upper limit to the 0.5 keV - 10 MeV flux, and report their values in Table 3.2 within square brackets. The lower limit is estimated by integrating the best-fit model only in the energy range where data are actually available (i.e., no extrapolation is performed). The upper limit is instead estimated by extrapolating the best-fit model up to 10 MeV and/or down to 0.5 keV. Figure 3.9 (left panel) shows the peak and break energies as a function of the flux. It has been shown in several studies (Ghirlanda, Nava, and Ghisellini, 2010; Ghirlanda, Ghisellini, and Nava, 2011; Ghirlanda et al., 2011) that in single GRBs a correlation between the time-resolved $E_{\rm peak}$ and the instantaneous flux is present. I mark different GRBs with different colors and verify that such a correlation is present also in our sample (circles). The investigation of the existence of a similar correlation also for $E_{\rm break}$ (stars) is more difficult, given the small range spanned by $E_{\rm break}$ and the smaller number of points. For the subsample of GRBs with measured redshift, I estimate the rest-frame characteristic energies ($E^{\rm rest}_{\rm peak}$ and $E^{\rm rest}_{\rm break}$) and plot them as a function of the luminosity (Figure 3.9, right panel). A standard flat ΛCDM cosmological model

with $\Omega_\Lambda = 0.69$ and $H_0 = 68\,\mathrm{km\,s^{-1}Mpc^{-1}}$ has been adopted for the estimate of the luminosity distance.

3.4 Discussion

3.4.1 Reliability of the analysis

The necessity to introduce low-energy breaks in the spectral models is motivated by a hardening of the spectra in the XRT energy range. One might wonder if such a hardening can be the result of an incorrect estimate of the N_H and/or an insufficient correction for pileup. The fact that the value of E_break ranges from 2 to 20 keV and varies with time during a single GRB might suggest that these breaks are intrinsic features. In any case, to test how robust are the results against possible absorption and pileup effects, I performed a series of tests, which confirmed the solidity of my claim on the spectral hardening at low energy.

I briefly summarize here the tests performed and the results obtained. I test how pileup effects and intrinsic absorption in the soft X-ray energy band can affect the results on the presence of the low-energy break. I have performed systematics tests on the spectra of three GRBs: GRB 140206A, GRB 110102A, and GRB 140512A. The tests performed showed that the results are robust: the corrections adopted for pileup are sufficient to remove any spurious effect on the spectral shape at low energy, and the estimates of N_H are not responsible for the need of an intrinsically curved spectrum in the XRT band. In the following, I explain in detail the tests applied and I show, as an example, the results obtained on GRB 140512A.

Pileup

A hardening in the observed soft X-ray spectrum can be caused by pileup effects when two or more low-energy photons are detected as one single photon of higher energy. The spectra of bright X-ray sources, like the ones in this sample, observed by the Swift/XRT instrument in WT mode might be heavily piledup and very accurate corrections are needed in order to extract clean spectral files. For the analysis presented in this Chapter, I adopted the following method. I excluded the central region of the X-ray images, in order to have a maximum count rate smaller than 150 counts $\mathrm{s^{-1}}$. To check whether this is enough to avoid contamination from pileup effects, one possibility is to further reduce the maximum count rate (i.e. excluding an even larger region), repeat the spectral analysis, and verify whether the results are affected.

In Table 3.4 I show the results of this analysis applied to one time-resolved spectrum taken from GRB 140512A (128.46-133.58 s). With a maximum count rate of 150 counts $\mathrm{s^{-1}}$, I found that the best-fit model is a BPL with $\alpha_1 = -0.76^{+0.18}_{0.14}$, $\alpha_2 = -1.45^{+0.04}_{0.04}$, and $E_\mathrm{break} = 6.1^{+2.2}_{-1.6}$. I progressively decreased the maximum count rate and refitted the spectrum with all four spectral models. I performed the $F-test$ to compare models with and without a low-energy break and verified that even when

TABLE 3.4: Results of the test performed to verify the possible effects of pileup on the presence of a break energy in the XRT energy range. The test is applied to one time-resolved spectrum of GRB 140512A (from 128.46 to 133.58s). The first column reports the maximum rate of the light curve after the central region of the source has been excluded. Columns 2-5 list the χ^2 (d.o.f.) of the four different spectral models. Models that differ from each other for the presence of a break (i.e. PL vs BPL and CPL vs BCPL) are compared in the last two columns, where the significance of the F-test is reported.

Rate [cts/s]	PL	CPL	BPL	BCPL	F_{PL-BPL}	$F_{CPL-BCPL}$
120	412.97 (228)	243.89 (227)	217.09 (226)	210.95 (225)	1.11e-16 (8.4)	8.14e-08 (5.4)
90	264.89 (220)	224.17 (219)	216.90 (218)	211.05 (217)	3.45e-10 (6.3)	1.44e-03 (3.2)
70	253.40 (218)	218.80 (217)	213.14 (216)	207.45 (215)	7.67e-09 (5.8)	3.26e-03 (2.9)

the count rate is reduced to 70 counts s^{-1} (where pileup is completely negligible) the presence of a break is still significant at more than 3σ.

The test was performed also for two fainter events (GRB 110102A and GRB 140512A) and it was found that the results are unchanged: by progressively decreasing the maximum count rate down to 70 counts s^{-1}, the presence of a spectral break in the XRT band is always significant. Moreover, I find that, within the errors, its location is unaffected.

Intrinsic Absorption

A spurious hardening in the soft X-ray band can also be caused by an incorrect estimate of the amount of absorption by neutral hydrogen. Absorption is energy dependent and can then produce a curvature in the observed spectrum below a few keV, depending also on the redshift of the source. There is then a degeneracy between the amount of absorption and the intrinsic spectral curvature. If absorption is underestimated, a curvature in the spectral model must be introduced in order to model the data. Conversely, to fail in recognizing the presence of a spectral break/curvature and/or spectral evolution in the intrinsic spectrum leads to overestimating the value of N_H (Butler and Kocevski, 2007a). In this analysis, I have estimated the column density from late-time X-ray spectra, selecting a region where the light curve decays in time as a power law and the photon index is roughly constant. The derived value has then been used as a fixed input parameter for the joint XRT+BAT spectral analysis. In order to exclude a possible influence of intrinsic absorption on the low-energy breaks found in this work, I perform two different tests which I have applied to GRB 140206A, GRB 110102A, and GRB 140512A. In the first test, I consider the intrinsic absorption a free parameter and refit the data with a CPL and a BCPL models. I then perform the $F-test$ to compare the two different fits and verify the significance of the improvement obtained thanks to the addition of the break. An example is proposed in Figure 3.10 and refers to the time-averaged spectrum of the second emission episode of GRB 140512A (integrated from 102.86 to 158.16 s). Even

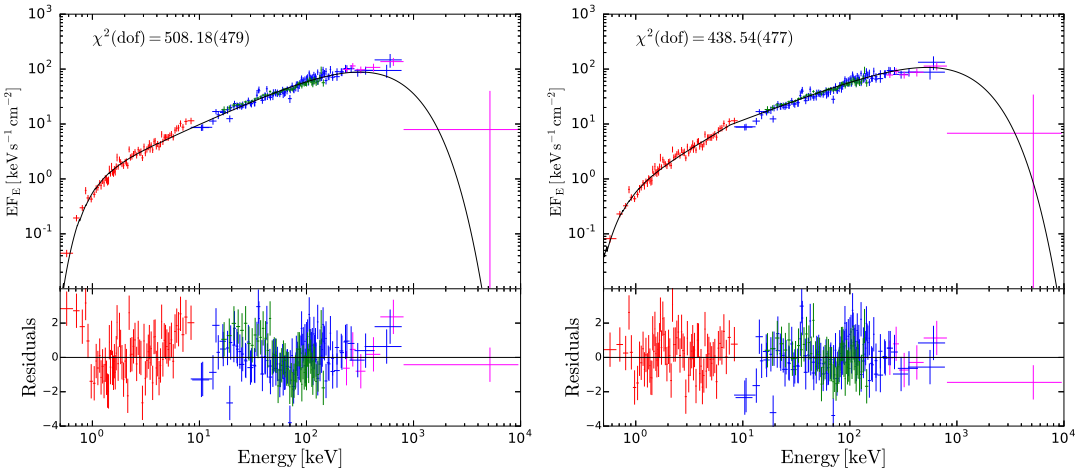

FIGURE 3.10: Time-integrated spectrum of GRB 140512A during the second pulse, fitted by CPL (left) and BCPL (right) models with intrinsic $N_{\rm H}$ as a free parameter. The value of the chi-square is reported in the upper left corner of each panel. The addition of the low-energy break improves the fit with a significance level corresponding to 8.1σ.

when the intrinsic absorption is a free parameter, the addition of a break improves the fit at more than 8σ (see Figure 3.10).

In the second test, I exclude XRT data below 3 keV, and refit the data. Also in this case, a break in the spectrum is still required by the data. Taking again the second emission episode of GRB 140512A as an example, I find that a BCPL improves the fit as compared to the CPL at more than 6σ (see Figure 3.11).

3.4.2 Comparison with previous studies

XRT+BAT joint spectral analysis of simultaneous observations has been already performed in several studies. However, to my knowledge, this is the first time that break energies in the XRT energy range are identified as a common feature. In this section I address the question why this X-ray hardening - which, according to my investigation, appears to be a common feature - has never been reported before.

For GRBs in this sample for which the XRT+BAT joint spectral analysis has been already performed and published in previous papers, I report a detailed comparison between previous model fits and the fits proposed in my analysis.

GRBs in My Sample

For most of the GRBs included in my sample, the analysis of XRT+BAT spectral data has already been published in the literature. In this section, I discuss, case by case, the modeling proposed by different authors, as compared to those proposed in this Chapter.

A systematic analysis of GRBs with prompt XRT+BAT observations has been performed by Peng et al. (2014) (hereafter P14). A comparison with my findings is not straightforward, since the methods for data extraction and modeling are quite

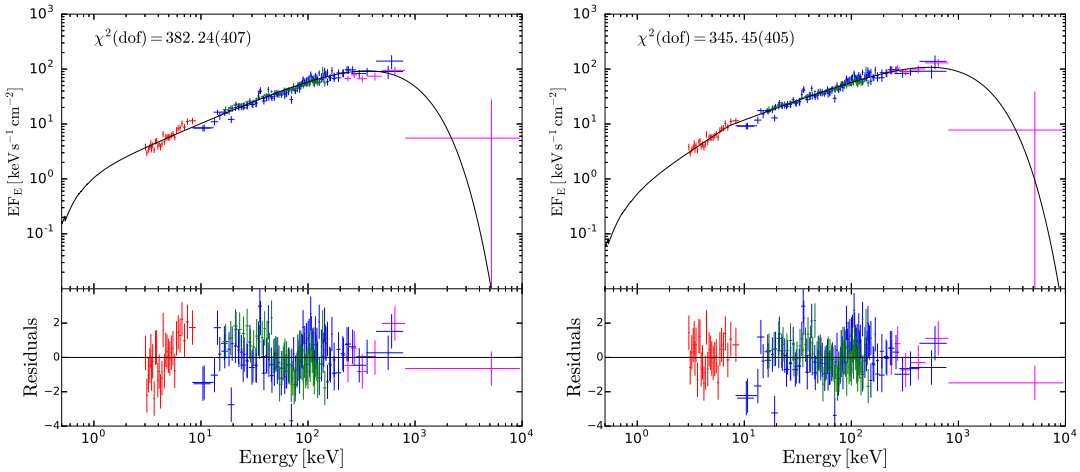

FIGURE 3.11: Time-integrated spectrum of GRB 140512A during the second pulse, fitted by CPL (left) and BCPL (right) models when data below 3 keV are excluded. The improvement of the chi-square (reported in the upper left corner of each panel) when the low-energy break is added is significant at 6.1σ, according to the $F-test$.

different. First, P14 considered intrinsic absorption as a free parameter. Moreover, they never discuss correction for the pileup effect, and it is not clear whether and how pileup has been treated. Time bins chosen for the analysis also differ from those chosen in this Chapter. The spectral models tested by P14 are a single PL, a blackbody plus a PL (BB+PL), and the Band model. Sometimes, fits are performed by fixing to -1 the value of the low-energy spectral index. With these differences in mind, I report in the following a comparison between my modeling and the modeling proposed by P14 for the 10 GRBs common to both studies. In P14, the spectra of GRB 060814, GRB 061121, and GRB 100725A are fitted by BB+PL. The PL dominates at low and high energies, and the BB contributes to the flux at intermediate energies. In my analysis I proposed that the best-fit model for these three GRBs is a BPL. I choose one of these GRBs (GRB 060814) as an example, to understand how two apparently completely different interpretations (a BPL and a BB+PL) can both give a satisfactory description of the same data, and perform spectral analysis with the two different models: a BPL and the combination of a BB plus a PL (Figure 3.12). To be consistent with the method applied by P14, I leave the intrinsic $N_{\rm H}$ free to vary and choose the same time interval analyzed by P14 (from 121 to 151 s). Both modelings return an acceptable fit: the reduced chi-square values for the BPL and BB+PL are $\chi^2_{\rm BPL} = 1.01$ and $\chi^2_{\rm BB+PL} = 1.04$, for the same number of degrees of freedom. First, I note that, even though the value of the intrinsic $N_{\rm H}$ is a free parameter, a BPL model returns a well-constrained break energy $E_{\rm break} = 4.54^{+3.48}_{-1.56}$ keV. The BB+PL fit returns a BB temperature $kT = 1.80^{+1.00}_{-0.60}$ keV. The role of the BB is to contribute to the emission at intermediate energies, producing a deviation from a single PL behavior between 4 and 8 keV. The overall shape of the BB+PL model mimics than a BPL behavior. I verified that the same explanation applies to the other two GRBs in my sample for which P14 claim the presence of a BB.

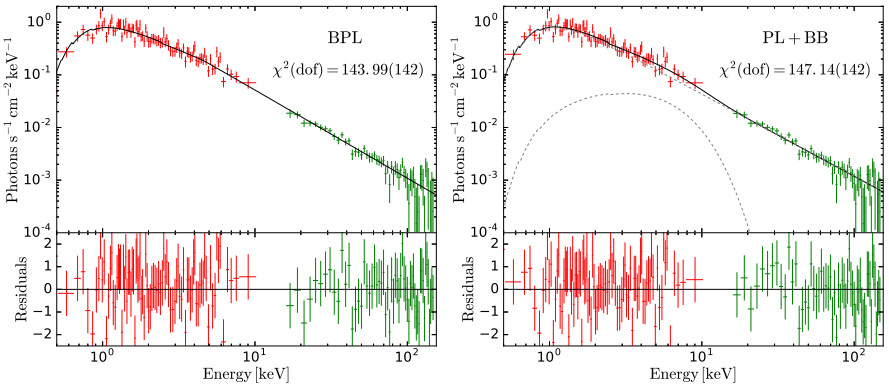

FIGURE 3.12: Spectrum of GRB 060814A integrated from 121 to 151 s. XRT data points are shown in red, and BAT data points are shown in green. Two different spectral modelings are compared: a BPL with a break at ~ 5 keV, and a PL+BB, where the BB temperature is $kT \sim 2$ keV.

For GRB 100619A and GRB 110102, the best fit proposed by P14 is a Band function with $\beta > -2$, and $E_{\rm peak}$ around 10 keV. Since $\beta > -2$ the characteristic energy cannot be properly identified with the spectral peak energy and must be more properly identified with what I called in this Chapter the break energy, making their analysis of these two GRBs consistent with the one proposed in this Chapter. Also, the analysis of GRB 100906A is consistent, since for this GRB I also find a peak energy but no evidence of a break energy. For GRB 100728A and GRB 121123 the differences can also be easily understood: the break energy is very small (2 keV) and can be hardly constrained (see also Abdo et al. 2011), especially in the time interval studied by P14. There is agreement instead on the measure of $E_{\rm peak}$, which is large in the first case, and can be constrained only thanks to the inclusion of GBM data, and is around 50 keV in the second GRB. Similar considerations hold for GRB 140206A: the small value of $E_{\rm break}$ during the temporal window studied by P14 makes it difficult to recognize the presence of a break, while the peak energy, inside the BAT range, is constrained in both their and my analysis to be around 100 keV. Finally, a strong break around 7-8 keV is found in this Chapter in the spectrum of GRB 140108A, while in P14 it is claimed that the best model is a single PL. However, their spectrum is mainly accumulated over a time where I also find that the best fit is a PL, with the very same slope reported by P14 (-1.4).

I conclude that the analysis either is consistent or differs owing to the interpretation of the X-ray hardening as the result of a combination of two different components, one of which is assumed to be a BB in P14. Comparison between these two different interpretations is discussed below in more detail.

GRB 061121 In Page et al. (2007), time-resolved spectra (from 62 to 90 s) are fitted by a broken power-law model with photon indices below and above the break $\Gamma_1 = -0.69^{+0.07}_{-0.13}$ and $\Gamma_2 = -1.61^{+0.13}_{-0.14}$, and a break energy varying in time in the $1 - 6$ keV range (see their Figure 5), in agreement with the analysis reported in this

Chapter. The XRT+BAT time-averaged spectrum has been considered also by Peng et al. (2014) and Friis and Watson (2013). They proposed a model composed of a single PL plus a BB with kT $\sim$ 3 keV. As discussed before, I then believe that the same change of spectral slope is found also in these studies, but is interpreted as the result of the composition of two different spectral components (see below for further details).

GRB 070616 In my analysis, this GRB is best fit by a BCPL, with $E_{\rm break}$ ranging between 8 and 3 keV and $E_{\rm peak}$ evolving from 170 to 16 keV. The joint XRT+BAT time-resolved spectral analysis of this GRB has been performed also by Starling et al. (2008). They tested both a BPL and a Band model and found that they are both acceptable, though the χ^2 of the Band model is systematically higher (see their Table 2). Their BPL fit identifies a break in the range 4-8 keV, in agreement with my findings. Their Band fit identifies a peak energy in the range 135 to 14 keV, also in agreement with my findings. A model including both features (i.e. a low-energy break and a high-energy peak) is never tested by these authors.

GRB 110205A I find a break energy around 4-6 keV, and a peak energy at $\sim$ 100 keV. The peak energy is constrained only in two time-resolved spectra (GBM observations are not available for this GRB). In Zheng et al. (2012) joint Swift/XRT+BAT and Suzaku/WAM time-resolved spectra are best fitted by a Band function with a high-energy exponential cutoff. The photon indices below and above the break energy vary in the ranges $-0.8 < \alpha_1 < -0.1$ and $-1.8 < \alpha_2 < -1.2$ (within 90% confidence level). The break energy is found to be located at $\sim$ 5 keV. These best-fit parameters estimated in Zheng et al. (2012) with an inclusion of Suzaku/WAM observations are consistent with my spectral fit. An alternative modeling has been proposed by Guiriec et al. (2016a), who included also data from Suzaku/WAM. Their modeling is composed of the superposition of three spectral components: a modified blackbody and two CPL. The reason why two completely different modelings can both give a good fit to the data is clear from Figure 2 in Guiriec et al. (2016a): their best-fit model (black line), which in their interpretation is the sum of three different components, can be alternatively seen as a single component from X-rays to MeV energies: a broken power law with a high-energy cutoff (BCPL). A change of slope around 5 keV is clearly visible also in their data. The difference then is not in a different extraction/analysis of the data, but in a different interpretation of the same spectral features. However, a BCPL model does not reproduce the optical emission and would require an additional component at low energy. The three-component model proposed in Guiriec et al. (2016a) explains both the optical and the gamma-ray emission.

Thermal Components

A two-component model, including a BB and a nonthermal component, has been often suggested to describe XRT+BAT spectral data. To compare this interpretation with the one-component models proposed in this Chapter, I considered all time-resolved spectra for which I claim the presence of a keV spectral break and refit them with a BB+PL or BB+CPL model. I chose the best fit among BB+PL and BB+CPL by adopting an $F-test$ and requiring a significance level of at least 3σ. The results of this analysis and comparison with one-component models are shown in Figure 3.13. I plot the reduced chi-square of models with a BB component (y-axis) versus the reduced chi-square of models without a BB component (i.e., either a BPL or a BCPL). Gray filled circles identify those cases where the best fits for models without and with a BB component are a BPL and a BB+PL, respectively. In this case, the number of dof for the two different fits is the same. Red filled circles refer to cases where the best-fit models are a BPL and a BB+CPL: in these cases the models with a BB component have one more free parameter. Blue filled circles refer to cases where the best-fit models are a BCPL and a BB+CPL (same dof). The comparison shows that both modelings return acceptable fits in terms of reduced chi-square, with a tendency of single-component models to give a smaller value. Note that when the best-fit model is a BPL, in most cases the alternative model invoking a BB component also requires the addition of a high-energy cutoff, i.e., the nonthermal component is not a simple PL, but a CPL (red filled circles in Figure 3.13). The high-energy cutoff is required because a simple PL would be too hard at high energies, overpredicting the flux around 100-150 keV. A cutoff is then required to suppress the predicted flux. The actual presence of the peak energy identified by the BB+CPL fits can be tested with data at higher energies (> 150 keV) when Konus-*Wind* and/or Suzaku/WAM data are available (GBM data are not available for these GRBs).

I found that, for GRB 061121, BB+CPL time-resolved fits between 62 and 90 s require peak energies in the range of 143-423 keV, while, according to Konus-*Wind* data, the time-averaged spectrum from 61.9 to 83.4 s peaks at $E_{\rm peak} = 606^{+90}_{-72}$ keV (Page et al., 2007). For GRB 070616, spectra between 138 and 210 s can be fitted by BB+CPL with peak energies between 91 and 139 keV, while the addition of Suzaku-WAM data shows that the spectrum integrated between 133 and 159 s peaks at $E_{\rm peak} = 356 \pm 78$ keV (Starling et al., 2008). For GRB 110205A, three time-resolved spectra at 160-193 s, 193-210 s, and 240-350 s can be fitted by the BB+CPL model with peak energies at 58-98 keV. The time-integrated spectrum observed by Konus-Wind (up to 330 s) is fitted by CPL with peak energy 222 ± 74 keV (Golenetskii et al., 2011). The spectrum observed by Suzaku/WAM jointly with Swift/BAT from 20.2 to 318.2 s is fitted by CPL with $E_{\rm peak} = 230^{+135}_{-65}$ keV (Sakamoto et al., 2011a). In the context of models including a thermal component, XRT+BAT+WAM data for this GRB have been fitted by Guiriec et al. (2016a). They find that a third non-thermal component is necessary in order to explain the peak at ~ 200 keV. Finally, for GRB 130907A two spectra at 71-79 s and 220-250 s can be fitted with BB+CPL

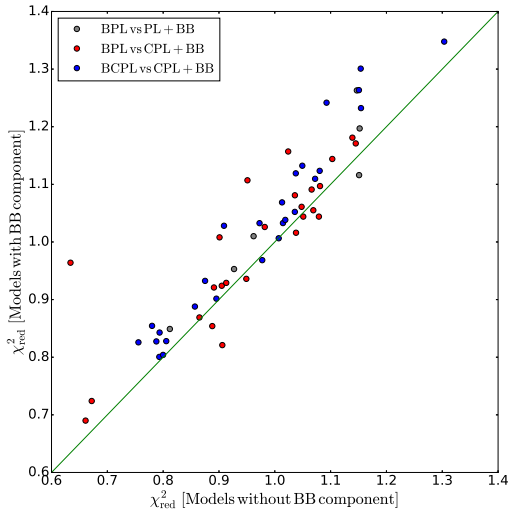

FIGURE 3.13: Comparison between the reduced chi-square of models adopted in this Chapter (labeled as *Models without BB component*; x-axis) and models invoking the presence of a thermal component plus an unbroken nonthermal component (labeled as *Models with BB component*; y-axis). Each point represents one of the time-resolved spectra for which I claim the presence of a break in the ∼keV range. Gray filled circles refer to cases where, according to my analysis, the best-fit model is a BPL, while if a BB is included, the best-fit model is a BB+PL. The number of dof for the two different modelings in this case is the same. Red filled circles show cases for which the best-fit models are a BPL and a BB+CPL for models without and with a thermal component, respectively. In this case the model including a BB has one more free parameter. Blue filled circles show cases where the best-fit models are a BCPL and a BB+CPL (same number of dof), for fits without and with a thermal component,respectively.

with peak energies at 323 and at 95 keV. The time-averaged spectrum observed by the Konus-*Wind* experiment up to 206 s shows has a peak energy of 394 ± 11 keV (Golenetskii et al., 2013). A proper comparison would require spectral analysis on the same temporal bin. However, at least in some cases, it seems evident that the BB+CPL fits predict a peak energy that is in conflict with spectral data available at higher energies.

Summary of a comparison

I found that in some cases breaks have been indeed identified in studies focusing on single GRBs (Page et al., 2007; Starling et al., 2008; Zheng et al., 2012). Systematic studies of larger samples of GRBs whose flaring activity was detected simultaneously by BAT and XRT have been performed by Friis and Watson (2013) and Peng et al. (2014). These analyses proposed, for most of the spectra, a two-component model including a blackbody (BB) and a nonthermal component (see also a similar model proposed by Guiriec et al. (2016a) to explain the spectrum of GRB 110205A). The reason why two completely different models can both account for the same data can be understood from Figure 3.12, showing the same spectrum fitted with a BPL

(left panel) and with a BB+PL (right panel). In general, the role of the BB is to contribute to the flux at intermediates energies, while the PL segment of the nonthermal component dominates at low and high energies. The total spectrum then mimics the shape of a BPL.

I find that in the two-component fits the role of the BB is to contribute to the flux at low energies, modifying the low-energy PL behavior of the nonthermal component producing an overall change in the spectral slope. The empirical fitting function proposed in this Chapter suggests an alternative description of the data, where the overall spectrum can be modeled with one single component (nonthermal with a low-energy break), with a spectral shape resembling the one predicted by the synchrotron model. A simple comparison of the reduced chi-square values (Figure 3.13) shows that both models return acceptable fits, with a tendency of single-component models proposed in this Chapter to give a smaller chi-square. I stress that a completely different case is represented by GRBs where a BB component has been clearly identified (Ghirlanda, Celotti, and Ghisellini, 2003; Ghirlanda, Pescalli, and Ghisellini, 2013; Ryde et al., 2010; Guiriec et al., 2016b), and dominates the emission (typically in the initial phase of the prompt). The presence of a thermal component in a small fraction of GRBs is not called into question by my findings. Conversely, however, I suggest that the addition of a blackbody component when not explicitly required can hide important features, such as spectral breaks, which might shed light on the nature of the dominant emission mechanism in GRB prompt radiation.

In general, I conclude that similar studies on the same GRBs have failed in recognizing that GRB spectra at low energy are characterized by a change in slope consistent with the synchrotron fast-cooling model for several reasons. First, a peak and break feature have rarely been introduced in the fitting model at the same time. Moreover, even when a BPL or a Band model with $\beta > -2$ has been identified as a best fit model, the feature has been often referred to as peak energy (Peng et al., 2014). In other cases, the change in slope at a few keV has been interpreted as being caused by the contribution of an additional, thermal component with a temperature at $\sim 1\,\mathrm{keV}$. More importantly, even in analyses recognizing the break feature, the study has been performed on one single GRB (Page et al., 2007; Starling et al., 2008; Zheng et al., 2012).

Finally, several studies have focused on joint XRT+BAT spectra with the aim of investigating X-ray flare spectral properties, focusing on the question of the evolution of the peak energy down to the XRT energy range (Butler and Kocevski, 2007a; Margutti et al., 2010). My requirement to have bright signal in BAT probably excluded these cases and selected cases where the spectral peak is still in the BAT energy range and where XRT is observing a large part of the prompt emission, rather than the late-time flaring activity.

3.4.3 Interpretation

The hard photon index ($N_\nu \propto \nu^{-1}$) describing prompt emission spectra at low energies represents a serious challenge for an interpretation in terms of synchrotron radiation. In the standard synchrotron fast-cooling model, the spectrum below the νF_ν peak is expected to have a softer index (-3/2), which hardens only at even lower energies, reaching the limiting value -2/3 below the cooling break frequency (Preece et al., 1998; Ghisellini, Celotti, and Lazzati, 2000). A marginally fast cooling regime (i.e. a situation where $\nu_c \lesssim \nu_m$ rather than $\nu_c << \nu_m$) has been considered as a possible solution to the inconsistency between the expected and measured photon index (Derishev, 2007; Daigne, Bošnjak, and Dubus, 2011; Beniamini and Piran, 2013; Uhm and Zhang, 2014). In the context of prompt emission, a theoretical prediction of the location of the cooling break frequency and of the ratio ν_c/ν_m is difficult to make, given the large uncertainties on the properties of the emitting region, such as dissipation radius, bulk Lorentz factor, magnetic field, and particle acceleration mechanism and efficiency. Daigne, Bošnjak, and Dubus (2011) showed that if $0.01 < \nu_c/\nu_m < 1$, the spectrum displays a continuous curvature toward the value -2/3. In this case, between ν_c and ν_m a PL behavior with index -3/2 provides a satisfactory description of the spectrum only in a very narrow range of energies. Only well below ν_c will the spectrum be satisfactorily approximated by a PL, with index -2/3. In this case, the spectral index inferred from spectral analysis does not necessarily need to be equal to -1.5: its value will depend on the relative location of ν_c, ν_m, the low-energy threshold of the detector, and also the empirical fitting function adopted to model the data.

Even though such a situation can in principle explain why the value -3/2 is not typically observed and why the inferred slope is higher than this expected value, the question now is what are the physical conditions required to attain a regime of marginally fast cooling and whether such a conditions are realistic. Daigne, Bošnjak, and Dubus (2011) addressed this question and found that a regime of marginally fast cooling can be obtained for small radii, and/or large Lorentz factors, and/or small magnetic fields. A similar study on physical conditions leading to $\nu_c \lesssim \nu_m$ is discussed also in Beniamini and Piran (2013), and in Beniamini and Piran (2014) in the context of magnetically dominated jets. These studies have assumed a homogeneous magnetic field and an instantaneous, one-shot acceleration. Other scenarios leading to a similar spectral shape invoke a magnetic field that decays downstream with a strength that depends on the distance from the shock front (Derishev, 2007; Uhm and Zhang, 2014), or continuous electron acceleration (Kumar and McMahon, 2008; Asano and Terasawa, 2009).

3.5 Summary

To more properly characterize the shape of the prompt spectra at low energy, where observations are in tension with the theory, it would be very beneficial to dispose of observations extending well below the low-energy threshold of instruments dedicated

to prompt emission studies (typically $\sim 10 - 20\,\mathrm{keV}$). This can be done in several fortunate cases thanks to XRT observations of prompt emission. With the aim of improving our knowledge on the shape of the low-energy part of the prompt spectrum, I looked for cases where the XRT started observations during the prompt emission. For these GRBs, simultaneous XRT and BAT spectral data allowed me to study the prompt emission (or part of it; see Figure 3.1) down to 0.5 keV. I selected events where the emission in the BAT is bright enough to allow reliable time-resolved spectral analysis in at least four temporal bins. Fourteen long GRBs satisfy the selection criteria. In 12 cases, I found robust evidence for a change in the spectral slope around a few keV. *Fermi*-GBM observations, available for seven GRBs, have been included in the spectral analysis. The list of GRBs and their redshift (available for eight events) is reported in Table 3.1. Their BAT and XRT (and, if available, also GBM) lightcurves can be found in Figure 3.1. In 10 cases, the XRT is observing the main emission episode, while in the remaining four GRBs, the XRT is observing secondary peaks.

For all 14 GRBs in my sample, I have performed time-integrated (26 time bins) and time-resolved (128 time bins) spectral analysis, covering the entire prompt emission. For time bins where XRT observations are not available, I found standard results: the spectra are well modeled by a single PL or a CPL. The peak energy and spectral index distributions (Figure 3.7) are consistent with those derived from spectral analysis of larger samples of BAT and GBM GRBs. In particular, when the peak energy is constrained, the low-energy index α has a distribution peaked around -1 (see α_{CPL} in the right panel of Figure 3.7 and in Table 3.3). The value of the spectral index is instead softer when the best-fit model is a single PL: $\langle \alpha_{\mathrm{PL}} \rangle \simeq -1.5$. Both results perfectly agree with spectral index distributions derived in spectral catalogs of BAT (Lien et al., 2016) and GBM (Gruber et al., 2014) long GRBs.

The situation is different for temporal bins where XRT observations are available. The spectra in the whole energy range ($0.5 - 150\,\mathrm{keV}$ or $0.5 - 1000\,\mathrm{keV}$) can still be fitted by one single spectral component, but in the 67% of the cases a low-energy break must be added to the empirical fitting function, resulting in a significant (more than 3σ) improvement of the fit (see an example in Figure 3.4, right panels). This led us to introduce two additional spectral models: a cutoff PL with a low-energy break (BCPL), describing cases where both the low-energy break E_{break} and the peak energy E_{peak} are constrained (31% of time-resolved spectra with XRT data), and a BPL with both indices $\alpha_1, \alpha_2 > -2$ (36%), describing cases where E_{break} is constrained, while E_{peak} falls near or above the high-energy threshold, and cannot be determined. A summary of the models and notation chosen for the model parameters can be found in Figure 3.2.

This systematic difference between best-fit models in spectra with and without XRT observations suggests that our knowledge of the prompt emission spectral shape is usually limited (and possibly biased) by the lack of low-energy observations. The results of spectral analysis down to 0.5 keV revealed that the typical GRB spectrum

has two characteristic energies ($E_{\rm break}$ and $E_{\rm peak}$, with $E_{\rm break} < E_{\rm peak}$) and three power-law segments ($\alpha_1, \alpha_2 > -2$, and $\beta < -2$). I speculate that this result might be quite general: the sample investigated in this Chapter has been selected based on the main requirement of simultaneous XRT and BAT observations of the prompt emission (and relatively bright BAT emission). The selected GRBs have fluences and energies in the range $7 \times 10^{-6} - 8 \times 10^{-4}$erg cm^{-2} and $6 \times 10^{52} - 3 \times 10^{54}$erg, respectively, indicating that these are not necessarily the brightest events. Their light curves differ in morphology one from the other, and the redshift spans the range $z = 0.725$ to $z = 2.73$. From the point of view of temporal properties, energetics, and redshift, these GRBs do not seem to belong to a subclass of peculiar events.

In the sample studied in this Chapter, the break energy $E_{\rm break}$ has a distribution peaked around 4 keV in the observer frame (10 keV in the rest frame), and the peak energy $E_{\rm peak}$ has a distribution peaked around 120 keV in the observer frame (300 keV in the rest frame). The typical ratio $E_{\rm break}/E_{\rm peak}$ is around 0.03. It is very likely that the observed distribution of $E_{\rm break}$ is significantly biased by the fact that values smaller than ~ 2 keV cannot be constrained. It is very tempting to associate these characteristic energies with the synchrotron cooling and typical frequencies $\nu_{\rm c}$ and $\nu_{\rm m}$. This is supported by the average values of the photon indices. In a synchrotron context, the expected values are $\alpha_1 = -2/3$ below $\nu_{\rm c}$ and $\alpha_2 = -3/2$ between $\nu_{\rm c}$ and $\nu_{\rm m}$. From spectral analysis I found $\langle\alpha_1\rangle = -0.66$ ($\sigma = 0.35$) and $\langle\alpha_2\rangle = -1.46$ ($\sigma = 0.31$).

In the synchrotron-prompt emission scenario, the physical parameters of the emitting region have not been constrained yet. Observations of typical prompt fluxes, peak energies, and timescales are not enough to constrain all the unknown parameters governing the physics of acceleration, dissipation, and emission. Studies that use observations to constrain the theory can only identify an allowed parameter space (Kumar and McMahon, 2008; Daigne, Bošnjak, and Dubus, 2011; Beniamini and Piran, 2013; Beniamini and Piran, 2014). These studies can now take advantage of an additional, important constraint: the location of the cooling break frequency. Further constraints on the properties of the emission region (dissipation radius, strength of the magnetic field, Lorentz factor, particle acceleration) can be derived.

Even though the spectra are qualitatively consistent with synchrotron radiation, additional studies are required to firmly assess the consistency of data with theoretical expectations from the synchrotron process. Recent studies have pointed out the importance of reproducing also the narrowness of the spectral shape (Beloborodov, 2013; Axelsson and Borgonovo, 2015; Yu et al., 2015; Vurm and Beloborodov, 2016), arguing that most prompt emission spectra are too narrow to be reproduced by synchrotron radiation, even in the limiting case of a Maxwellian electron distribution. Moreover, it is unclear how spectra with a low-energy photon index higher than -0.67 (present both in this sample and in the BATSE and GBM GRB catalogs) can be reconciled with the synchrotron scenario. While the results found in this Chapter clearly show that a spectral break is present in the keV range, the interpretation of

the spectral shape in terms of synchrotron radiation (although encouraged by the average values of the photon indices) demands a more quantitative investigation.

3.6 Conclusions

In this Chapter I reported the main observational results of my thesis. The inclusion of soft X-ray data revealed a hardening of the spectral shape towards low energies, well described by adding a break (typically located between 2 and 20 keV) and an additional power-law segment to the fitting function below such break energy.

Prompt emission spectra have been modeled with empirical functions for almost three decades. These functions allow only for one power-law segment below the peak energy in νF_ν. The slope of this segment is inconsistent with any radiative processes including the synchrotron mechanism.

My findings show that the average values of the photon indices below and above the break energy are very close (i.e., consistent within 1σ) to the expectations from synchrotron radiation ($\alpha_1^{\rm syn} = -0.67$ and $\alpha_2^{\rm syn} = -1.5$) in a scenario where the break energy corresponds to the cooling break. However, my analysis consists of only 14 bright GRBs. In the next Chapter I focus on testing this result on larger sample of GRBs with joint X-ray/gamma-ray data during the prompt phase.

Chapter 4

Characterization of Gamma-Ray Burst prompt emission spectra down to soft X-rays

In this Chapter I extend the analysis performed previously considering fainter GRBs, for which time-resolved analysis cannot be performed. I selected 20 additional GRBs observed simultaneously by XRT and BAT, having significant signal to perform at least time-integrated analysis (one spectrum for each GRB). I also address the question of why, in the usual situation (i.e., when data below 10 keV are not available), the typical low-energy photon index has a value $\alpha \sim -1$. I compare the sample of GRBs with low-energy breaks with the sample showing no hint for X-ray hardening and with the more general population of *Swift* GRBs, with the aim of correlating the presence of the break to other observables. The presence of the break seems independent from the fluence, flux, and duration, or a combination of these quantities.

4.1 Sample selection

The full sample of GRBs with significant emission detected simultaneously by XRT and BAT includes 77 GRBs (as of January 2016, see Chapter 3 for details). Time-resolved spectral analysis in at least four time bins can be performed only in 14 GRBs and the results of this analysis have been reported in Chapter 3. Spectral breaks between $\sim$2 and 20 keV were found in 67% of the 128 time-resolved spectra.

In this Section, to further explore the occurrence of this spectral feature in GRBs' prompt emission spectra, I enlarge the sample by including fainter sources. I relax the requirement of performing time-resolved analysis and select all cases with enough signal for a joint XRT+BAT time-integrated spectral analysis. More specifically, I consider all cases where the BAT signal-to-noise ratio (S/N) is larger than 30 (in the time interval where significant signal is detected simultaneously by XRT and BAT). This requirement is satisfied by 20 additional GRBs that, together with the 14 GRBs included in the analysis of Chapter 3, form a sample of 34 GRBs. In 11 cases (out of 34), *Fermi* Gamma-ray Burst Monitor (GBM) data are also available and have been included in the spectral analysis. For two additional GRBs, GBM data are available

but have not been included because of inconsistencies between different NaI detectors. For 17 GRBs, the redshift has been measured, and ranges from 0.73 to 5.91. The list of GRBs and their redshift can be found in Table 4.1.

4.2 Data extraction

For each GRB, I analyze the spectrum integrated over the time where significant signal is detected both by BAT and XRT. When GBM data are included, I re-define the edges of the time interval to match the coarser temporal resolution of GBM CSPEC data.

A detailed description of how data from the different instruments have been extracted and processed can be found in Section 2.4. The difference on the data extraction procedure in this Chapter is on *Fermi* instrument. The extraction of GBM spectra has been performed using the GTBURST tool. [1] I selected pre- and post-burst data to model the background, and fit it with a energy- and time-dependent polynomial. Two NaI (in the range 8-1000 keV) and one BGO detector (300 keV-40 MeV) have been used for the spectral analysis. I excluded channels in the range 30-40 keV due to the presence of the Iodine K-edge at 33.17 keV.

4.3 Spectral analysis

Spectral analysis has been performed with XSPEC (v12.9.1). Different likelihoods have been used for different detectors: CSTAT for XRT data, Gaussian for BAT, and PGSTAT for GBM data. The list of tested models and the procedure applied to select the best fit model are discussed in the following sections.

Following the same procedure adopted in Chapter 3, I have introduced multiplicative factors between different instruments, in order to account for uncertainties in their cross-calibration. For cases with XRT and BAT data, I leave the calibration constant free to vary between 0.9 and 1.1. When GBM data are also available, I freeze the calibration constant between XRT and BAT and adopt a calibration constant for the GBM spectrum, free to vary between 0.9 and 1.1. I do not find significant correlation (Pearson correlation coefficient $R>0.5$ and p-value <0.001) between the photon index below the break energy and the normalization constant. In the following sections, I summarize how metal absorption has been treated, which spectral models have been tested, and how the best fit is chosen among all the spectral models that provide a reasonable fit to the data.

4.3.1 Treatment of the absorption

I take into account Galactic and intrinsic absorption by applying the multiplicative `tbabs` and `ztbabs` models (Wilms, Allen, and McCray, 2000) in XSPEC, respectively. Galactic absorption by neutral hydrogen in the direction of the GRB is estimated from

[1] http://fermi.gsfc.nasa.gov/

TABLE 4.1: List of the 34 GRBs analyzed in this Chapter. The GRB's name and redshift are reported in the first and second columns. The third column lists the values of the intrinsic $N_{\rm H}$, derived from spectral analysis of late time XRT observations (see Sect. 4.3 for the method used to estimate $N_{\rm H}$ for GRBs with and without measured redshift). The late time interval (LTI, from the BAT trigger time) chosen for the estimate of $N_{\rm H}$ can be found in the last column.

GRB	Redshift	$N_{\rm H}$ $10^{22}\,{\rm cm}^{-2}$	LTI $10^4\,{\rm s}$
060510B	4.940	0.00	0.05 – 62.41
060814	1.92	1.93	16.83 – 137.78
061121	1.314	0.82	3.46 – 9.25
070616	...	0.49	0.46 – 37.11
070721B	3.626	0.00	0.02 – 13.95
080906	...	0.34	0.54 – 73.69
080928	1.69	0.62	0.42 – 3.34
081008	1.969	0.69	0.06 – 1.77
090709A	...	0.27	0.41 – 6.27
090715B	3.000	2.02	0.02 – 164.88
100413A	...	0.25	0.63 – 17.46
100619A	...	0.45	5.34 – 100.59
100704A	...	0.37	1.26 – 131.81
100725B	...	0.59	2.18 – 80.35
100728A	1.567	3.43	0.50 – 68.29
100814A	1.440	0.25	21.20 – 671.30
100906A	1.727	0.94	1.06 – 46.86
110102A	...	0.19	1.04 – 24.32
110119A	...	0.16	0.49 – 26.09
110205A	2.22	0.70	0.14 – 38.29
111103B	...	0.35	4.55 – 30.06
111123A	3.152	4.81	0.42 – 4.06
121123A	...	0.05	1.66 – 13.91
121217A	...	0.63	2.87 – 547.65
130514A	...	0.36	1.15 – 38.81
130606A	5.913	9.12	0.53 – 1.26
130907A	1.238	1.05	0.76 – 238.41
140108A	...	1.70	1.05 – 43.16
140206A	2.73	2.03	2.12 – 8.71
140323A	...	0.39	2.82 – 9.84
140512A	0.725	0.44	2.79 – 32.94
141031A	...	0.30	4.57 – 84.70
150724A	...	0.55	0.13 – 13.26
151021A	2.330	2.40	0.49 – 67.93

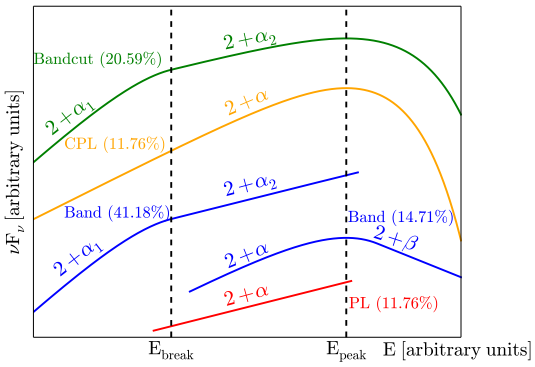

FIGURE 4.1: Spectral models (in νF_ν representation) tested in this Chapter. From top to bottom: a Band function with a high-energy exponential cutoff (Bandcut, green), a Cutoff power-law model (CPL, orange), a Band function (Band, blue) and a single power-law model (PL, red). The Band model can describe two different cases: either both spectral indices are larger than -2, or the second one is smaller than -2. In all models, I use the letter α for spectral segments where the νF_ν flux increases with energy (and distinguish between α_1 and α_2 in case two increasing segments, separated by a spectral break, are present), and β to refer to a decreasing spectral segment. The number within brackets next to the model name refers to the percentage of cases for which each model provides the best fit to the data.

Kalberla et al. (2005). To account for intrinsic absorption within the host galaxy, I apply the method described in Chapter 3: I infer the intrinsic column density of neutral hydrogen from a late time X-ray spectrum taken during the power-law decay phase of the afterglow emission, provided that no significant spectral evolution is evident at that time (Butler and Kocevski, 2007b). The inferred value is used as fixed input value for the intrinsic column density, $N_{\rm H}$, in the joint XRT and BAT (and eventually GBM) spectral analysis. For GRBs without redshift, late-time X-ray spectra are fitted by applying the `tbabs` model only. The values of the intrinsic $N_{\rm H}$ and the late time interval used to constrain $N_{\rm H}$ are reported in Table 4.1. For the 14 GRBs already included in the sample studied in Chapter 3, some values of $N_{\rm H}$ might differ from those reported in Chapter 3. The reason is that I choose CSTAT likelihood to fit the late-time X-ray spectra.

4.3.2 Spectral models

The standard models generally used to fit prompt spectra (PL, CPL, Band and smoothly broken PL) have the possibility to describe at most one change of the spectral slope, typically corresponding to a peak energy $E_{\rm peak}$ of the νF_ν spectrum. In order to capture an additional change in the slope, I first need to introduce an appropriate empirical fitting function. I consider a Band function modified to include a high-energy exponential cutoff (see the model named Bandcut in Fig 4.1). This model was introduced in Zheng et al. (2012). In this model, $E_{\rm peak}$ is located around the high-energy exponential cutoff, while the additional break feature that I

want to describe is located at the smooth connection between the two low-energy PL segments.

The Bandcut model is defined as follows:

$$N_{\rm E}^{\rm Bandcut} \propto \begin{cases} E^{\alpha_1} e^{-\frac{E}{E_1}} & \text{for} \quad E \leq E_{\rm break} \\ \left[\frac{E_1 E_2}{E_2 - E_1}(\alpha_1 - \alpha_2)\right]^{\alpha_1 - \alpha_2} e^{\alpha_1 - \alpha_2} E^{\alpha_2} e^{-\frac{E}{E_2}} & \text{for} \quad E > E_{\rm break} \end{cases}, \tag{4.1}$$

where $E_{\rm break} = \frac{E_1 E_2}{E_2 - E_1}(\alpha_1 - \alpha_2)$. The peak energy is defined by $E_{\rm peak} = E_2(2 + \alpha_2)$. The introduction of this model represents a difference as compared to the analysis presented in Chapter 3, where a broken power-law with an exponential cutoff was used. The difference is then in the description of the shape around the break energy (sharp break in Chapter 3 and smooth break in this Chapter).

I also modeled the spectra with functions including three PL segments. However, I did not succeed in constraining the photon index above $E_{\rm peak}$ for any of the spectra in my sample. Therefore, the final set of tested models includes PL, CPL, Band, and Bandcut. All these models are shown schematically in Fig. 4.1. Note that a Band model is found to describe two different situations: standard cases where a peak energy is present, and cases where the νF_ν flux increases with energy over the full spectral range, but with a change in slope that identifies a break energy $E_{\rm break}$. According to the notation introduced in Chapter 3, I adopt the following terminology when referring to photon indices:

1. The letter α refers to the photon index of spectral segments increasing in νF_ν (i.e., photon indices larger than -2). If there are two consecutive segments (separated by a break) with photon indices larger than -2, I call them α_1 and α_2 (below and above the break, respectively).

2. The letter β is used to refer to a part of the spectrum that is decreasing in νF_ν (i.e., $\beta < -2$).

4.3.3 Selection of the best fit model

From the joint usage of different likelihoods (CSTAT for XRT data, Gaussian for BAT and PGSTAT for GBM data) it is possible to derive an overall likelihood from the product of the single likelihoods obtained separately for each instrument. For each GRB, I then derive the overall likelihood for all tested models. In practice, I define the likelihood ($\mathcal{L}$) as the sum of χ^2, CSTAT, and PGSTAT given by the best fit in XSPEC. To identify the best model, I compare pairs of models and I associate to a given improvement (i.e., a $\delta\mathcal{L} = \mathcal{L}_{modelB} - \mathcal{L}_{modelA}$) a chance probability, and select the most complex model only if the chance probability is less than 1%. The association between a given $\delta\mathcal{L}$ and its chance probability has been obtained by performing simulations, as described in the following.

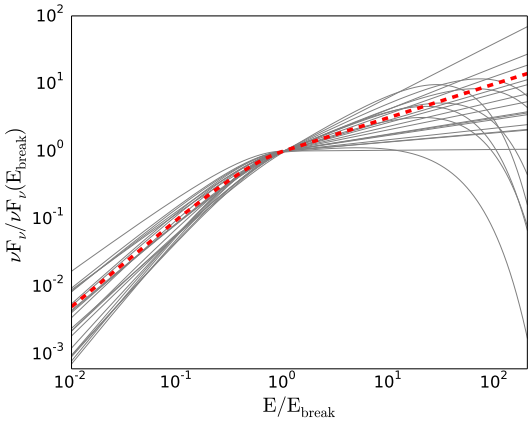

FIGURE 4.2: Best fit models (in νF_ν representation) for all cases where the break energy is found (gray lines), i.e., all cases where the best fit model is either a Band function continuously rising in νF_ν or a Bandcut (see Fig. 4.1). A Band model with photon indices equal to those expected from fast cooling synchrotron radiation ($\alpha_1^{\rm syn} = -2/3$ and $\alpha_2^{\rm syn} = -3/2$) is shown with a dashed, red curve.

For each GRB, I fit a simple model (e.g., PL) to the spectrum. Then, I simulate 10^3 fake spectra using as input this model and its best-fit parameters obtained from the fit of the real spectrum. I re-fit the fake spectra using both the input model and using more complex models (e.g., BPL). As a result, I have a distribution of $\delta\mathcal{L} = \mathcal{L}_{\rm PL} - \mathcal{L}_{\rm BPL}$. The distribution allows to associate a chance probability to a given $\delta\mathcal{L}$: large improvements correspond to a small probability of being obtained by chance.

A more complex model is preferred over a simpler one whenever the improvement derived from the fit of real spectra corresponds to a probability of less than 1% of being a chance improvement. In the example in Fig. 4.4, the two panels show the distributions of $\delta\mathcal{L}_{\rm PL-CPL}$ and $\delta\mathcal{L}_{\rm PL-BPL}$ for simulated spectra. The $\delta\mathcal{L}$ obtained when the real GRB spectrum is fitted with PL and CPL is 59, and is 162 when comparing fits with PL and BPL models (as reported in the figure title). As can be seen from the comparison with the red horizontal line (corresponding to 1% chance probability), the probability that such improvements are obtained by chance are much smaller than 1%. Both CPL and BPL models are in this example preferred over the PL. The whole procedure is repeated replacing the PL model with more complex models, until the best fit model is found. The example refers to the joint XRT+BAT+GBM spectrum of GRB 080928.

4.4 Results

I fit the 34 time-integrated spectra (one for each GRB) with all the models (PL, CPL, Band, and Bandcut, see Fig. 4.1) and define the best-fit model according to the method explained previously. The results are reported in Table 4.2 and Figure 4.5. For each GRB, the table reports the time interval used for the spectral analysis, the

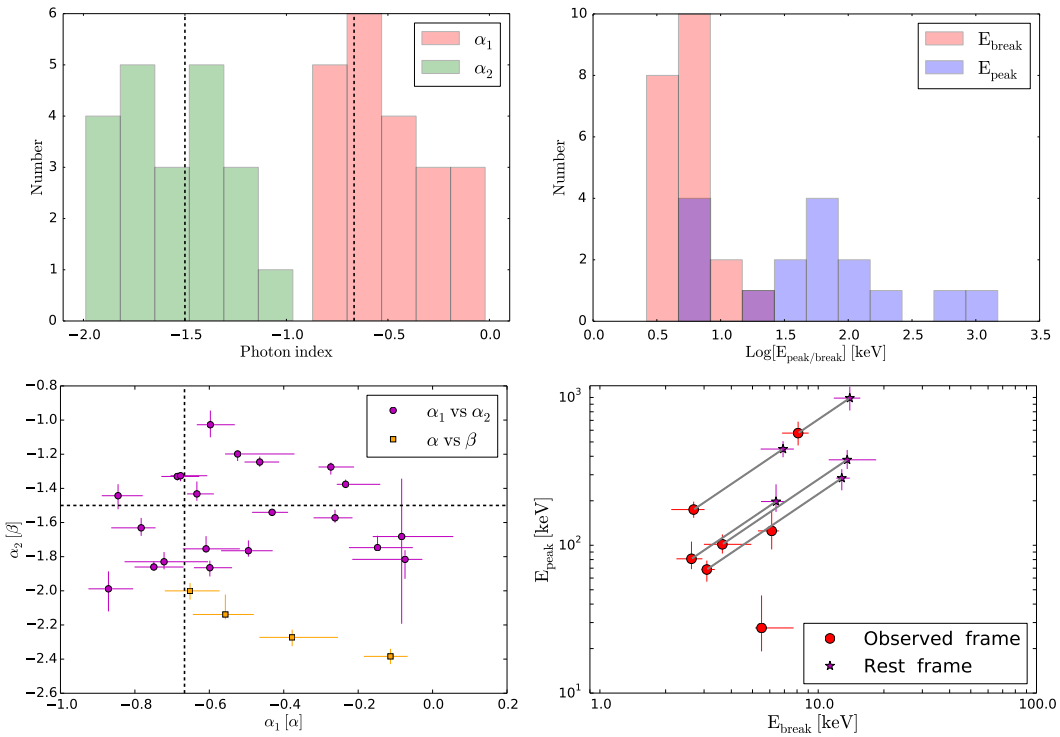

FIGURE 4.3: Best fit parameters resulting from the spectral analysis of the full sample. Left-hand panels: photon indices. Right-hand panels: peak and break energies. Top left: distribution of α_1 (red) and α_2 (green), representing the indices below and above the break energy. Bottom left: α_1 vs. α_2 (circles) and α vs. β for GRBs with a spectrum modeled by a Band function with second index < -2 (squares). In both left-hand panels, the values for α_1 and α_2 predicted from fast cooling synchrotron emission are drawn as dashed lines. In the bottom panel they should be used as reference lines for the circle symbols only. Top right: $E_{\rm peak}$ (blue) and $E_{\rm break}$ (red) distributions. Bottom right: $E_{\rm peak}$ vs. $E_{\rm break}$ for spectra where both features can be constrained (Bandcut model). Circles refer to the observer frame, while stars are used for the rest frame, for those GRBs with measured redshift. The positions before and after cosmological redshift correction are connected with a solid line.

best fit model, the best fit parameters, the average energy flux (in the energy range 0.5 keV - 10 MeV), the $\mathcal{L}$ and d.o.f., and the instruments included in the analysis. Figure 4.5 shows, for each GRB, the XRT, BAT (and eventually GBM) light curve (with the time interval used for spectral analysis highlighted) and the photon spectrum obtained with the best fit model.

The best fit model is a PL in 4 cases (GRB 070721B, GRB 080906, GRB 100413A and GRB 130606A), a CPL in 5 cases, a Band model with a νF_ν peak in 4 cases, a Band model with both photon indices > -2 in 14 cases, and a Bandcut model in the remaining 7 cases. This means that 62% of prompt emission spectra in my sample (i.e., 21 out of 34 GRBs) display a low-energy spectral break $E_{\rm break}$ separating two power-law segments with photon indices > -2.

I first focus on these 21 cases and show the best-fit model in νF_ν units (gray curves) in Fig. 4.2. For reference, I also plot a Band model with photon indices

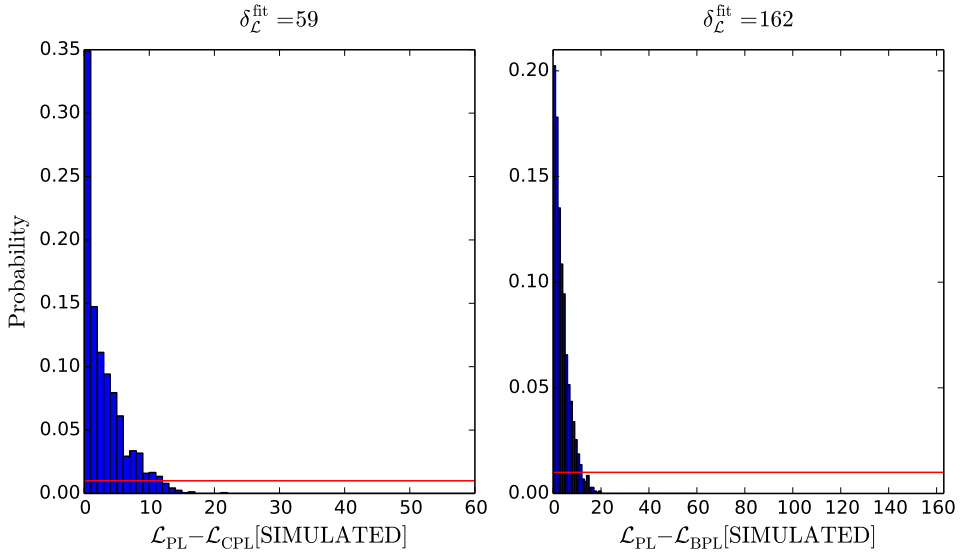

FIGURE 4.4: Left panel: distribution of the improvement of the CPL fit with respect to the PL fit, for 1000 fake spectra. All fake spectra have been simulated adopting the best fit model obtained fitting a PL model to the observed spectrum of GRB 080928. A $\delta\mathcal{L} > 11$ corresponds to a probability $< 1\%$ to have a stochastic improvement (horizontal red line in the figure). The $\delta\mathcal{L}$ obtained when the real spectrum is fitted with a PL and a CPL is $\delta\mathcal{L}_{\rm PL-CPL} = 59$, corresponding to a chance probability much smaller than 1%. Right panel: As in the left panel, but the PL fits are compared to BPL fits. Also in this case, the improvement $\delta\mathcal{L} = 162$ exceeds the critical value of 12.

$\alpha_1^{\rm syn} = -0.67$ and $\alpha_2^{\rm syn} = -1.5$ (dashed, red curve). As can be seen, the dashed red curve is on average a good representation of the observed spectra.

TABLE 4.2: Results of the spectral analysis. The table lists the GRB name, the best fit model name (PL = power-law, CPL = cutoff power-law, Band = Band function, Bandcut = Band function with a high energy cutoff), the best fit parameters (columns 4 to 8, for a definition see Fig. 3.2), the average flux, the overall likelihood $\mathcal{L}$, and the degrees of freedom (d.o.f.). The last column reports the instruments included in the spectral analysis: X = XRT, B = BAT, G = GBM.

GRB	Time interval	Model	α_1	$E_{\rm break}$ keV	α/α_2	$E_{\rm peak}$ keV	β	Flux 10^{-7}erg s^{-1} cm^{-2}	$\mathcal{L}$ (d.o.f.)	Instr.
060510B	[127.00,325.00]	Band	$-0.61^{+0.09}_{-0.06}$	$6.15^{+1.21}_{-1.08}$	$-1.75^{+0.07}_{-0.02}$			$[0.22-0.79]$	1052(1002)	XB
060814	[77.50,200.00]	Band	$-0.15^{+0.09}_{-0.08}$	$3.37^{+0.34}_{-0.37}$	$-1.75^{+0.07}_{-0.01}$			$[0.40-1.45]$	848(1002)	XB
061121	[62.00,110.00]	Band	$-0.23^{+0.09}_{-0.02}$	$4.54^{+0.53}_{-0.40}$	$-1.38^{+0.03}_{-0.02}$			$[5.32-76.78]$	794(1002)	XB
070616	[138.00,615.00]	Bandcut	$-0.63^{+0.05}_{-0.03}$	$6.12^{+0.48}_{-0.82}$	$-1.43^{+0.07}_{-0.04}$	$125.10^{+44.05}_{-31.35}$		$0.64^{+0.10}_{-0.08}$	968(1001)	XB
070721B	[311.00,361.00]	PL			$-1.20^{+0.08}_{-0.05}$			$[0.09-2.60]$	721(1004)	XB
080906	[78.00,95.00]	PL			$-1.72^{+0.09}_{-0.04}$			$[0.11-0.43]$	700(1004)	XB
080928	[197.93,256.30]	Band	$-0.72^{+0.12}_{-0.11}$	$4.79^{+0.87}_{-1.20}$	$-1.83^{+0.06}_{-0.04}$			$[0.66-1.13]$	1054(1233)	XBG
081008	[94.00,193.00]	Band	$-0.75^{+0.08}_{-0.05}$	$4.34^{+0.22}_{-0.63}$	$-1.86^{+0.03}_{-0.02}$			$[0.28-0.74]$	900(1002)	XB
090709A	[75.00,101.00]	Band	$-0.85^{+0.07}_{-0.04}$	$22.06^{+12.08}_{-4.19}$	$-1.44^{+0.07}_{-0.08}$			$[1.07-12.55]$	897(1002)	XB
090715B	[53.00,295.00]	CPL			$-1.56^{+0.03}_{-0.03}$	$27.81^{+3.10}_{-7.40}$		$0.13^{+0.02}_{-0.00}$	909(1003)	XB

TABLE 4.2: continued.

GRB	Time interval	Model	α_1	$E_{\rm break}$ keV	α/α_2	$E_{\rm peak}$ keV	β	Flux 10^{-7}erg s^{-1} cm^{-2}	$\mathcal{L}$ (d.o.f.)	Instr.
100413A	[147.00,228.00]	PL			$-1.48^{+0.01}_{-0.04}$			$[0.25-2.38]$	902(1004)	XB
100619A	[80.68,100.13]	Band	$-0.60^{+0.06}_{-0.04}$	$6.95^{+0.71}_{-0.85}$	$-1.86^{+0.04}_{-0.05}$			$[3.30-5.40]$	1147(1218)	XBG
100704A	[93.37,197.82]	Band			$-0.38^{+0.12}_{-0.09}$	$4.70^{+0.50}_{-0.56}$	$-2.27^{+0.04}_{-0.05}$	$0.50^{+0.38}_{-0.17}$	1476(1234)	XBG
100725B	[89.49,229.78]	Band			$-0.65^{+0.08}_{-0.07}$	$5.10^{+0.57}_{-0.70}$	$-2.00^{+0.05}_{-0.05}$	$1.10^{+0.44}_{-0.31}$	818(1002)	XB
100728A	[81.53,158.33]	Bandcut	$-0.69^{+0.06}_{-0.04}$	$2.69^{+0.33}_{-0.57}$	$-1.33^{+0.02}_{-0.02}$	$174.41^{+22.86}_{-20.88}$		$1.92^{+0.49}_{-0.29}$	1945(1352)	XBG
100814A	[94.70,180.71]	Bandcut	$-0.68^{+0.07}_{-0.03}$	$2.63^{+0.32}_{-0.38}$	$-1.33^{+0.02}_{-0.03}$	$80.98^{+24.92}_{-12.04}$		$0.35^{+0.11}_{-0.05}$	1418(1349)	XBG
100906A	[85.72,125.65]	Band			$-0.11^{+0.05}_{-0.07}$	$6.48^{+0.70}_{-0.36}$	$-2.38^{+0.04}_{-0.05}$	$1.36^{+0.32}_{-0.43}$	1274(1234)	XBG
110102A	[195.17,290.40]	Band	$-0.43^{+0.04}_{-0.05}$	$5.49^{+0.54}_{-0.29}$	$-1.54^{+0.01}_{-0.01}$			$[1.29-9.90]$	949(1002)	XB
110119A	[162.56,214.79]	Band	$-0.26^{+0.05}_{-0.06}$	$5.42^{+0.70}_{-0.63}$	$-1.57^{+0.05}_{-0.03}$			$[0.90-2.52]$	1238(1233)	XBG
110205A	[160.00,350.00]	Band	$-0.50^{+0.07}_{-0.07}$	$7.60^{+2.75}_{-1.05}$	$-1.77^{+0.06}_{-0.03}$			$[0.65-2.36]$	926(1002)	XB
111103B	[104.00,127.00]	CPL			$-1.38^{+0.06}_{-0.08}$	$64.22^{+47.80}_{-12.26}$		$0.47^{+0.02}_{-0.08}$	756(1003)	XB
111123A	[106.00,274.00]	Bandcut	$-0.27^{+0.06}_{-0.03}$	$3.09^{+0.27}_{-0.17}$	$-1.27^{+0.03}_{-0.04}$	$68.55^{+10.27}_{-11.81}$		$0.31^{+0.08}_{-0.04}$	994(1001)	XB
121123A	[193.15,299.65]	CPL			$-0.89^{+0.02}_{-0.03}$	$70.15^{+4.52}_{-5.26}$		$1.11^{+0.08}_{-0.02}$	1029(1003)	XB
121217A	[717.30,767.48]	Band	$-0.78^{+0.04}_{-0.08}$	$8.49^{+1.65}_{-1.61}$	$-1.63^{+0.06}_{-0.05}$			$[1.20-2.97]$	1383(1233)	XBG
130514A	[96.00,158.00]	Band	$-0.87^{+0.07}_{-0.05}$	$8.86^{+3.21}_{-1.82}$	$-1.99^{+0.10}_{-0.13}$			$[0.53-1.07]$	936(1002)	XB
130606A	[117.00,166.00]	PL			$-1.15^{+0.04}_{-0.02}$			$[0.35-12.83]$	878(1004)	XB
130907A	[71.00,87.00]	Band	$-0.52^{+0.15}_{-0.03}$	$5.83^{+1.15}_{-1.26}$	$-1.20^{+0.01}_{-0.04}$			$[6.87-203.28]$	919(1002)	XB
140108A	[76.76,101.33]	CPL			$-1.28^{+0.02}_{-0.02}$	$915.40^{+405.32}_{-236.34}$		$8.40^{+0.51}_{-0.50}$	1209(1234)	XBG
140206A	[50.25,100.00]	Bandcut	$-0.60^{+0.07}_{-0.04}$	$3.64^{+1.30}_{-0.64}$	$-1.03^{+0.08}_{-0.07}$	$101.49^{+16.82}_{-13.54}$		$3.51^{+0.45}_{-0.79}$	844(1001)	XB
140323A	[101.52,122.00]	Bandcut	$-0.07^{+0.05}_{-0.14}$	$5.50^{+2.21}_{-0.36}$	$-1.82^{+0.05}_{-0.11}$	$27.59^{+18.19}_{-8.44}$		$0.74^{+0.09}_{-0.40}$	1210(1001)	XBG
140512A	[102.86,158.16]	Bandcut	$-0.46^{+0.05}_{-0.04}$	$8.09^{+0.95}_{-1.26}$	$-1.25^{+0.03}_{-0.03}$	$573.93^{+111.73}_{-100.43}$		$6.07^{+1.31}_{-0.87}$	1475(1338)	XBG
141031A	[857.00,893.00]	Band	$-0.08^{+0.14}_{-0.08}$	$4.59^{+0.54}_{-0.82}$	$-1.68^{+0.34}_{-0.51}$			$[0.25-1.15]$	934(1002)	XB
150724A	[216.00,235.00]	CPL			$-1.50^{+0.09}_{-0.11}$	$21.13^{+9.78}_{-3.62}$		$0.31^{+0.02}_{-0.06}$	732(1003)	XB
151021A	[95.00,128.00]	Band			$-0.56^{+0.08}_{-0.09}$	$5.34^{+0.75}_{-0.61}$	$-2.14^{+0.12}_{-0.03}$	$1.05^{+0.27}_{-0.40}$	868(1002)	XB

Figure 4.3 shows the distribution of the photon indices α_1 and α_2 (upper left-hand panel) and the relation between them (circled symbols in the bottom left-hand panel). In both panels, the dashed lines mark the values expected for $\alpha_1^{\rm syn}$ and $\alpha_2^{\rm syn}$ in the case of the fast-cooling regime. A Gaussian fit to the distributions returns $\langle\alpha_1\rangle = -0.51$ ($\sigma = 0.24$) and $\langle\alpha_2\rangle = -1.56$ ($\sigma = 0.26$). These values are consistent within 1σ with the values found in Chapter 3 and with the synchrotron values. The bottom left-hand panel in Fig. 4.3 also reports α versus β values for those spectra best modeled by a peaked Band model (square symbols).

The right-hand panels in Fig. 4.3 summarize the results on $E_{\rm peak}$ and $E_{\rm break}$. A Gaussian fit to the $E_{\rm break}$ logarithmic distribution returns $\langle\log(E_{\rm break})\rangle = 0.74$ ($\sigma = 0.20$), in agreement within 1σ with the results from Chapter 3. The $E_{\rm peak}$ distribution (blue histogram) is wide and flat, and values range from 5 to 915 keV. The bottom right-hand panel of Fig. 4.3 shows $E_{\rm peak}$ versus $E_{\rm break}$ for the subsample of spectra for which both features are constrained (i.e., for spectra best modeled by a Bandcut function). Red circles refer to energies in the observer frame, while purple

stars refer to the rest frame values obtained after redshift correction (for GRBs with known redshift). No hint of a correlation between $E_{\rm peak}$ and $E_{\rm break}$ is found.

FIGURE 4.5: Light curves (left-hand panel) and spectra (middle and right-hand panel) for each GRB in the sample. The light-blue shaded area in the left-hand panels highlights the time interval chosen for the spectral analysis. The middle panels show the νF_ν spectra and the best fit model. Note that the data points in the νF_ν panels have been derived for a specific model, and should not be used to perform comparisons with a different model. The right-hand panels show the count spectra. In all panels, XRT data are shown in red, BAT in green, GBM-NaI in blue and light-blue, and GBM-BGO in purple.

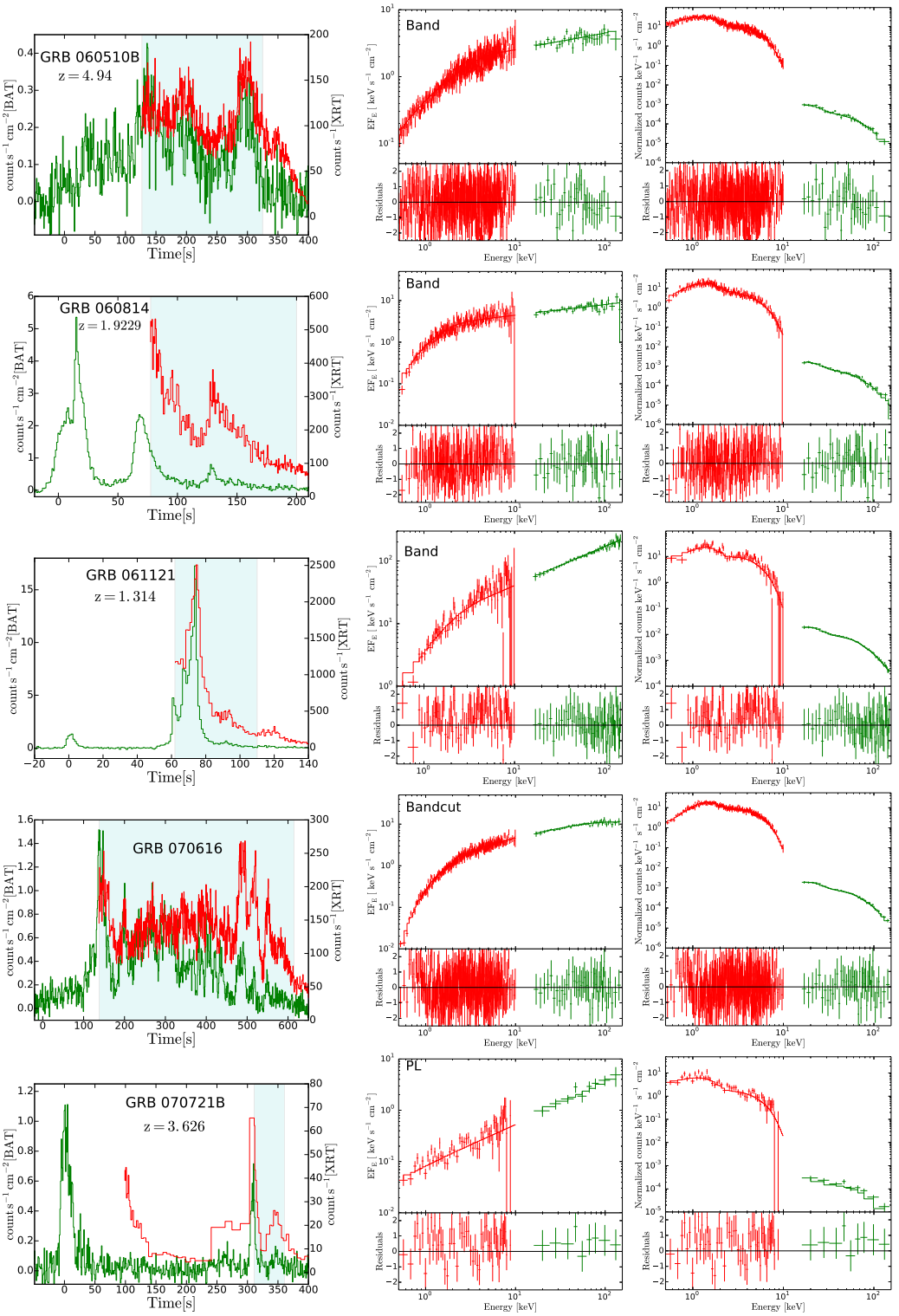

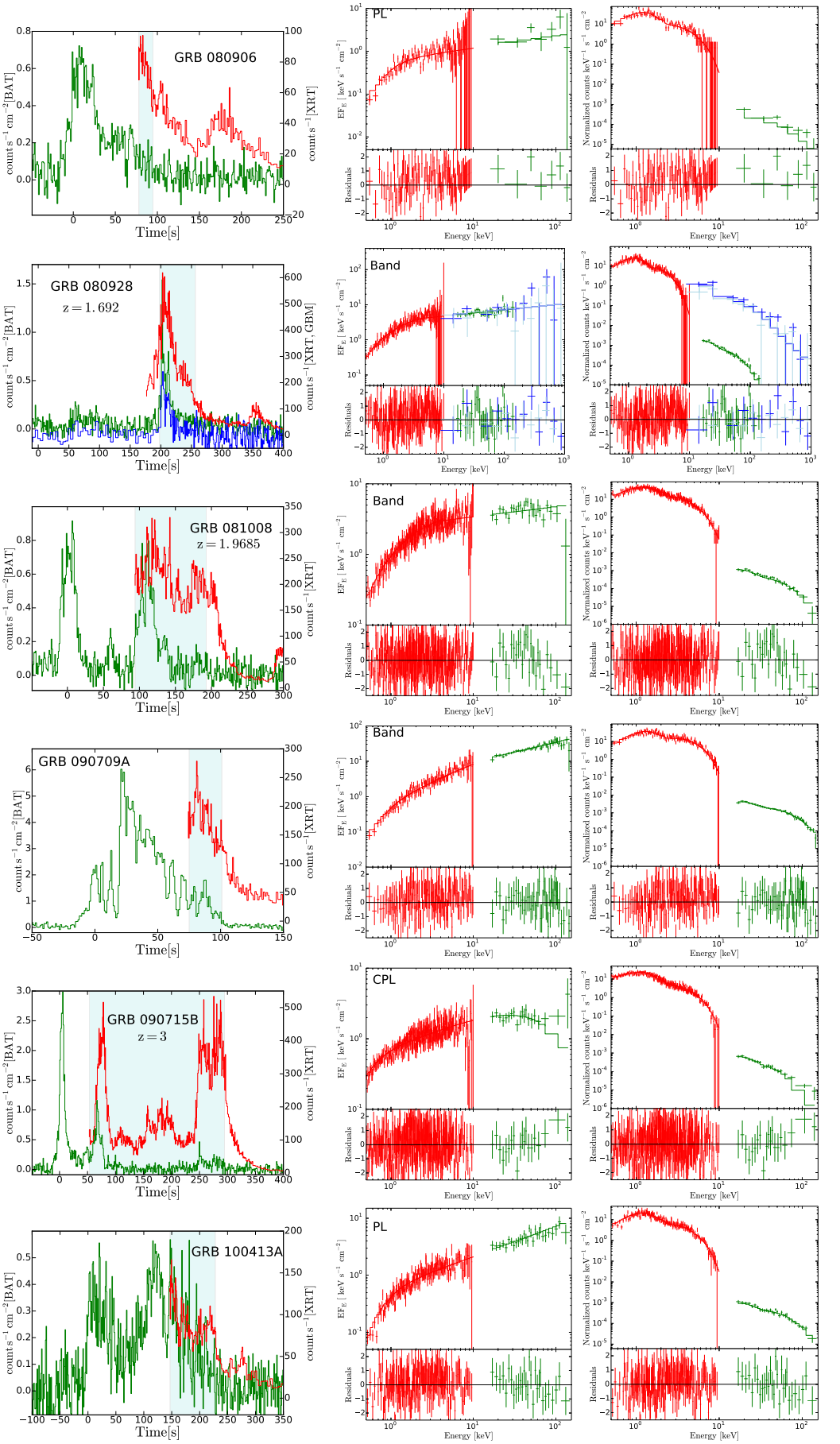
GRB 080906
PL
GRB 080928
z = 1.692
Band
GRB 081008
z = 1.9685
Band
GRB 090709A
Band
GRB 090715B
z = 3
CPL
GRB 100413A
PL
Time[s]
Energy [keV]
Residuals
Normalized counts keV^{-1} s^{-1} cm^{-2}
EF$_E$ [keV s^{-1} cm^{-2}]
count s^{-1} cm^{-2}[BAT]
count s^{-1}[XRT]
count s^{-1}[XRT, GBM]

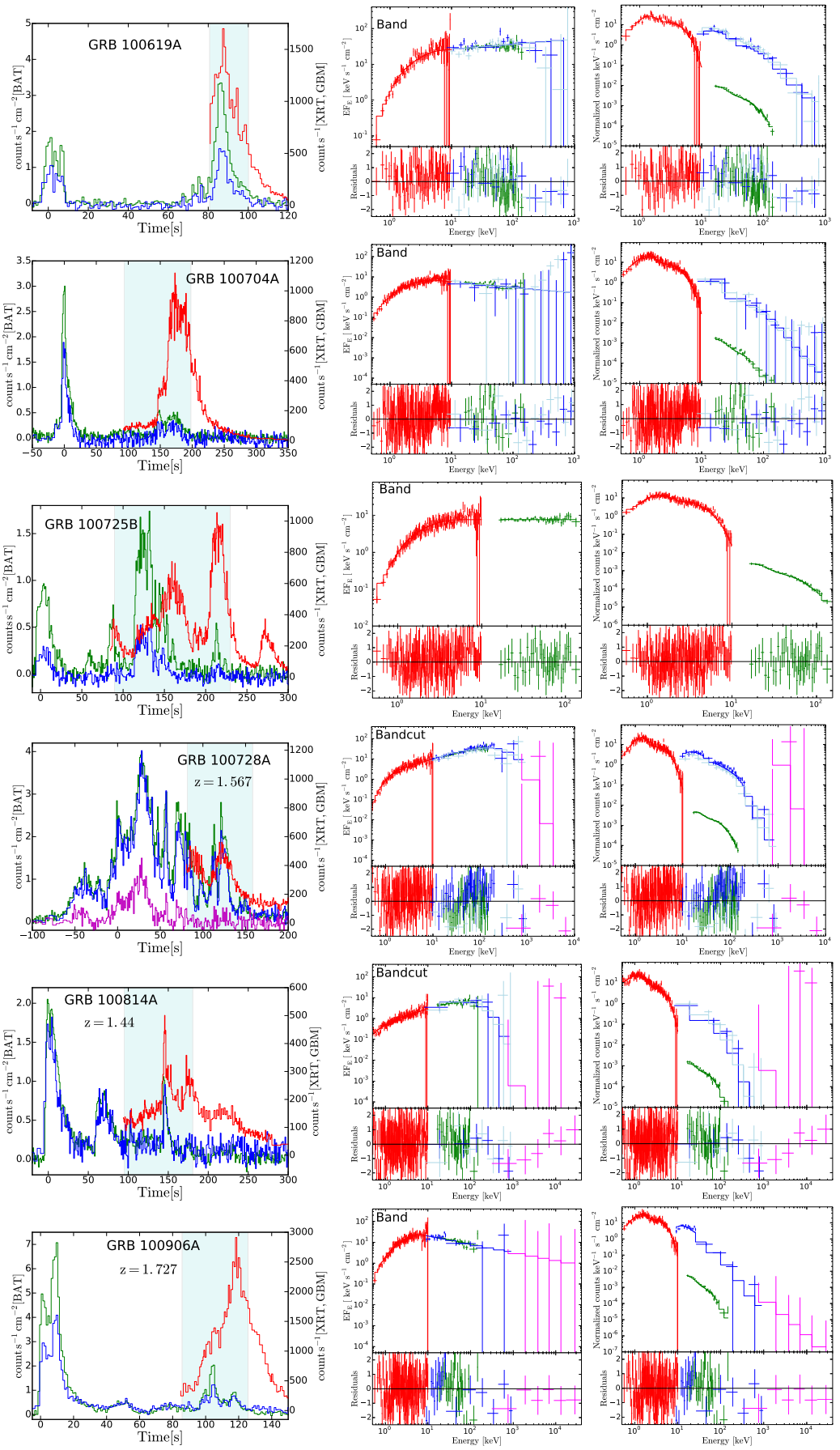
GRB 100619A
Band
GRB 100704A
Band
GRB 100725B
Band
GRB 100728A
z = 1.567
Bandcut
GRB 100814A
z = 1.44
Bandcut
GRB 100906A
z = 1.727
Band
Time[s]
Energy [keV]
Residuals

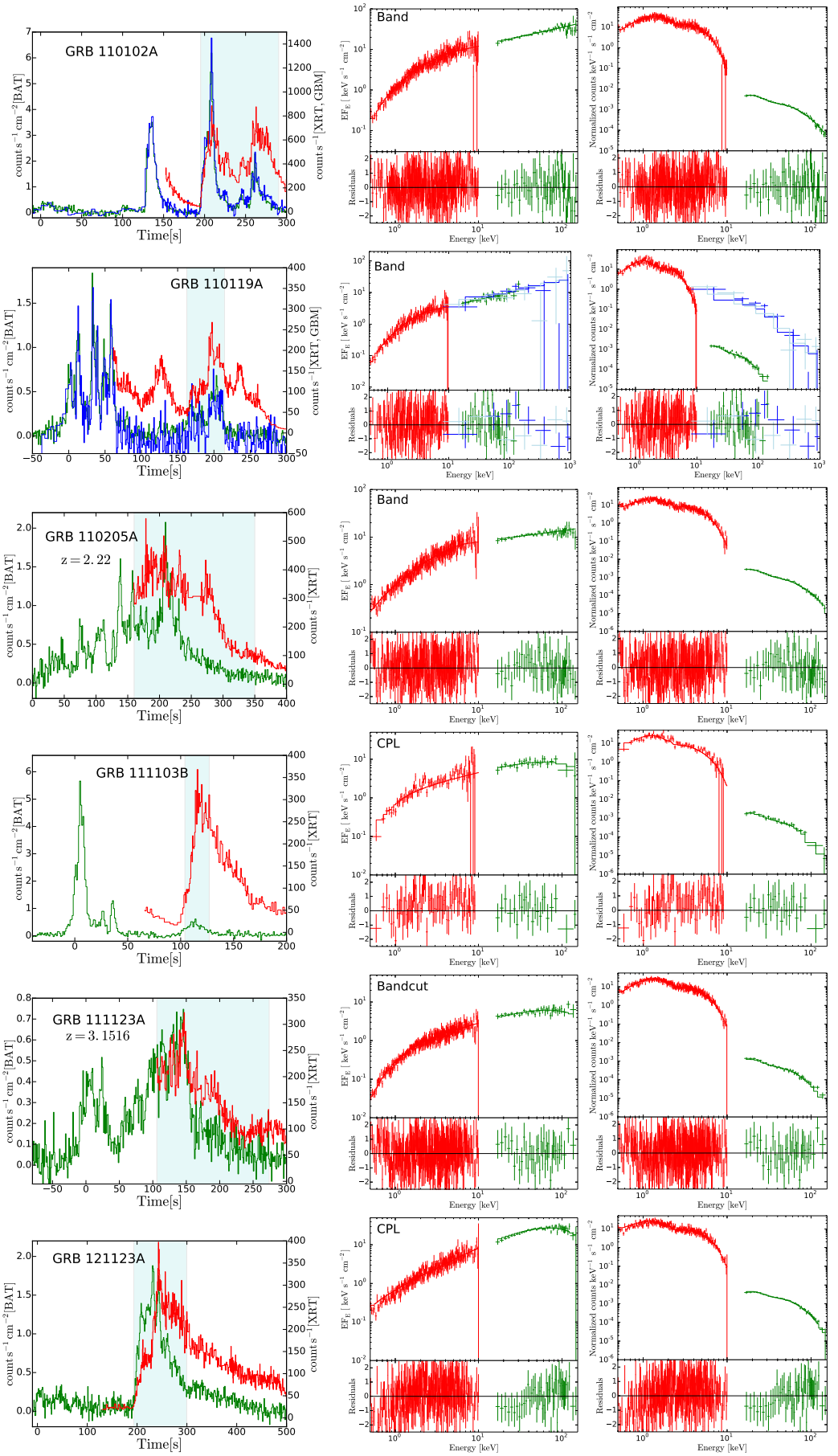
GRB 110102A
Band
GRB 110119A
Band
GRB 110205A
z = 2.22
Band
GRB 111103B
CPL
GRB 111123A
z = 3.1516
Bandcut
GRB 121123A
CPL
Time[s]
Energy [keV]
Residuals

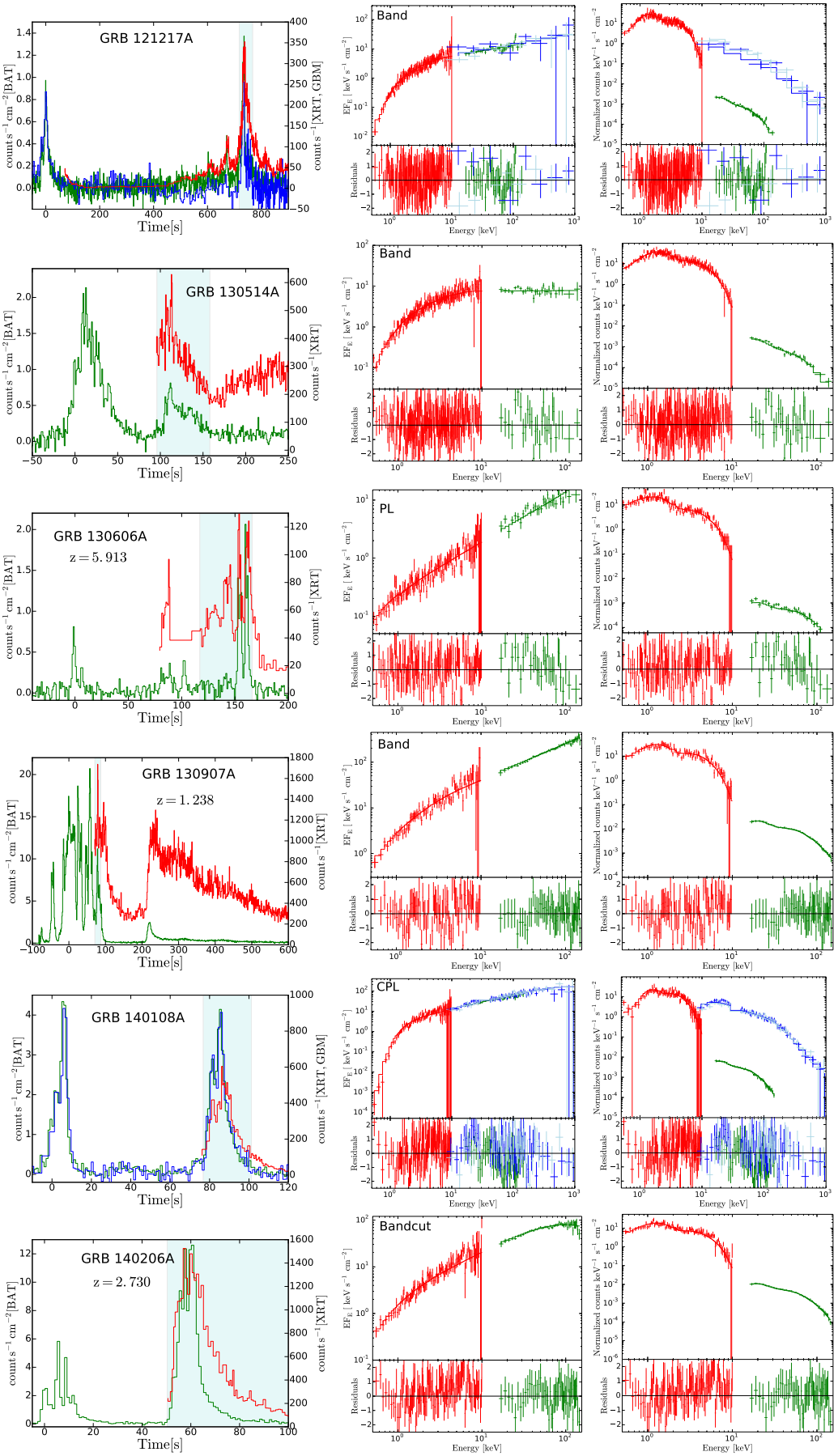
GRB 121217A
Band
GRB 130514A
Band
GRB 130606A
z = 5.913
PL
GRB 130907A
z = 1.238
Band
GRB 140108A
CPL
GRB 140206A
z = 2.730
Bandcut
Time[s]
Energy [keV]
Residuals

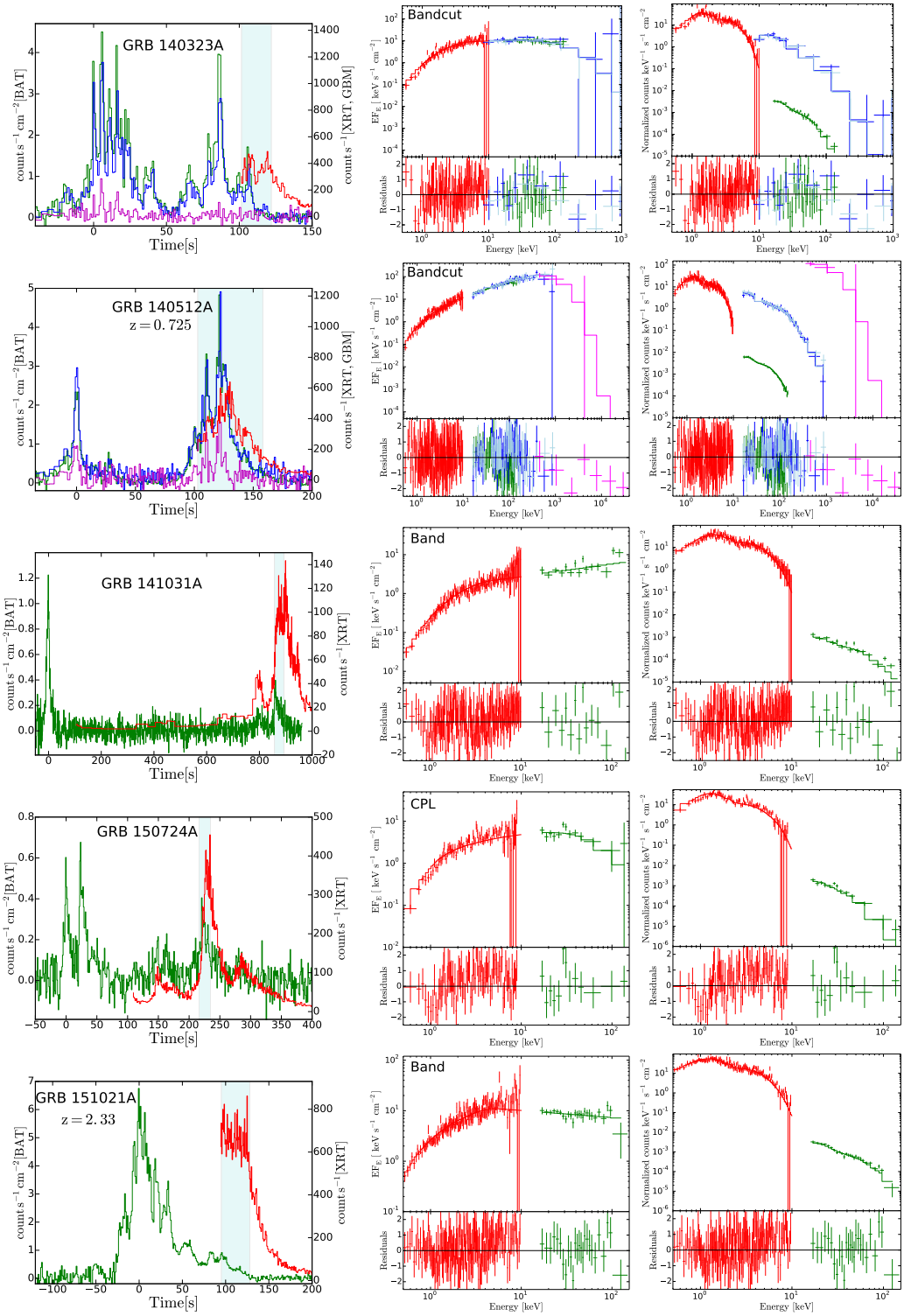
GRB 140323A
Bandcut
GRB 140512A
z = 0.725
Bandcut
GRB 141031A
Band
GRB 150724A
CPL
GRB 151021A
z = 2.33
Band
Time[s]
Energy [keV]
Residuals

4.4.1 Origin of the typically observed value $\alpha = -1$

The typical value $\alpha \sim -1$ describing the part of the spectrum below $E_{\rm peak}$ was inferred from studies of prompt spectra down to 8-25 keV, mainly from BATSE, *Swift*-BAT, and *Fermi*-GBM. In Chapter 3 and in this Section, I found that when soft X-ray data are available and require a model including a low-energy spectral break, the part of the spectrum immediately below the peak energy is described by a value $\alpha_2 \sim -1.5$, softer than α and consistent with the synchrotron theory. These results, in apparent contradiction, seem to suggest that fit results depend on the extension of the energy range over which observations are available and/or on the shape of the function used to model the data. Another explanation is that the subsample of events studied here is somehow peculiar and not representative of the whole population.

To test all these possibilities, I perform the following exercise. I collect all the spectra (among those presented here and in Chapter 3) displaying a low-energy break, and plot their α_2 distribution (green histogram) in Fig. 4.6. Subsequently, for all these spectra, I re-do the spectral analysis by excluding XRT data. The best-fit model, after excluding XRT, is either a PL or a CPL. The distributions of the photon indices are shown in Fig. 4.6, separately for $\alpha_{\rm PL}$ (blue histogram) and $\alpha_{\rm CPL}$ (red histogram). I find $\langle\alpha_{\rm PL}\rangle = -1.70$ ($\sigma = 0.23$) and $\langle\alpha_{\rm CPL}\rangle = -1.15$ ($\sigma = 0.21$). A Kolmogorov-Smirnov (KS) test between the distributions of $\alpha_{\rm PL}$ and $\alpha_{\rm CPL}$ has a probability of $\mathbf{3} \times 10^{-9}$ that the two populations are drawn from the same parent distribution. A similar separation between $\alpha_{\rm PL}$ and $\alpha_{\rm CPL}$ and similar mean values are found in the population of BAT (Lien et al., 2016), GBM (Gruber et al., 2014), and BATSE bursts (Kaneko et al., 2006a). I conclude that when XRT data are removed, the best fit model has a shape similar to the typical shape of the general GRB population. The KS tests for $\alpha_{\rm PL} - \alpha_2$ and $\alpha_{\rm CPL} - \alpha_2$ give probabilities of 3×10^{-3} and 9×10^{-5}, respectively. This shows that this is not a peculiar subsample of GRBs: when XRT data are excluded, the best-fit parameters are in full agreement with the general population. In Fig. 4.7, the values of α_2 are shown versus the values of α derived after excluding XRT data. Different colors and symbols are used to distinguish between cases in which the best-fit model after XRT exclusion is a PL (blue) or a CPL (red). First of all, I note the separation between red and blue points, which was already evident from Fig. 4.6. Most of the points are consistent within 1σ with the equality line (dashed gray line). However, almost half of the CPL fits return a harder value of α. On the contrary, PL fits tend to return softer spectra.

The extension of the energy range and the introduction of a function with a low-energy break (necessary for a good description of the overall spectral shape) have then a strong impact on the inferred value of the photon index describing the spectral shape at energies below the spectral peak energy. The overall result is that when XRT data are available, the part of the spectrum below $E_{\rm peak}$ is described by a theoretically motivated value, but when XRT data are removed and the spectrum is modeled with a CPL function, the best fit photon index describing the part below $E_{\rm break}$ has a harder value, that if taken as face value leads to the opposite conclusion: the inconsistency

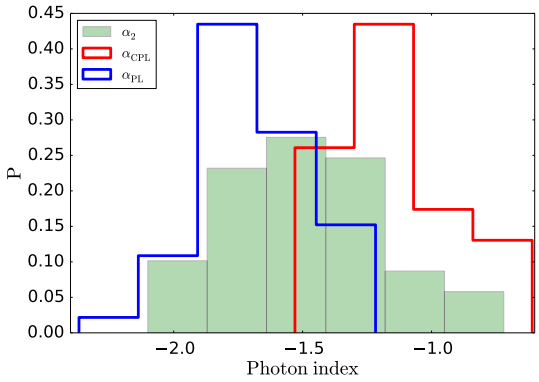

FIGURE 4.6: Distribution of photon indices describing the spectrum below the peak energy, for the merged sample studied in Chapter 3 and this Chapter. The green histogram shows the indices α_2 describing the spectrum between $E_{\rm break}$ and $E_{\rm peak}$. The blue and red histograms show the distribution of α for the same sample of spectra, obtained when the analysis is performed without including XRT. The red histogram denotes cases where the best model is a CPL, and the blue histogram cases where the best-fit model is a single PL.

of observed spectra with synchrotron radiation.

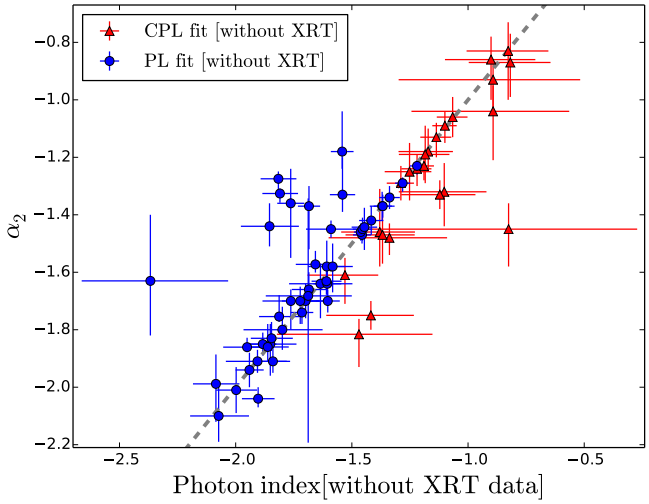

FIGURE 4.7: Comparison between the photon index α_2 and the photon index α derived after removing XRT data from the spectral analysis. In this last analysis, the best-fit model is either a PL (and the index is called $\alpha_{\rm PL}$, blue points) or a CPL ($\alpha_{\rm CPL}$, red points). The identity line is drawn as a dashed gray line.

4.4.2 Comparison with the full BAT catalog

Figure 4.8 shows the average energy-flux versus T_{90} (upper panel), and the fluence versus T_{90} (bottom panel) for my sample (blue and red triangles) and for a large sample of *Swift*-BAT GRBs (gray circles, from Lien et al. 2016). The values of fluences and fluxes are integrated in the BAT energy range 15-150 keV. The sample of GRBs studied in this Section is clearly biased towards long prompt emission durations. This

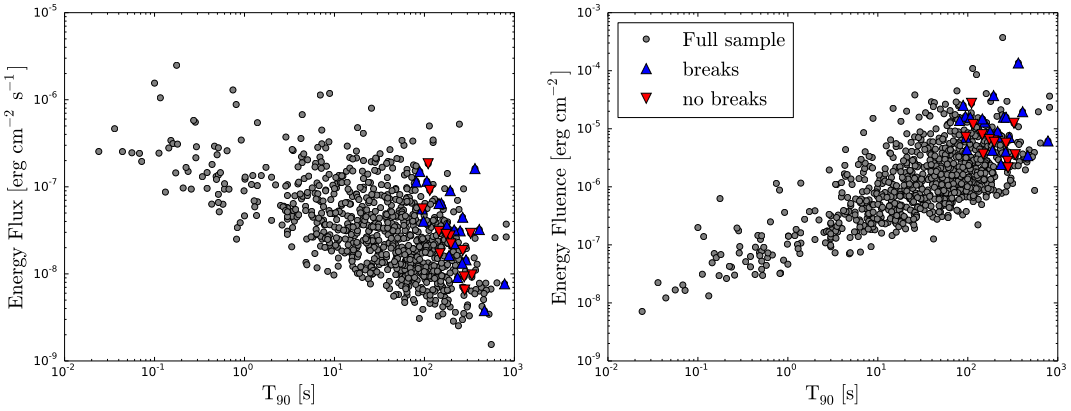

FIGURE 4.8: Comparison in terms of flux, fluence, and T_{90} between the sample studied in this Chapter (triangles) and the full catalog of BAT GRBs, from Lien et al. (2016) (gray circles). My sample is divided into two classes: GRBs with a low-energy break (blue triangles) and GRBs without a low-energy break (red upside-down triangles). Upper panel: average flux vs. T_{90}. Lower panel: fluence vs. T_{90}.

reflects the slew time required by the satellite to place the BAT source within the XRT field of view: prompt emission can be observed with the XRT only if it lasts longer than the typical slewing time. In some cases however, the T_{90} does not reflect the duration of the main emission episode, since the large T_{90} duration is caused by the presence of a precursor, while the main emission (detected by the XRT) has a more standard duration (the light curves of all 34 GRBs can be seen in Fig. 4.5). Limiting the comparison to GRBs with a similar duration, I note that the whole range of fluxes of the full sample is spanned also by my sample. To look for differences within my sample, I mark GRBs with a low-energy break (blue triangles) and GRBs with no evidence of a break (red upside-down triangles). The two different subsamples do not display any relevant difference in terms of flux, fluence, duration, or a combination of these quantities. The question of whether GRBs with spectral breaks in the soft X-ray band have some characteristics that distinguish them from GRBs without X-ray breaks remains therefore an open question.

4.5 Summary

I studied a sample of 34 GRBs for which the prompt emission (or part of it) was detected simultaneously by XRT and BAT. I performed time-integrated joint spectral analysis over the time interval where signal above background is observed in both instruments. In particular, since the signal in BAT is, in general, fainter, I required a BAT signal-to-noise ration (S/N) >30 to guarantee a reliable spectral analysis.

These results confirm the results obtained in Chapter 3 on a smaller sample, and can be summarized as follows.

- 62% of the prompt spectra display a change in slope at low energy, (between 3 and 22 keV, observer frame). In other words, the data in the soft X-ray band

do not lie on the power-law extrapolation of the Band spectrum describing the 10 keV-MeV data. The change in slope can be well described by adding a break into the fitting function and an additional power-law segment below the break.

- The spectral indices α_1 and α_2 below and above the break energy have a distribution centered around the values $\langle\alpha_1\rangle = -0.51$ ($\sigma = 0.24$) and $\langle\alpha_2\rangle = -1.56$ ($\sigma = 0.26$), consistent within 1σ with the values predicted in case of fast cooling synchrotron radiation.

- The value of the spectral index describing the part of the spectrum below the peak energy is sensitive to the inclusion of low-energy data and to the fitting function. If XRT data are included in the analysis and if the break is modeled, the average value is around -1.5, consistent with synchrotron radiation. If XRT data are removed and a CPL model is used to describe the spectrum, the photon index is harder, leading to the opposite conclusion of an inconsistency with synchrotron radiation.

- GRBs with low-energy breaks share similar observational properties in terms of flux and fluence as compared to those without a break in their soft X-ray band.

The average values of the photon indices allow me to speculate about a possible synchrotron origin of the observed spectrum. In such a scenario, the break energy $E_{\rm break}$ would correspond to the cooling frequency, and the peak energy $E_{\rm peak}$ to the typical synchrotron frequency. The ratio between the two characteristic energies ranges from ~ 5 to ~ 71, implying a ratio $\gamma_{\rm m}/\gamma_{\rm c} \sim 2 - 8$, where $\gamma_{\rm m}$ is the typical energy of the particles injected by the acceleration process, and $\gamma_{\rm c}$ is the cooling Lorentz factor.

For these values of $\gamma_{\rm m}/\gamma_{\rm c}$, particle cooling is still very efficient (Daigne, Bošnjak, and Dubus, 2011). Such a regime has been extensively discussed in the literature, and is often referred to as a moderately fast cooling regime.

Chapter 5

Bright Fermi GRB 160625B

XRT+BAT(+GBM) joint spectral analysis has revealed the necessity of going beyond the standard fitting models, by adding a further, hard power-law segment at low energy. In the GRBs considered previously, the break energy $E_{\rm break}$ assumes values in the range 2–30 keV. Since the $E_{\rm break}$ distribution inferred by my studies extends up to 30 keV, an immediate follow-up question is whether in the *Fermi* database there are bursts showing a similar spectral break. It should be possible to find these breaks and study whether they are also present at higher energies. Moreover, if a low-energy spectral break is found in bright GBM GRBs, a time-resolved analysis would then allow to study, for the first time in detail, if and how this break energy evolves in time and with respect to the peak energy.

In the work of Ravasio et al. (2018), a test case event (GRB 160625B) was suggested to study. GRB 160625B satisfies two conditions: it has a great deal of photon statistics and it is poorly fitted by standard fitting functions, as reported in the online GBM GRB spectral catalogue[1].

GRB 160625B is the third burst with the largest fluence (5.7×10^{-4} erg cm^{-2} in the $10-10^3$ keV energy range) detected by *Fermi*. At a redshift of $z = 1.406$ (Xu et al., 2016) its isotropic energy is $E_{\rm iso} \sim 5\times10^{54}$ erg. This GRB has been extensively studied in the literature, due to its extremely large fluence and long duration (Zhang et al., 2016; Wang et al., 2017; Lü et al., 2017), to the rich data sets covering its afterglow emission, and to polarization measurements (Alexander et al., 2017; Troja et al., 2017).

Time-resolved prompt spectral analysis performed by Zhang et al. (2016), suggested the presence of a black-body (BB) spectrum in the first peak (the precursor), and a non-thermal spectrum during the main emission episode. This spectral transition was interpreted as being caused by the transition from a matter-dominated jet to a magnetically dominated jet. Wang et al. (2017) adopted a composition of Band function (Band et al., 1993) with a high-energy cut-off and BB component. A similar two-component model is adopted by Lü et al. (2017). What appears common in these models is the presence, sometimes simultaneous, of a BB and a non-thermal component. Ravasio et al. (2018, hereafter R18) revisit these analyses in light of my

[1] https://heasarc.gsfc.nasa.gov/W3Browse/fermi/fermigbrst.html

findings and test one single component with a spectral break in the low-energy part of the spectrum.

In this Chapter I discuss the findings from the spectral analysis of the bright Fermi GRB 160625B performed in R18. This analysis shows the possibility to model the time-resolved spectra of GRB 160625B by one-component model with a low energy break at $100 - 300$ keV. The photon indices below and above the break energy are consistent with synchrotron scenario. These findings point towards a common nature of the prompt emission spectra.

5.1 Temporal structure

Three different emission episodes separated by long quiescent times are visible in the light curve of GRB 160625B (Fig. 5.1): a precursor at $T = T_0$, the main event ~ 180 s later (lasting approximately 30 s), and a faint, soft, long-lasting (~ 300 s) emission starting at $T \sim T_0 + 500$ s. R18 presents the results of time-integrated and time-

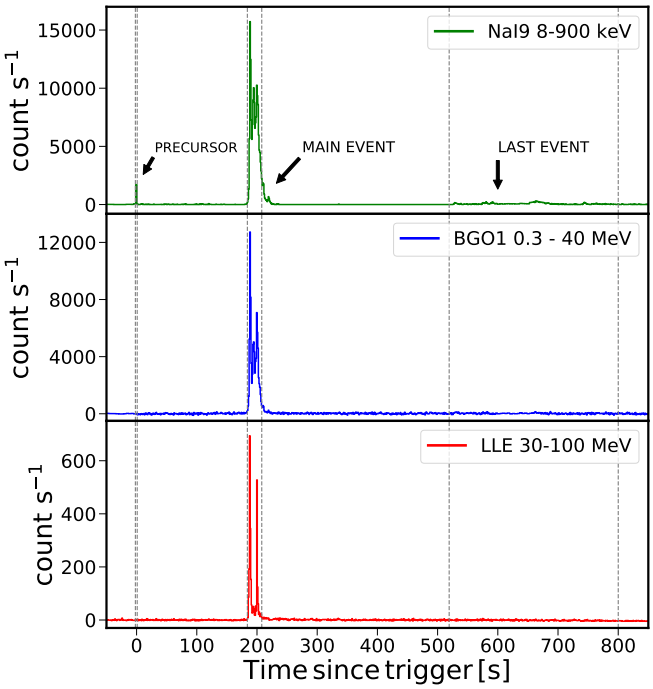

FIGURE 5.1: Background-subtracted light curves of GRB 160625B detected by NaI 9 (8 keV–900 keV, top), BGO 1 (300 keV–40 MeV, middle), and LAT–LLE (30 MeV–100 MeV, bottom).

resolved spectral analysis on the main emission episode. For all three episodes, the time intervals are marked with vertical dashed lines in Fig. 5.1.

The time interval for spectral analysis was selected requiring a signal-to-noise ratio (S/N) higher than 20 in the brightest BGO (BGO 1). This criterion results in the selection of the time interval 186.40–207.91 s. R18 performed the analysis of the spectrum integrated over this time interval (time-integrated spectrum) and of the 21

bins (time-resolved spectra), with time integration of 1.024 s each, distributed within the above time interval.

5.2 The spectral model

The single-component spectral models traditionally used to fit the GBM spectra (e.g. Kaneko et al. 2006c) include a PL, a CPL, the Band model, and a SBPL. The advantage of the SBPL with respect to the Band model is that it allows the smoothness of the curvature connecting the two PL segments to be changed. The SBPL function used in the GBM Catalog is defined in Kaneko et al. (2006c). In order to easily extend the definition of the SBPL to more than one break, in R18 the function is defined as

$$N_{\mathrm{E}}^{\mathrm{SBPL}} = A E_{\mathrm{j}}^{\alpha} \left[\left(\frac{E}{E_{\mathrm{j}}} \right)^{-\alpha n} + \left(\frac{E}{E_{\mathrm{j}}} \right)^{-\beta n} \right]^{-\frac{1}{n}} , \tag{5.1}$$

where

$$E_{\mathrm{j}} = E_{\mathrm{peak}} \cdot \left(-\frac{\alpha + 2}{\beta + 2} \right)^{\frac{1}{(\beta - \alpha) n}} . \tag{5.2}$$

In 5.1 N_{E} is the photon spectrum (i.e. number of photons per unit area, per unit time, and per unit energy). The free parameters are the amplitude A, the low-energy spectral index α, the peak energy of the $E^2 N_{\mathrm{E}}$ spectrum E_{peak}, the high-energy spectral index β, and the smoothness parameter n (higher values of n correspond to sharper curvatures).

In the GBM Catalog the smoothness parameter is called Λ and is kept fixed to $\Lambda = 0.3$ for all GRBs (see Kaneko et al. 2006c for an explanation). In order to perform a fit that can be compared to the one reported in the GBM Catalog, the smoothness parameter n, which has a different definition, has been fixed to the value $n = 2.69$ in R18, corresponding to $\Lambda = 0.3$.

The extension of SBPL which includes a second break energy and a third power-law segment is defined as

$$\begin{aligned} N_{\mathrm{E}}^{\mathrm{2SBPL}} = A\, E_{\mathrm{break}}^{\alpha_1} \Bigg[\left[\left(\frac{E}{E_{\mathrm{break}}} \right)^{-\alpha_1 n_1} + \left(\frac{E}{E_{\mathrm{break}}} \right)^{-\alpha_2 n_1} \right]^{\frac{n_2}{n_1}} + \\ + \left(\frac{E}{E_{\mathrm{j}}} \right)^{-\beta\, n_2} \cdot \left[\left(\frac{E_{\mathrm{j}}}{E_{\mathrm{break}}} \right)^{-\alpha_1 n_1} + \left(\frac{E_{\mathrm{j}}}{E_{\mathrm{break}}} \right)^{-\alpha_2 n_1} \right]^{\frac{n_2}{n_1}} \Bigg]^{-\frac{1}{n_2}} , \end{aligned} \tag{5.3}$$

where

$$E_{\mathrm{j}} = E_{\mathrm{peak}} \cdot \left(-\frac{\alpha_2 + 2}{\beta + 2} \right)^{\frac{1}{(\beta - \alpha_2)\, n_2}} . \tag{5.4}$$

The free parameters are the amplitude A, the photon index α_1 below the break energy, the break energy E_{break}, the photon index α_2 between the break and the peak

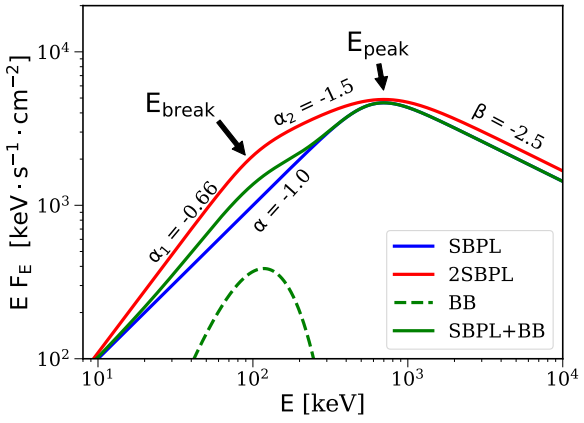

FIGURE 5.2: Comparison between the SBPL model (blue curve), SBPL+BB (green solid curve), and 2SBPL (red curve). Normalizations are arbitrary.

energies, the peak energy $E_{\rm peak}$, the high-energy photon index β, and the smoothness parameters n_1 (for the break) and n_2 (for the peak).

As before, the curvature around the peak energy is fixed to the value $n_2 = 2.69$. After performing time-resolved spectral fitting by leaving n_1 free to vary, it was realized that the model parameters of the fit are not always constrained, and so it was also decided to fix the value of n_1. The value of n_1 is fixed to the mean value of the distribution inferred when it is left free to vary: $n_1 = 5.38$. This corresponds to a sharper curvature than the curvature around the peak energy.

These models are shown (assuming typical parameters for the photon indices) in Fig. 5.2 (SBPL in blue and 2SBPL in red). For comparison, a SBPL+BB (green line) is also shown. As is evident, the overall effect of adding a (non-dominant) BB is similar to the effect of considering a softer SBPL (i.e. more consistent with synchrotron, $\alpha_2 = -1.5$) and adding a break at low energies. The final functions have a similar shape (red and green solid lines in Fig. 5.2).

5.3 Time-integrated analysis

The 2SBPL function, defined in equation 5.1, is fitted to the time-integrated spectrum of the main emission episode (time interval 186.40–207.91 s). In the time interval for the time-integrated analysis LAT observations are also available. It was found that the LLE data do not lie on the extrapolation of the BGO data: they instead reveal the presence of a softening at high energies. In order to model this softening, the 2SBPL was modified by adding an exponential cut-off at high energy. The fit shown in Fig. 5.3 with the solid black line. The LLE data are shown with purple symbols. The best fit value of the cut-off energy (defined as the energy at which the flux is suppressed by a factor $\sim 1/e$ as compared to the simple PL extrapolation) is $E_{\rm cut} = 50.3^{+7.4}_{-13.2}$ MeV, and the reduced chi-square is $\chi^2_{\rm red} = 1.51$. All the other spectral parameters (photon indices, low-energy break and peak energies) are consistent with those obtained when

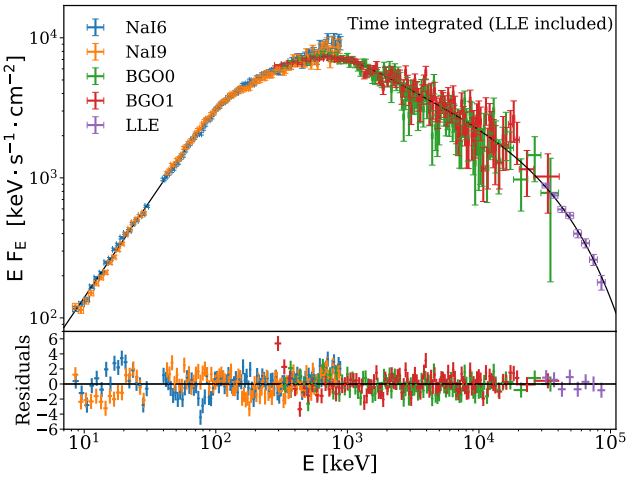

FIGURE 5.3: Time-integrated spectrum (186.40–207.91 s) from 8 keV to 100 MeV, including LAT-LLE data. The model (black solid line) is a 2SBPL with a high-energy exponential cut-off.

LLE data are not included: $\alpha_1 = -0.62 \pm 0.01$, $E_{\rm break} = 107.3^{+1.9}_{-1.6}$, $\alpha_2 = -1.49 \pm 0.02$, $E_{\rm peak} = 668.7^{+14.4}_{-9.2}$, and $\beta = -2.54^{+0.03}_{-0.02}$. If interpreted as being caused by photon-photon annihilation, the cut-off at ~ 50 MeV corresponds to a Lorentz factor $\sim 200 - 250$, for a variability timescale $\sim 1 - 0.1$ s (Lithwick and Sari, 2001).

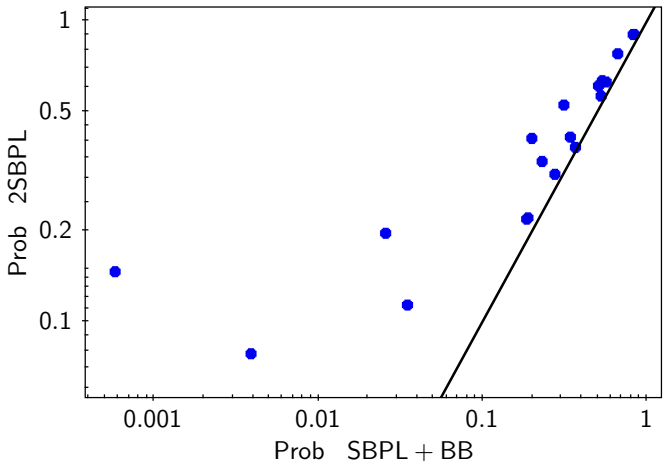

FIGURE 5.4: Fit probability for time-resolved spectra: comparison between fits performed with a 2SBPL model (y-axis) and with a SBPL+BB model (x-axis). The two models have the same number of degrees of freedom. The equality line is shown as a solid black line.

5.4 Time-resolved analysis

In order to check whether the low-energy break identified in the time-integrated spectrum is also present in the time-resolved spectra and study its evolution with time,the time interval 186.40–207.91 s was divided into 21 time bins, with 1.024 s integration

each. Three models were tested: SBPL, 2SBPL, and SBPL+BB (see Fig. 5.2). First, the SBPL and 2SBPL models were compared through an F-test. In 19 spectra (i.e. all spectra except the last two, where the flux is small), the 2SBPL improves the SBPL fit at more than 3σ, which was taken as the threshold value for the definition of the best fit model. More specifically, in all these 19 spectra the fit improves at more than 4.8σ (more than 8σ in 13 cases).

The SBPL+BB model also leads to a significant improvement of the fit over the SBPL. A comparison between SBPL and SBPL+BB in terms of F-test, however, cannot be performed. A comparison between 2SBPL and SBPL+BB can instead be performed in terms of probability of their χ^2 since they are not nested models, but have the same number of parameters and degrees of freedom. The two probabilities are compared in Fig. 5.4, where the equality line is shown as a solid black line. The probabilities of the 2SBPL are systematically larger than those resulting from an SBPL+BB fit. Notably, the break energy of the 2SBPL coincides with the peak of the BB component. The results obtained from the spectrum at the peak of the light curve (time bin 188.45 s–189.47 s) are shown in Fig. 5.5. SBPL model (top panel) has large residuals, displaying a characteristic trend. The situation largely improves both when a BB component is added (middle panel) and when the SBPL is modified to have one additional PL (2SBPL, bottom panel).

In the peak spectrum the statistical comparison based on the chi-square firmly favours a 2SBPL model over the SBPL+BB: $\chi^2_{\rm 2SBPL} = 1.07$ ($P_{\rm 2SBPL} = 0.15$) and $\chi^2_{\rm SBPL+BB} = 1.23$ ($P_{\rm 2SBPL} = 6 \times 10^{-4}$). In particular, the SBPL+BB function seems to underestimate the energy of the spectral peak ($E^{\rm SBPL+BB}_{\rm peak} \sim 1\,{\rm MeV}$), which is instead better modelled by the 2SBPL function ($E^{\rm 2SBPL}_{\rm peak} \sim 1.5\,{\rm MeV}$).

The temporal evolution of the spectral parameters inferred from the 2SBPL fits are reported in Fig. 5.6. The upper panel shows the light curve of the main emission episode with a 1.024 s temporal resolution. The vertical dashed lines denote the time bins selected for time-resolved spectral analysis. In the second and third panel, the evolution of the photon indices are displayed. The fourth panel shows the temporal evolutions of $\rm E_{peak}$ (red symbols) and $\rm E_{break}$ (blue symbols). Their ratio is given in the bottom panel. $\rm E_{peak}$ exhibits a strong evolution (a softening) in the first 5 seconds, after which it settles to a nearly constant value ($\rm E_{peak} \sim 500 - 600\,keV$). $\rm E_{break}$ displays a similar evolution, but the initial softening is much less pronounced. After the first few seconds, $\rm E_{break}$ also displays a nearly constant behaviour ($E_{break} \sim 100\,{\rm keV}$). The ratio $E_{\rm peak}/E_{\rm break}$ varies from ~ 35 at the very beginning to $\sim$5 at later times. Figure 5.7 shows the distributions of the spectral indices of the 2SBPL model fits. If modelled with Gaussian functions, the mean values are $\langle\alpha_1\rangle = -0.63$ ($\sigma = 0.08$) and $\langle\alpha_2\rangle = -1.48$ ($\sigma = 0.09$). These values are remarkably consistent with standard synchrotron fast cooling emission, predicting $\alpha_1^{\rm syn} = -2/3$ and $\alpha_2^{\rm syn} = -3/2$.

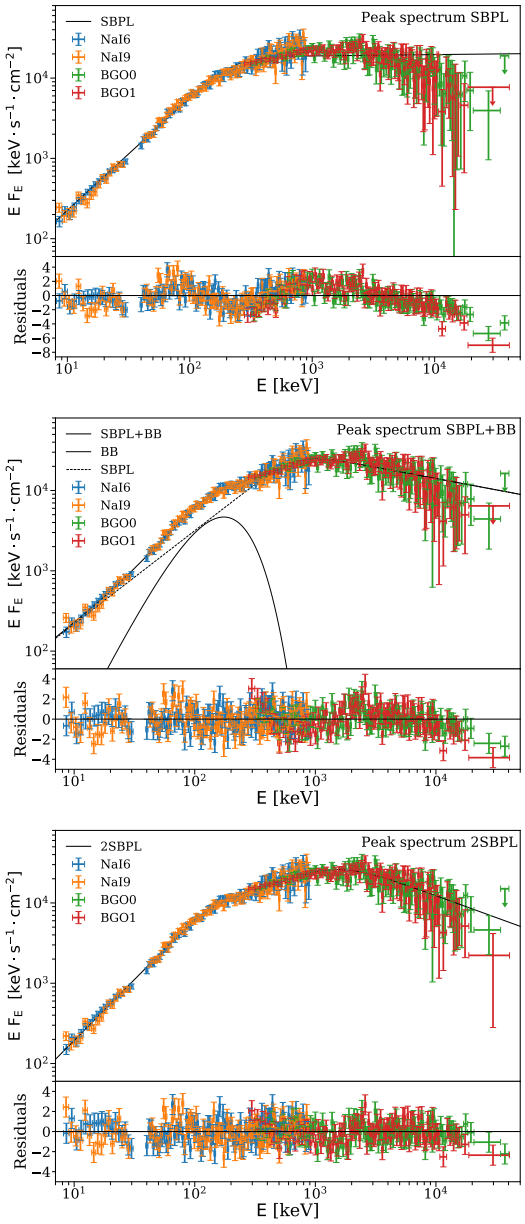

FIGURE 5.5: Time-resolved spectrum accumulated in the time interval 188.45–189.47 s (peak of the light curve). Different spectral models are tested: a SBPL (upper panel), SBPL+BB (middle), and 2SBPL (lower panel).

5.5 Summary

GRB 160625B is one of the brightest GRBs ever detected by *Fermi*-GBM during its nine years of activity. Its light curve is composed of three distinct emission episode: a precursor, a main event, and a long-lasting, late time, soft emission (see Fig. 5.1).

R18 performed time-integrated and time-resolved spectroscopy of the main event, testing different fitting models. A new fitting function, called 2SBPL (Eq. 5.3), was introduced. It consists of three smoothly connected power laws. Standard models with at most two power laws (e.g. Band and SBPL) fail to give a reasonable fit, both to the time-integrated and time-resolved spectra.

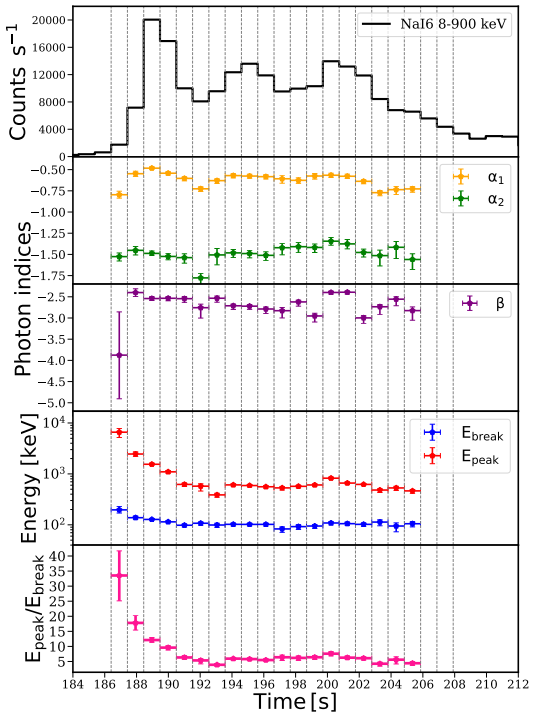

FIGURE 5.6: Time evolution of the spectral parameters of the 2SBPL model for time-resolved spectra where the 2SBPL fit improves at more than 3σ the SBPL fit (all bins but the last two). From top to bottom: Count rate light curve (with 1.024 s time resolution), photon indices below and above the break (yellow and green symbols, respectively), spectral index above the peak energy (purple symbols), peak and break energy (red and blue symbols, respectively), and ratio between peak and break energy (pink symbols). For an explanation of the notation used for the 2SBPL parameters, see Fig. 5.2 (red line).

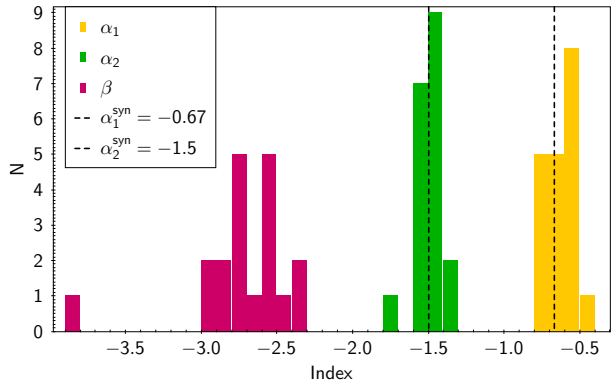

FIGURE 5.7: Distributions of the spectral indices of the three power-law segments of the 2SBPL model. The vertical dashed lines are the expected values for synchrotron emission in the fast cooling regime.

Fitting a 2SBPL model to the data, R18 obtain well-constrained spectral parameters and significantly improving fits (F-test$> 3\sigma$) both for the time-integrated spectrum and for 19 out of the 21 time-resolved spectra. The additional PL segment (compared to the Band and SBPL functions) describes the low-energy, hardest part of the spectrum, connected to the usual peaked function by a break that is quite

sharp.

The break energy is around 100 keV, with little evolution in time. Moreover, the indices of the power laws below and above the low-energy break are $\langle\alpha_1\rangle = -0.63$ ($\sigma = 0.08$) and $\langle\alpha_2\rangle = -1.48$ ($\sigma = 0.09$). These values are remarkably consistent with those predicted for synchrotron emission from a population of non-thermal electrons.

A 2SBPL, however, is not the only possible model for the observed spectrum. In fact, the spectral hardening below $E_{\rm break}$ could be produced by adding a BB component to a typical single break spectrum (e.g. SBPL or Band), as can be understood from Fig. 5.2. On the other hand, this extra BB component must be fine tuned in order to mimic the incomplete cooling case, and this fine tuning must be present in each of the time-resolved spectra analyzed. Moreover, the detailed analysis of the spectrum at the peak of the light curve, where the 2SBPL model is a preferable fit, gave arguments in support of the 2SBPL model. A comparison between the fit probability of the two models in all the time-resolved spectra is shown in Fig. 5.4: the 2SBPL probability is always higher than or equal to the SBPL+BB probability.

5.6 Conclusions

The findings of spectral breaks in prompt emission at different energies and obtained by different instruments suggests it to be a common feature. The photon indices below and above the break have typical values close to the values expected from the synchrotron radiation. The comparisons between the photon indices derived from the empirical model and the predictions of the synchrotron scenario represent a first consistency check, but they do not prove the validity of the synchrotron interpretation. Several studies (Beloborodov, 2013; Axelsson and Borgonovo, 2015; Yu et al., 2015; Vurm and Beloborodov, 2016) have argued that the observed spectral width around the peak energy is narrower than the one characterizing synchrotron spectra. A more detailed, theory-driven analysis is now required in order to assess the validity of the synchrotron interpretation. In the following Chapter I fit XRT+BAT (and if available GBM) data with a synchrotron model instead of using an empirical function.

As it was discussed, the spectral hardening below the break could be produced by adding a thermal component to a typical single break spectrum. Different modeling provides similar spectral curvature in the X-ray energy range. It is quite difficult to decide whether the entire prompt emission spectrum is made by one- or two-component model. However, these models predict very different fluxes at lower frequencies. In the next Chapter I compare the flux predicted by the best fit of the synchrotron model with the observed optical flux for the GRBs with available optical observations during the prompt phase.

Chapter 6

Prompt optical emission as signature of synchrotron radiation in Gamma-Ray Bursts

Prompt emission spectra in soft X-rays showed that more than 60 % of the spectra require an additional PL segment, describing the spectrum below $2-20$ keV (Chapters 3-4). The proposed empirical model was found successful for one of the brightest Fermi GRB 160625B with similar spectral shapes and break energies at $100-300$keV (Ravasio et al., 2018). The average photon indices below and above the break are close to the values predicted in the synchrotron scenario in fast cooling regime (-2/3 and -3/2). In my studies, the presence of a break has been investigated only adopting empirical models. The evidence of consistency with the spectral indices expected from synchrotron radiation demands now for a more detailed investigation. Observations extending to lower frequencies would be required, to test the consistency of the index with the -2/3 predicted by the synchrotron model.

Recently the presence of a sub-dominant black-body (BB) component (in addition to a non-thermal component) has been claimed to be present in several GRBs. It is quite clear that the addition of a BB component is an alternative to a modeling with one single component with a spectral break at low-energies. The reason is that when a BB is added in the low-energy part of a PL non-thermal spectrum, the sum of the two components mimics a broken PL behaviour. There are two different approaches to model the very same data. While it is now clear that a simple Band function is not enough to capture the complexity of the prompt spectra, it is less obvious which one of the two different models is the correct one. The question is of paramount importance, since the two different descriptions of the spectra implies two very different theoretical scenarios.

While the two different models predict similar spectral shapes in the X-ray energy range, making very difficult to understand which one should be preferred, they are expected to predicts very different fluxes at lower frequencies. The hard index of the synchrotron-like modeling, once extrapolated to lower frequencies, will indeed predict smaller fluxes, as compared to a non-thermal+BB model. The latter, is indeed dominated by the non-thermal component at low frequencies, for which the

photon index is in general much softer than -2/3. An important tool to test prompt emission spectral models is then the inclusion of the early optical observations seen simultaneously with X-ray / γ-ray detections.

Early optical observations were successfully performed for the limited number of GRBs, thanks to robotic telescopes (e.g. ROTSE-III (Akerlof et al., 2003), TAROT (Klotz et al., 2009), MASTER (Lipunov et al., 2004), Pi of the Sky (Burd et al., 2005), TORTORA (Beskin et al., 2017)).

One caveat with the use of early optical observations as a test for prompt emission models is however its possible contamination by emission with a different origin, e.g. forward and/or reverse shock radiation once the fireball propagates into the interstellar medium (Mészáros and Rees, 1997; Sari, Piran, and Narayan, 1998).

This diversity has been pointed out in a number of studies (see Kopač et al. 2013 for a systematic study). In a number of cases, the optical emission is explained simply as a tail of prompt emission, e.g. GRB 041219A (Vestrand et al., 2005), GRB 060526 (Thöne et al., 2010), GRB 100901A (Gorbovskoy et al., 2012), GRB 140430 (Kopač et al., 2015). In other cases early optical counterparts are dominated by the afterglow component, produced by a reverse shock (e.g. GRB 990123 (Akerlof et al., 1999), GRB 060111B (Klotz et al., 2006)) or by a forward shock (e.g. GRB 050820A (Cenko et al., 2006), GRB 061007 (Mundell et al., 2007), GRB 081008 (Yuan et al., 2010), GRB 080810 (Page et al., 2009), GRB 100906 (Gorbovskoy et al., 2012)) or by both forward and reverse shocks, e.g. GRB 091024A (Virgili et al., 2013). Particularly bright optical components have been interpreted as the synchrotron seed photons producing the prompt X-ray emission through inverse Compton mechanism (e.g. one of the possible scenarios for GRB 990123 (Panaitescu and Kumar, 2007) and for GRB 080319B (Woźniak et al., 2009)). The Comptonization of prompt γ-ray photons by an electron cloud can also produce an early optical counterpart (e.g. one possibility for GRB 041219A (Zheng, Lu, and Zhao, 2006)). The extremely bright optical emission of naked-eye 080319B exceeds the predicted tail of prompt emission by 3-4 orders invoking unusual scenarios such as two component jet model (Racusin et al., 2008) or internal dissipation with a significant neutrons load (Beskin et al., 2010).

In this Chapter, I start from the sample of 34 GRBs with simultaneous XRT and BAT prompt observations considered in Chapter 4 and select a subsample for which simultaneous optical observations are also available. I re-analyse the spectra in the temporal window where optical observations are available. As compared to the analysis presented in Chapter 4, I introduce two major differences: i) I fit XRT+BAT (and if available GBM) data with a synchrotron model instead of using an empirical function, and ii) I compare the flux predicted by the best fit synchrotron model with the observed optical flux.

6.1 The sample and analysis

I consider the sample collected by Chapter 4, composed by 34 GRBs with XRT observations available during the prompt emission. I defined a sub-sample for which also optical prompt observations are available. Published optical detections and upper limits around were searched for each burst the same time of the XRT+BAT joint spectral analysis performed in Chapter 4. If available, published calibrated magnitudes from papers in journals were collected, otherwise, the information reported in GRB Circular Network were considered. The final sample is composed by 21 GRBs. The observed magnitudes were corrected for Galactic extinction (according to Schlafly and Finkbeiner 2011) and for extinction in the host galaxy (if known) of the correspondent optical filter. Lastly, the de-reddened magnitudes were converted into flux densities. Table 6.1 lists, for each GRB, the time-intervals over which the analysis has been performed, the optical filter, the flux density, whether the extinction has been estimated only for the Galaxy (G) or also for the host galaxy (HG), and the reference.

TABLE 6.1: For the optical data I list the estimate of flux in the time interval of the fit (F_{opt}) and the optical filter, information about Galactic (G) or intrinsic (HG) absorption correction applied, and the reference to literature.

Time interval s	F_{opt} mJy	Filter	Ext.	Ref.
GRB 060510B				
$180.00 - 210.00$	0.03952 ± 0.01591	R	G	Melandri et al. (2008)
GRB 060814				
$123.00 - 213.00$	< 0.4297	r	G	Klotz, Boer, and Atteia (2006)
GRB 061121				
$63.99 - 68.83$	0.2797 ± 0.0361	White	G+HG	Page et al. (2007)
$68.83 - 71.89$	0.5547 ± 0.0707			
$71.89 - 74.89$	0.5748 ± 0.0728			
$74.90 - 76.96$	1.041 ± 0.1539			
$76.96 - 79.00$	1.0370 ± 0.1547			
$79.00 - 81.54$	0.7476 ± 0.09889			
$81.54 - 84.68$	0.5386 ± 0.0675			
$84.68 - 89.68$	0.2613 ± 0.03461			
$89.69 - 95.79$	0.1961 ± 0.02681			
GRB 070616				

TABLE 6.1: continued.

Time interval s	F_{opt} mJy	Filter	Ext.	Ref.
250.30 – 385.30	0.3112 ± 0.105	V	G	Starling et al. (2008)
385.40 – 448.00	1.4597 ± 0.154			
448.20 – 509.60	1.7352 ± 0.155			
509.70 – 572.10	1.5534 ± 0.155			
572.30 – 631.50	2.3411 ± 0.160			
GRB 080928				
199.00 – 219.00	0.05755 ± 0.01337	White	G+HG	Rossi et al. (2011)
219.00 – 239.00	0.0780 ± 0.0152			
239.00 – 259.00	0.0991 ± 0.0156			
259.00 – 278.70	0.0453 ± 0.0131			
GRB 081008				
104.81 – 109.81	0.8832	r	G+HG	Yuan et al. (2010)
113.34 – 118.34	1.2598			
120.96 – 125.96	1.7969			
127.41 – 132.41	2.2769			
GRB 090715B				
53.10 – 200.10	0.0266 ± 0.0037	White	G	Vetere et al. (2009)
GRB 100906A				
116.30 – 136.30	22.3 ± 2.057	R	G+HG	Gorbovskoy et al. (2012)
GRB 110102A				
156.00 – 303.00	0.1496 ± 0.0083	White	G	Oates and de Pasquale (2011)
GRB 110119A				
67.00 – 214.00	0.6121 ± 0.0169	White	G	Pritchard and Troja (2011)
GRB 110205A				
163.50 – 168.50	0.0686 ± 0.0218	White	G	Cucchiara et al. (2011)
168.50 – 173.50	0.0581 ± 0.0208			
173.50 – 178.50	0.0620 ± 0.0221			
181.00 – 191.00	0.0745 ± 0.0216			

TABLE 6.1: continued.

Time interval s	F_{opt} mJy	Filter	Ext.	Ref.
198.50 – 203.50	0.0692 ± 0.0227			
203.50 – 208.50	0.0794 ± 0.0230			
208.50 – 213.50	0.2089 ± 0.0329			
213.50 – 218.50	0.1585 ± 0.0279			
218.50 – 223.50	0.1117 ± 0.0260			
223.50 – 228.50	0.0824 ± 0.0223			
228.50 – 233.50	0.0847 ± 0.0237			
234.00 – 248.00	0.0745 ± 0.0223			
251.00 – 281.00	0.0643 ± 0.0217			
	GRB 111103B			
68.00 – 215.00	< 0.0204	White	G	Oates and Grupe (2011)
	GRB 111123A			
110.00 – 257.00	< 0.007178	White	G	Holland and Stamatikos (2011)
	GRB 121123A			
131.00 – 278.00	0.0368 ± 0.0051	White	G	Holland, Helder, and Xu (2012)
	GRB 121217A			
598.50 – 639.50	0.1823 ± 0.0151	H	G	Elliott et al. (2014)
	0.1003 ± 0.0130	K		
	0.1985 ± 0.0238	J		
723.50 – 764.50	0.1926 ± 0.0107	H		
	0.1195 ± 0.0110	K		
	0.2217 ± 0.0184	J		
	GRB 130514A			
106.20 – 166.20	0.2357 ± 0.0437	r	G	Schmidl, Kann, and Greiner (2013)
	GRB 130907A			
266.00 – 306.00	1.069 ± 0.0394	u	G+HG	Veres et al. (2015)
	GRB 140108A			
78.00 – 225.00	0.1141 ± 0.0211	White	G	Breeveld and Racusin (2014)

TABLE 6.1: continued.

Time interval s	F_{opt} mJy	Filter	Ext.	Ref.
		GRB 140206A		
$52.00 - 199.00$	1.178 ± 0.0217	White	G	Oates and Lien (2014)
		GRB 140512A		
$126.00 - 146.00$	24.49 ± 0.203	R	G+HG	Huang et al. (2016)
		GRB 151021A		
$111.90 - 141.90$	5.664 ± 1.049	I	G	Trotter et al. (2015)

6.1.1 The spectral analysis

For some of 21 GRBs in the selected sample, optical observations at different times are available and allowed me to perform time-resolved spectral analysis. For each GRB, I limited the analysis to the temporal window optical observations are available and there is significant signal detected also in XRT and BAT. I identified in total 56 time bins. I performed XRT+BAT spectral analysis in the time-bin simultaneous to the optical observation. I took the estimate of the $N_{\rm H}$ column density from Chapter 4. In order to account for the uncertainty in the inter-calibration between the two instruments, I allow for a 10% discrepancy in the normalization factor of one of the two instruments. Since I want to extrapolate the best fit model down to the optical band and compare with the measured optical flux, different results might be derived depending whether I decide to fix the XRT normalization and allow for uncertainties in the BAT normalization or the opposite. I then fixed first the normalization of XRT and allowed for a 10% variation in the normalization of BAT, and then repeated the spectral analysis by fixing BAT and allowing for a 10% variation in XRT. When GBM observations are also available, I included them in the joint spectral fitting, considering a possible 10% uncertainty in the calibration of the GBM as compared to Swift instruments.

I modeled the spectra both with a synchrotron model and with a two-component model (a cutoff-PL plus a BB). Since a synchrotron model is not available in XSPEC, I added the possibility to fit synchrotron spectra as a table model. Synchrotron table models have been built as described in the following section.

6.1.2 The synchrotron model

Population of emitting electrons accelerated into a PL energy distribution is considered with spectral index p and cooling via synchrotron radiation. In case of fast cooling regime, the distribution starts at γ_c and breaks at $\gamma_m > \gamma_c$. In the opposite case, the distribution is considered to be $-p$ from γ_m to γ_c and above γ_c steepens to $-p-1$. The synchrotron spectrum is built starting from this simplified electron distribution. The overall shape of the photon spectrum depends on two quantities: the ratio γ_m/γ_c, and p. Several spectra are built by changing the values of γ_m/γ_c from 0.1 to 100, and p from -2 to -3. I then built a table model to include the synchrotron model in XSPEC.

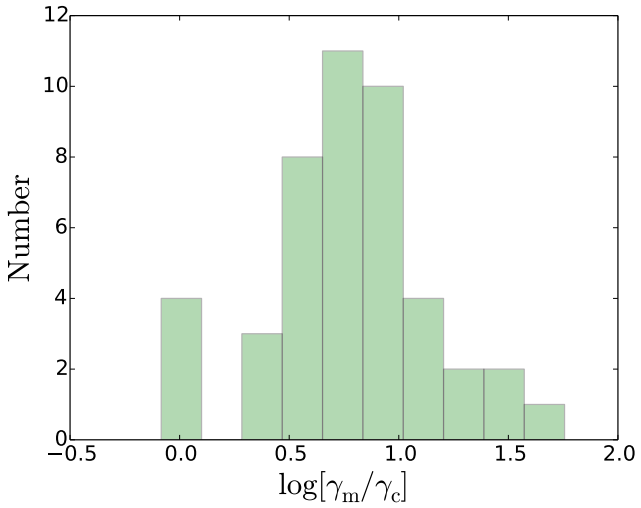

FIGURE 6.1: Distribution of $\log[\gamma_m/\gamma_c]$ found by the joint XRT+BAT+(GBM) spectral fitting by the synchrotron model.

6.2 Results

The results of the spectral analysis are shown in Section 6.4 for each of the 56 time-resolved spectra from the 21 GRBs in the sample. The upper panel shows the lightcurves: XRT (red), BAT (green), GBM (blue, only if available) and optical (black data points). The other panels show the results of the spectral analysis: synchrotron fits are shown in the left-hand panels, while CPL+BB fits are in the right-hand panels. Different rows of panels, for the same GRB, refer to different time-bins. The name of the GRB and the time bin are reported in the title of each panel. The best fit parameters are reported in Table 6.2. The distribution of γ_m/γ_c is shown in Figure 6.1. The mean value for $\log[\gamma_m/\gamma_c]$ and its dispersion are 0.78 and 0.38 suggesting a typical value of $\gamma_m/\gamma_c \sim 6$.

Few GRBs contain rich early optical data. This allows to draw more detailed conclusions about the origin of the prompt optical emission. For two GRBs (GRB 061121 and GRB 110205A) the optical light curves track the prompt emission observed by BAT. The extrapolation from the synchrotron model is consistent with the

optical fluxes from these GRBs. For four GRBs (GRB 070616, GRB 081008, GRB 100906A, GRB 121217A) the prompt optical emission is dominated by the afterglow radiation and the synchrotron model under-predicts the optical flux. Remaining 15 GRBs have poor optical data represented by a single exposure during the prompt phase. For this subsample of 15 GRBs the synchrotron model over/under-predicts the optical fluxes or it is consistent with it. The overall analysis shows that in half of the cases the optical data is consistent with the synchrotron model. Instead, the two-component modeling (CPL plus BB) over-predicts the optical fluxes in most of the cases.

TABLE 6.2: Best-fit parameters of the synchrotron model for the time resolved spectra. The table lists the time interval (since the BAT trigger time), the best fit parameters (cooling energy E_c, ratio γ_m/γ_c, normalisation N, total chi-square χ^2 and degrees of freedom (d.o.f.). The power-law index of the injected electron spectrum p, defined as $dN_{inj}/d\gamma \propto \gamma^{-p}$, is fixed to 2.6).

Time interval s	E_c keV	γ_m/γ_c	N 10^{-2}	χ^2 (d.o.f.)
GRB 060510B				
$180.00 - 210.00$	$2.5^{+0.5}_{-0.4}$	$4.8^{+1.8}_{-1.7}$	$0.65^{+0.14}_{-0.03}$	188 (196)
GRB 060814				
$123.00 - 213.00$	< 0.2	$29.3^{+4.2}_{-11.9}$	$3.34^{+0.07}_{-0.70}$	292 (298)
GRB 061121				
$63.99 - 68.83$	$14.3^{+3.5}_{-4.2}$	> 20.8	$4.99^{+0.93}_{-0.38}$	113 (87)
$68.83 - 71.89$	$10.7^{+2.8}_{-3.6}$	$6.3^{+4.0}_{-1.5}$	$8.06^{+1.78}_{-0.78}$	76 (67)
$71.89 - 74.89$	$24.1^{+3.4}_{-3.6}$	> 13.5	$10.72^{+0.64}_{-0.59}$	83 (74)
$74.90 - 76.96$	$32.7^{+5.0}_{-5.0}$	> 6.6	$8.08^{+0.41}_{-0.60}$	69 (68)
$76.96 - 79.00$	$3.6^{+2.0}_{-1.7}$	> 9.1	$5.79^{+2.26}_{-1.14}$	69 (61)
$79.00 - 81.54$	< 1.6	$12.1^{+38.8}_{-5.3}$	$6.79^{+13.62}_{-2.06}$	61 (68)
$81.54 - 84.68$	< 1.1	$13.9^{+34.5}_{-6.0}$	$4.56^{+7.89}_{-1.07}$	80 (79)
$84.68 - 89.68$	$1.1^{+0.9}_{-0.7}$	$8.3^{+9.3}_{-3.6}$	$2.30^{+1.35}_{-0.47}$	74 (80)
$89.69 - 95.79$	< 1.6	$31.8^{+21.5}_{-25.3}$	$8.62^{+1.02}_{-8.62}$	102 (86)
GRB 070616				
$250.30 - 385.30$	$3.5^{+0.7}_{-0.3}$	$9.6^{+3.3}_{-2.0}$	$1.14^{+0.04}_{-0.11}$	304 (301)
$385.40 - 448.00$	$2.7^{+0.4}_{-0.4}$	$6.8^{+2.2}_{-1.1}$	$1.03^{+0.03}_{-0.07}$	223 (241)
$448.20 - 509.60$	$1.8^{+0.4}_{-0.3}$	$4.4^{+1.0}_{-0.9}$	$1.17^{+0.15}_{-0.07}$	150 (186)
$509.70 - 572.10$	$0.9^{+0.3}_{-0.3}$	$3.7^{+1.9}_{-0.8}$	$1.35^{+0.19}_{-0.25}$	234 (234)
$572.30 - 631.50$	< 0.3	$8.6^{+1.8}_{-3.5}$	$3.50^{+0.41}_{-1.43}$	260 (226)

TABLE 6.2: continued.

Time interval s	E_c keV	γ_m/γ_c	N 10^{-2}	χ^2 (d.o.f.)
GRB 080928				
$199.00 - 219.00$	$2.5^{+0.6}_{-0.5}$	$3.9^{+1.1}_{-0.8}$	$2.23^{+0.13}_{-0.07}$	137 (137)
$219.00 - 239.00$	$1.3^{+0.4}_{-0.3}$	$3.0^{+2.0}_{-0.8}$	$1.60^{+0.16}_{-0.11}$	127 (143)
$239.00 - 259.00$	< 0.4	$10.9^{+7.7}_{-5.8}$	$2.87^{+0.15}_{-1.47}$	114 (108)
$259.00 - 278.70$	< 0.2	$10.1^{+4.7}_{-4.8}$	$2.11^{+0.24}_{-1.03}$	120 (122)
GRB 081008				
$104.81 - 109.81$	$11.6^{+43.4}_{-6.8}$	$0.9^{+1.6}_{-0.5}$	$1.07^{+0.31}_{-0.09}$	81 (72)
$113.34 - 118.34$	$2.7^{+2.0}_{-0.6}$	$7.6^{+10.5}_{-3.3}$	$1.59^{+0.17}_{-0.40}$	57 (73)
$120.96 - 125.96$	$6.8^{+25.5}_{-4.6}$	$0.8^{+2.1}_{-0.6}$	$1.39^{+0.37}_{-0.18}$	68 (74)
$127.41 - 132.41$	$2.8^{+3.4}_{-1.6}$	$1.1^{+1.4}_{-0.7}$	$1.35^{+0.55}_{-0.14}$	74 (92)
GRB 090715B				
$53.10 - 200.10$	< 0.2	$18.7^{+3.2}_{-2.1}$	$2.29^{+0.18}_{-0.75}$	363 (329)
GRB 100906A				
$116.30 - 136.30$	$1.7^{+1.6}_{-0.3}$	$1.0^{+0.4}_{-0.3}$	$9.79^{+1.20}_{-1.11}$	250 (178)
GRB 110102A				
$156.00 - 303.00$	$1.9^{+0.1}_{-0.1}$	> 57.1	$1.83^{+0.04}_{-0.04}$	425 (305)
GRB 110119A				
$67.00 - 214.00$	$1.8^{+0.2}_{-0.2}$	$6.6^{+1.3}_{-0.9}$	$0.57^{+0.02}_{-0.01}$	421 (475)
GRB 110205A				
$163.50 - 168.50$	$4.9^{+2.8}_{-1.2}$	$3.3^{+1.8}_{-1.1}$	$1.69^{+0.18}_{-0.13}$	82 (78)
$168.50 - 173.50$	$10.4^{+37.0}_{-3.6}$	$2.4^{+1.6}_{-1.5}$	$1.33^{+0.09}_{-0.10}$	76 (78)
$173.50 - 178.50$	$6.2^{+2.6}_{-1.6}$	$2.4^{+1.3}_{-1.0}$	$1.69^{+0.25}_{-0.13}$	102 (77)
$181.00 - 191.00$	$5.6^{+1.6}_{-1.1}$	$2.6^{+0.9}_{-0.8}$	$1.64^{+0.12}_{-0.09}$	120 (106)
$198.50 - 203.50$	$4.7^{+1.3}_{-1.1}$	$4.8^{+2.8}_{-1.5}$	$1.86^{+0.22}_{-0.14}$	83 (77)
$203.50 - 208.50$	$5.6^{+1.3}_{-1.2}$	> 5.8	$2.04^{+0.24}_{-0.15}$	83 (79)
$208.50 - 213.50$	$9.9^{+2.4}_{-3.3}$	> 7.6	$2.01^{+0.15}_{-0.17}$	74 (77)
$213.50 - 218.50$	$7.7^{+5.0}_{-1.1}$	$5.2^{+4.4}_{-2.2}$	$1.79^{+0.15}_{-0.36}$	88 (75)
$218.50 - 223.50$	$6.1^{+1.5}_{-1.7}$	$4.9^{+2.8}_{-1.5}$	$2.02^{+0.36}_{-0.16}$	87 (76)

TABLE 6.2: continued.

Time interval s	E_c keV	γ_m/γ_c	N 10^{-2}	χ^2 (d.o.f.)
$223.50 - 228.50$	$4.5^{+1.4}_{-1.2}$	$5.4^{+4.2}_{-1.9}$	$1.60^{+0.25}_{-0.14}$	89 (75)
$228.50 - 233.50$	$6.0^{+0.8}_{-1.4}$	$3.5^{+0.8}_{-1.2}$	$1.69^{+0.27}_{-0.13}$	85 (77)
$234.00 - 248.00$	$3.5^{+1.0}_{-0.8}$	$3.5^{+1.3}_{-1.0}$	$1.51^{+0.13}_{-0.09}$	128 (101)
$251.00 - 281.00$	$2.0^{+0.6}_{-0.5}$	$3.7^{+1.2}_{-1.0}$	$1.63^{+0.12}_{-0.11}$	143 (117)
GRB 111103B				
$68.00 - 215.00$	$0.4^{+0.1}_{-0.1}$	$9.2^{+2.1}_{-1.5}$	$1.11^{+0.06}_{-0.12}$	194 (167)
GRB 111123A				
$110.00 - 257.00$	$2.3^{+0.2}_{-0.2}$	$6.4^{+1.2}_{-0.9}$	$0.82^{+0.02}_{-0.05}$	283 (310)
GRB 121123A				
$131.00 - 278.00$	$28.8^{+51.7}_{-6.0}$	$1.0^{+0.7}_{-0.4}$	$0.62^{+0.04}_{-0.03}$	231 (242)
GRB 121217A				
$598.50 - 639.50$	$1.9^{+0.6}_{-0.5}$	$8.5^{+10.0}_{-3.9}$	$0.34^{+0.07}_{-0.07}$	143 (134)
$723.50 - 764.50$	$3.6^{+0.6}_{-0.6}$	$8.8^{+5.9}_{-2.4}$	$1.02^{+0.07}_{-0.02}$	204 (180)
GRB 130514A				
$106.20 - 166.20$	$1.5^{+0.3}_{-0.3}$	$4.9^{+1.0}_{-0.7}$	$2.06^{+0.12}_{-0.21}$	188 (179)
GRB 130907A				
$266.00 - 306.00$	$5.5^{+1.6}_{-1.4}$	$0.4^{+0.1}_{-0.1}$	$7.06^{+1.51}_{-0.86}$	211 (199)
GRB 140108A				
$78.00 - 225.00$	$10.3^{+0.9}_{-0.8}$	$40.6^{+0.0}_{-0.0}$	$0.34^{+0.01}_{-0.01}$	428 (436)
GRB 140206A				
$52.00 - 199.00$	$9.1^{+0.9}_{-2.2}$	> 23.9	$1.15^{+0.17}_{-0.04}$	87 (101)
GRB 140512A				
$126.00 - 146.00$	$10.3^{+0.9}_{-1.4}$	$16.1^{+11.8}_{-5.1}$	$1.65^{+0.12}_{-0.05}$	268 (233)

TABLE 6.2: continued.

Time interval s	E_c keV	γ_m/γ_c	N 10^{-2}	χ^2 (d.o.f.)
GRB 151021A				
$111.90 - 141.90$	$1.0^{+1.0}_{-0.4}$	$1.9^{+1.4}_{-1.0}$	$2.94^{+0.24}_{-0.59}$	150 (164)

6.2.1 Constrains on the emitting region

The best fit values of the synchrotron model are used to put constrains on the emitting region of GRBs in prompt phase. The measured cooling energy E_c can be expressed in the following way:

$$E_c = \frac{3qh}{4\pi mc}\left(\frac{1}{1+z}\right)\Gamma B'\gamma_c^2 \tag{6.1}$$

where z is the redshift, q and m are the charge and the mass of electron, Γ is the bulk Lorentz factor, B' is the magnetic field strength in the comoving frame and γ_c is the Lorentz factor down to which electrons cool.

The characteristic observed variability time scale can be linked to the cooling time of the electrons. The energy loss time of an electron with a Lorentz factor γ in observed frame is

$$t_c = \frac{\gamma mc^2}{P'_{syn}}\frac{1+z}{\Gamma} = \frac{6\pi mc}{\sigma_T \gamma B'^2}\frac{1+z}{\Gamma} \tag{6.2}$$

where $P'_{syn} = \sigma_T c\gamma^2 B'^2/6\pi$ is the synchrotron power. If one associates t_c with the typical observed variability time scale, constrains on the $B' - \Gamma$ can be obtained by combining 6.1 and 6.2:

$$B' = \left(\frac{27\pi qmhc(1+z)}{\sigma_T^2 t_c^2 E_c \Gamma}\right)^{1/3} \tag{6.3}$$

I use E_c from the best fits to constrain the allowed lines in $\Gamma - B'$ parameter space (Figure 6.2). I fix t_c to 1 s and I use z=2 for GRBs without measured redshifts.

6.3 Summary

In this Chapter, I performed a direct test of the synchrotron model on joint X- and γ-ray prompt emission spectra in the range 0.5 keV- 150 keV (40 MeV). Most of the spectra are well fitted with the synchrotron model of radiation in moderately fast cooling regime. The average ratio γ_m/γ_c is 6. Cooling frequencies estimated by the synchrotron fits have allowed me to put constrains on the magnetic field in the jet if one-shot acceleration of electrons is assumed (Figure 6.2). For the range of bulk Lorentz factors of $\Gamma \sim 10^2 - 10^3$ the magnetic field in the comoving frame is B' $\sim 10 - 100$ G.

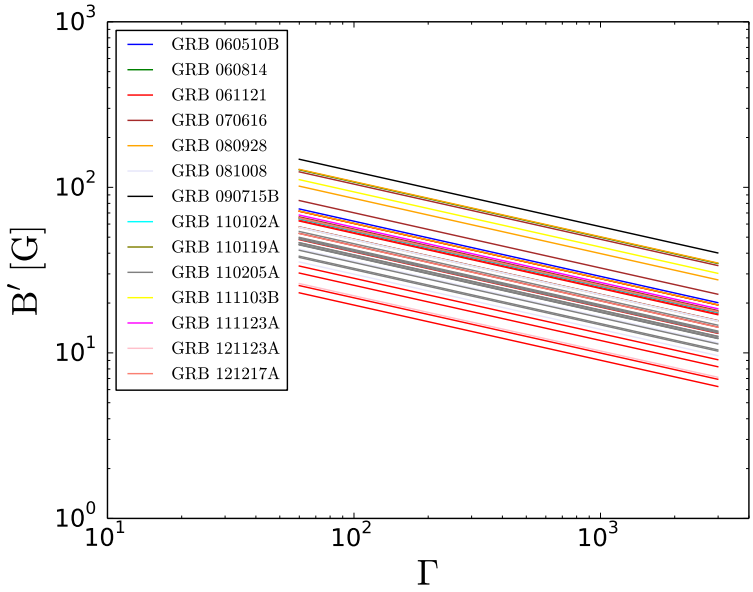

FIGURE 6.2: Allowed lines in $\Gamma - B'$ parameter space estimated in the synchrotron scenario with one-shot acceleration of electrons.

The prompt optical data is crucial to test the synchrotron radiation model. However, the early optical radiation can be contaminated by the afterglow. I compare the prediction of the synchrotron model in the optical band with the data available for 56 spectra from 21 GRBs. This comparison returns three cases. In half of the cases the optical data is consistent with the synchrotron model. For the remaining cases the predicted optical flux is over- or under-estimated. An additional emission component such as afterglow can explain the optical fluxes under-estimated by the model of the prompt emission since the prompt radiation pulses are present prior to the detected optical component. The over-estimated optical flux can be caused by an unaccounted intrinsic absorption. Two-component model (CPL plus BB) over-predicts the optical fluxes in most of the cases. Therefore, the single component model (synchrotron radiation) is preferred.

The full implication of the preliminary results discussed in this Chapter will be presented in G. Oganesyan, L. Nava, A. Melandri, G. Ghirlanda, A. Celotti, *Prompt optical emission as signature of synchrotron radiation in Gamma-Ray Bursts*, in preparation.

6.4 Lightcurves and Spectra

In this section, I report the lightcurve and the time-resolved spectra for each GRB in the sample. Spectra are fitted with the synchrotron and CPL+BB models. The optical point is not considered during the fitting procedure, and is added in the figure to test its consistency with predictions from the fit of X-ray data.

GRB 060510B

FIGURE 6.3: Light curve (left-hand panel) and spectrum (right-hand panel) of GRB 060510B. Green symbols are used for BAT data, black for optical and red for XRT. The joint νF_ν spectrum (XRT+BAT) is fitted with the synchrotron and CPL+BB models. The best fit contour regions of synchrotron model are showed in orange: light orange is used for model derived when the calibration constant in fixed on BAT data, and dark orange when it is fixed on XRT data. The CPL+BB model is shown in red. The shaded gray region is the time interval where the spectrum has been extracted.

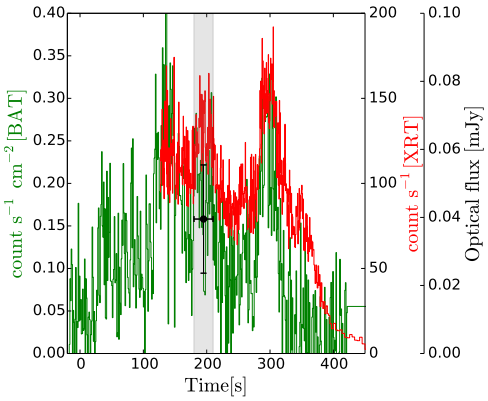

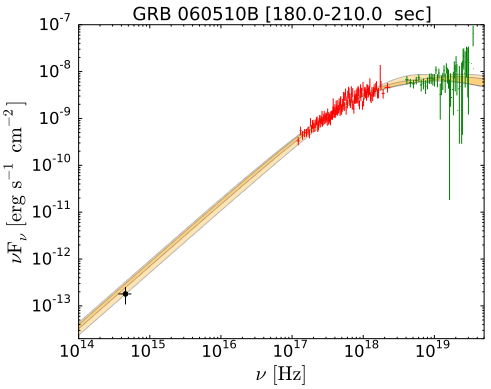

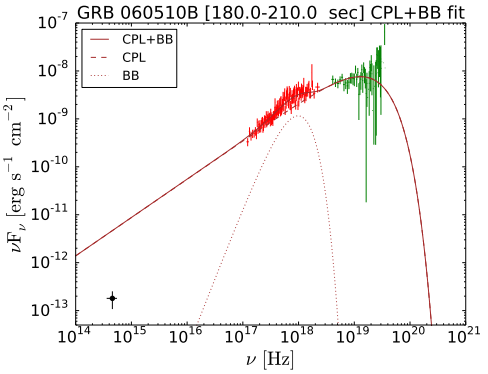

GRB 060814

FIGURE 6.4: Light curve (left-hand panel) and spectrum (right-hand panel) of GRB 060814. Green symbols are used for BAT data, black for optical and red for XRT. The joint νF_ν spectrum (XRT+BAT) is fitted with the synchrotron and CPL+BB models. The best fit contour regions of the synchrotron model are showed in orange: light orange is used for model derived when the calibration constant in fixed on BAT data, and dark orange when it is fixed on XRT data. Only an upper limit can be inferred for the value of the cooling energy, as shown by the orange arrow. The CPL+BB model is shown in red. The shaded gray region is the time interval where the spectrum has been extracted.

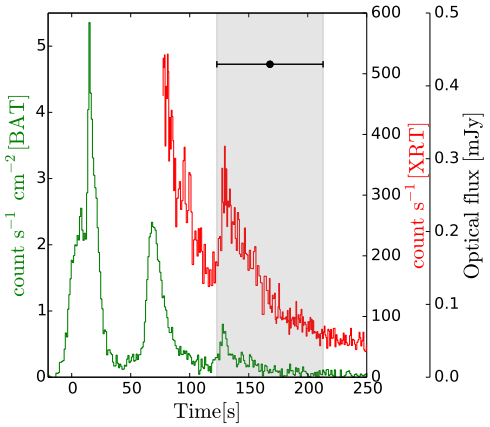

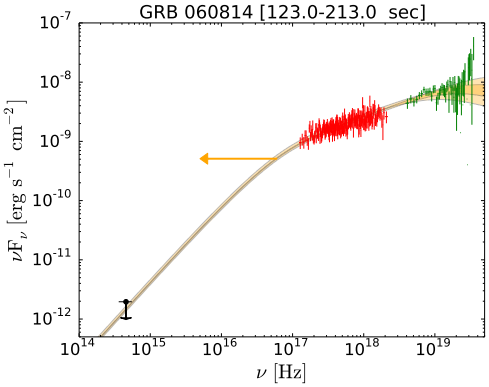

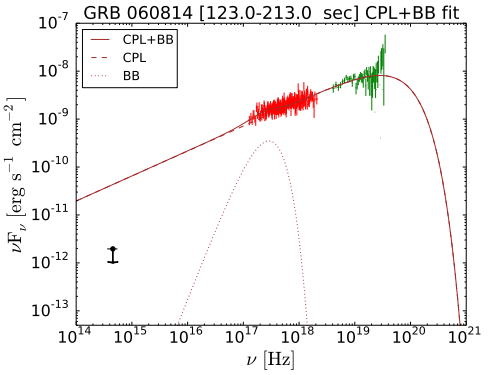

GRB 061121

FIGURE 6.5: Light curve (upper panel) and time-resolved spectra of GRB 061121. Green symbols are used for BAT data, black for optical and red for XRT. The joint νF_ν spectra (XRT+BAT) are fitted with the synchrotron and CPL+BB models. The best fit contour regions of the synchrotron model are showed in orange: light orange is used for model derived when the calibration constant in fixed on BAT data, and dark orange when it is fixed on XRT data. When an upper limit can be inferred for the value of the cooling energy the orange arrow is drawn. The CPL+BB model is shown in red. The shaded gray region is the time interval where the spectrum has been extracted.

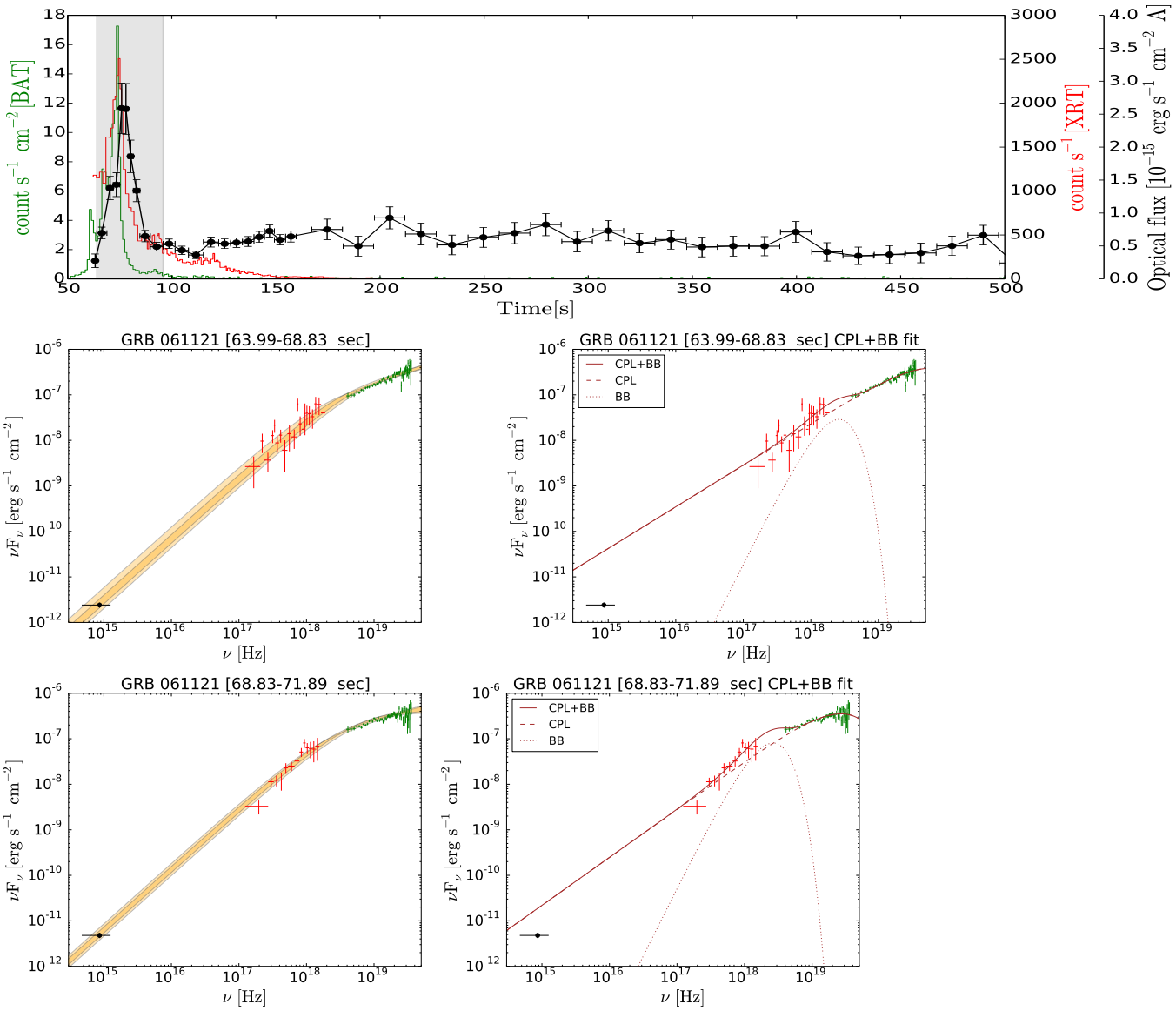

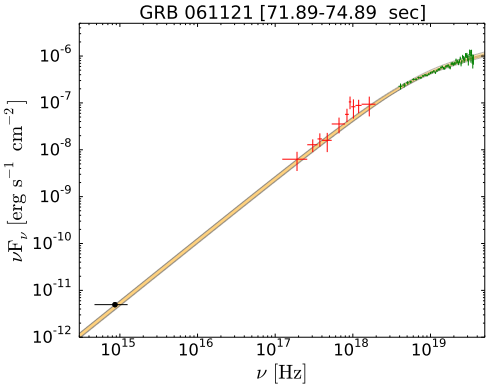
GRB 061121 [71.89-74.89 sec]
νF_ν [erg s^{-1} cm^{-2}]
ν [Hz]

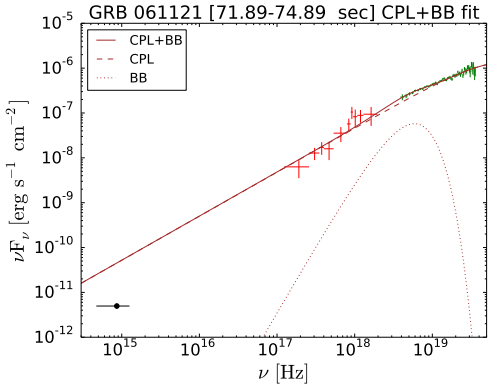
GRB 061121 [71.89-74.89 sec] CPL+BB fit
CPL+BB
CPL
BB
νF_ν [erg s^{-1} cm^{-2}]
ν [Hz]

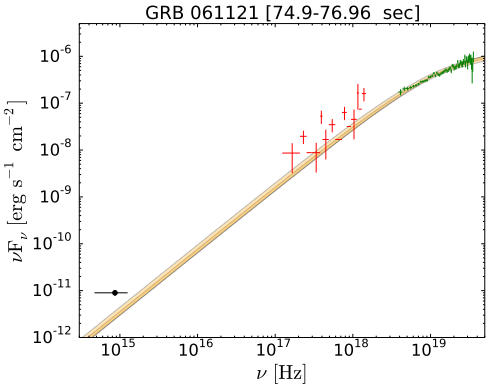
GRB 061121 [74.9-76.96 sec]
νF_ν [erg s^{-1} cm^{-2}]
ν [Hz]

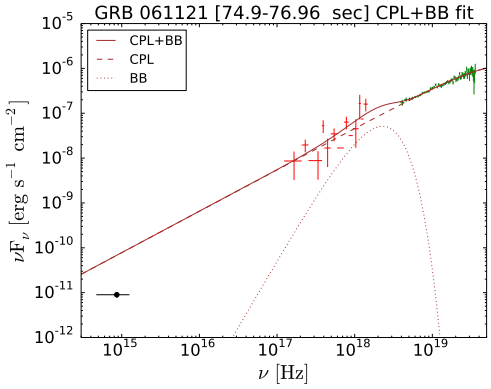
GRB 061121 [74.9-76.96 sec] CPL+BB fit
CPL+BB
CPL
BB
νF_ν [erg s^{-1} cm^{-2}]
ν [Hz]

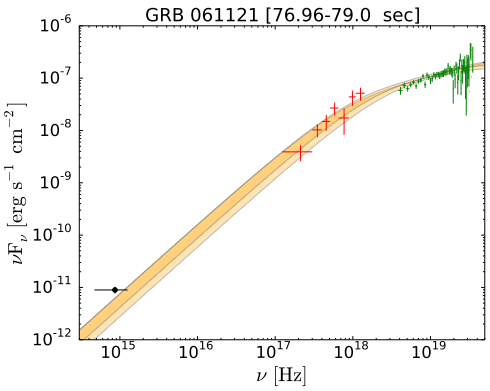
GRB 061121 [76.96-79.0 sec]
νF_ν [erg s^{-1} cm^{-2}]
ν [Hz]

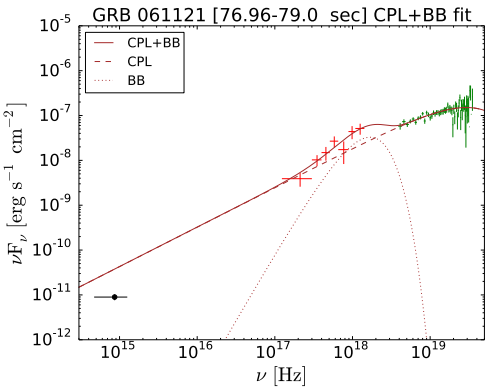
GRB 061121 [76.96-79.0 sec] CPL+BB fit
CPL+BB
CPL
BB
νF_ν [erg s^{-1} cm^{-2}]
ν [Hz]

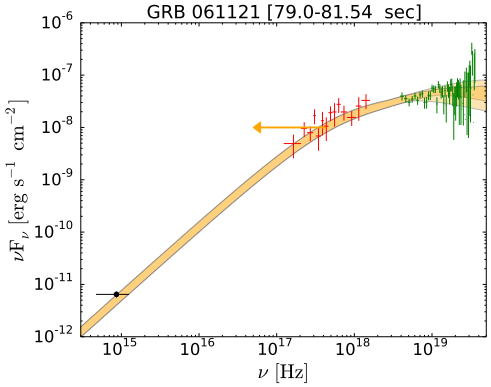
GRB 061121 [79.0-81.54 sec]
νF_ν [erg s^{-1} cm^{-2}]
ν [Hz]

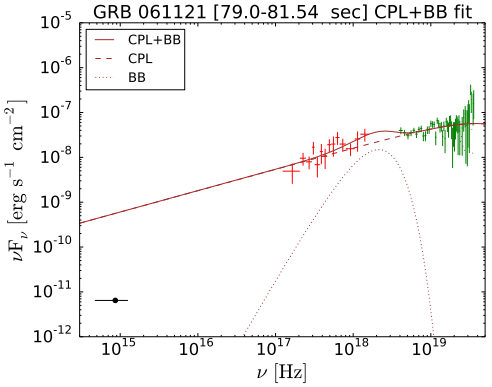
GRB 061121 [79.0-81.54 sec] CPL+BB fit
CPL+BB
CPL
BB
νF_ν [erg s^{-1} cm^{-2}]
ν [Hz]

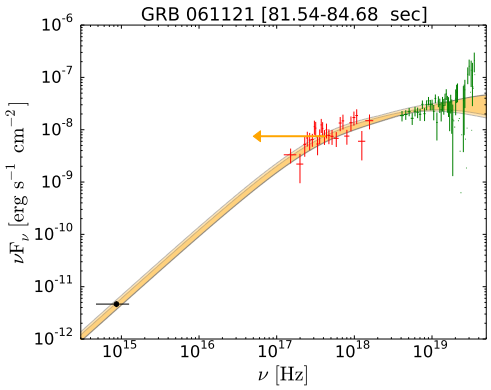
GRB 061121 [81.54-84.68 sec]
νF_ν [erg s^{-1} cm^{-2}]
ν [Hz]

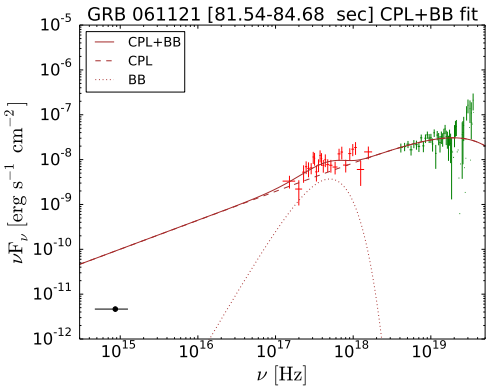
GRB 061121 [81.54-84.68 sec] CPL+BB fit
CPL+BB
CPL
BB
νF_ν [erg s^{-1} cm^{-2}]
ν [Hz]

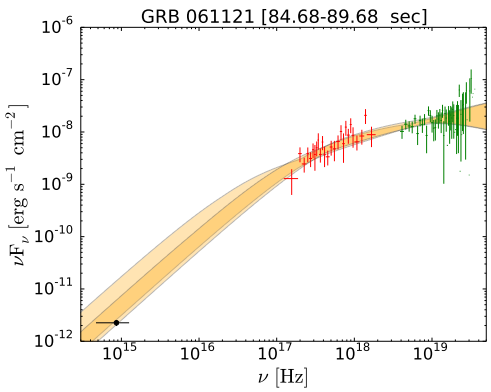
GRB 061121 [84.68-89.68 sec]
νF_ν [erg s^{-1} cm^{-2}]
ν [Hz]

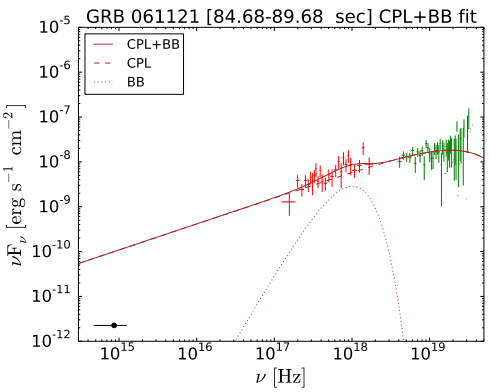
GRB 061121 [84.68-89.68 sec] CPL+BB fit
CPL+BB
CPL
BB
νF_ν [erg s^{-1} cm^{-2}]
ν [Hz]

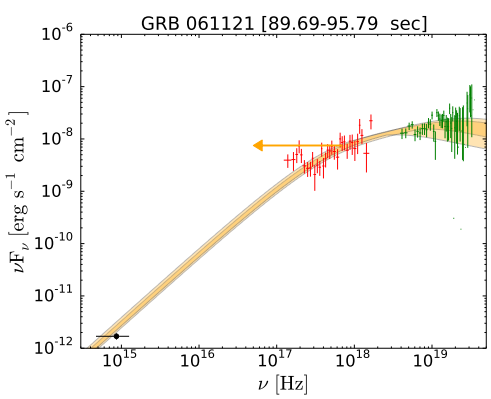
GRB 061121 [89.69-95.79 sec]
νF_ν [erg s^{-1} cm^{-2}]
ν [Hz]

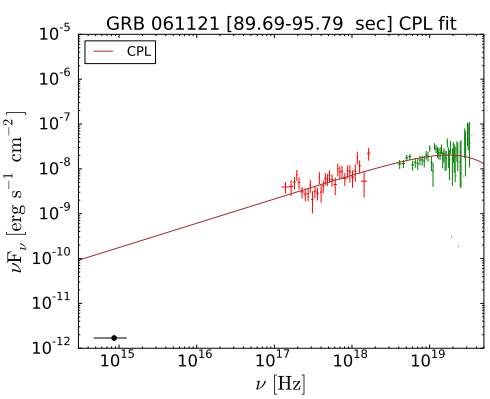
GRB 061121 [89.69-95.79 sec] CPL fit
CPL
νF_ν [erg s^{-1} cm^{-2}]
ν [Hz]

GRB 070616

FIGURE 6.6: Light curve (upper panel) and time-resolved spectra of GRB 070616. Green symbols are used for BAT data, black for optical and red for XRT. The joint νF_ν spectra (XRT+BAT) are fitted with the synchrotron and CPL+BB models. The best fit contour regions of the synchrotron model are showed in orange: light orange is used for model derived when the calibration constant in fixed on BAT data, and dark orange when it is fixed on XRT data. When an upper limit can be inferred for the value of the cooling energy the orange arrow is drawn. The CPL+BB model is shown in red. The shaded gray region is the time interval where the spectrum has been extracted.

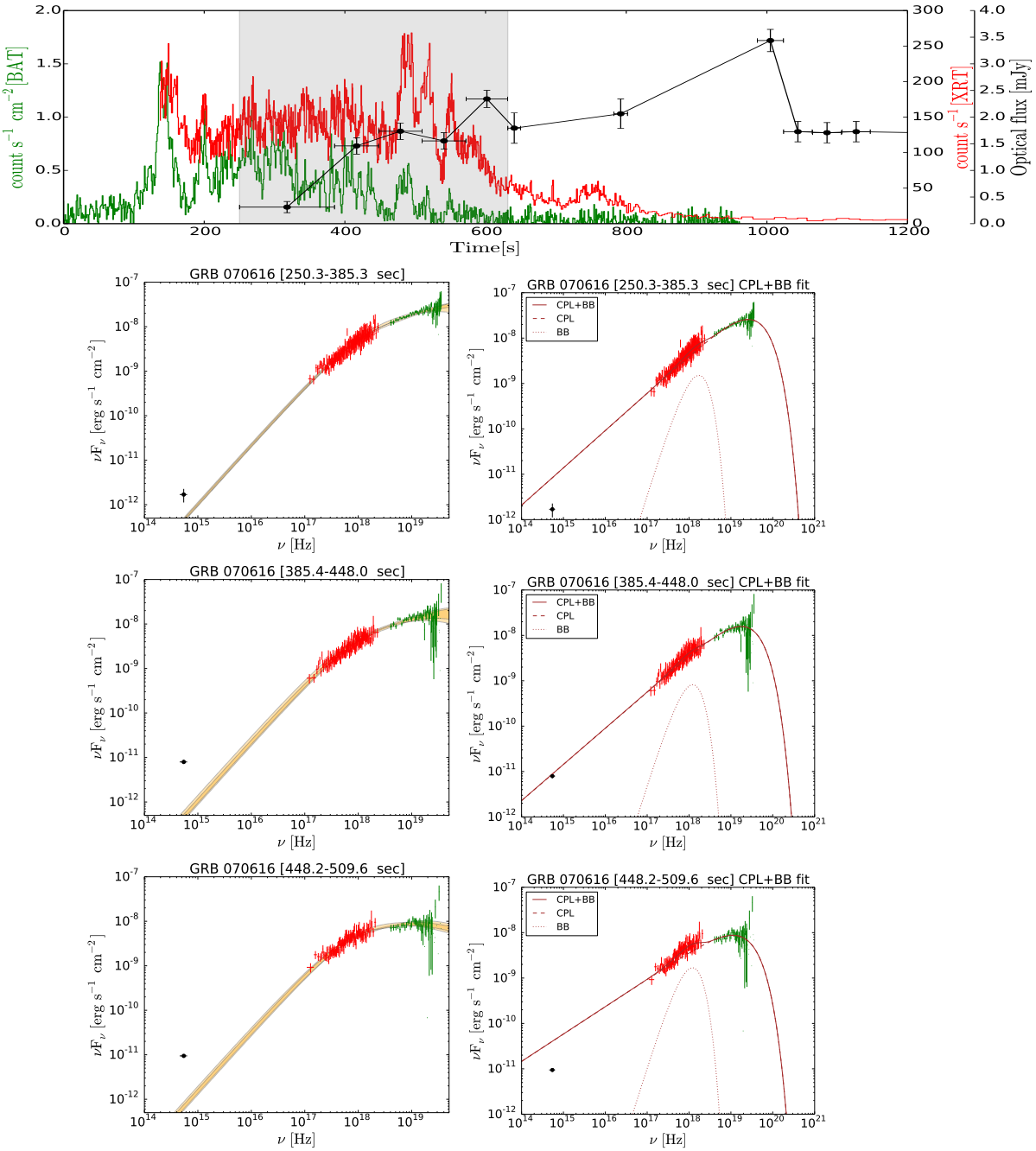

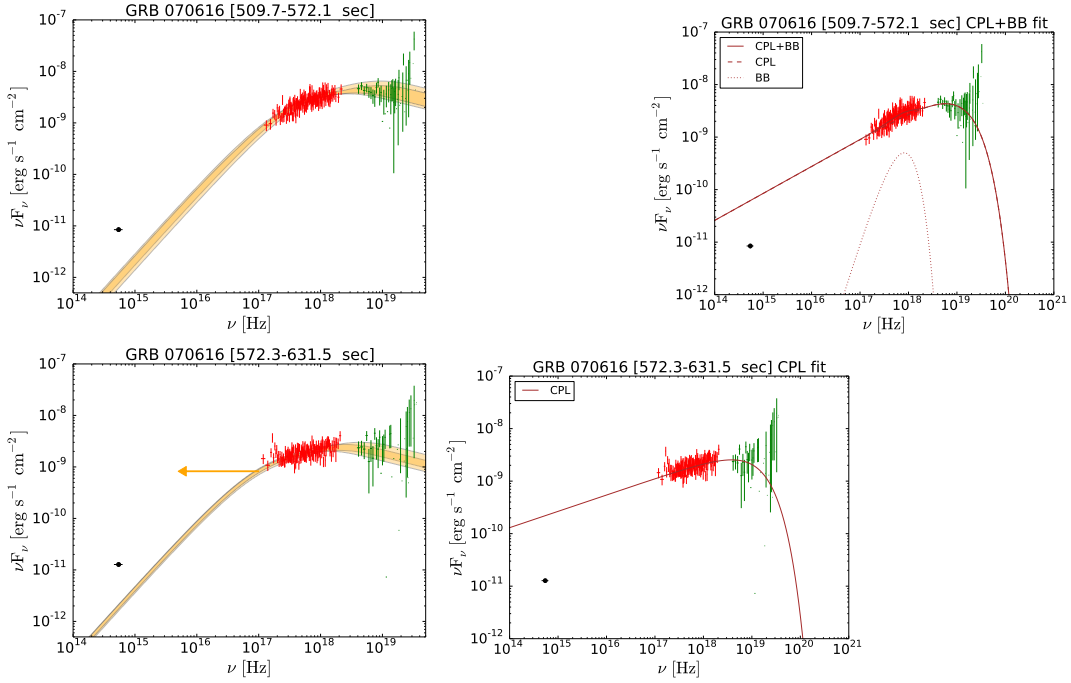
GRB 070616 [509.7-572.1 sec]
GRB 070616 [509.7-572.1 sec] CPL+BB fit
CPL+BB
CPL
BB
GRB 070616 [572.3-631.5 sec]
GRB 070616 [572.3-631.5 sec] CPL fit
CPL
ν [Hz]
νF_ν [erg s^{-1} cm^{-2}]

GRB 080928

FIGURE 6.7: Light curve (upper panel) and time-resolved spectra of GRB 080928. Green symbols are used for BAT data, black for optical and red for XRT. The joint νF_ν spectra (XRT+BAT) are fitted with the synchrotron and CPL+BB models. The best fit contour regions of the synchrotron model are showed in orange: light orange is used for model derived when the calibration constant in fixed on BAT data, and dark orange when it is fixed on XRT data. When an upper limit can be inferred for the value of the cooling energy the orange arrow is drawn. The CPL+BB model is shown in red. The shaded gray region is the time interval where the spectrum has been extracted.

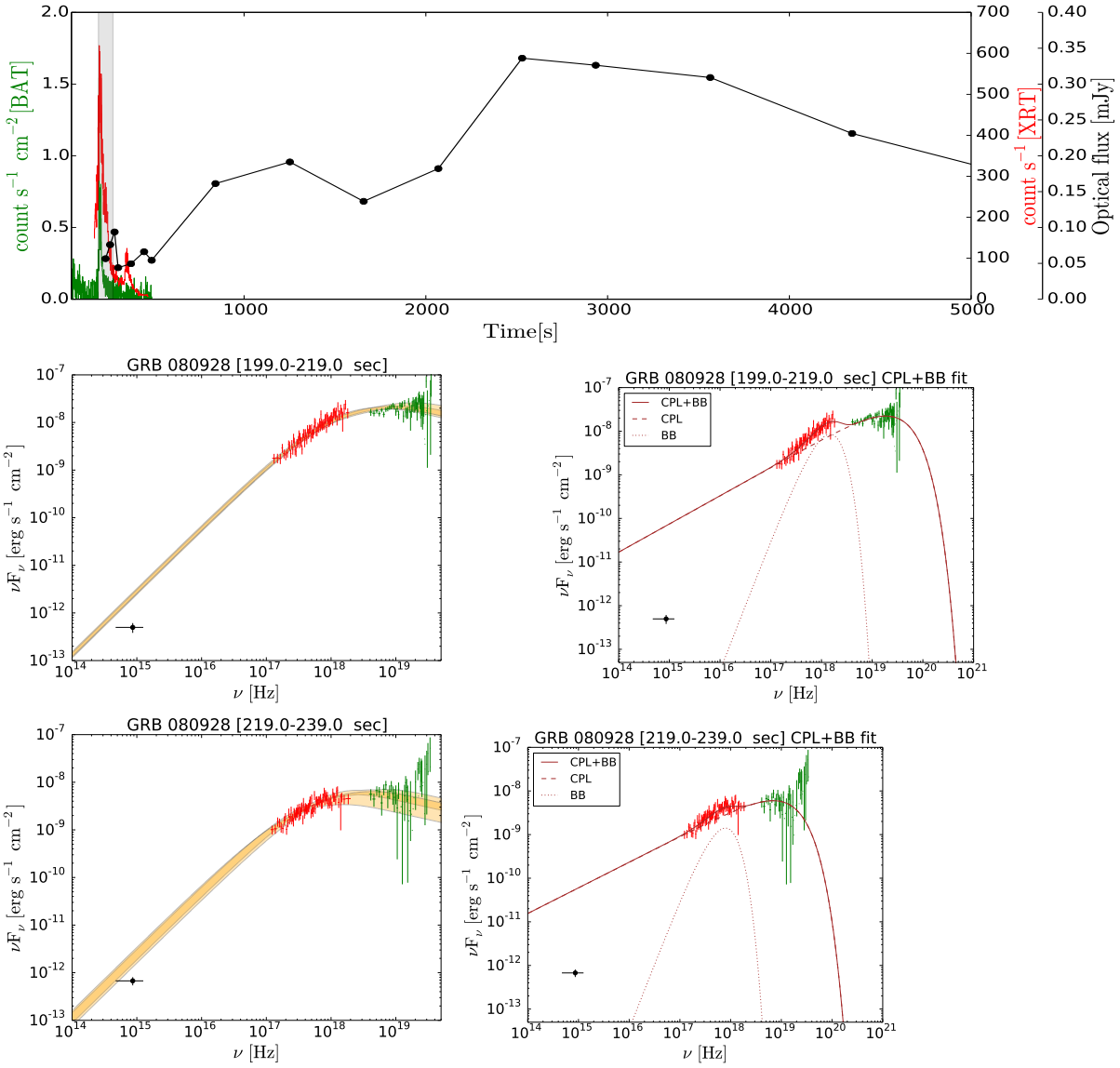

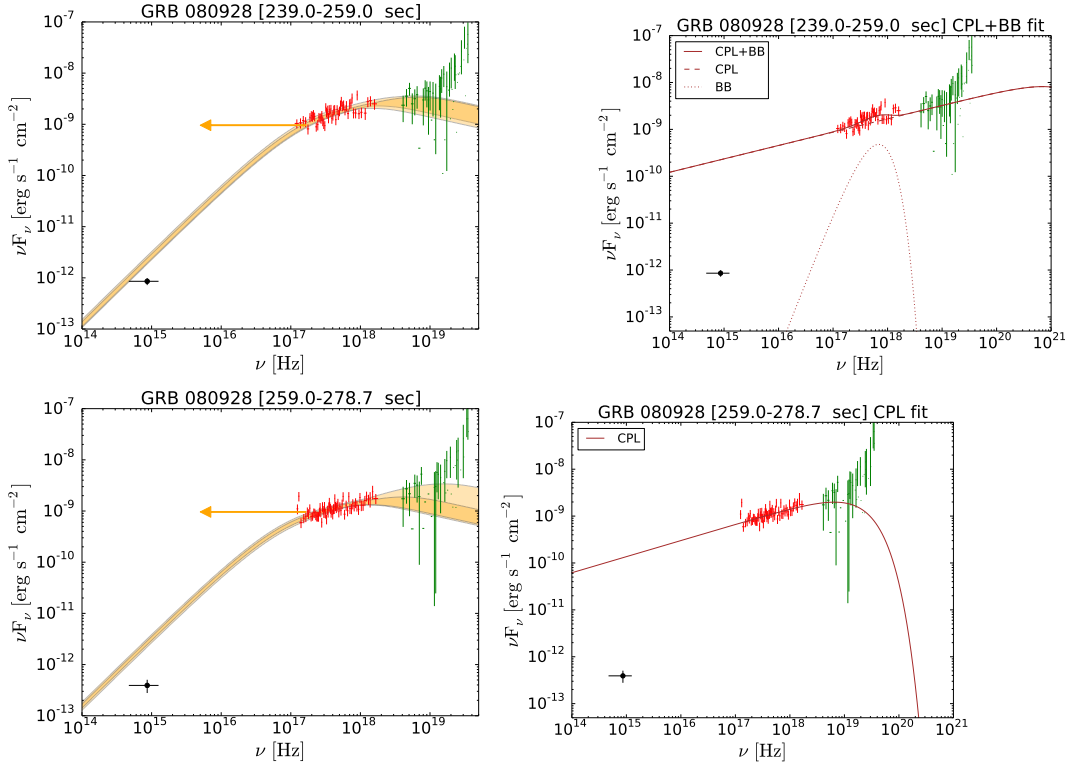
GRB 080928 [239.0-259.0 sec]
GRB 080928 [239.0-259.0 sec] CPL+BB fit
CPL+BB
CPL
BB
GRB 080928 [259.0-278.7 sec]
GRB 080928 [259.0-278.7 sec] CPL fit
CPL
νF_ν [erg s^{-1} cm^{-2}]
ν [Hz]

GRB 081008

FIGURE 6.8: Light curve (upper panel) and time-resolved spectra of GRB 081008. Green symbols are used for BAT data, black for optical and red for XRT. The joint νF_ν spectra (XRT+BAT) are fitted with the synchrotron and CPL+BB models. The best fit contour regions of the synchrotron model are showed in orange: light orange is used for model derived when the calibration constant in fixed on BAT data, and dark orange when it is fixed on XRT data. The CPL+BB model is shown in red. The shaded gray region is the time interval where the spectrum has been extracted.

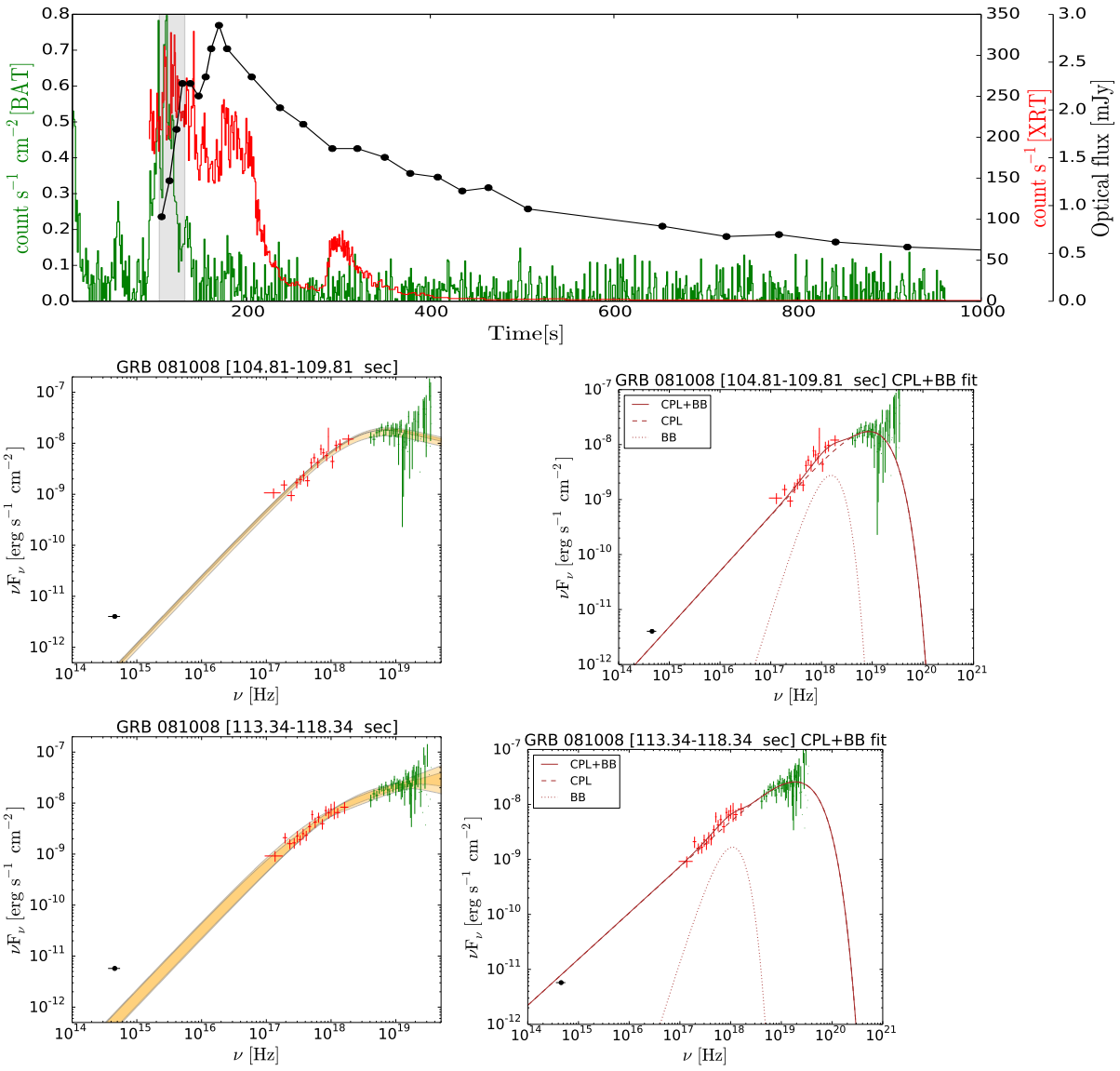

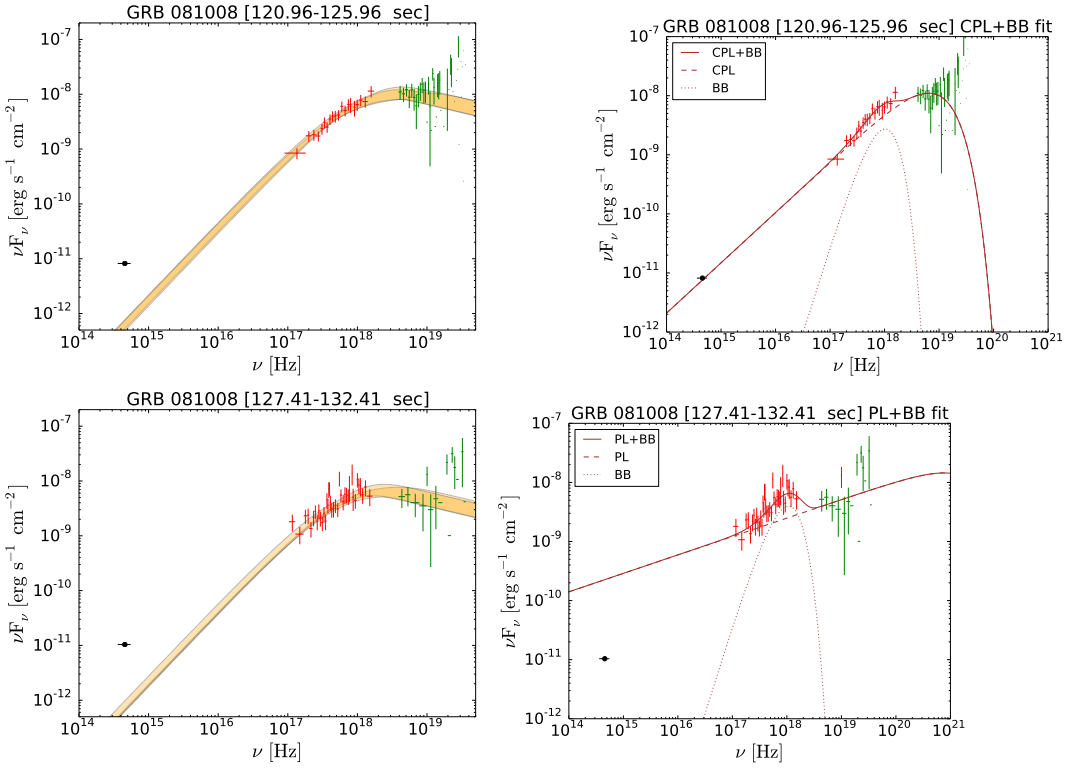
GRB 081008 [120.96-125.96 sec]
GRB 081008 [120.96-125.96 sec] CPL+BB fit
CPL+BB
CPL
BB
GRB 081008 [127.41-132.41 sec]
GRB 081008 [127.41-132.41 sec] PL+BB fit
PL+BB
PL
BB
νF_ν [erg s^{-1} cm^{-2}]
ν [Hz]

GRB 090715B

FIGURE 6.9: Light curve (left-hand panel) and spectrum (right-hand panel) of GRB 090715B. Green symbols are used for BAT data, black for optical and red for XRT. The joint νF_ν spectrum (XRT+BAT) is fitted with the synchrotron and CPL+BB models. The best fit contour regions of the synchrotron model are showed in orange: light orange is used for model derived when the calibration constant in fixed on BAT data, and dark orange when it is fixed on XRT data. An upper limit can be inferred for the value of the cooling energy and the orange arrow is drawn. The CPL+BB model is shown in red. The shaded gray region is the time interval where the spectrum has been extracted.

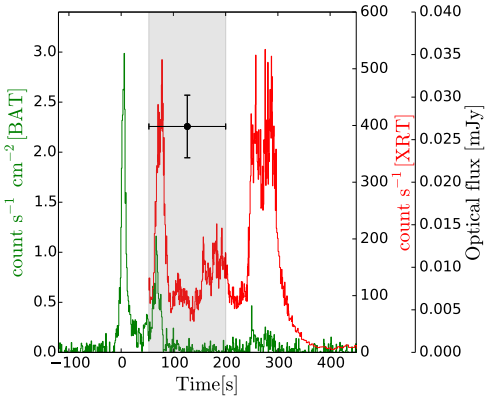

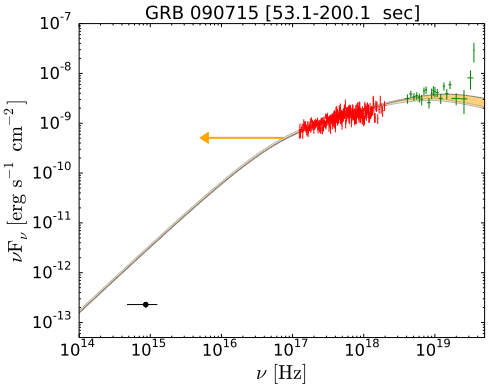

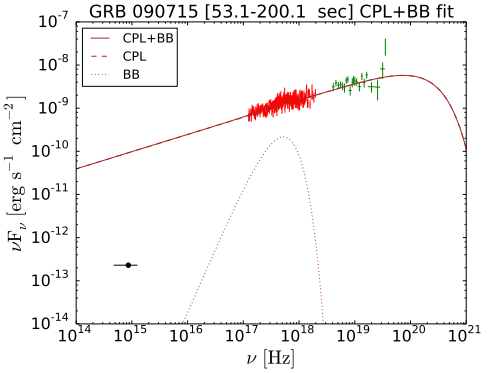

GRB 100906A

FIGURE 6.10: Light curve (left-hand panel) and spectrum (right-hand panel) of GRB 100906A. Green symbols are used for BAT data, black for optical and red for XRT. The joint νF_ν spectrum (XRT+BAT+GBM) is fitted with the synchrotron and CPL+BB models. The best fit contour regions of the synchrotron model are showed in orange: light orange is used for model derived when the calibration constant in fixed on BAT data, and dark orange when it is fixed on GBM data. The CPL+BB model is shown in red. The shaded gray region is the time interval where the spectrum has been extracted.

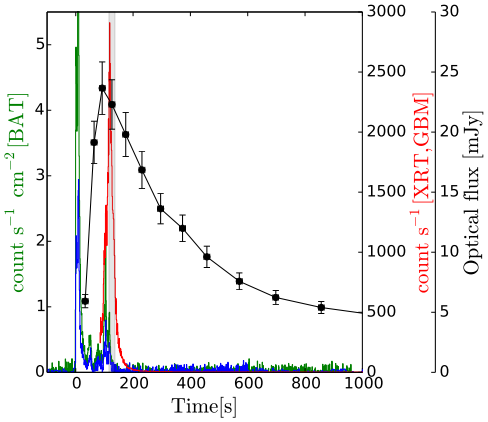

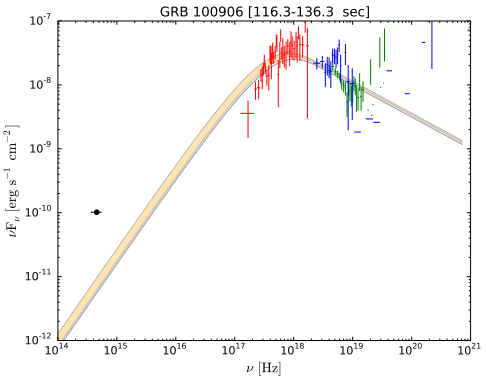

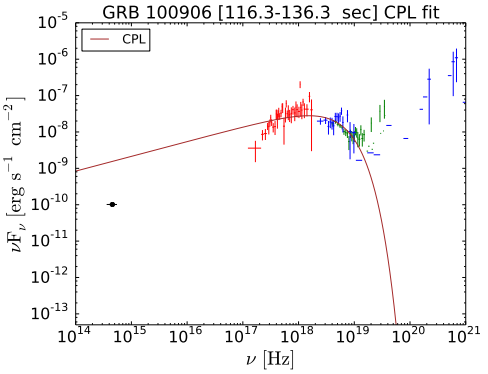

GRB 110102A

FIGURE 6.11: Light curve (left-hand panel) and spectrum (right-hand panel) of GRB 110102A. Green symbols are used for BAT data, black for optical and red for XRT. The joint νF_ν spectrum (XRT+BAT) is fitted with the synchrotron and CPL+BB models. The best fit contour regions of the synchrotron model are showed in orange: light orange is used for model derived when the calibration constant in fixed on BAT data, and dark orange when it is fixed on XRT data. The CPL+BB model is shown in red. The shaded gray region is the time interval where the spectrum has been extracted.

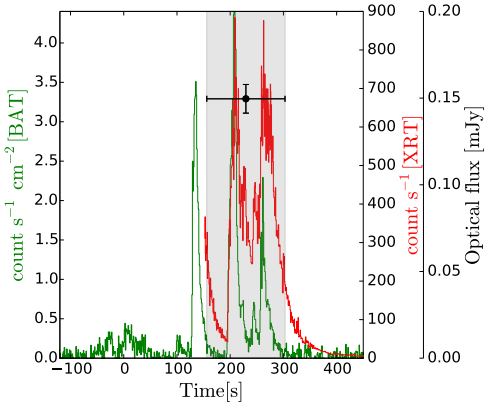

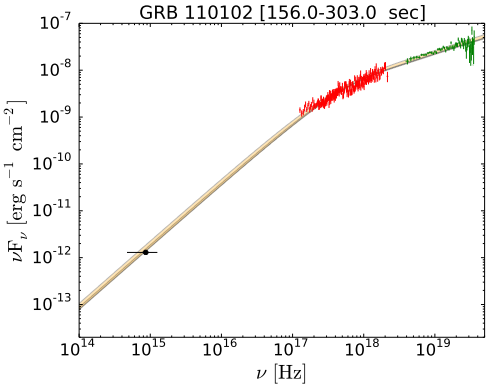

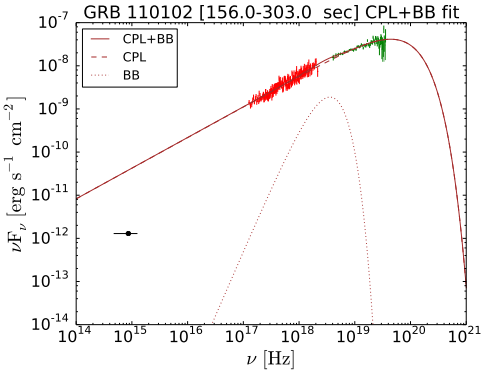

GRB 110119A

FIGURE 6.12: Light curve (left-hand panel) and spectrum (right-hand panel) of GRB 110119A. Green symbols are used for BAT data, blue for GBM data, black for optical and red for XRT. The joint νF_ν spectrum (XRT+BAT+GBM) is fitted with the synchrotron and CPL+BB models. The best fit contour regions of the synchrotron model are showed in orange: light orange is used for model derived when the calibration constant in fixed on BAT data, and dark orange when it is fixed on GBM data. The CPL+BB model is shown in red. The shaded gray region is the time interval where the spectrum has been extracted.

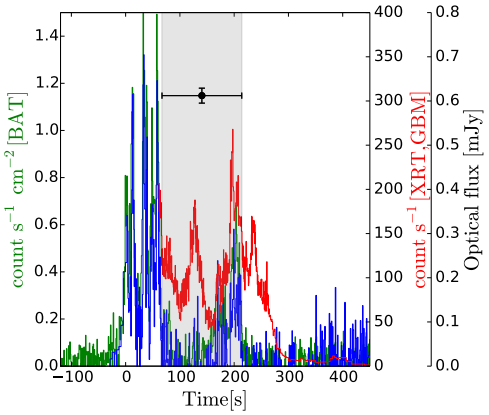

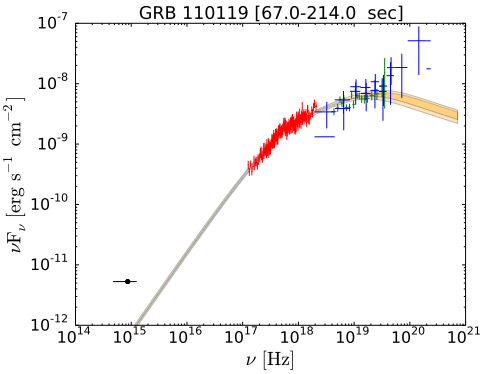

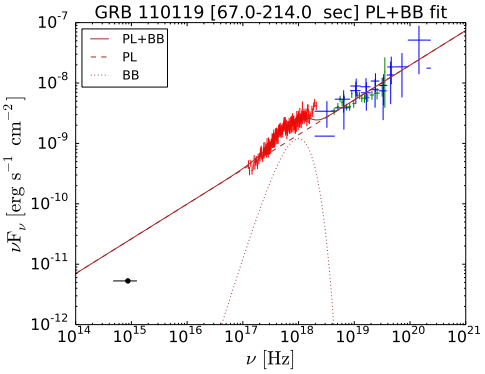

GRB 110205

FIGURE 6.13: Light curve (upper panel) and time-resolved spectra of GRB 110205. Green symbols are used for BAT data, black for optical and red for XRT. The joint νF_ν spectra (XRT+BAT) are fitted with the synchrotron and CPL+BB models. The best fit contour regions of the synchrotron model are showed in orange: light orange is used for model derived when the calibration constant in fixed on BAT data, and dark orange when it is fixed on XRT data. The CPL+BB model is shown in red. The shaded gray region is the time interval where the spectrum has been extracted.

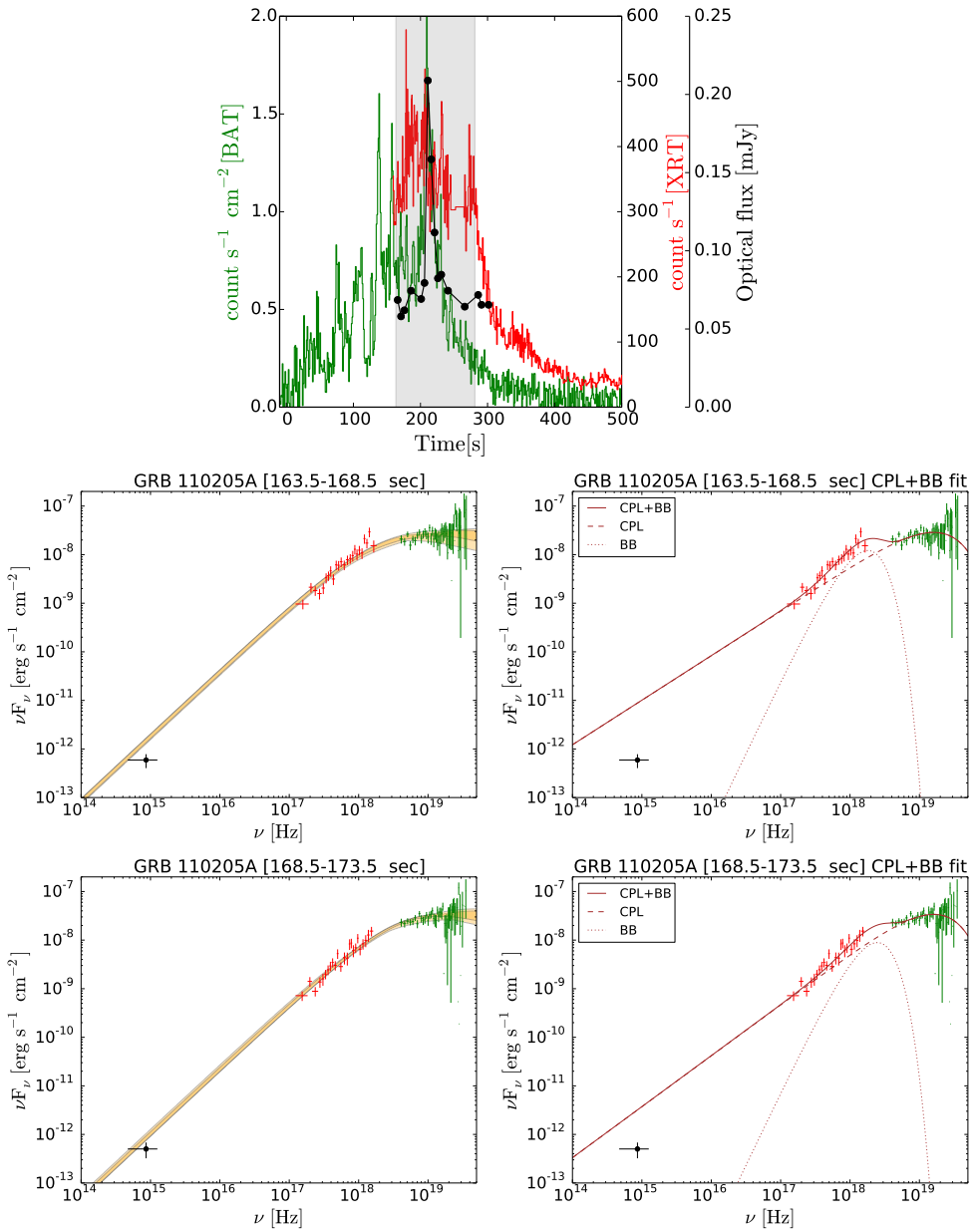

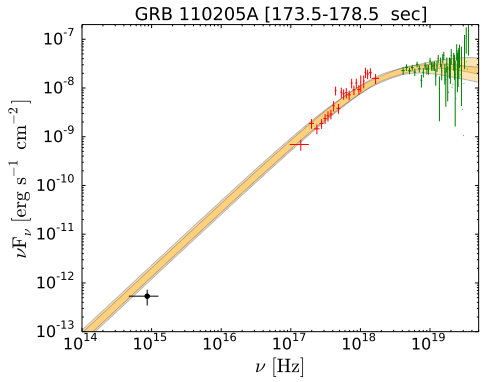
GRB 110205A [173.5-178.5 sec]
νF_ν [erg s^{-1} cm^{-2}]
ν [Hz]

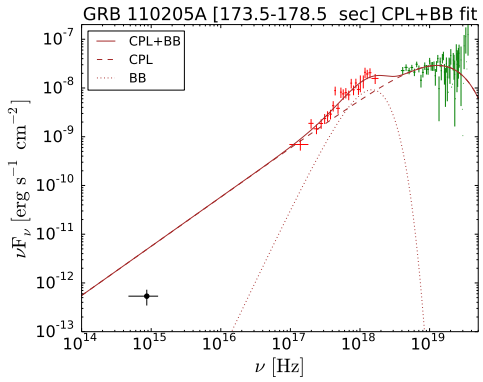
GRB 110205A [173.5-178.5 sec] CPL+BB fit
CPL+BB
CPL
BB
νF_ν [erg s^{-1} cm^{-2}]
ν [Hz]

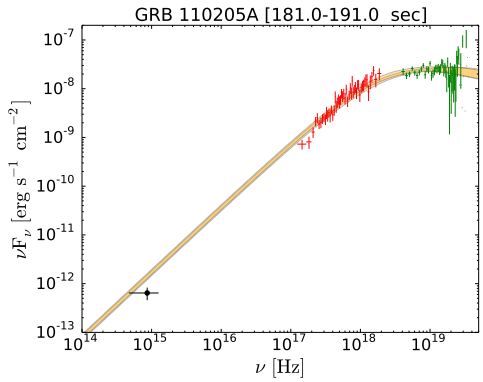
GRB 110205A [181.0-191.0 sec]
νF_ν [erg s^{-1} cm^{-2}]
ν [Hz]

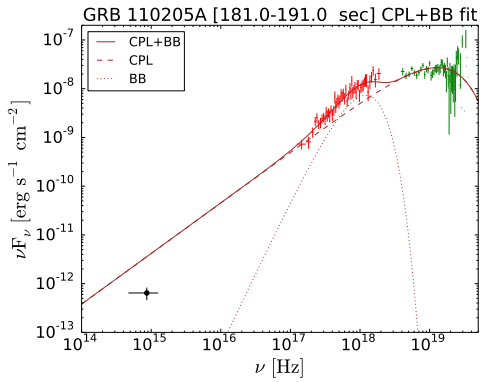
GRB 110205A [181.0-191.0 sec] CPL+BB fit
CPL+BB
CPL
BB
νF_ν [erg s^{-1} cm^{-2}]
ν [Hz]

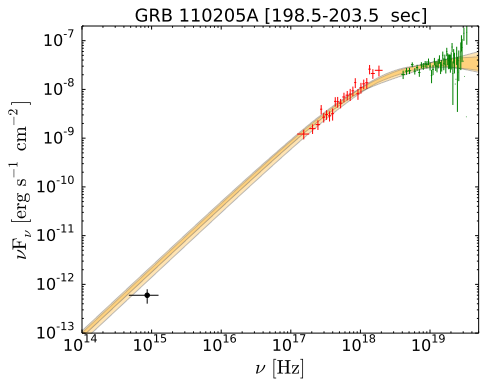
GRB 110205A [198.5-203.5 sec]
νF_ν [erg s^{-1} cm^{-2}]
ν [Hz]

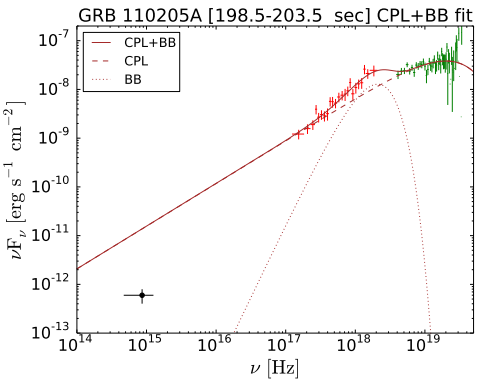
GRB 110205A [198.5-203.5 sec] CPL+BB fit
CPL+BB
CPL
BB
νF_ν [erg s^{-1} cm^{-2}]
ν [Hz]

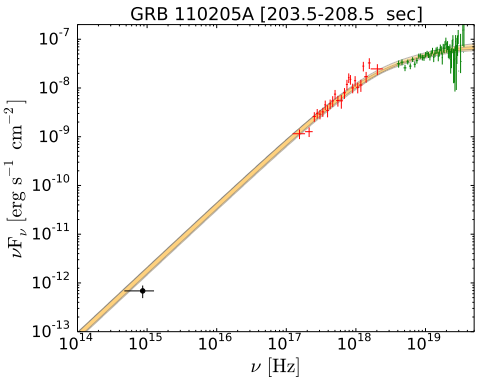
GRB 110205A [203.5-208.5 sec]
νF_ν [erg s^{-1} cm^{-2}]
ν [Hz]

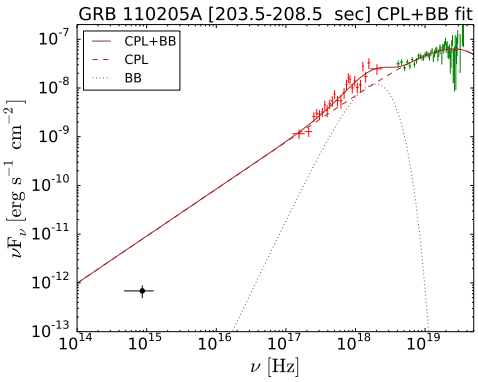
GRB 110205A [203.5-208.5 sec] CPL+BB fit
CPL+BB
CPL
BB
νF_ν [erg s^{-1} cm^{-2}]
ν [Hz]

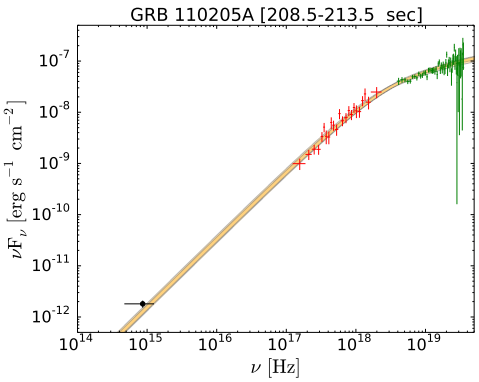
GRB 110205A [208.5-213.5 sec]
νF_ν [erg s^{-1} cm^{-2}]
ν [Hz]

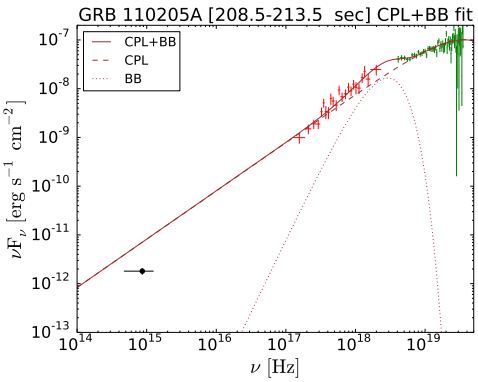
GRB 110205A [208.5-213.5 sec] CPL+BB fit
CPL+BB
CPL
BB
νF_ν [erg s^{-1} cm^{-2}]
ν [Hz]

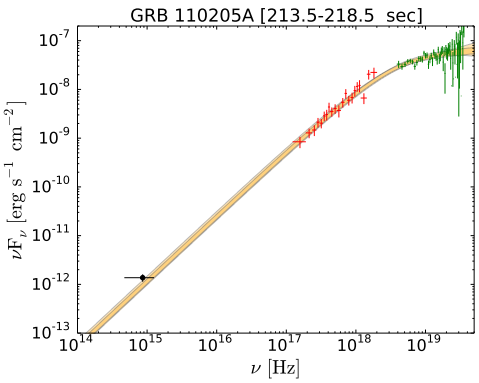
GRB 110205A [213.5-218.5 sec]
νF_ν [erg s^{-1} cm^{-2}]
ν [Hz]

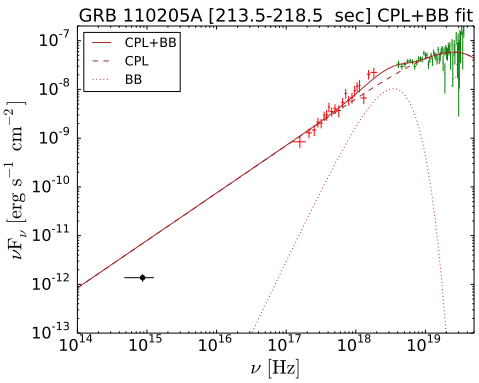
GRB 110205A [213.5-218.5 sec] CPL+BB fit
CPL+BB
CPL
BB
νF_ν [erg s^{-1} cm^{-2}]
ν [Hz]

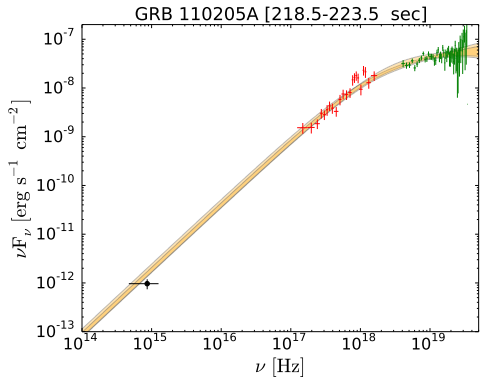
GRB 110205A [218.5-223.5 sec]
νF_ν [erg s^{-1} cm^{-2}]
ν [Hz]

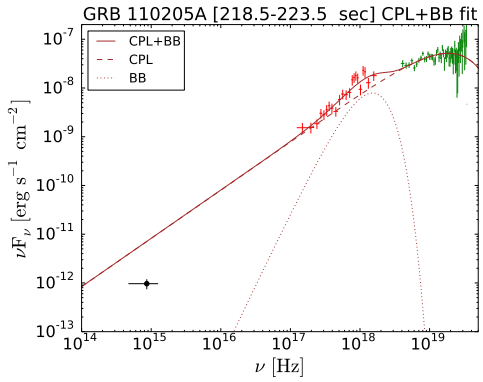
GRB 110205A [218.5-223.5 sec] CPL+BB fit
CPL+BB
CPL
BB
νF_ν [erg s^{-1} cm^{-2}]
ν [Hz]

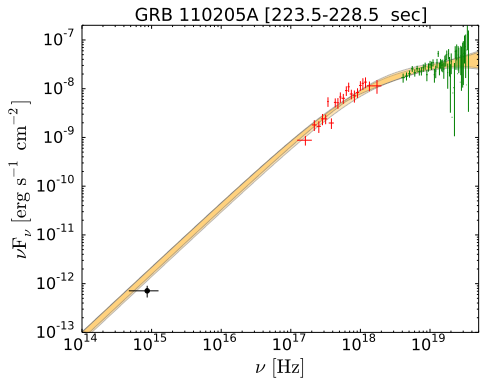
GRB 110205A [223.5-228.5 sec]
νF_ν [erg s^{-1} cm^{-2}]
ν [Hz]

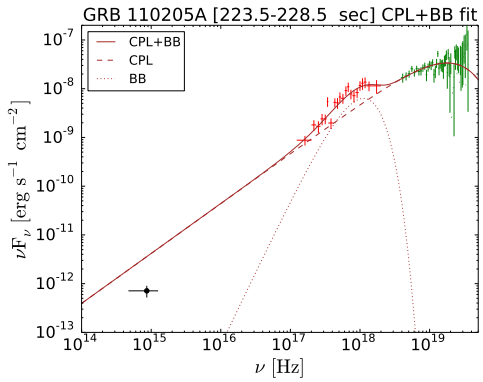
GRB 110205A [223.5-228.5 sec] CPL+BB fit
CPL+BB
CPL
BB
νF_ν [erg s^{-1} cm^{-2}]
ν [Hz]

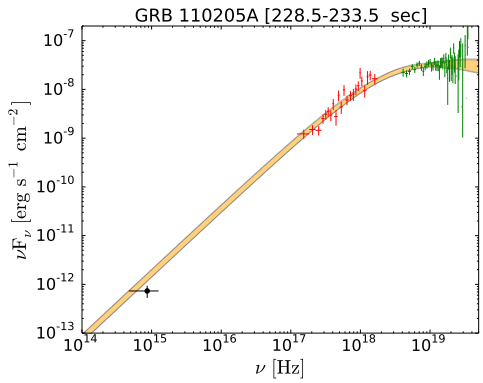
GRB 110205A [228.5-233.5 sec]
νF_ν [erg s^{-1} cm^{-2}]
ν [Hz]

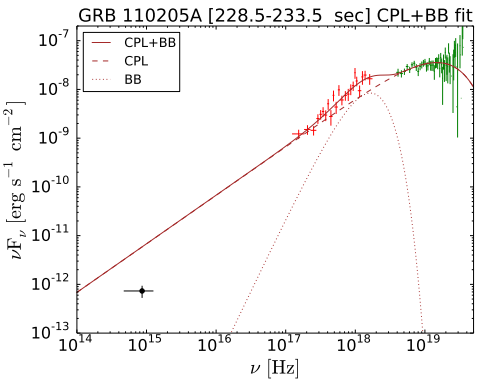
GRB 110205A [228.5-233.5 sec] CPL+BB fit
CPL+BB
CPL
BB
νF_ν [erg s^{-1} cm^{-2}]
ν [Hz]

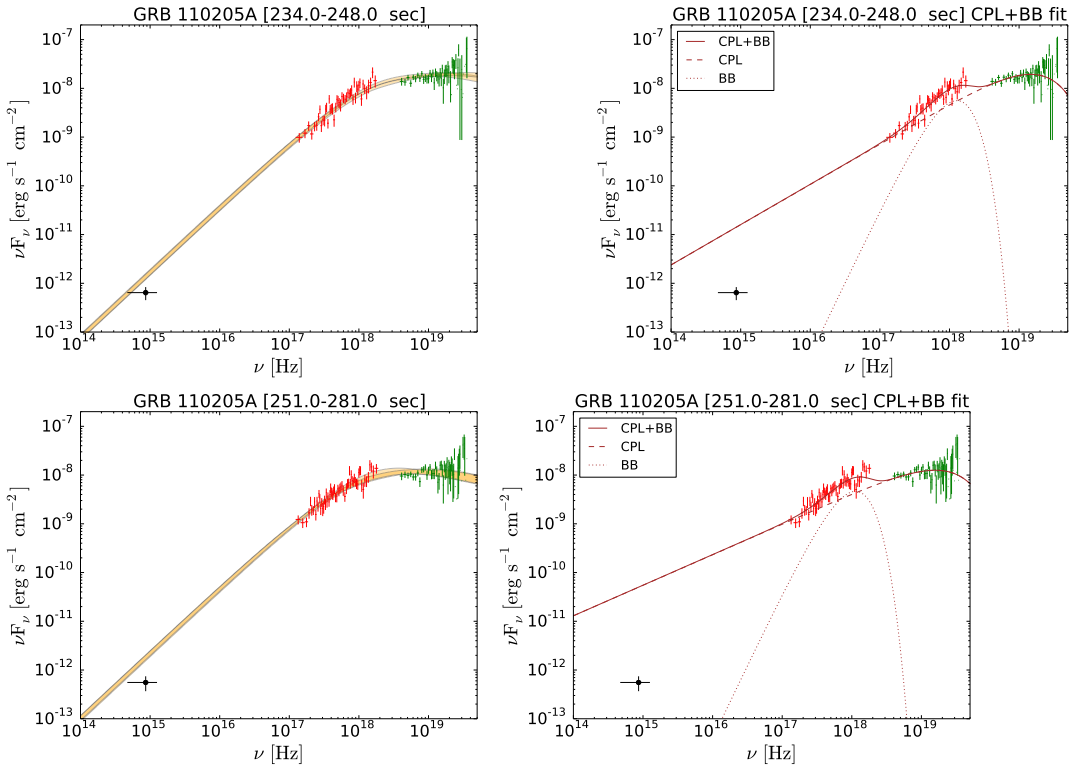
GRB 110205A [234.0-248.0 sec]
GRB 110205A [234.0-248.0 sec] CPL+BB fit
GRB 110205A [251.0-281.0 sec]
GRB 110205A [251.0-281.0 sec] CPL+BB fit
CPL+BB
CPL
BB
νF_ν [erg s^{-1} cm^{-2}]
ν [Hz]

GRB 111103B

FIGURE 6.14: Light curve (left-hand panel) and spectrum (right-hand panel) of GRB 111103B. Green symbols are used for BAT data, black for optical and red for XRT. The joint νF_ν spectrum (XRT+BAT) is fitted with the synchrotron and CPL+BB models. The best fit contour regions of the synchrotron model are showed in orange: light orange is used for model derived when the calibration constant in fixed on BAT data, and dark orange when it is fixed on XRT data. The CPL+BB model is shown in red. The shaded gray region is the time interval where the spectrum has been extracted.

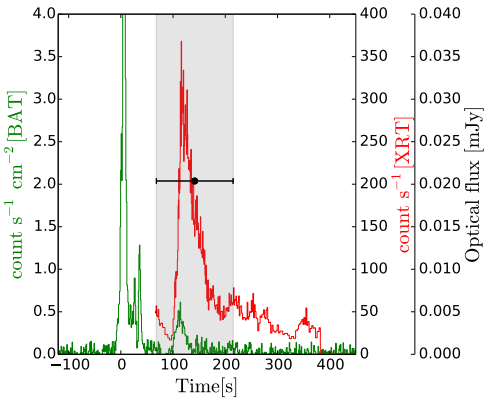

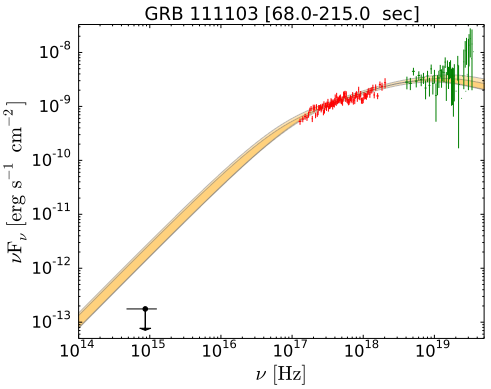

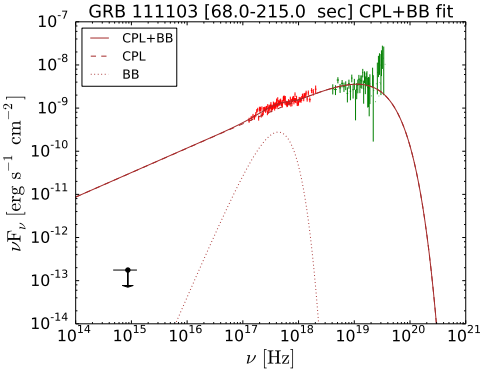

GRB 111123A

FIGURE 6.15: Light curve (left-hand panel) and spectrum (right-hand panel) of GRB 111123A. Green symbols are used for BAT data, black for optical and red for XRT. The joint νF_ν spectrum (XRT+BAT) is fitted with the synchrotron and CPL+BB models. The best fit contour regions of the synchrotron model are showed in orange: light orange is used for model derived when the calibration constant in fixed on BAT data, and dark orange when it is fixed on XRT data. The CPL+BB model is shown in red. The shaded gray region is the time interval where the spectrum has been extracted.

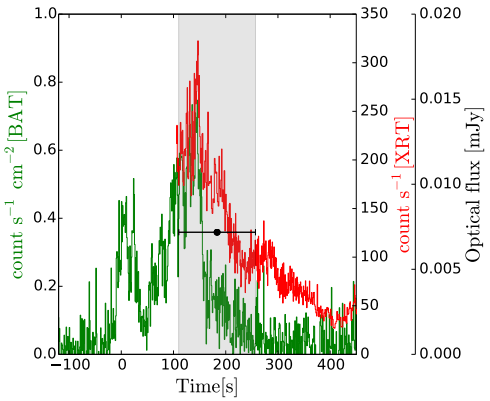

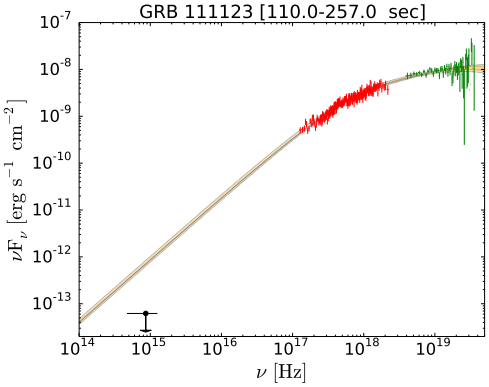

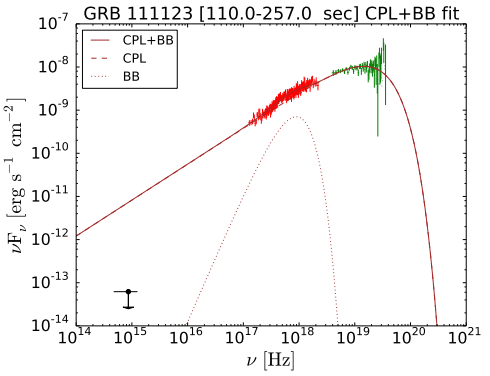

GRB 121123A

FIGURE 6.16: Light curve (left-hand panel) and spectrum (right-hand panel) of GRB 121123A. Green symbols are used for BAT data, black for optical and red for XRT. The joint νF_ν spectrum (XRT+BAT) is fitted with the synchrotron and CPL+BB models. The best fit contour regions of the synchrotron model are showed in orange: light orange is used for model derived when the calibration constant in fixed on BAT data, and dark orange when it is fixed on XRT data. The CPL+BB model is shown in red. The shaded gray region is the time interval where the spectrum has been extracted.

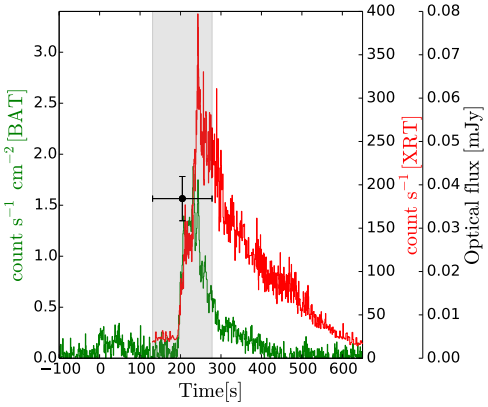

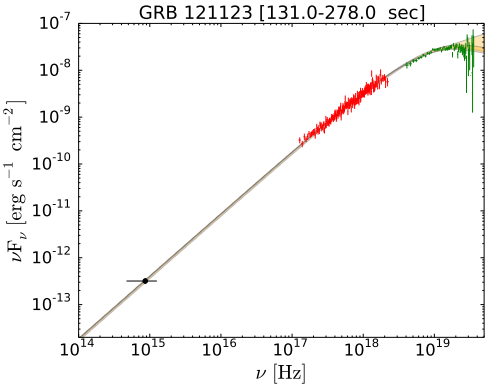

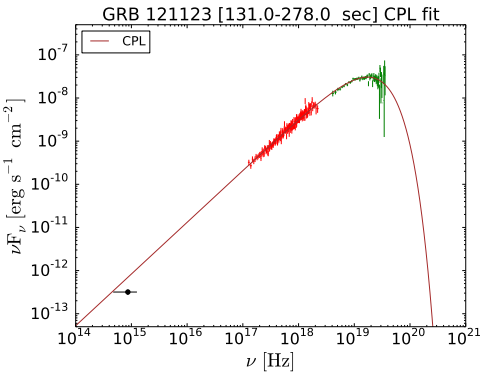

GRB 121217A

FIGURE 6.17: Light curve (upper panel) and time-resolved spectra of GRB 121217A. Green symbols are used for BAT data, blue for GBM data, black for optical and red for XRT. The joint νF_ν spectra (XRT+BAT+GBM) are fitted with the synchrotron and CPL+BB models. The best fit contour regions of the synchrotron model are showed in orange: light orange is used for model derived when the calibration constant in fixed on BAT data, and dark orange when it is fixed on GBM data. The CPL+BB model is shown in red. The shaded gray region is the time interval where the spectrum has been extracted.

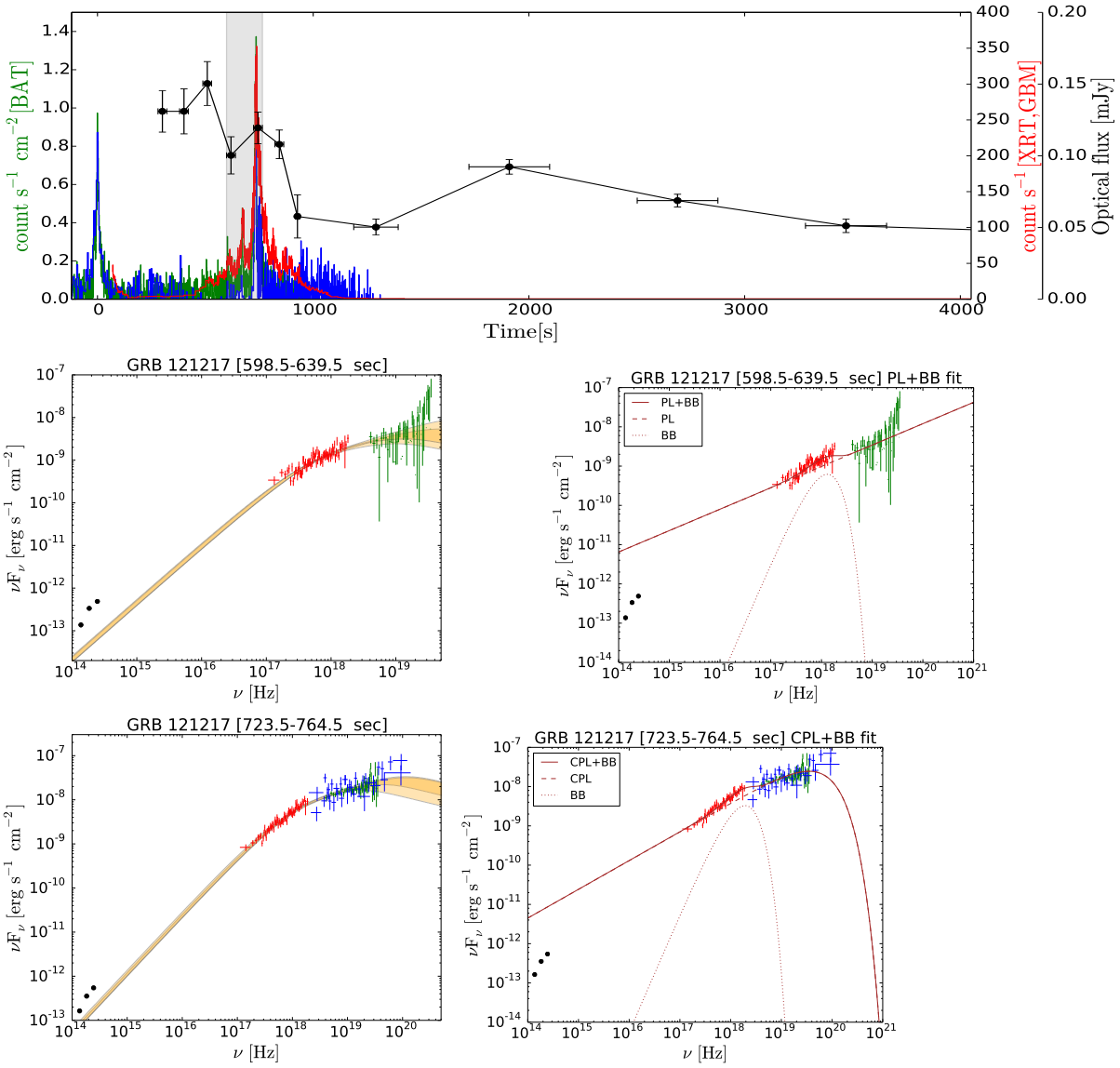

GRB 130514A

FIGURE 6.18: Light curve (left-hand panel) and spectrum (right-hand panel) of GRB 130514A. Green symbols are used for BAT data, black for optical and red for XRT. The joint νF_ν spectrum (XRT+BAT) is fitted with the synchrotron and CPL+BB models. The best fit contour regions of the synchrotron model are showed in orange: light orange is used for model derived when the calibration constant in fixed on BAT data, and dark orange when it is fixed on XRT data. The CPL+BB model is shown in red. The shaded gray region is the time interval where the spectrum has been extracted.

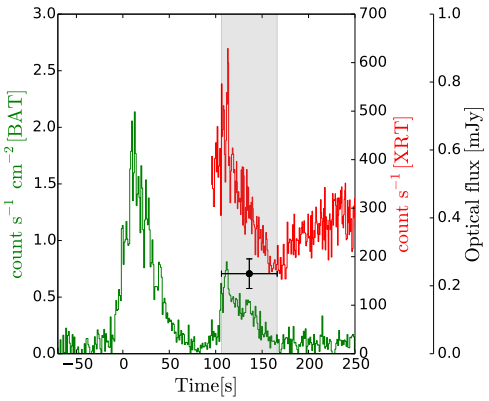

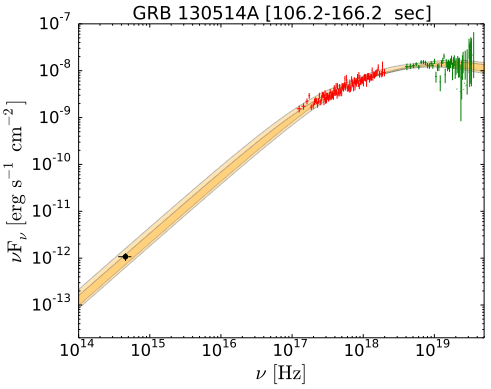

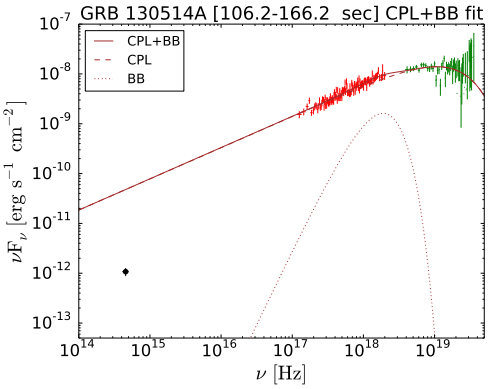

GRB 130907A

FIGURE 6.19: Light curve (left-hand panel) and spectrum (right-hand panel) of GRB 130907A. Green symbols are used for BAT data, black for optical and red for XRT. The joint νF_ν spectrum (XRT+BAT) is fitted with the synchrotron and CPL+BB models. The best fit contour regions of the synchrotron model are showed in orange: light orange is used for model derived when the calibration constant in fixed on BAT data, and dark orange when it is fixed on XRT data. The CPL+BB model is shown in red. The shaded gray region is the time interval where the spectrum has been extracted.

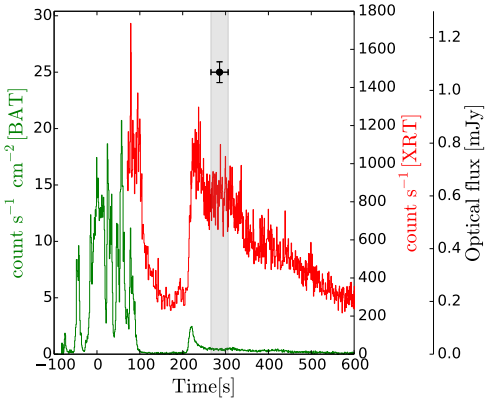

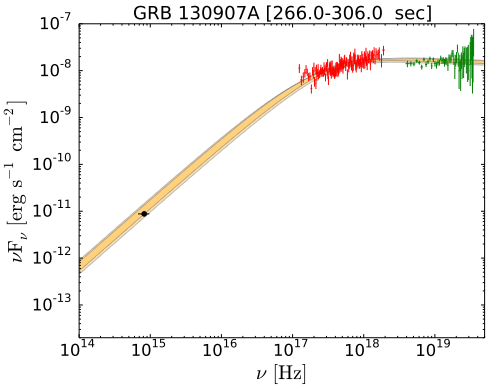

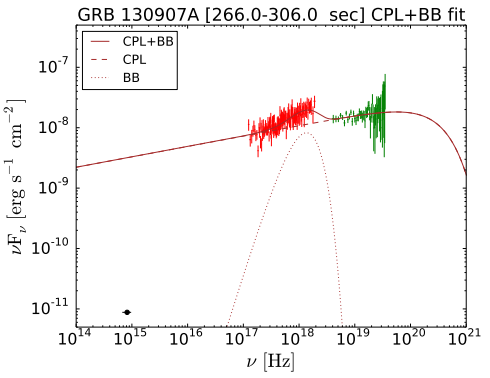

GRB 140108A

FIGURE 6.20: Light curve (left-hand panel) and spectrum (right-hand panel) of GRB 140108A. Green symbols are used for BAT data, black for optical and red for XRT. The joint νF_ν spectrum (XRT+BAT+GBM) is fitted with the synchrotron and CPL+BB models. The best fit contour regions of the synchrotron model are showed in orange: light orange is used for model derived when the calibration constant in fixed on BAT data, and dark orange when it is fixed on GBM data. The CPL+BB model is shown in red. The shaded gray region is the time interval where the spectrum has been extracted.

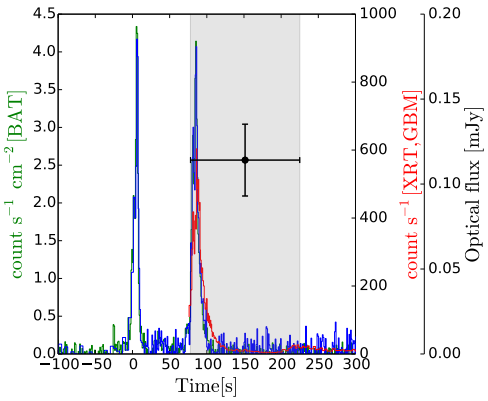

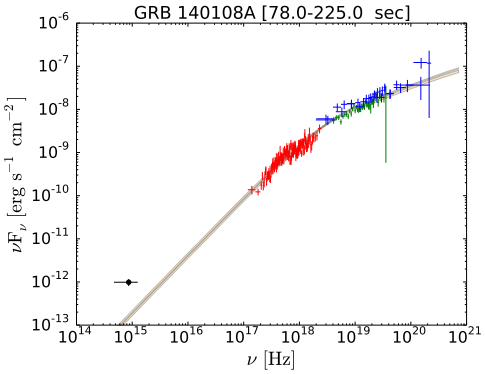

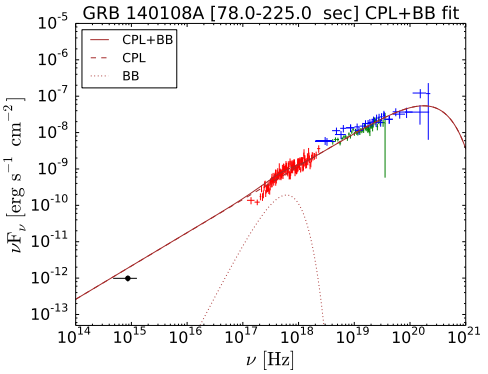

GRB 140206A

FIGURE 6.21: Light curve (left-hand panel) and spectrum (right-hand panel) of GRB 140206A. Green symbols are used for BAT data, black for optical and red for XRT. The joint νF_ν spectrum (XRT+BAT) is fitted with the synchrotron and CPL+BB models. The best fit contour regions of the synchrotron model are showed in orange: light orange is used for model derived when the calibration constant in fixed on BAT data, and dark orange when it is fixed on XRT data. The CPL+BB model is shown in red. The shaded gray region is the time interval where the spectrum has been extracted.

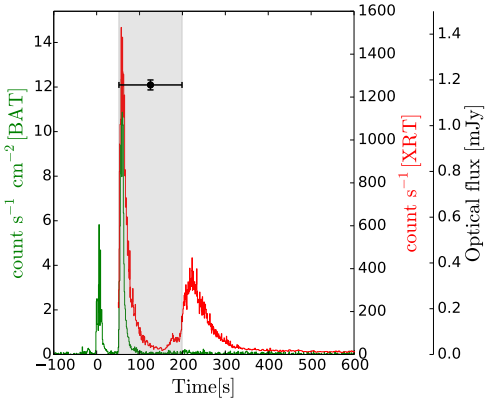

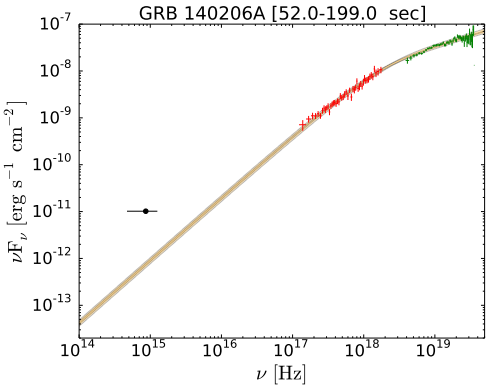

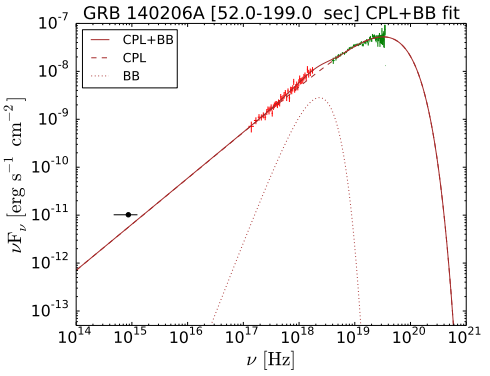

GRB 140512A

FIGURE 6.22: Light curve (left-hand panel) and spectrum (right-hand panel) of GRB 140512A. Green symbols are used for BAT data, black for optical and red for XRT. The joint νF_ν spectrum (XRT+BAT+GBM) is fitted with the synchrotron and CPL+BB models. The best fit contour regions of the synchrotron model are showed in orange: light orange is used for model derived when the calibration constant in fixed on BAT data, and dark orange when it is fixed on GBM data. The CPL+BB model is shown in red. The shaded gray region is the time interval where the spectrum has been extracted.

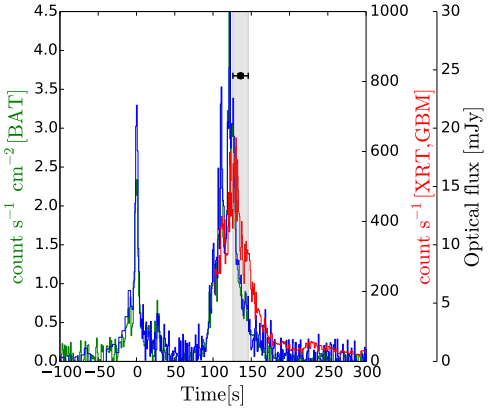

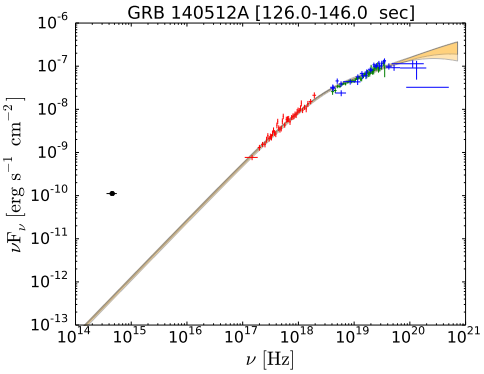

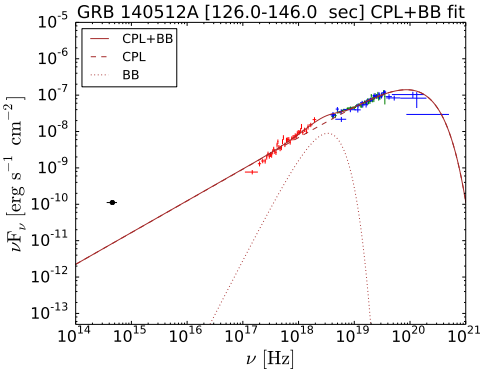

GRB 151021A

FIGURE 6.23: Light curve (left-hand panel) and spectrum (right-hand panel) of GRB 151021A. Green symbols are used for BAT data, black for optical and red for XRT. The joint νF_ν spectrum (XRT+BAT) is fitted with the synchrotron and CPL+BB models. The best fit contour regions of the synchrotron model are showed in orange: light orange is used for model derived when the calibration constant in fixed on BAT data, and dark orange when it is fixed on XRT data. The CPL+BB model is shown in red. The shaded gray region is the time interval where the spectrum has been extracted.

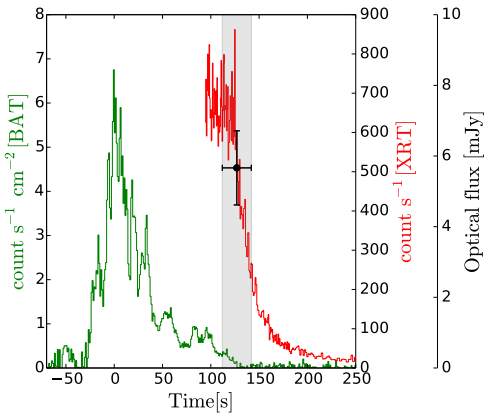

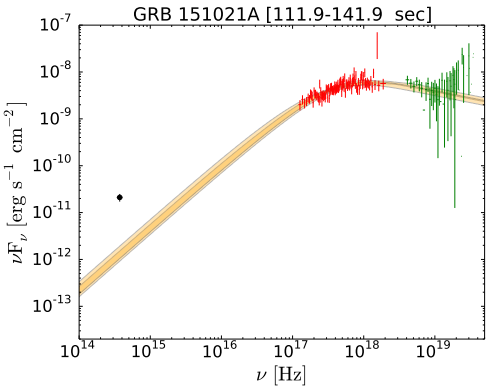

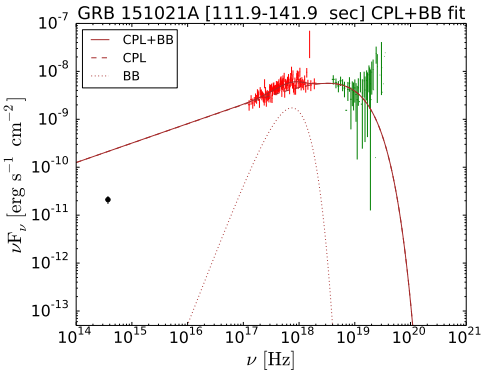

Chapter 7

Future perspectives

In 34 GRBs studied in this thesis the prompt emission has been (at least partially) observed by XRT (0.5-10 keV). The frequent presence of a spectral break located between 2 keV and 30 keV was discovered (Chapters 3-4). Below the break energy, the spectrum is well described by a power-law function. A similar result has been found also in GRB 160525B (Chapter 5), one of the brightest GRBs ever detected by the *Fermi*-GBM (8 keV-40 MeV). For this GRB, XRT observations during the prompt emission are not available, but the break energy is located around $\sim$100 keV, well within the GBM range of sensitivity. GBM data alone were sufficient to constrain the energy of this spectral break and the index of the PL below the break, with no need for soft X-ray observations.

Remarkably, the spectral analysis of these spectra featuring a break in the low-energy part, revealed a general agreement with the synchrotron model: the spectral slope below and above the break are, on average, consistent with the synchrotron slopes if the break identified at a few keV corresponds to the cooling frequency, and the peak energy corresponds to the characteristic synchrotron energy.

For some of these GRBs, previous spectral studies proposed a different modeling: the convolution of a thermal and a non-thermal components. The two different models (single component with low-energy break and two-components) fit the spectra equally well above a few keV. However, they predict very different behaviours at lower energies. A larger number of spectra with data extending to energies < 1 keV and covering the full prompt emission phase is required before reaching a conclusion of the viability of the two different models.

Results obtained in the thesis are mainly found thanks to a tiny fraction of available observations of the prompt emission in the soft X-ray band. The slewing time needed for *Swift* gives a limitation on the number of GRBs with the XRT observations during the prompt phase. Moreover, the prompt emission should last for long enough time to be observed by XRT. The study of prompt spectra from 0.5 keV was possible, thanks to XRT, only for 34 GRBs in 13 years of operations. Among these cases, around 20 have a clear feature at $\sim$keV energies. For a subsample of 4-5 GRBs, the feature is better described by a break rather than by the inclusion of a BB. For the remaining cases, both models give an acceptable fit.

Till now, the prompt emission has been detected by the hard X-ray/gamma-ray

instruments (> 8 keV). However, Lobster-type X-ray missions are planned/proposed for studies of the transient sky. The advantages of wide-field X-ray missions are (1) an accurate positioning of GRBs, (2) a possibility to detect GRBs at higher redshifts, (3) a broad-band spectral characterization of prompt/afterglow emission. Future X-ray missions (the *Space Variable Objects Monitor (SVOM)* and THESEUS) will allow the systematic study of spectra below 10 keV, down to soft X-rays. The joint fit of soft and hard X-ray spectra will allow to model them over a large range of energies and discriminate between the two models: the model with a break and the model with a thermal component. We will also have the chance to follow the low-energy spectral evolution at earlier times.

SVOM (Wei et al., 2016) is under development by the Chinese and French space agencies and it is planned to be launched in 2021. *SVOM* will be composed by two X- and gamma-ray instruments: (1) ECLAIRs is a 2 sr-wide field X-ray camera (operating in the 4keV $-$ 120 keV range), (2) Gamma-ray Burst Monitor (GRM) operating in the 50keV $-$ 5 MeV. It will allow us to observe GRBs in the 4 keV $-$ 5 MeV range.

THESEUS (Amati et al., 2018; Stratta et al., 2018) is a space mission concept proposed as M-class mission to the European Space Agency (ESA). With the main focus of probing the early Universe, THESEUS will be particularly suited for the study of X-ray transients, covering the energy range from 0.3 keV to several MeV. Sensitivity to emission in this energy range is achieved thanks to the Soft X-ray Imager (SXI, 0.3-6 keV) and the X-Gamma ray Imaging Spectrometer (XGIS, 2 keV-20 MeV). THESEUS is expected to detect $\sim$400–800 GRBs per year. A sizable fraction will be simultaneously detected by SXI and XGIS during the prompt emission. In the following I discuss briefly the capability of THESEUS to distinguish the above-mentioned prompt emission spectral models.

THESEUS will allow the systematic study of spectra below 10 keV, down to $\sim$0.3 keV thanks to the SXI. The joint fit of SXI and XGIS will allow to model the spectrum over a large range of energies and discriminate between the two models. Figure 7.1 shows that models can be ruled out if the available data extend well below the location of the break energy (or the location of the black-body peak, in the two-component interpretation).

To understand how a GRB prompt spectrum will be observed by THESEUS and whether the detection of spectral breaks at $\sim$keV energies will be possible, I performed spectral simulations for the the Proceedings of the THESEUS Workshop in 2017. THESEUS was selected by ESA on 2018 May 7 to enter an assessment phase study.

I simulated XGIS and SXI data, assuming three different models: i) CPL, ii) CPL with a break, and iii) CPL+BB. For the second model, the photon indices below and above the break energy have been fixed to the synchrotron values, the peak energy has been fixed to 100 keV, and the break energy E_{break} is around 10 keV. I chose an average flux (integrated between 0.1 keV and 10 MeV) equal to 5×10^{-7} erg cm^{-2} s^{-1}, and duration $T = 20$ s. The chosen values for the column densities are $N_{H,Galactic} =$

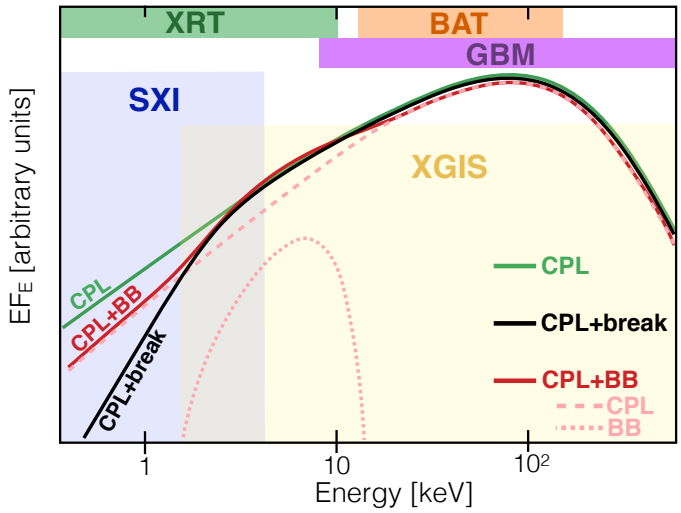

FIGURE 7.1: Schematic comparison between three different models: a standard a CPL (solid green), a CPL with a low-energy break (black solid line), and a CPL+BB (red solid line, the separated components are in dashed and dotted lines). The three models have a very similar shape above a few keV, but they predict different behaviours at lower energies. Shaded areas show the comparison between the sensitivity ranges of different instruments.

5×10^{20} cm^{-2}, and $N_{\rm H,intrinsic} = 10^{22}$ cm^{-2}, and the redshift is z= 2. The remaining

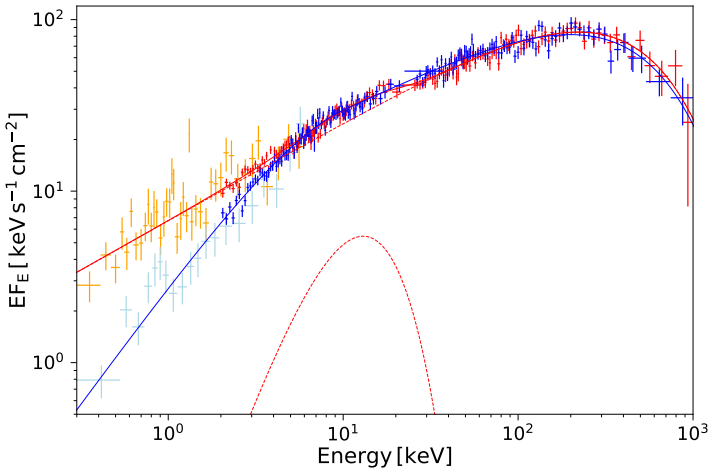

FIGURE 7.2: Simulation of a SXI and XGIS spectral data for two different models: CPL with a low-energy break (blue solid line) and a CPL+BB (red solid line for the sum of the two components, dashed red lines for the two separated components). SXI data are in light-blue and orange. XGIS data are in blue and red.

free parameters of the other two models (CPL and CPL+BB) have been chosen so that above the break energy, all three models have the same shape (as in the schematic example proposed in Fig. 7.1, right-hand panel), to reproduce the current observational picture. This resulted in a black-body temperature $kT = 2.85$ keV and a total black-body flux $F_{\rm BB} = 8.1 \times 10^{-9}$erg cm^{-2} s^{-1}. Current facilities would not

be able to discriminate among the different models, unless the emission is detected with good statistics also by the XRT well below 10 keV.

For each model, I simulate the spectra as detected by THESEUS adopting the following procedure. I generate the fake SXI and XGIS spectra using the *fakeit* command in *XSPEC*. This procedure creates adjusted and randomized spectral files for the defined exposure time using instrumental responses and background files. For the SXI, only energy channels below 6 keV are included. For the low- and high-energy XGIS detectors, only the channels between 2 to 50 keV and between 25 keV to 1 MeV (respectively) are considered. The energy channels are re-binned using the *grppha* tool, with the requirement of having at least 10 and 1000 counts in each channel for SXI and XGIS instruments, respectively.

Once the simulated spectra have been obtained, a joint SXI+XGIS fit is performed, using Gaussian statistic. The results of these simulations can be found in Fig. 7.2 and 7.3. Note that in these figures I chose to show the de-absorbed best fit models and data.

In the first figure, (Fig. 7.2), the CPL+break model (blue solid line) is compared to the CPL+BB model (red solid line). The simulated XGIS data are shown in blue and red, and the SXI data are in light-blue and orange, respectively for the two models. The simulated spectra are hardly distinguishable above ∼4 keV, but they predict very different behaviours at lower energies. The difference between the two spectra is already visible in the low-energy channels of the XGIS instrument, and becomes evident with the inclusion of SXI data.

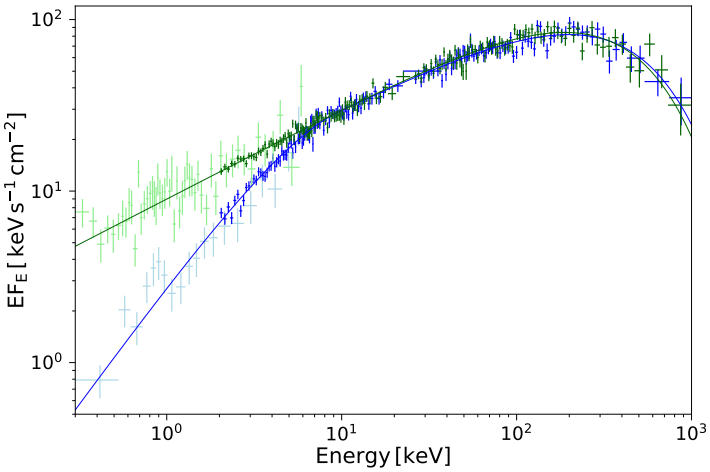

FIGURE 7.3: Simulation of a SXI and XGIS spectrum for two different models: CPL with a low-energy break (blue solid line) and a CPL (green solid line). SXI data are in light-green and light-blue. XGIS data are in green and blue.

Fig. 7.3 reports the same CPL+break simulated spectrum (blue and light-blue) this time compared to a simple CPL case. The CPL model is shown by a green solid line. XGIS and SXI data are marked in dark-green and light-green, respectively. Also in this case, the difference appears already clear below ∼4 keV, in the lowest energy

channels of the XGIS instrument. At even lower energies, the flux predicted by the two models differs by a factor 2-to-10, much larger than the typical error on the SXI simulated spectral data.

Future observations by THESEUS will unveil whether the feature at low-energy is ubiquitous, how it evolves with time, and whether a modeling in terms of a single (synchrotron) component is the correct one. I have indeed shown that the combined spectral analysis of XGIS and SXI will allow to discriminate between the synchrotron model and a thermal+non–thermal case.

Chapter 8

Conclusions

GRBs were discovered more than 40 years ago. Tens of years of data accumulation and significant theoretical efforts allowed us to establish the nature of GRBs progenitors. Today we can certainly rely on the fact that the GRB progenitor is powering an ultra-relativistic jet. Internal dissipation of the jet's energy produces the prompt emission. However, we do face a large gap in our knowledge on how the relativistic jets are formed, what is their composition and through which physical processes the jet's energy is dissipated.

In principle, it should be possible to extract information about the location of the emitting region, the strength of the magnetic field and the physics of particle acceleration from the study of prompt emission spectra. However, this requires good understanding of the emission mechanism of the observed radiation. Relativistic electrons in strong magnetic field are expected to emit synchrotron radiation. The emission regime should be in fast-cooling regime which corresponds to the case of electrons cooling on time scales much shorter than the dynamical one (e.g. Ghisellini, Celotti, and Lazzati 2000). The resulting spectrum from fast-cooling electrons has fixed photon spectrum ($N_E \propto E^{-1.5}$) below the νF_ν peak energy (corresponding, in the synchrotron scenario, to the typical energy of photons emitted by the electrons with minimum Lorentz factor γ_m). However, the observed prompt emission spectra are much harder than the fast-cooling synchrotron prediction: the photon spectrum $N_E \propto E^\alpha$ below the peak energy has an average photon index $\alpha \sim -1$ (e.g. Preece et al., 1998, Kaneko et al., 2006a, Goldstein et al., 2012, Lien et al., 2016).

This major inconsistency between theory and observations led to noticeble efforts to solve it. Different scenarios, mostly based on the modification of the synchrotron emission regime, were proposed to explain observed hard spectra. One possibility within the synchrotron scenario is to have cooling frequency close to the characteristic synchrotron frequency (so called marginally fast cooling synchrotron emission) (e.g. Daigne, Bošnjak, and Dubus, 2011): this regime would harden the observed spectra up to $\alpha \sim -2/3$. Another possibility is to invoke cooling of electrons via inverse Compton in Klein-Nishina regime (Derishev, Kocharovsky, and Kocharovsky, 2001; Nakar, Ando, and Sari, 2009). If the synchrotron radiation is in fast cooling regime and the electron's cooling via inverse Compton is in Klein-Nishina regime, the resulting spectrum below the peak energy becomes harder (with photon index up to $\alpha \sim -1$

Daigne, Bošnjak, and Dubus, 2011). If the magnetic field decays with the distance from the central engine, harder spectra can be obtained also in the natural fast cooling synchrotron regime (e.g. Uhm and Zhang, 2014). Another solution includes an anisotropic distribution of electrons' pitch angles (Lloyd and Petrosian, 2000; Medvedev, 2000). All these proposals suggest specific configuration of the physical environments in which the observed emission is produced.

In this thesis I have extended prompt emission spectra down to the soft X-rays and the optical band. My investigation started with a sample of 14 bright GRBs (Chapter 3) with simultaneous observations of prompt emission by Swift/XRT (0.3-10 keV), Swift/BAT (15-150 keV) and Fermi/GBM (8 keV-40 MeV) instruments. This combination of data sets allowed me to model the time-resolved spectra of the prompt emission from 0.5 keV to 40 MeV. I showed that the low energy extrapolation of the peaked functions (in νF_ν) typically used for modeling spectra at 10 keV - 40 MeV does not fit the data in the soft X-rays. I noticed that the inclusion of a low-energy break in the fitting function solves this discrepancy. I have then modeled spectra with this new empirical function and obtained unprecedented results: the photon indices (below and above the soft X-ray break) have typical values close to the values expected from synchrotron radiation (Fig. 3.7).

The further test of the proposed empirical model with a low-energy spectral break was performed for the enlarged sample of 34 GRBs (Chapter 4). This study has confirmed the presence of a break varying between 3 keV and 30 keV from burst to burst. I have also shown that fits without soft X-ray data confirm standard results: the spectrum below the peak energy is described by a power law with $< \alpha >= -1.15$. This shows the relevance of soft X-ray data in revealing prompt emission spectra consistent with synchrotron spectra. I do not find any correlation between the presence of the X-ray break energy and the flux, fluence or duration of the prompt emission.

The modeling of the prompt emission spectra with the inclusion of a break was tested for one of the brightest Fermi GRB 160625B (Ravasio et al., 2018, Chapter 5). It was shown that the break energy can be located at hard X-rays (100-300 keV) with the possibility to obtain spectral shapes close to the expectation of the synchrotron scenario (Fig. **??**). I performed a direct test of the synchrotron model on joint X- and γ-ray prompt emission spectra (Chapter 6). The spectra are well fitted with the synchrotron model of radiation in moderately fast cooling regime. It proofs the consistency of the synchrotron shape and curvature with the prompt emission spectra below the peak energy. I also compared the prediction of the synchrotron model in optical range with the data available for 56 spectra from 21 GRBs. In the one hand, the availability of prompt optical observations is crucial for testing of the synchrotron model since the optical flux is predicted by the extrapolation of the low-energy tail $N_E \sim E^{-2/3}$. In the other hand, the early optical radiation is sometimes contaminated by the afterglow emission. For several GRBs the high time-resolution of optical light curves allowed me to link them to the prompt/afterglow

emission. When the optical light curve tracks the prompt emission at hard X-rays (GRB 061121 and GRB 110205A), I have found the optical fluxes to be consistent with the extrapolation from the synchrotron model. In the opposite case, when the temporal behavior in the optical band is not correlated with the prompt emission (GRB 070616, GRB 081008, GRB 100906A, GRB 121217A), the extrapolation of the synchrotron spectral model under-estimates the optical flux. This is expected, since the prompt optical emission is dominated by the afterglow. Remaining GRBs have poor optical data, mainly represented by a single exposure during the prompt phase. For these GRBs, the predicted optical flux is over/under-estimated or consistent with the synchrotron model from burst to burst. An additional contribution from the afterglow radiation in the case of under-estimation of the prompt optical emission is the possible explanation since the prompt radiation pulses are present prior to the detected optical component. The over-estimated optical flux can be caused by an unaccounted intrinsic absorption. The overall analysis shows that in half of the cases the optical data is consistent with the synchrotron model. I have also modeled the spectra with a two-component model (a cutoff power-law plus a black body). I have shown that in the most of the cases the two-component model over-estimates the optical flux. Therefore, the single component model is preferred.

To summarize, my investigation has proceeded into two main steps. In the first step, I have shown that empirical modeling of prompt emission spectra extended down to soft X-rays require a break to account for the low-energy hardening. I have analyzed the instrumental effects (X-ray pileup and the inter-instrumental calibration), the effect of intrinsic absorption estimation and I have demonstrated the robustness of my findings. The averaged ratio between the peak and the break energy ~ 30 has motivated to search for the breaks in higher energies where the peak energy is approaching MeV range. Spectral breaks at hard X-rays were found in the time-resolved spectra of the bright *Fermi* GRB 160625B. Similar findings at different energies suggest that the spectral break is a common feature in the prompt emission and it is independent of the instrument used for the analysis. These findings are completely changing the way prompt emission spectra should be modeled. The averaged spectral shapes below and above the breaks were found to be consistent with expectation of the synchrotron scenario. Breaks can then be interpreted as the cooling frequency of the electrons' population. In this case, the observed spectra point towards a synchrotron scenario in a moderately fast cooling regime. This supported a more theory-driven analysis, that was the second step of my research. The direct application of the synchrotron model to the prompt emission spectra in the $0.5\,\mathrm{keV} - 150\,\mathrm{keV}(10\,\mathrm{MeV})$ range returned adequate fits. This modeling suggested a relatively small ratio between synchrotron and cooling electrons' Lorentz factors (~ 6) allowing the cooling frequency to enter the soft X-ray band.

The finding of this thesis support the marginally fast cooling synchrotron scenario. This regime of radiation is present in some physical conditions. Adiabatic cooling effects have been widely discussed by Daigne, Bošnjak, and Dubus (2011),

and can explain the large cooling frequencies if the dissipation takes place at large radii ($>10^{15}$ cm) in a region characterized by a relatively weak magnetic field (10-100 G in the comoving frame) and moving with large bulk Lorentz factor ($\Gamma > 400$). A variation of the magnetic field as a function of the distance from the shock front (Pe'er and Zhang, 2006; Derishev, 2007) can also lead to cooling timescales larger than the one inferred from typical magnetic field values. Another possibility is to modify the standard assumption on particle acceleration, and invoke slow particle heating (Asano and Terasawa, 2009) or particle re-acceleration (Kumar and McMahon, 2008; Beniamini and Piran, 2013).

The studies performed in this thesis have opened new questions about the nature of observed prompt emission spectra. If the results are interpreted in marginally fast cooling scenario, the following questions are relevant: 1) What is the reason for such weak magnetic field in the jet? 2) Does the magnetic field decay while transported to large radii? 3) Does the continuous re-acceleration of particles take a place?

A more extensive analysis of *Fermi* data and the direct application of the synthetic synchrotron spectra are now required. As demonstrated by the work presented in this thesis, broadband modeling and direct synchrotron fits seem to be the correct way of testing the marginally fast cooling scenario and extract physical information from the prompt spectral shapes.

Bibliography

Abbott, B. P. et al. (2017). "Gravitational Waves and Gamma-Rays from a Binary Neutron Star Merger: GW170817 and GRB 170817A". In: *ApJ* 848, L13, p. L13. DOI: 10.3847/2041-8213/aa920c. arXiv: 1710.05834 [astro-ph.HE].

Abdo, A. A. et al. (2011). "Detection of High-energy Gamma-Ray Emission During the X-Ray Flaring Activity in GRB 100728A". In: *ApJ* 734, L27, p. L27. DOI: 10.1088/2041-8205/734/2/L27. arXiv: 1104.5496 [astro-ph.HE].

Akerlof, C. et al. (1999). "Observation of contemporaneous optical radiation from a γ-ray burst". In: *Nature* 398, pp. 400–402. DOI: 10.1038/18837. eprint: astro-ph/9903271.

Akerlof, C. W. et al. (2003). "The ROTSE-III Robotic Telescope System". In: *PASP* 115, pp. 132–140. DOI: 10.1086/345490. eprint: astro-ph/0210238.

Alexander, K. D. et al. (2017). "A Reverse Shock and Unusual Radio Properties in GRB 160625B". In: *ApJ* 848, 69, p. 69. DOI: 10.3847/1538-4357/aa8a76. arXiv: 1705.08455 [astro-ph.HE].

Amati, L. et al. (2008). "Measuring the cosmological parameters with the $E_{p,i}$-E_{iso} correlation of gamma-ray bursts". In: *MNRAS* 391, pp. 577–584. DOI: 10.1111/j.1365-2966.2008.13943.x. arXiv: 0805.0377.

Amati, L. et al. (2018). "The THESEUS space mission concept: science case, design and expected performances". In: *Advances in Space Research* 62, pp. 191–244. DOI: 10.1016/j.asr.2018.03.010. arXiv: 1710.04638 [astro-ph.IM].

Asano, K. and T. Terasawa (2009). "Slow Heating Model of Gamma-ray Burst: Photon Spectrum and Delayed Emission". In: *ApJ* 705, pp. 1714–1720. DOI: 10.1088/0004-637X/705/2/1714. arXiv: 0905.1392 [astro-ph.HE].

Axelsson, M. and L. Borgonovo (2015). "The width of gamma-ray burst spectra". In: *MNRAS* 447, pp. 3150–3154. DOI: 10.1093/mnras/stu2675. arXiv: 1412.5692 [astro-ph.HE].

Band, D. et al. (1993). "BATSE observations of gamma-ray burst spectra. I - Spectral diversity". In: *ApJ* 413, pp. 281–292. DOI: 10.1086/172995.

Beloborodov, A. M. (2013). "Regulation of the Spectral Peak in Gamma-Ray Bursts". In: *ApJ* 764, 157, p. 157. DOI: 10.1088/0004-637X/764/2/157. arXiv: 1207.2707 [astro-ph.HE].

Beniamini, P. and T. Piran (2013). "Constraints on the Synchrotron Emission Mechanism in Gamma-Ray Bursts". In: *ApJ* 769, 69, p. 69. DOI: 10.1088/0004-637X/769/1/69. arXiv: 1301.5575 [astro-ph.HE].

Beniamini, P. and T. Piran (2014). "The emission mechanism in magnetically dominated gamma-ray burst outflows". In: *MNRAS* 445, pp. 3892–3907. DOI: 10.1093/mnras/stu2032. arXiv: 1402.4113 [astro-ph.HE].

Bernardini, M. G. et al. (2013). "How to Switch a Gamma-Ray Burst On and Off through a Magnetar". In: *ApJ* 775, 67, p. 67. DOI: 10.1088/0004-637X/775/1/67. arXiv: 1306.0013 [astro-ph.HE].

Beskin, G. et al. (2010). "Fast Optical Variability of a Naked-eye Burst. Manifestation of the Periodic Activity of an Internal Engine". In: *ApJ* 719, pp. L10–L14. DOI: 10.1088/2041-8205/719/1/L10. arXiv: 0905.4431 [astro-ph.HE].

Beskin, G. M. et al. (2017). "Wide-field optical monitoring with Mini-MegaTORTORA (MMT-9) multichannel high temporal resolution telescope". In: *Astrophysical Bulletin* 72, pp. 81–92. DOI: 10.1134/S1990341317030105.

Blandford, R. D. and C. F. McKee (1976). "Fluid dynamics of relativistic blast waves". In: *Physics of Fluids* 19, pp. 1130–1138. DOI: 10.1063/1.861619.

Blandford, R. D. and R. L. Znajek (1977). "Electromagnetic extraction of energy from Kerr black holes". In: *MNRAS* 179, pp. 433–456. DOI: 10.1093/mnras/179.3.433.

Blinnikov, S. I., A. V. Kozyreva, and I. E. Panchenko (1999). "Gamma-ray bursts: When does a blackbody spectrum look non-thermal?" In: *Astronomy Reports* 43, pp. 739–747. eprint: astro-ph/9902378.

Breeveld, A. A. and J. L. Racusin (2014). "GRB 140108A: Swift/UVOT detection." In: *GRB Coordinates Network, Circular Service, No. 15708, #1 (2014)* 15708.

Briggs, M. S. et al. (1999). "Observations of GRB 990123 by the Compton Gamma Ray Observatory". In: *ApJ* 524, pp. 82–91. DOI: 10.1086/307808.

Burd, A. et al. (2005). "Pi of the Sky - all-sky, real-time search for fast optical transients". In: *New A* 10, pp. 409–416. DOI: 10.1016/j.newast.2005.02.002. eprint: astro-ph/0411456.

Burgess, J. M. et al. (2014). "An Observed Correlation between Thermal and Non-thermal Emission in Gamma-Ray Bursts". In: *ApJ* 784, L43, p. L43. DOI: 10.1088/2041-8205/784/2/L43. arXiv: 1403.0374 [astro-ph.HE].

Butler, N. R. and D. Kocevski (2007a). "X-Ray Hardness Evolution in GRB Afterglows and Flares: Late-Time GRB Activity without N_H Variations". In: *ApJ* 663, pp. 407–419. DOI: 10.1086/518023. eprint: astro-ph/0612564.

— (2007b). "X-Ray Hardness Evolution in GRB Afterglows and Flares: Late-Time GRB Activity without N_H Variations". In: *ApJ* 663, pp. 407–419. DOI: 10.1086/518023. eprint: astro-ph/0612564.

Cenko, S. B. et al. (2006). "Multiwavelength Observations of GRB 050820A: An Exceptionally Energetic Event Followed from Start to Finish". In: *ApJ* 652, pp. 490–506. DOI: 10.1086/508149. eprint: astro-ph/0608183.

Cohen, E. et al. (1997). "Possible Evidence for Relativistic Shocks in Gamma-Ray Bursts". In: *ApJ* 488, pp. 330–337. DOI: 10.1086/304699.

Costa, E. et al. (1997). "Discovery of an X-ray afterglow associated with the γ-ray burst of 28 February 1997". In: *Nature* 387, pp. 783–785. DOI: 10.1038/42885. eprint: astro-ph/9706065.

Crider, A. et al. (1997). "Evolution of the Low-Energy Photon Spectral in Gamma-Ray Bursts". In: *ApJ* 479, pp. L39–L42. DOI: 10.1086/310574. eprint: astro-ph/9612118.

Cucchiara, A. et al. (2011). "Constraining Gamma-Ray Burst Emission Physics with Extensive Early-time, Multiband Follow-up". In: *ApJ* 743, 154, p. 154. DOI: 10.1088/0004-637X/743/2/154. arXiv: 1107.3352 [astro-ph.HE].

Daigne, F., Ž. Bošnjak, and G. Dubus (2011). "Reconciling observed gamma-ray burst prompt spectra with synchrotron radiation?" In: *A&A* 526, A110, A110. DOI: 10.1051/0004-6361/201015457. arXiv: 1009.2636 [astro-ph.HE].

Derishev, E. V. (2007). "Synchrotron emission in the fast cooling regime: which spectra can be explained?" In: *Ap&SS* 309, pp. 157–161. DOI: 10.1007/s10509-007-9421-z. eprint: astro-ph/0611260.

Derishev, E. V., V. V. Kocharovsky, and V. V. Kocharovsky (2001). "Physical parameters and emission mechanism in gamma-ray bursts". In: *A&A* 372, pp. 1071–1077. DOI: 10.1051/0004-6361:20010586. eprint: astro-ph/0006239.

Eichler, D. et al. (1989). "Nucleosynthesis, neutrino bursts and gamma-rays from coalescing neutron stars". In: *Nature* 340, pp. 126–128. DOI: 10.1038/340126a0.

Elliott, J. et al. (2014). "Prompt emission of GRB 121217A from gamma-rays to the near-infrared". In: *A&A* 562, A100, A100. DOI: 10.1051/0004-6361/201322600. arXiv: 1312.4547 [astro-ph.HE].

Evans, P. A. et al. (2009). "Methods and results of an automatic analysis of a complete sample of Swift-XRT observations of GRBs". In: *MNRAS* 397, pp. 1177–1201. DOI: 10.1111/j.1365-2966.2009.14913.x. arXiv: 0812.3662.

Fenimore, E. E., R. I. Epstein, and C. Ho (1993). "The escape of 100 MeV photons from cosmological gamma-ray bursts". In: *A&AS* 97, pp. 59–62.

Fermi, E. (1949). "On the Origin of the Cosmic Radiation". In: *Physical Review* 75, pp. 1169–1174. DOI: 10.1103/PhysRev.75.1169.

Filippenko, A. V. (1997). "Optical Spectra of Supernovae". In: *ARA&A* 35, pp. 309–355. DOI: 10.1146/annurev.astro.35.1.309.

Fong, W., E. Berger, and D. B. Fox (2010). "Hubble Space Telescope Observations of Short Gamma-Ray Burst Host Galaxies: Morphologies, Offsets, and Local Environments". In: *ApJ* 708, pp. 9–25. DOI: 10.1088/0004-637X/708/1/9. arXiv: 0909.1804 [astro-ph.HE].

Friis, M. and D. Watson (2013). "Thermal Emission in the Early X-Ray Afterglows of Gamma-Ray Bursts: Following the Prompt Phase to Late Times". In: *ApJ* 771, 15, p. 15. DOI: 10.1088/0004-637X/771/1/15. arXiv: 1305.3165 [astro-ph.HE].

Frontera, F. et al. (2000). "Prompt and Delayed Emission Properties of Gamma-Ray Bursts Observed with BeppoSAX". In: *ApJS* 127, pp. 59–78. DOI: 10.1086/313316. eprint: astro-ph/9911228.

Frontera, F. et al. (2004). "A Decreasing Column Density during the Prompt Emission from GRB 000528 Observed with BeppoSAX". In: *ApJ* 614, pp. 301–308. DOI: 10.1086/423335. eprint: astro-ph/0406575.

Fruchter, A. S. et al. (2006). "Long γ-ray bursts and core-collapse supernovae have different environments". In: *Nature* 441, pp. 463–468. DOI: 10.1038/nature04787. eprint: astro-ph/0603537.

Galama, T. J. et al. (1998). "An unusual supernova in the error box of the γ-ray burst of 25 April 1998". In: *Nature* 395, pp. 670–672. DOI: 10.1038/27150. eprint: astro-ph/9806175.

Gehrels, N. et al. (2004). "The Swift Gamma-Ray Burst Mission". In: *ApJ* 611, pp. 1005–1020. DOI: 10.1086/422091.

Ghirlanda, G., A. Celotti, and G. Ghisellini (2002a). "Time resolved spectral analysis of bright gamma ray bursts". In: *A&A* 393, pp. 409–423. DOI: 10.1051/0004-6361:20021038. eprint: astro-ph/0206377.

— (2002b). "Time resolved spectral analysis of bright gamma ray bursts". In: *A&A* 393, pp. 409–423. DOI: 10.1051/0004-6361:20021038. eprint: astro-ph/0206377.

— (2003). "Extremely hard GRB spectra prune down the forest of emission models". In: *A&A* 406, pp. 879–892. DOI: 10.1051/0004-6361:20030803. eprint: astro-ph/0210693.

Ghirlanda, G., G. Ghisellini, and L. Nava (2011). "Short and long gamma-ray bursts: same emission mechanism?" In: *MNRAS* 418, pp. L109–L113. DOI: 10.1111/j.1745-3933.2011.01154.x. arXiv: 1109.1833 [astro-ph.HE].

Ghirlanda, G., L. Nava, and G. Ghisellini (2010). "Spectral-luminosity relation within individual Fermi gamma rays bursts". In: *A&A* 511, A43, A43. DOI: 10.1051/0004-6361/200913134. arXiv: 0908.2807 [astro-ph.HE].

Ghirlanda, G., A. Pescalli, and G. Ghisellini (2013). "Photospheric emission throughout GRB 100507 detected by Fermi". In: *MNRAS* 432, pp. 3237–3244. DOI: 10.1093/mnras/stt681. arXiv: 1305.3287 [astro-ph.HE].

Ghirlanda, G. et al. (2004). "Gamma-Ray Bursts: New Rulers to Measure the Universe". In: *ApJ* 613, pp. L13–L16. DOI: 10.1086/424915. eprint: astro-ph/0408350.

Ghirlanda, G. et al. (2011). "Spectral evolution of Fermi/GBM short gamma-ray bursts". In: *MNRAS* 410, pp. L47–L51. DOI: 10.1111/j.1745-3933.2010.00977.x. arXiv: 1008.4767 [astro-ph.HE].

Ghisellini, G. and A. Celotti (1999). "Quasi-thermal comptonization and GRBs". In: *A&AS* 138, pp. 527–528. DOI: 10.1051/aas:1999339. eprint: astro-ph/9906145.

Ghisellini, G., A. Celotti, and D. Lazzati (2000). "Constraints on the emission mechanisms of gamma-ray bursts". In: *MNRAS* 313, pp. L1–L5. DOI: 10.1046/j.1365-8711.2000.03354.x. eprint: astro-ph/9912461.

Goldstein, A. et al. (2012). "The Fermi GBM Gamma-Ray Burst Spectral Catalog: The First Two Years". In: *ApJS* 199, 19, p. 19. DOI: 10.1088/0067-0049/199/1/19. arXiv: 1201.2981 [astro-ph.HE].

Golenetskii, S. et al. (2011). "Konus-wind observation of GRB 110205A." In: *GRB Coordinates Network, Circular Service, No. 11659, #1 (2011)* 11659.

Golenetskii, S. et al. (2013). "Konus-wind observation of GRB 130907A." In: *GRB Coordinates Network, Circular Service, No. 15203, #1 (2013)* 15203.

Golenetskii, S. V. et al. (1983). "Correlation between luminosity and temperature in gamma-ray burst sources". In: *Nature* 306, pp. 451–453. DOI: 10.1038/306451a0.

Goodman, J. (1986). "Are gamma-ray bursts optically thick?" In: *ApJ* 308, pp. L47–L50. DOI: 10.1086/184741.

Goodman, J., A. Dar, and S. Nussinov (1987). "Neutrino annihilation in Type II supernovae". In: *ApJ* 314, pp. L7–L10. DOI: 10.1086/184840.

Gorbovskoy, E. S. et al. (2012). "Prompt, early and afterglow optical observations of five γ-ray bursts: GRB 100901A, GRB 100902A, GRB 100905A, GRB 100906A and GRB 101020A". In: *MNRAS* 421, pp. 1874–1890. DOI: 10.1111/j.1365-2966.2012.20195.x. arXiv: 1111.3625 [astro-ph.HE].

Gruber, D. et al. (2014). "The Fermi GBM Gamma-Ray Burst Spectral Catalog: Four Years of Data". In: *ApJS* 211, 12, p. 12. DOI: 10.1088/0067-0049/211/1/12. arXiv: 1401.5069 [astro-ph.HE].

Guiriec, S. et al. (2011). "Detection of a Thermal Spectral Component in the Prompt Emission of GRB 100724B". In: *ApJ* 727, L33, p. L33. DOI: 10.1088/2041-8205/727/2/L33. arXiv: 1010.4601 [astro-ph.HE].

Guiriec, S. et al. (2015a). "GRB 131014A: A Laboratory for Studying the Thermal-like and Non-thermal Emissions in Gamma-Ray Bursts, and the New ${L^{nTh}}_i$-${E^{nTh,rest}}_{peak,i}$ Relation". In: *ApJ* 814, 10, p. 10. DOI: 10.1088/0004-637X/814/1/10. arXiv: 1507.06976 [astro-ph.HE].

Guiriec, S. et al. (2015b). "Toward a Better Understanding of the GRB Phenomenon: a New Model for GRB Prompt Emission and its Effects on the New ${L_i}^{NT}$-${E_{peak,i}}^{rest,NT}$ Relation". In: *ApJ* 807, 148, p. 148. DOI: 10.1088/0004-637X/807/2/148. arXiv: 1501.07028 [astro-ph.HE].

Guiriec, S. et al. (2016a). "A Unified Model for GRB Prompt Emission from Optical to γ-Rays: Exploring GRBs as Standard Candles". In: *ApJ* 831, L8, p. L8. DOI: 10.3847/2041-8205/831/1/L8. arXiv: 1606.07193 [astro-ph.HE].

Guiriec, S. et al. (2016b). "CGRO/BATSE Data Support the New Paradigm for GRB Prompt Emission and the New ${L_i}^{nTh}$-${E_{peak,i}}^{nTh,rest}$ Relation". In: *ApJ* 819, 79, p. 79. DOI: 10.3847/0004-637X/819/1/79. arXiv: 1507.04081 [astro-ph.HE].

Harrison, F. A. et al. (1999). "Optical and Radio Observations of the Afterglow from GRB 990510: Evidence for a Jet". In: *ApJ* 523, pp. L121–L124. DOI: 10.1086/312282. eprint: astro-ph/9905306.

Holland, S. T., E. A. Helder, and D. Xu (2012). "GRB 121123A: Swift/UVOT observations." In: *GRB Coordinates Network, Circular Service, No. 14003, #1 (2012)* 14003.

Holland, S. T. and M. Stamatikos (2011). "GRB 111123A: Swift/UVOT upper limits." In: *GRB Coordinates Network, Circular Service, No. 12597, #1 (2011)* 12597.

Huang, X.-L. et al. (2016). "Very Bright Prompt and Reverse Shock Emission of GRB 140512A". In: *ApJ* 833, 100, p. 100. DOI: 10.3847/1538-4357/833/1/100. arXiv: 1608.08884 [astro-ph.HE].

Kalberla, P. M. W. et al. (2005). "The Leiden/Argentine/Bonn (LAB) Survey of Galactic HI. Final data release of the combined LDS and IAR surveys with improved stray-radiation corrections". In: *A&A* 440, pp. 775–782. DOI: 10.1051/0004-6361:20041864. eprint: astro-ph/0504140.

Kaneko, Y. et al. (2006a). "The Complete Spectral Catalog of Bright BATSE Gamma-Ray Bursts". In: *ApJS* 166, pp. 298–340. DOI: 10.1086/505911. eprint: astro-ph/0601188.

— (2006b). "The Complete Spectral Catalog of Bright BATSE Gamma-Ray Bursts". In: *ApJS* 166, pp. 298–340. DOI: 10.1086/505911. eprint: astro-ph/0601188.

— (2006c). "The Complete Spectral Catalog of Bright BATSE Gamma-Ray Bursts". In: *ApJS* 166, pp. 298–340. DOI: 10.1086/505911. eprint: astro-ph/0601188.

Katz, J. I. (1994). "Low-frequency spectra of gamma-ray bursts". In: *ApJ* 432, pp. L107–L109. DOI: 10.1086/187523. eprint: astro-ph/9312034.

Klebesadel, R. W., I. B. Strong, and R. A. Olson (1973). "Observations of Gamma-Ray Bursts of Cosmic Origin". In: *ApJ* 182, p. L85. DOI: 10.1086/181225.

Klotz, A., M. Boer, and J. L. Atteia (2006). "GRB 060814: TAROT optical observations." In: *GRB Coordinates Network* 5448.

Klotz, A. et al. (2006). "Continuous optical monitoring during the prompt emission of <ASTROBJ>GRB 060111B</ASTROBJ>". In: *A&A* 451, pp. L39–L42. DOI: 10.1051/0004-6361:20065158. eprint: astro-ph/0604061.

Klotz, A. et al. (2009). "Early Optical Observations of Gamma-Ray Bursts by the TAROT Telescopes: Period 2001-2008". In: *AJ* 137, pp. 4100–4108. DOI: 10.1088/0004-6256/137/5/4100. arXiv: 0902.0898 [astro-ph.HE].

Kobayashi, S., T. Piran, and R. Sari (1997). "Can Internal Shocks Produce the Variability in Gamma-Ray Bursts?" In: *ApJ* 490, p. 92. DOI: 10.1086/512791. eprint: astro-ph/9705013.

Kopač, D. et al. (2013). "GRB 090727 and Gamma-Ray Bursts with Early-time Optical Emission". In: *ApJ* 772, 73, p. 73. DOI: 10.1088/0004-637X/772/1/73. arXiv: 1305.6897 [astro-ph.HE].

Kopač, D. et al. (2015). "Limits on Optical Polarization during the Prompt Phase of GRB 140430A". In: *ApJ* 813, 1, p. 1. DOI: 10.1088/0004-637X/813/1/1. arXiv: 1509.03099 [astro-ph.HE].

Kouveliotou, C. et al. (1993). "Identification of two classes of gamma-ray bursts". In: *ApJ* 413, pp. L101–L104. DOI: 10.1086/186969.

Kumar, P. and E. McMahon (2008). "A general scheme for modelling γ-ray burst prompt emission". In: *MNRAS* 384, pp. 33–63. DOI: 10.1111/j.1365-2966.2007.12621.x. arXiv: 0802.2704.

Kumar, P. and A. Panaitescu (2000). "Afterglow Emission from Naked Gamma-Ray Bursts". In: *ApJ* 541, pp. L51–L54. DOI: 10.1086/312905. eprint: astro-ph/0006317.

Lazzati, D. and R. Perna (2003). "Time-dependent photoionization in a dusty medium - III. The effect of dust on the photoionization of metals". In: *MNRAS* 340, pp. 694–704. DOI: 10.1046/j.1365-8711.2003.06334.x. eprint: astro-ph/0212105.

Lazzati, D. et al. (2000). "Compton-dragged Gamma-Ray Bursts Associated with Supernovae". In: *ApJ* 529, pp. L17–L20. DOI: 10.1086/312452. eprint: astro-ph/9910191.

Liang, E. et al. (1997). "Physical Model of Gamma-Ray Burst Spectral Evolution". In: *ApJ* 479, pp. L35–L38. DOI: 10.1086/310568.

Lien, A. et al. (2016). "The Third Swift Burst Alert Telescope Gamma-Ray Burst Catalog". In: *ApJ* 829, 7, p. 7. DOI: 10.3847/0004-637X/829/1/7. arXiv: 1606.01956 [astro-ph.HE].

Lipunov, V. M. et al. (2004). "MASTER: The Mobile Astronomical System of Telescope-Robots". In: *Astronomische Nachrichten* 325, pp. 580–582. DOI: 10.1002/asna.200410284. eprint: astro-ph/0411757.

Lithwick, Y. and R. Sari (2001). "Lower Limits on Lorentz Factors in Gamma-Ray Bursts". In: *ApJ* 555, pp. 540–545. DOI: 10.1086/321455. eprint: astro-ph/0011508.

Lloyd, N. M. and V. Petrosian (2000). "Synchrotron Radiation as the Source of Gamma-Ray Burst Spectra". In: *ApJ* 543, pp. 722–732. DOI: 10.1086/317125. eprint: astro-ph/0007061.

Lü, H.-J. et al. (2017). "Extremely bright GRB 160625B with multi-episodes emission: Evidences for long-term ejecta evolution". In: *ArXiv e-prints*. arXiv: 1702.01382 [astro-ph.HE].

Margutti, R. et al. (2010). "Lag-luminosity relation in γ-ray burst X-ray flares: a direct link to the prompt emission". In: *MNRAS* 406, pp. 2149–2167. DOI: 10.1111/j.1365-2966.2010.16824.x. arXiv: 1004.1568 [astro-ph.HE].

Maselli, A. et al. (2014). "GRB 130427A: A Nearby Ordinary Monster". In: *Science* 343, pp. 48–51. DOI: 10.1126/science.1242279. arXiv: 1311.5254 [astro-ph.HE].

Medvedev, M. V. (2000). "Theory of "Jitter" Radiation from Small-Scale Random Magnetic Fields and Prompt Emission from Gamma-Ray Burst Shocks". In: *ApJ* 540, pp. 704–714. DOI: 10.1086/309374. eprint: astro-ph/0001314.

Meegan, C. et al. (2009). "The Fermi Gamma-ray Burst Monitor". In: *ApJ* 702, 791-804, pp. 791–804. DOI: 10.1088/0004-637X/702/1/791. arXiv: 0908.0450 [astro-ph.IM].

Meegan, C. A. et al. (1992). "Spatial distribution of gamma-ray bursts observed by BATSE". In: *Nature* 355, pp. 143–145. DOI: 10.1038/355143a0.

Meegan, C. A. et al. (1996). "The Third BATSE Gamma-Ray Burst Catalog". In: *ApJS* 106, p. 65. DOI: 10.1086/192329.

Melandri, A. et al. (2008). "The Early-Time Optical Properties of Gamma-Ray Burst Afterglows". In: *ApJ* 686, pp. 1209–1230. DOI: 10.1086/591243. arXiv: 0804.0811.

Mészáros, P. and M. J. Rees (1997). "Optical and Long-Wavelength Afterglow from Gamma-Ray Bursts". In: *ApJ* 476, pp. 232–237. DOI: 10.1086/303625. eprint: astro-ph/9606043.

— (2000). "Steep Slopes and Preferred Breaks in Gamma-Ray Burst Spectra: The Role of Photospheres and Comptonization". In: *ApJ* 530, pp. 292–298. DOI: 10.1086/308371. eprint: astro-ph/9908126.

Mundell, C. G. et al. (2007). "The Remarkable Afterglow of GRB 061007: Implications for Optical Flashes and GRB Fireballs". In: *ApJ* 660, pp. 489–495. DOI: 10.1086/512605. eprint: astro-ph/0610660.

Nakar, E., S. Ando, and R. Sari (2009). "Klein-Nishina Effects on Optically Thin Synchrotron and Synchrotron Self-Compton Spectrum". In: *ApJ* 703, pp. 675–691. DOI: 10.1088/0004-637X/703/1/675. arXiv: 0903.2557 [astro-ph.HE].

Narayana Bhat, P. et al. (2016). "The Third Fermi GBM Gamma-Ray Burst Catalog: The First Six Years". In: *ApJS* 223, 28, p. 28. DOI: 10.3847/0067-0049/223/2/28. arXiv: 1603.07612 [astro-ph.HE].

Nava, L. et al. (2011a). "Fermi/GBM and BATSE gamma-ray bursts: comparison of the spectral properties". In: *MNRAS* 415, pp. 3153–3162. DOI: 10.1111/j.1365-2966.2011.18928.x. arXiv: 1012.3968 [astro-ph.HE].

— (2011b). "Spectral properties of 438 GRBs detected by Fermi/GBM". In: *A&A* 530, A21, A21. DOI: 10.1051/0004-6361/201016270. arXiv: 1012.2863 [astro-ph.HE].

Nava, L. et al. (2018). "THESEUS and Gamma-Ray Bursts: a valuable contribution to the understanding of prompt emission". In: *ArXiv e-prints*. arXiv: 1802.01683 [astro-ph.HE].

Norris, J. P. et al. (1986). "Spectral evolution of pulse structures in gamma-ray bursts". In: *ApJ* 301, pp. 213–219. DOI: 10.1086/163889.

Norris, J. P. et al. (2005). "Long-Lag, Wide-Pulse Gamma-Ray Bursts". In: *ApJ* 627, pp. 324–345. DOI: 10.1086/430294. eprint: astro-ph/0503383.

Oates, S. R. and M. de Pasquale (2011). "GRB110102A: Swift/UVOT observations." In: *GRB Coordinates Network, Circular Service, No. 11514, #1 (2011)* 11514.

Oates, S. R. and D. Grupe (2011). "GRB111103B Swift/UVOT upper limits." In: *GRB Coordinates Network, Circular Service, No. 12528, #1 (2011)* 12528.

Oates, S. R. and A. Y. Lien (2014). "GRB 140206A: Swift/UVOT detection." In: *GRB Coordinates Network, Circular Service, No. 15795, #1 (2014)* 15795.

Oates, S. R. et al. (2009). "A statistical study of gamma-ray burst afterglows measured by the Swift Ultraviolet Optical Telescope". In: *MNRAS* 395, pp. 490–503. DOI: 10.1111/j.1365-2966.2009.14544.x. arXiv: 0901.3597 [astro-ph.HE].

Paczynski, B. (1986). "Gamma-ray bursters at cosmological distances". In: *ApJ* 308, pp. L43–L46. DOI: 10.1086/184740.

Page, K. L. et al. (2007). "GRB 061121: Broadband Spectral Evolution through the Prompt and Afterglow Phases of a Bright Burst". In: *ApJ* 663, pp. 1125–1138. DOI: 10.1086/518821. arXiv: 0704.1609.

Page, K. L. et al. (2009). "Multiwavelength observations of the energetic GRB 080810: detailed mapping of the broad-band spectral evolution". In: *MNRAS* 400, pp. 134–146. DOI: 10.1111/j.1365-2966.2009.15462.x. arXiv: 0907.4578 [astro-ph.HE].

Panaitescu, A. and P. Kumar (2007). "A unified picture for the γ-ray and prompt optical emissions of GRB 990123". In: *MNRAS* 376, pp. 1065–1072. DOI: 10.1111/j.1365-2966.2007.11398.x. eprint: astro-ph/0612504.

Parker, E. N. (1957). "Sweet's Mechanism for Merging Magnetic Fields in Conducting Fluids". In: *J. Geophys. Res.* 62, pp. 509–520. DOI: 10.1029/JZ062i004p00509.

Pe'er, A. and B. Zhang (2006). "Synchrotron Emission in Small-Scale Magnetic Fields as a Possible Explanation for Prompt Emission Spectra of Gamma-Ray Bursts". In: *ApJ* 653, pp. 454–461. DOI: 10.1086/508681. eprint: astro-ph/0605641.

Peng, F.-K. et al. (2014). "Photosphere Emission in the X-Ray Flares of Swift Gamma-Ray Bursts and Implications for the Fireball Properties". In: *ApJ* 795, 155, p. 155. DOI: 10.1088/0004-637X/795/2/155. arXiv: 1409.5261 [astro-ph.HE].

Perna, R. and D. Lazzati (2002). "Time-dependent Photoionization in a Dusty Medium. I. Code Description and General Results". In: *ApJ* 580, pp. 261–277. DOI: 10.1086/343081. eprint: astro-ph/0206445.

Perna, R., D. Lazzati, and F. Fiore (2003). "Time-dependent Photoionization in a Dusty Medium. II. Evolution of Dust Distributions and Optical Opacities". In: *ApJ* 585, pp. 775–784. DOI: 10.1086/346109. eprint: astro-ph/0211235.

Piran, T. and A. Shemi (1993). "Fireballs in the Galactic halo and gamma-ray bursts". In: *ApJ* 403, pp. L67–L69. DOI: 10.1086/186723. eprint: astro-ph/9211009.

Popham, R., S. E. Woosley, and C. Fryer (1999). "Hyperaccreting Black Holes and Gamma-Ray Bursts". In: *ApJ* 518, pp. 356–374. DOI: 10.1086/307259. eprint: astro-ph/9807028.

Preece, R. D. et al. (1998). "The Synchrotron Shock Model Confronts a "Line of Death" in the BATSE Gamma-Ray Burst Data". In: *ApJ* 506, pp. L23–L26. DOI: 10.1086/311644. eprint: astro-ph/9808184.

— (2000). "The BATSE Gamma-Ray Burst Spectral Catalog. I. High Time Resolution Spectroscopy of Bright Bursts Using High Energy Resolution Data". In: *ApJS* 126, pp. 19–36. DOI: 10.1086/313289. eprint: astro-ph/9908119.

Pritchard, T. and E. Troja (2011). "GRB110119: Swift/UVOT detection." In: *GRB Coordinates Network, Circular Service, No. 11587, #1 (2011)* 11587.

Protassov, R. et al. (2002). "Statistics, Handle with Care: Detecting Multiple Model Components with the Likelihood Ratio Test". In: *ApJ* 571, pp. 545–559. DOI: 10.1086/339856. eprint: astro-ph/0201547.

Racusin, J. L. et al. (2008). "Broadband observations of the naked-eye γ-ray burst GRB080319B". In: *Nature* 455, pp. 183–188. DOI: 10.1038/nature07270. arXiv: 0805.1557.

Ramirez-Ruiz, E. and E. E. Fenimore (2000). "Pulse Width Evolution in Gamma-Ray Bursts: Evidence for Internal Shocks". In: *ApJ* 539, pp. 712–717. DOI: 10.1086/309260. eprint: astro-ph/9910273.

Ravasio, M. E. et al. (2018). "Consistency with synchrotron emission in the bright GRB 160625B observed by Fermi". In: *A&A* 613, A16, A16. DOI: 10.1051/0004-6361/201732245. arXiv: 1711.03106 [astro-ph.HE].

Rees, M. J. and P. Meszaros (1994a). "Unsteady outflow models for cosmological gamma-ray bursts". In: *ApJ* 430, pp. L93–L96. DOI: 10.1086/187446. eprint: astro-ph/9404038.

— (1994b). "Unsteady outflow models for cosmological gamma-ray bursts". In: *ApJ* 430, pp. L93–L96. DOI: 10.1086/187446. eprint: astro-ph/9404038.

Rees, M. J. and P. Mészáros (2005). "Dissipative Photosphere Models of Gamma-Ray Bursts and X-Ray Flashes". In: *ApJ* 628, pp. 847–852. DOI: 10.1086/430818. eprint: astro-ph/0412702.

Rhoads, J. E. (1999). "The Dynamics and Light Curves of Beamed Gamma-Ray Burst Afterglows". In: *ApJ* 525, pp. 737–749. DOI: 10.1086/307907. eprint: astro-ph/9903399.

Romano, P. et al. (2006). "Panchromatic study of GRB 060124: from precursor to afterglow". In: *A&A* 456, pp. 917–927. DOI: 10.1051/0004-6361:20065071. eprint: astro-ph/0602497.

Rossi, A. et al. (2011). "The Swift/Fermi GRB 080928 from 1 eV to 150 keV". In: *A&A* 529, A142, A142. DOI: 10.1051/0004-6361/201015324. arXiv: 1007.0383 [astro-ph.HE].

Rybicki, G. B. and A. P. Lightman (1986). *Radiative Processes in Astrophysics*, p. 400.

Ryde, F. and A. Pe'er (2009). "Quasi-blackbody Component and Radiative Efficiency of the Prompt Emission of Gamma-ray Bursts". In: *ApJ* 702, pp. 1211–1229. DOI: 10.1088/0004-637X/702/2/1211. arXiv: 0811.4135.

Ryde, F. et al. (2010). "Identification and Properties of the Photospheric Emission in GRB090902B". In: *ApJ* 709, pp. L172–L177. DOI: 10.1088/2041-8205/709/2/L172. arXiv: 0911.2025 [astro-ph.HE].

Sakamoto, T. et al. (2005). "Global Characteristics of X-Ray Flashes and X-Ray-Rich Gamma-Ray Bursts Observed by HETE-2". In: *ApJ* 629, pp. 311–327. DOI: 10.1086/431235.

Sakamoto, T. et al. (2011a). "GRB 110205A: Swift/BAT and Suzaku/WAM joint spectral analysis." In: *GRB Coordinates Network, Circular Service, No. 11692, #1 (2011)* 11692.

Sakamoto, T. et al. (2011b). "The Second Swift Burst Alert Telescope Gamma-Ray Burst Catalog". In: *ApJS* 195, 2, p. 2. DOI: 10.1088/0067-0049/195/1/2. arXiv: 1104.4689 [astro-ph.HE].

Sari, R., R. Narayan, and T. Piran (1996). "Cooling Timescales and Temporal Structure of Gamma-Ray Bursts". In: *ApJ* 473, p. 204. DOI: 10.1086/178136. eprint: astro-ph/9605005.

Sari, R., T. Piran, and R. Narayan (1998). "Spectra and Light Curves of Gamma-Ray Burst Afterglows". In: *ApJ* 497, pp. L17–L20. DOI: 10.1086/311269. eprint: astro-ph/9712005.

Savchenko, V. and A. Neronov (2009). "Where are Swift γ-ray bursts beyond the 'synchrotron deathline'?" In: *MNRAS* 396, pp. 935–945. DOI: 10.1111/j.1365-2966.2009.14747.x. arXiv: 0903.3556 [astro-ph.HE].

Scargle, J. D. (1998). "Studies in Astronomical Time Series Analysis. V. Bayesian Blocks, a New Method to Analyze Structure in Photon Counting Data". In: *ApJ* 504, pp. 405–418. DOI: 10.1086/306064. eprint: astro-ph/9711233.

Schlafly, E. F. and D. P. Finkbeiner (2011). "Measuring Reddening with Sloan Digital Sky Survey Stellar Spectra and Recalibrating SFD". In: *ApJ* 737, 103, p. 103. DOI: 10.1088/0004-637X/737/2/103. arXiv: 1012.4804 [astro-ph.GA].

Schmidl, S., D. A. Kann, and J. Greiner (2013). "GRB 130514A: GROND optical-NIR afterglow discovery and photo-z." In: *GRB Coordinates Network, Circular Service, No. 14634, #1 (2013)* 14634.

Shemi, A. and T. Piran (1990). "The appearance of cosmic fireballs". In: *ApJ* 365, pp. L55–L58. DOI: 10.1086/185887.

Starling, R. L. C. et al. (2008). "Swift captures the spectrally evolving prompt emission of GRB070616". In: *MNRAS* 384, pp. 504–514. DOI: 10.1111/j.1365-2966.2007.12763.x. arXiv: 0711.3753.

Stern, B. E. and J. Poutanen (2004). "Gamma-ray bursts from synchrotron self-Compton emission". In: *MNRAS* 352, pp. L35–L39. DOI: 10.1111/j.1365-2966.2004.08163.x. eprint: astro-ph/0405488.

Stratta, G. et al. (2018). "THESEUS: A key space mission concept for Multi-Messenger Astrophysics". In: *Advances in Space Research* 62, pp. 662–682. DOI: 10.1016/j.asr.2018.04.013. arXiv: 1712.08153 [astro-ph.HE].

Tavani, M. (1996). "A Shock Emission Model for Gamma-Ray Bursts. II. Spectral Properties". In: *ApJ* 466, p. 768. DOI: 10.1086/177551.

Thöne, C. C. et al. (2010). "Photometry and spectroscopy of GRB 060526: a detailed study of the afterglow and host galaxy of a z = 3.2 gamma-ray burst". In: *A&A* 523, A70, A70. DOI: 10.1051/0004-6361/200810340. arXiv: 0806.1182.

Toy, V. L. et al. (2016). "Optical and Near-infrared Observations of SN 2013dx Associated with GRB 130702A". In: *ApJ* 818, 79, p. 79. DOI: 10.3847/0004-637X/818/1/79. arXiv: 1508.00575 [astro-ph.HE].

Troja, E. et al. (2017). "Significant and variable linear polarization during the prompt optical flash of GRB 160625B". In: *Nature* 547.7664. Letter, pp. 425–427. ISSN: 0028-0836. URL: http://dx.doi.org/10.1038/nature23289.

Trotter, A. et al. (2015). "GRB 151021A: Skynet PROMPT-CTIO/DSO17 observations of the optical afterglow." In: *GRB Coordinates Network, Circular Service, No. 18472, #1 (2015)* 18472.

Uhm, Z. L. and B. Zhang (2014). "Fast-cooling synchrotron radiation in a decaying magnetic field and γ-ray burst emission mechanism". In: *Nature Physics* 10, pp. 351–356. DOI: 10.1038/nphys2932. arXiv: 1303.2704 [astro-ph.HE].

Usov, V. V. (1992). "Millisecond pulsars with extremely strong magnetic fields as a cosmological source of gamma-ray bursts". In: *Nature* 357, pp. 472–474. DOI: 10.1038/357472a0.

van Paradijs, J. et al. (1997). "Transient optical emission from the error box of the γ-ray burst of 28 February 1997". In: *Nature* 386, pp. 686–689. DOI: 10.1038/386686a0.

Veres, P. et al. (2015). "Early-time VLA Observations and Broadband Afterglow Analysis of the Fermi/LAT Detected GRB 130907A". In: *ApJ* 810, 31, p. 31. DOI: 10.1088/0004-637X/810/1/31. arXiv: 1411.7368 [astro-ph.HE].

Vestrand, W. T. et al. (2005). "A link between prompt optical and prompt γ-ray emission in γ-ray bursts". In: *Nature* 435, pp. 178–180. DOI: 10.1038/nature03515. eprint: astro-ph/0503521.

Vetere, L. et al. (2009). "Swift observations of GRB 090715B." In: *GCN Report* 236.

Virgili, F. J. et al. (2013). "GRB 091024A and the Nature of Ultra-long Gamma-Ray Bursts". In: *ApJ* 778, 54, p. 54. DOI: 10.1088/0004-637X/778/1/54. arXiv: 1310.0313 [astro-ph.HE].

Vurm, I. and A. M. Beloborodov (2016). "Radiative Transfer Models for Gamma-Ray Bursts". In: *ApJ* 831, 175, p. 175. DOI: 10.3847/0004-637X/831/2/175. arXiv: 1506.01107 [astro-ph.HE].

Wang, Y.-Z. et al. (2017). "Evaluating the Bulk Lorentz Factors of Outflow Material: Lessons Learned from the Extremely Energetic Outburst GRB 160625B". In: *ApJ* 836, 81, p. 81. DOI: 10.3847/1538-4357/aa56c6. arXiv: 1611.04879 [astro-ph.HE].

Wei, J. et al. (2016). "The Deep and Transient Universe in the SVOM Era: New Challenges and Opportunities - Scientific prospects of the SVOM mission". In: *ArXiv e-prints*. arXiv: 1610.06892 [astro-ph.IM].

Weibel, Erich S. (1959). "Spontaneously Growing Transverse Waves in a Plasma Due to an Anisotropic Velocity Distribution". In: *Phys. Rev. Lett.* 2 (3), pp. 83–84. DOI: 10.1103/PhysRevLett.2.83. URL: https://link.aps.org/doi/10.1103/PhysRevLett.2.83.

Wilms, J., A. Allen, and R. McCray (2000). "On the Absorption of X-Rays in the Interstellar Medium". In: *ApJ* 542, pp. 914–924. DOI: 10.1086/317016. eprint: astro-ph/0008425.

Woosley, S. E. (1993). "Gamma-ray bursts from stellar mass accretion disks around black holes". In: *ApJ* 405, pp. 273–277. DOI: 10.1086/172359.

Woosley, S. E. and A. Heger (2006). "The Progenitor Stars of Gamma-Ray Bursts". In: *ApJ* 637, pp. 914–921. DOI: 10.1086/498500. eprint: astro-ph/0508175.

Woźniak, P. R. et al. (2009). "Gamma-Ray Burst at the Extreme: "The Naked-Eye Burst" GRB 080319B". In: *ApJ* 691, pp. 495–502. DOI: 10.1088/0004-637X/691/1/495. arXiv: 0810.2481.

Xu, D. et al. (2016). "GRB 160625B: VLT/X-shooter redshift." In: *GRB Coordinates Network, Circular Service, No. 19600, #1 (2016)* 9600.

Yu, H.-F. et al. (2015). "The sharpness of gamma-ray burst prompt emission spectra". In: *A&A* 583, A129, A129. DOI: 10.1051/0004-6361/201527015. arXiv: 1507.05589 [astro-ph.HE].

Yu, H.-F. et al. (2016). "The Fermi GBM gamma-ray burst time-resolved spectral catalog: brightest bursts in the first four years". In: *A&A* 588, A135, A135. DOI: 10.1051/0004-6361/201527509. arXiv: 1601.05206 [astro-ph.HE].

Yuan, F. et al. (2010). "GRB 081008: From Burst to Afterglow and the Transition Phase in Between". In: *ApJ* 711, pp. 870–880. DOI: 10.1088/0004-637X/711/2/870. arXiv: 1002.0581 [astro-ph.HE].

Zalamea, I. and A. M. Beloborodov (2011). "Neutrino heating near hyper-accreting black holes". In: *MNRAS* 410, pp. 2302–2308. DOI: 10.1111/j.1365-2966.2010.17600.x. arXiv: 1003.0710 [astro-ph.HE].

Zhang, B. et al. (2006). "Physical Processes Shaping Gamma-Ray Burst X-Ray Afterglow Light Curves: Theoretical Implications from the Swift X-Ray Telescope Observations". In: *ApJ* 642, pp. 354–370. DOI: 10.1086/500723. eprint: astro-ph/0508321.

Zhang, B.-B. et al. (2016). "Transition from Fireball to Poynting-flux-dominated Outflow in Three-Episode GRB 160625B". In: *ArXiv e-prints*. arXiv: 1612.03089 [astro-ph.HE].

Zheng, W. et al. (2012). "Panchromatic Observations of the Textbook GRB 110205A: Constraining Physical Mechanisms of Prompt Emission and Afterglow". In: *ApJ* 751, 90, p. 90. DOI: 10.1088/0004-637X/751/2/90. arXiv: 1111.0283 [astro-ph.HE].

Zheng, Z., Y. Lu, and Y.-H. Zhao (2006). "A Comptonization Model for the Prompt Optical and Infrared Emission of GRB 041219A". In: *ApJ* 646, pp. L25–L28. DOI: 10.1086/506608. eprint: astro-ph/0606312.